

**BIOMECHANICS OF *C. ELEGANS***



# BIOMECHANICS OF *C. ELEGANS* AS PROBED BY MICROPIPETTE DEFLECTION

By

MATILDA BACKHOLM, B.Sc., M.Sc.

A Thesis

Submitted to the School of Graduate Studies  
in Partial Fulfillment of the Requirements  
for the Degree

Doctor of Philosophy

McMaster University

©Copyright by Matilda Backholm, 2015.

DOCTOR OF PHILOSOPHY (2015)  
(Physics)

McMaster University  
Hamilton, Ontario

TITLE: Biomechanics of *C. elegans* as probed by micropipette deflection

AUTHOR: Matilda Backholm, B.Sc., M.Sc. (University of Helsinki, Aarhus University)

SUPERVISOR: Dr. Kari Dalnoki-Veress

NUMBER OF PAGES: xi, 147

# Abstract

In this PhD thesis, a novel experimental technique has been implemented to study the variables controlling the undulatory locomotion of a tiny worm. Well known for its elegant slithering motion and simple biology, the millimetre-sized nematode *Caenorhabditis elegans* was chosen to serve as a model organism for our work. The emphasis of this thesis, as embodied by three separate research projects, has been to study the passive and active biomechanical properties of *C. elegans*, as well as to investigate inter-worm interactions. Micropipette deflection has been used to directly probe forces in a time-resolved manner and with high dynamic resolution. The viscoelastic material properties of *C. elegans* were explored on a biologically and structurally relevant length scale, and the elastic properties of the body were quantified. Furthermore, the soft tissue was found to behave as a shear-thinning fluid: a non-Newtonian property that has interesting implications on the undulatory locomotion strategy of the nematode. Micropipette deflection furthermore allowed for measurements of the active swimming dynamics of *C. elegans*. Our experiments quantified the drag coefficients of the tiny worm as well as the viscous forces present in its swimming motion. Swimming experiments were performed in a normal buffer solution, in the confinement of solid boundaries, as well as in fluids with increased viscosities, and the dynamics of the gait modulating worm was investigated. Finally, the binary interactions between two swimming nematodes were studied, utilizing the high micromechanical control provided by the micropipette-based technique. Our findings provide new insight into the physics of undulatory locomotion and active materials in general.

# Preface

This is a “sandwich” thesis and thereby first includes an in-depth introduction to the concepts and theories necessary to grasp the general focus of my PhD research. The introduction is followed by a chapter describing the experimental details relevant to this study, as well as any other advice that could be helpful for someone pursuing a similar scientific pathway. The publications that form the framework for this work are then summarized and have furthermore been included at the end of the thesis. As interdisciplinary science is highly collaborative, a clear description of my own contribution to each project is given for each publication. The concluding chapter finally summarizes this work with a focus on the common theme of the thesis, highlighting our most significant findings as well as future avenues that could be explored.

# Acknowledgements

I believe it takes an entire university to raise a scientist, and there are in other words a lot of people I want to thank. First of all, I would like to acknowledge the Department of Physics and Astronomy at McMaster for setting up a supportive and organized graduate student environment. Approaching David, Tina, Cheryl, Mara, and Rose in the main office has always been a real pleasure and of tremendous help! I also thank faculty members Cécile, Laura, Maikel, and An-Chang for taking the time to discuss science and life in academia with me, and for acting as professional mentors and role models.

As research at its best is highly collaborative, I am very fortunate to have many collaborators to thank. Will at U of T introduced me to the wonderful world of worms at the very beginning of my PhD studies, and has since then provided great insight into our research and repeatedly opened up his lab to me, letting me steal more worms than I could possibly need. Having the opportunity to work with Yegor in Will's lab has also been very rewarding and fun! Since the beginning of my time at McMaster, I have been a member of the CREATE IDEM project, which turned out to be a fantastic learning experience. I thank Harald for his everlasting enthusiasm as well as Rachelle and Alison for putting up with me as a non-chemist! I have also had the absolute privilege to work with Élie, Michael, and Tom at the ESPCI in Paris. The Paris team has relentlessly introduced me to their vast universe of scaling concepts and thin film equations, and has easily become the best reason for any future trips to France! During my last summer at McMaster, I also had the great opportunity to learn about lipid bilayer research from Jenn and Maikel.

The graduate student community in ABB has been essential for my wellbeing in Canada. I especially thank the Liquid State team for their friendship; celebrating our burning defeats and occasional victories at the Phoenix was a highlight of my summers! Surviving in Hamilton would not have been possible without my wonderful research group. I am ever grateful for getting to know Jess, Josh, Sara, Mark, Rob, Olli, Paul, Raffi, Mike, and Solomon! You guys quickly became my family and life in the lab was never boring! Exploring the dark corners of grad life and science with so many talented and ambitious friends was a true honour! I especially thank Raffi for joining my lonely worm team; bouncing ideas and frustrations off you has been

incredibly helpful and I am very excited about the science we produced together! I have also had the great pleasure to co-supervise undergraduates Richard, Sean, and Alex in our lab, something I probably learned more from than you did. Here I would also like to thank the crawling members of our lab: although small, the worms never failed me in providing exciting new research results and ideas!

Scientifically, I could not have imagined a more challenging and rewarding environment than what I found in Kari's lab. Words fail me to express my gratitude for the opportunities I have been provided and the cutting-edge training I have received. Kari, you have been an extraordinary supervisor and mentor! My PhD time has been a true roller-coaster ride and you have excitedly celebrated all of our victories, but also always been there during the defeats. I am immensely thankful for your understanding and support!

Although geographically far away, my family and friends in Finland have been a great support, always providing a healthy reminder about life outside the grad student bubble. In terms of actually finishing this PhD with any sign of sanity left, I owe Kris the greatest of all thanks. My overly ambitious explorations in Canada have not been easy on you, and I am honestly amazed by your strength and determination. Your everlasting support and encouragement has, sometimes quite literally, carried me through this time and I hope you know what an important part you have played! Sharing this adventure with you has been a fantastic experience and I am looking very much forward to whatever comes next! Finally, I want to thank Edvin for introducing me to new areas of soft matter physics, and allowing me to finish the work for this thesis.

# Contents

Abstract . . . . .	iii
Preface . . . . .	iv
Acknowledgements . . . . .	v
List of Figures . . . . .	xi
<b>1 Introduction</b>	<b>1</b>
1.1 The model organism <i>C. elegans</i> . . . . .	3
1.1.1 Anatomy . . . . .	4
1.1.2 Life stages and development . . . . .	6
1.2 Material properties of soft condensed matter . . . . .	7
1.2.1 Elasticity . . . . .	8
1.2.2 Viscoelasticity . . . . .	11
1.2.3 Complex fluids . . . . .	17
1.3 Undulatory microswimming . . . . .	18
1.3.1 Flow at low Reynolds numbers . . . . .	19
1.3.2 Propulsion at low Reynolds numbers . . . . .	21
1.4 Interactions in active materials . . . . .	25
1.4.1 Knots and tangles . . . . .	27
1.5 Physical studies on <i>C. elegans</i> . . . . .	29
1.5.1 Passive material properties . . . . .	29
1.5.2 Active undulatory locomotion . . . . .	32
1.5.3 Collective swimming and crawling . . . . .	35

## CONTENTS

<b>2</b>	<b>Experimental details</b>	<b>37</b>
2.1	Micropipette deflection . . . . .	37
2.1.1	Pipette manufacturing . . . . .	39
2.1.2	Pipette calibration . . . . .	40
2.1.3	Bending experiment . . . . .	43
2.1.4	Swimming experiment . . . . .	45
2.1.5	Tangling experiment . . . . .	46
2.2	<i>C. elegans</i> maintenance . . . . .	47
2.2.1	Materials . . . . .	48
2.2.2	Chunking . . . . .	50
2.2.3	Picking . . . . .	51
<b>3</b>	<b>Summary of papers</b>	<b>53</b>
3.1	Paper I: Viscoelasticity . . . . .	55
3.2	Paper II: Complex relaxation . . . . .	57
3.3	Paper III: Swimming dynamics . . . . .	58
3.4	Paper IV: Swimming near boundaries . . . . .	59
3.5	Paper V: High-viscosity swimming . . . . .	60
3.6	Paper VI: Tangling . . . . .	61
<b>4</b>	<b>Conclusions and outlook</b>	<b>63</b>
	<b>Bibliography</b>	<b>66</b>
<b>A</b>	<b>Appended papers</b>	<b>81</b>
A.1	Paper I . . . . .	81
A.2	Paper II . . . . .	91
A.3	Paper III . . . . .	97
A.4	Paper IV . . . . .	105
A.5	Paper V . . . . .	121
A.6	Paper VI . . . . .	133
<b>B</b>	<b>List of additional papers</b>	<b>141</b>
B.1	Crawling dynamics . . . . .	141

## CONTENTS

B.2	Hole relaxation in viscous films . . . . .	142
B.3	Levelling of trenches in viscous films . . . . .	142
B.4	Mechanical properties of hydrogels . . . . .	143
<b>C</b>	<b>Derivations</b>	<b>145</b>
C.1	Area moment of inertia of a hollow cylinder . . . . .	145
C.2	Three-point bending of simply supported beam . . . . .	146

## CONTENTS

# List of Figures

1.1	<i>Caenorhabditis elegans</i> . . . . .	3
1.2	Cross section of <i>C. elegans</i> . . . . .	5
1.3	Life stages of <i>C. elegans</i> . . . . .	7
1.4	Transverse vs. longitudinal stiffness . . . . .	9
1.5	Elasticity of a cylinder . . . . .	10
1.6	The Maxwell model . . . . .	13
1.7	The Kelvin-Voigt model . . . . .	14
1.8	The Standard Linear Solid model . . . . .	16
1.9	Resistive force theory . . . . .	23
1.10	Conway tangles . . . . .	28
2.1	Comparison between micro-mechanical probes . . . . .	38
2.2	Micropipette deflection on <i>C. elegans</i> . . . . .	39
2.3	Calibration of straight pipettes . . . . .	41
2.4	Calibration of bent pipettes . . . . .	42
2.5	Bending experiment . . . . .	43
2.6	Swimming experiment . . . . .	46
2.7	Tangling experiment . . . . .	47
2.8	Effect of BDM and muscimol on <i>C. elegans</i> . . . . .	49
C.1	Area moment of inertia of a hollow cylinder . . . . .	145
C.2	Three-point bending of simply supported cylinder . . . . .	146

## LIST OF FIGURES

# Chapter 1

## Introduction

Undulatory locomotion is ubiquitous in nature and used by crawlers and swimmers like snakes and spermatozoa, spanning nearly seven orders of magnitude in length. The smooth, slithering motion of these slender bodies has fascinated researchers for nearly a century [1–7]. To this day, however, the complex interplay between the perfectly synchronized muscle contractions, the bending of the soft biological tissue, and the interactions between the animal body and the surrounding mud, sand, or water, is still not fully understood [8]. Natural evolution has produced an efficient and agile undulator able to interact with its surrounding environment through modulating its gait between crawling on high-friction surfaces [6, 7, 9] or in high-viscosity fluids [10], and swimming when immersed in water [11, 12] or sand [13, 14]. Despite intense efforts made into mimicing the properties of a natural crawler, the same performance has not been reproduced artificially [15, 16]. From a purely physical perspective, the complexity of the system can be narrowed down into two key questions that outline our understanding of undulatory locomotion in general, namely: What are the ideal passive properties of a crawler and how does it interact with its surrounding medium?

The passive material properties of a crawler determine its ability to bend its own body and thereby produce the required undulatory motion [17]. An optimization of the energy spent internally and externally has to be made, and all efforts spent on the continuous bending of the body (passive) should be minimized in order to maximize the energy spent on pushing off against the surrounding media to move forward. An ideal oscillatory system would be that of a spring with purely elastic material proper-

ties and no energy dissipation. In real biological systems, however, such a simplification would be unrealistic as tissue is composed of soft building blocks that typically possess viscous components, where damping causes energy to dissipate. Furthermore, the viscoelastic properties can be highly nonlinear and complex. Understanding these materials demand detailed experimental studies combined with physical modelling of the system.

Once the first key question dealing with the passive properties is addressed, the natural transition is to probe the active dynamics of the undulator. Defining the ideal interactions between undulatory swimmers or crawlers and their surrounding media is of importance, as these are essential for any propulsion to take place [18]. In viscous environments, any moving object (or stationary object in a moving fluid) is opposed by drag forces, which dissipate the energy. Many small organisms have developed to use these forces to achieve propulsion and the ability to do so is characterized by the drag coefficients of the undulator. These constants depend on the aspect ratio of the undulating body, as well as on the actual undulatory motion used by the swimmer itself. The study of swimming dynamics quickly thereby narrows down into investigating the drag coefficients of a natural undulator.

Having gained knowledge about undulatory locomotion, many new, interesting questions arise. How does the undulating swimmer change its dynamics when confined by the surrounding environment? What happens when the swimmer is close to another (or several) undulatory swimmer(s), and what kind of interactions will affect their interplay? Hydrodynamic interactions might, for example, cause collective features, such as phase or frequency locking, in the relative motions of the swimmers. Also other physical interactions, like steric or mechanosensory, can take place and dominate the final dynamics of the active system. The intricate interactions present in these types of active fluids are of immense interest in the current soft matter community, and contribute to the development of novel bioengineering applications.

In the work for this doctoral thesis, the tiny nematode *Caenorhabditis elegans*, well known as a model organism in the biological community, was studied to enhance our understanding of undulatory locomotion and is discussed in detail in this chapter. In Section 1.2, the physical modelling of the material properties of soft condensed matter in general is described and different, standardized viscoelastic models are

introduced. Section 1.3 covers the undulatory swimming dynamics of organisms in a purely viscous regime and highlights a simple model that can be used to capture the physics of this type of swimming. Finally, in Section 1.4, interactions between several such microswimmers are discussed. Before diving into the concepts of viscoelastic material properties and the dynamics of active materials, our workhorse (worm) *C. elegans* will be introduced in terms of its biological characteristics. At the end of this chapter (Section 1.5), previous physical studies performed by others on the passive and active properties of this nematode will finally be summarized.

## 1.1 The model organism *C. elegans*

*C. elegans* is a free-living, transparent, hermaphroditic<sup>1</sup> nematode with 959 somatic cells and 302 neurons [19]. The adult worm, shown in the optical microscopy image of Fig. 1.1(a), has a length of around 1 mm and a life cycle of a few days. As suggested by its name, the nematode moves in an elegant, undulatory fashion when crawling on a surface, leaving a sinusoidal pattern behind on the soft gel substrate in Fig. 1.1(b).

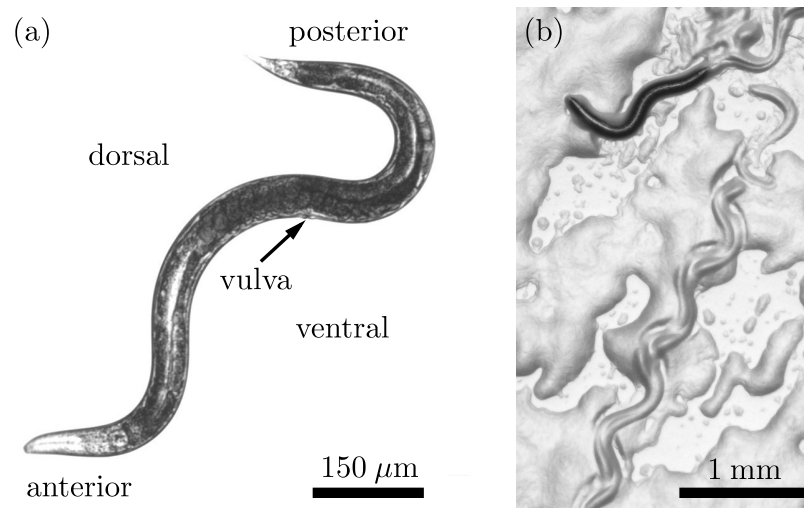


Figure 1.1: (a) An adult *C. elegans* nematode with some anatomical terms noted and the position of the vulva highlighted. (b) An adult worm crawling on an agar (gel) surface.

<sup>1</sup>Both hermaphroditic and male *C. elegans* nematodes exist, but for the scope of this thesis, only the former will be discussed.

The *C. elegans* nematode was first suggested as a model organism to the scientific community by Sydney Brenner in 1965 to study anatomy, genetics, behaviour, as well as neural and cellular development [19, 20]. The choice of this specific organism was based on its short life cycle, transparency, as well as the size of the worm, deeming it one of the smallest and least complicated organisms still with a central nervous system. The small size also made it possible to use electron microscopy to achieve a full anatomical description of the worm with a very high resolution.

The original *C. elegans* sample (the N2 strain) was isolated by L. N. Staniland from a mushroom compost in Bristol in the 1950s<sup>2</sup>, and the nematode later became the first animal to have its entire genome sequenced (1998), five years before that of the human [20]. To this date, three Nobel prizes have been awarded for research performed on *C. elegans*, the first of which was received by S. Brenner and collaborators J. Sulston and H. R. Horvitz in 2002 for their work on genetic regulation of organ development and programmed cell death. It is sufficient to say that this nematode is one of the most studied and best understood animals. Every single cell in the worm body has been located and characterized, it is well known when and how each of these cells divide, and the function of the neurological system has been mapped out in detail and correlated with behavioural features of the worm. The *C. elegans* nematode is, therefore, an ideal candidate for novel physical studies.

### 1.1.1 Anatomy

Some anatomical terms of the nematode are denoted in Fig. 1.1(a), where anterior-posterior and dorsal-ventral define the front (head) and back (tail), as well as the two sides of the worm, respectively. The vulva is located on the ventral side, slightly shifted towards the posterior end of the worm. The anatomy of *C. elegans* is that of a typical nematode, with an outer tube consisting of the cuticle, hypodermis, neurons, and muscles, and an inner body cavity (the pseudocoelomic space) containing the intestine and gonad [19]. A schematic illustration of a posterior cross section of an adult worm is shown in Fig. 1.2.

---

<sup>2</sup>Two original samples were collected. One in the United Kingdom, and one by V. Nigon in France a decade earlier. The British strain, however, has been used in the most significant studies [20].

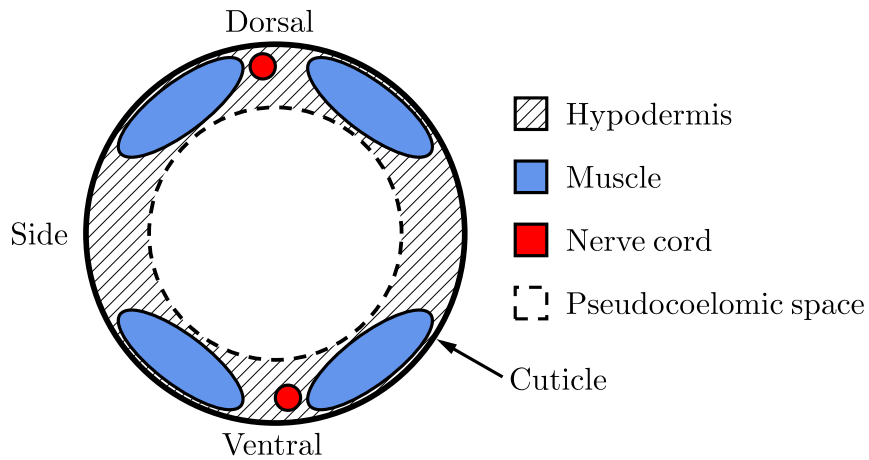


Figure 1.2: A schematic diagram (not to scale) of a posterior cross section through an adult worm. The outer tube consists of the cuticle, hypodermis, neurons, and muscles, whereas the inner pseudocoelomic space contains the intestine and gonad (not shown here).

The hypodermis is composed of epithelial tissue and makes up a large fraction of the outer worm tube. The nematodal body shape is maintained through a high internal hydrostatic pressure in the pseudocoelomic space. This pressure has been thought to contribute significantly to the rigidity of the worm as a hydrostatic skeleton [21], acting as a support against the forces of contracting muscles, and restoring the original length of a muscle after its contraction [6]. New biomechanical studies have, however, partly disproved this hypothesis, as will be discussed in Section 1.5.1.

The muscle cells (a total of 95) of *C. elegans* are located along the entire worm length in four longitudinal quadrants of the body. The worm moves by propagating travelling waves down its body, where small sections of the dorsal and ventral muscle quadrants contract simultaneously in a highly coordinated, anti-phase fashion [19]. The worm can thereby only actively bend its own body in the dorsal-ventral plane, with an exception in the head region where full three-dimensional motion is achievable due to a more extensive wiring of the head and neck muscles. For this reason, the worm always crawls on either of its two sides (where a side is as defined in Fig. 1.2) when placed on a solid substrate.

The cuticle of *C. elegans* is a highly flexible and resilient structure that covers the entire outside of the worm body. This tough layer is composed of a structured

extracellular matrix consisting mainly of cross-linked collagen. The cuticle acts as a barrier to protect the worm from the external environment and enables locomotion through its attachment to the body muscles. The cuticle is renewed at each larval<sup>3</sup> moult, as described in detail in the next section.

### 1.1.2 Life stages and development

In Fig. 1.3, a diagram of the life stages of *C. elegans* is shown. The development of the worm from the point of hatching of the egg to a fully grown adult takes around 2 days at 20°C, and is sped up with increased temperatures [19, 22]. The schematic illustration indicates the average lengths of the L1, L2, L3, L4, young adult, and adult worms, as well as the average time spent in each larval stage before moulting. The young adult stage is not an actual, separate life stage punctuated by a moult, but is part of the adult stage and is distinguished for practical reasons<sup>4</sup>. The adult *C. elegans* nematode is fertile for about 4 days and can live for a total of 14-19 days after the final L4-adult moult.

At each transition (except that between a young adult and adult worm), the old cuticle is shed and a new and larger version is synthesized as a replacement. The cuticle of each life stage is different both structurally and molecularly as compared to the others [23]. Other than that, the general anatomy of the worm, including the aspect ratio of the body [24, 25], remain intact throughout the life cycle, with an exception of the development of the reproductive system. Fertilized eggs will, for instance, start to accumulate in the uterus after the L4-adult moult.

#### The Dauer worm

An impressive feature in the development of *C. elegans* is the so called Dauer state, included as a special case in the diagram of Fig. 1.3. This life stage occurs if the worms find themselves in an environment that is too hot or cold, is overcrowded, or has a lack of food [19]. The L1 larva can, in that case, develop into a special L2d

---

<sup>3</sup>The use of the word larval in this thesis follows common *C. elegans* nomenclature and is to be understood in a highly figurative way. The development of *C. elegans* does, for example, not involve metamorphosis.

<sup>4</sup>Due to the long lifetime of adult worms, most measurements are usually performed on young adult worms to avoid any effects of aging.

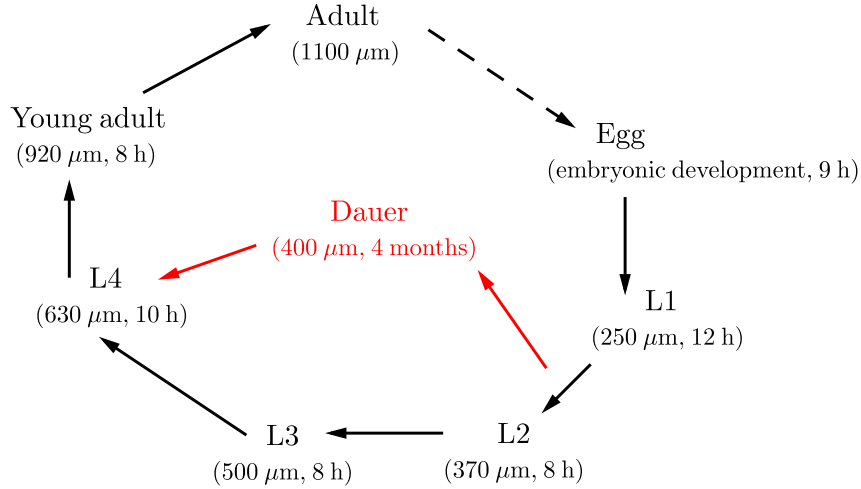


Figure 1.3: The life stages of *C. elegans* at  $\sim 20^\circ\text{C}$ . The average larval size and time spent in each stage is denoted in the brackets. The transition between the young adult and adult life stage is not a true transition and does not involve a moult. The worm can survive in the Dauer state for as long as 4 months without any food.

stage, followed by a transition into the Dauer state, in which the worm can survive for up to 4 months without any food. Once the environment is suitable for further growth, the Dauer worm moults and transitions into an L4 stage worm, identical to that developed through the normal pathway.

It has been shown that the cuticle of the Dauer worm is thicker as compared to that of a normal life stage worm [23]. In the Dauer state, the ratio between cuticle thickness and worm diameter has been measured as  $1/36$ , whereas the same ratio for normal worms is a constant of  $1/88$ . It is believed that the thickening of the cuticle has developed to increase the protection of the less mobile Dauer worm in a possibly more hostile environment.

## 1.2 Material properties of soft condensed matter

To study the passive material properties of *C. elegans*, an understanding of the mechanical properties of condensed matter in general is crucial. Mechanical properties are intrinsic features that describe how the solid material will respond to an external force [26]. For a normal solid, the initial deformation is generally purely Hookean

and reversible, and followed by some irreversible plastic deformation or fracture as the strain becomes larger. However, for soft condensed matter [27], such as colloidal or polymeric systems, emulsions, gels, and biological tissues, the response to external deformations can be much more complicated. Due to the complex (molecular, granular, cellular, etc.) arrangement of the material, interesting viscoelastic effects arise at time and length scales atypical from those of solid state materials. In the following sections, the treatment of elastic materials is initially discussed with a focus on the bending of a cylindrical structure. After this, viscoelasticity is introduced and different standardized models are discussed. Finally, a brief description of complex, non-Newtonian fluids is given.

### 1.2.1 Elasticity

Elasticity is a physical quantity describing the tendency of a deformed solid material to return to its original shape after the external stress has been removed [27]. To describe its deformation a continuum mechanical approach is taken. For most solids, the initial material deformation is linearly proportional to the applied force, as described by Hooke's law. The linear regime ends at the yield strength of the material, after which any further strain causes partially or fully irreversible deformations.

In the linear regime, defined by small deformations, the stiffness of the material is defined as the ratio between stress ( $\sigma$ , force per unit area) and strain ( $\epsilon$ , normalized deformation) of the material [26]

$$E = \frac{\sigma}{\epsilon}. \quad (1.1)$$

Here  $E$  is the Young's (or elastic) modulus and represents the intrinsic elastic property of the isotropic solid material. The exact definition of stress and strain depends on the geometry and dimensionality of the system as well as the type of strain applied. The extension of a string, bending of a sheet, splaying, twisting or bending of a rod, and shearing or compression of a cube are typical examples of ways to deform different objects. Below, the difference between the concept of transverse and longitudinal stiffness for a cylinder is defined. Then the specific case of the bending of a cylindrical beam will be discussed in detail, as this system later will be used as an approximation for the bending of the nematodes in this work.

### Transverse vs. longitudinal stiffness

Disregarding torsion and elongation, a cylinder can be deformed in two ways: by compression in the radial direction or by bending along the longitudinal axis, as illustrated in Figs. 1.4(a) and (b), respectively. Both of these deformations can be described by their corresponding elastic components, defined as the transverse and longitudinal stiffnesses. Most typical homogeneous solids are isotropic, and would have the same transverse and longitudinal stiffness. This is, however, not the case for many biological tissues [23], which are composed of heterogeneous and structurally anisotropic materials. The distinction between the two stiffnesses is important. The transverse stiffness of a cylindrical biological body, such as a nematode, would ideally be high enough to protect the body against any external perturbations and withstand the hydrostatic internal body pressure. The longitudinal counterpart, however, should preferably be designed to be significantly lower and thereby enhance the non-local bending of the body and allow for easy propulsion. In terms of undulatory locomotion, the longitudinal bending of a slender, cylindrical body is thus the relevant geometry to consider.

### Bending of a cylinder

Since the shape of the worm body can be approximated as cylindrical, the study of the longitudinal bending of the nematode can be simplified by investigating the

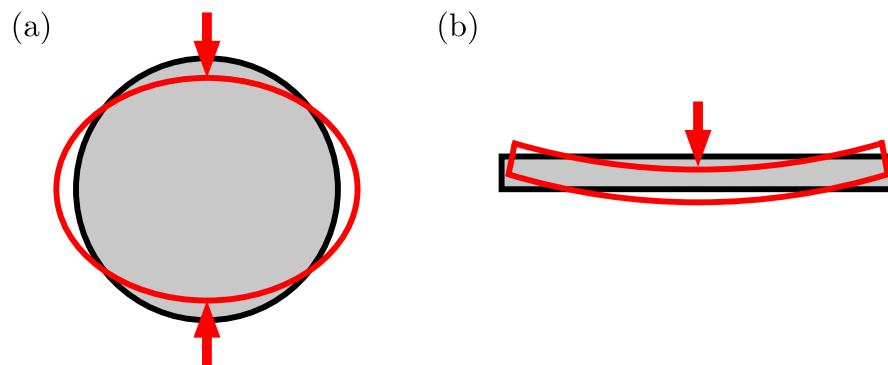


Figure 1.4: (a) The transverse compression of a cylinder (cross-sectional perspective). (b) The longitudinal bending of a cylinder (side view).

bending of a cylinder. The resistance to bending of a cylinder depends on the Young's modulus,  $E$ , of the material, and on how that material is distributed in the cylindrical structure, as captured by the so called area (or second) moment of inertia,  $I$  [28]. The product of these,  $EI$ , represents the bending stiffness of the cylinder. A detailed derivation of the area moment of inertia for a hollow cylinder is included in Appendix C.1, resulting in

$$I = \frac{\pi}{64} (D^4 - d^4), \quad (1.2)$$

where  $D$  and  $d$  are the outer and inner diameters of the cylinder, respectively. A cylinder with a thick shell will therefore be more difficult to bend as compared to a thin-walled cylinder with the same outer diameter, simply because the former has *more* stiff material to deform. For a cylinder with an unknown inner structure, the concept of stiffness should therefore always relate to the bending stiffness of the cylinder, and not only the Young's modulus of its material. Furthermore, for a cylinder with an unknown combination of potentially non-isotropic, stiff materials, such as a heterogeneous biological system [17], the bending stiffness still accurately describes the elasticity of the structure as a whole, although the concept of defining a Young's modulus of the cylinder becomes vague and ill-defined.

The bending stiffness of a cylinder can be measured by performing a three-point bending measurement on the beam as illustrated in Fig. 1.5 [28]. The beam is supported at both of its ends either by fixed supports, clamping the ends of the beam, or by simple supports, as shown here, allowing the ends to move upwards as the beam is

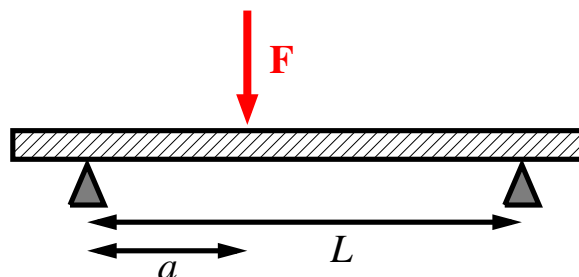


Figure 1.5: Schematic diagram of a three-point bending measurement on a simply supported beam. A known force ( $F$ ) is applied at a certain distance ( $a$ ) from one of the supports, separated at a distance of  $L$ , causing the uniform beam to bend.

bent. A known force  $F$  is then applied to the beam at a distance of  $a$  from one of the supports (separated at a distance of  $L$ ), causing the beam to bend. The force-bending relationship can be calculated as (see Appendix C.2 for a detailed derivation of this equation)

$$y(a) = \frac{a^2(L - a)^2}{3LEI}F, \quad (1.3)$$

where  $y(a)$  is the measurable bending of the beam at the location of the applied force. Knowing the geometry ( $a$  and  $L$ ) of the system, the bending stiffness can then be quantified. As an analogy to the elastic, Hookean deformation of a simple spring, the proportionality factor of Eq. 1.3 can be thought of as the inverse of the spring-like longitudinal stiffness ( $k$ ) of the cylinder.

### 1.2.2 Viscoelasticity

The elastic treatment of a solid material as described above works for certain materials within the limit of small deformations. It is, however, doomed to fail as the strain or stress becomes too large. Furthermore, the simplistic assumption of a Hookean stress-strain response is not applicable to most soft materials. A great example of this is the behaviour of a chunk of silly putty, which flows like a very viscous liquid when slow stresses are applied to it [27]. If the polymeric material, however, is rolled up into a ball and thrown at a solid substrate, the silly putty bounces with a purely elastic response. The timescale at which the external stress is applied clearly affects the response of the material, and is considered a typical feature of many soft matter systems. To extend our understanding of mechanical material properties to also take into account the liquid attributes of soft materials, elasticity needs to be combined with the properties of a fluid. This is done by introducing the concept of viscoelasticity.

When a sudden stress is applied to a soft material and then kept constant, the material will gradually deform as the subcomponents (like the colloidal particles, polymers, or cells) of the material slowly rearrange to accompany the applied stress [26]. This phenomenon is called creep, and will stop when the stress built up internally corresponds to the externally applied stress. A sudden strain can also be applied to the material and then be kept constant. This will give rise to the gradual decrease of

the stress induced on the system, and is called stress relaxation. These two features are characteristic of viscoelastic materials, and the time scale separating the elastic response with the viscous flow is called the relaxation time [27].

Eq. 1.1 defined the elasticity of a Hookean solid as the linear relationship between stress and strain. The response of an incompressible Newtonian fluid to an applied stress can similarly be defined as<sup>5</sup>

$$\sigma = \eta \dot{\epsilon}, \quad (1.4)$$

where  $\eta$  is the dynamic viscosity. In the same way as the Young's modulus (with units of pressure, Pa) quantifies the resistance to deformation of a solid due to an applied force, the viscosity (with units of Pa·s, i.e., N·s/m<sup>2</sup>) of a fluid acts as a measure of its inherent resistance to a gradual deformation. For the systems relevant to this thesis, it will be sufficient to include only forces ( $F$ ) and deformations ( $y$ ), and Eqs. 1.1 and 1.4 thus can be rewritten as

$$F_{\text{elastic}} = ky \quad (1.5)$$

and

$$F_{\text{viscous}} = c\dot{y}, \quad (1.6)$$

respectively, where  $k$  is the spring constant (with units of N/m) and  $c$  is the damping coefficient (with units of N·s/m).

Different soft materials have different viscoelastic responses and thus have to be modelled in slightly different ways. Some materials will, for example, flow like a liquid at long timescales after an initial elastic response, whereas others might support a longterm stress after an initial viscous response. In the following subsections, three standardized viscoelastic models (the Maxwell, Kelvin-Voigt, and Standard Linear Solid models)<sup>6</sup> are introduced to capture these differences in detail.

## The Maxwell model

A material modelled by the Maxwell model has an initial elastic response to an applied force, followed by a continuous viscous relaxation. Silly Putty and warm tar are two

---

<sup>5</sup>All time derivatives (d/dt) are denoted by a dot in this thesis.

<sup>6</sup>These models provide the most simple theoretical treatments available, but can of course all be extended to capture the complex flow patterns present in some systems.

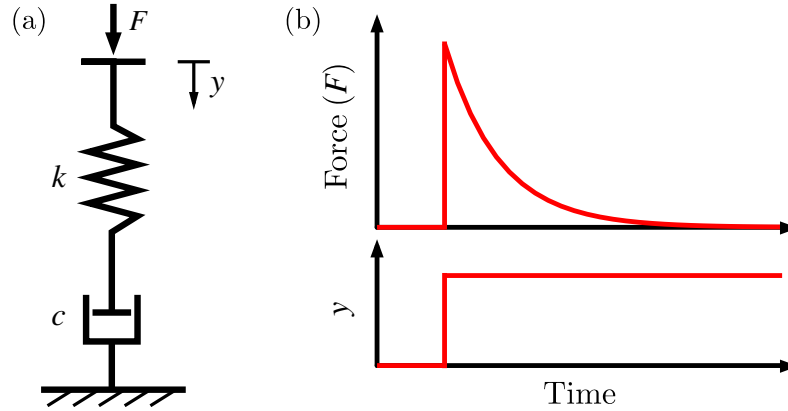


Figure 1.6: (a) Schematic diagram of the Maxwell model, where the spring (spring constant  $k$ ) and dashpot (damping coefficient  $c$ ) are connected in series. An applied force ( $F$ ) causes a certain time-dependent deformation ( $y$ ). (b) Force relaxation of a Maxwell material under constant deformation.

good examples of real Maxwell materials [29, 30]. As described in Section 1.2.2, Silly Putty bounces like a rubber ball at short timescales, but flows like a liquid when perturbed slowly. As suggested by the schematic illustration of Fig. 1.6(a), these viscoelastic requirements can be mimicked by connecting an elastic spring in series with a liquid-filled dashpot. Here, the spring is modelled as purely Hookean, with a spring constant of  $k$ , whereas the Newtonian fluid in the theoretical dashpot has a damping coefficient of  $c$ .

The force ( $F$ ) required to compress ( $y$ ) a Maxwell material is highly time and velocity-dependent. When an instantaneous deformation is applied to the system, as shown in the bottom graph of Fig. 1.6(b), the spring will be compressed instantaneously. The fluid in the theoretical dashpot, however, will initially not be deformed at all, as it possesses an infinite resistance to instantaneous deformation. As time progresses, the material will relax as the fluid component of the system starts to flow. This will cause the external force to decay until it reaches zero, as shown in the top graph of Fig. 1.6(b). A Maxwell material can, in other words, not support any longterm deformations, and will not retain its original shape when the external constraint is removed. Few real condensed materials can therefore be fully described by the Maxwell model.

A force applied to a Maxwell material will be absorbed fully by both the spring

and dashpot in the series connection. The compression speed of the entire system ( $\dot{y}$ ) is thus the sum of the separate deformation speeds of the spring ( $\dot{y}_s = \dot{F}/k$ ) and dashpot ( $\dot{y}_{ds} = F/c$ ) [26]. The total speed of the deformation will in other words be

$$\dot{y} = \frac{\dot{F}}{k} + \frac{F}{c}. \quad (1.7)$$

Solving this differential equation with respect to time will describe the viscoelastic response of the material. The initial condition for Eq. 1.7 will depend on how the compression experiment is performed. For the case of the example in Fig. 1.6(b), the initial condition would be  $y(0) = F(0)/k$  (assuming the compression was applied at  $t = 0$ ), since the dashpot does not respond instantaneously to the applied deformation.

### The Kelvin-Voigt model

The Kelvin-Voigt model is very similar to the Maxwell model, but here the elastic and viscous components are connected in parallel [26], as shown in the schematic diagram of Fig. 1.7. In comparison to the Maxwell model, the parallel connection ensures that a Kelvin-Voigt material retains its original shape after compression, since the spring would return to its equilibrium length when the external force is removed. For this reason, the Kelvin-Voigt model is successful in describing the viscoelastic features of many soft condensed materials, including biological tissues [31].

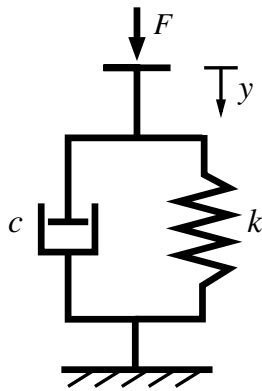


Figure 1.7: Schematic diagram of the Kelvin-Voigt model, where the spring and dashpot are connected in parallel.

The compression of the parallel connection of this model requires that both components deform equally with time. The total force absorbed by both of the components can thus be written as

$$F = ky + cj. \quad (1.8)$$

Initially, all external force will be absorbed by the dashpot, and the appropriate initial condition for differential Eq. 1.8 is thus  $y(0) = 0$  (again, assuming the deformation starts at  $t = 0$ ). When the fluid starts to flow, however, the force absorption will gradually be shifted onto the spring, which will be compressed until it supports the external force completely.

### The Standard Linear Solid (SLS) model

To successfully describe all features of real soft condensed materials, the initial response of a Maxwell material should ideally be combined with the final relaxation attributes captured with the Kelvin-Voigt model. This is achieved with the so called Standard Linear Solid (SLS) model [26]. A schematic diagram of this model is shown in Fig. 1.8(a), where a Maxwell series connection of a spring (spring constant  $k_2$ ) and dashpot (damping coefficient  $c$ ) is connected in parallel with a second spring (spring constant  $k_1$ ). The SLS model has been successful in describing the viscoelasticity of, for example, single cells [32]. An additional dashpot connected in series with the SLS model has, however, been shown to be necessary for the modelling of large cellular aggregates [33, 34].

A SLS material would initially respond elastically to an instantaneous deformation, during which the two springs share the absorption of the applied force. The instantaneous stiffness of a SLS material is thus  $k_1 + k_2$ . The force relaxation of this material is plotted as a function of time in Fig. 1.8(b). As the theoretical dashpot fluid starts to flow, the material will relax until all of the external force is absorbed by only Spring 1, maintaining some of the elastic features of the material at long times. The same spring is also responsible for reclaiming the original material shape upon removal of the external constraint. The SLS model thereby describes both the compression and relaxation response of soft condensed matter more successfully than either of the above described models separately, but has, as a drawback, to include a third parameter to do so.

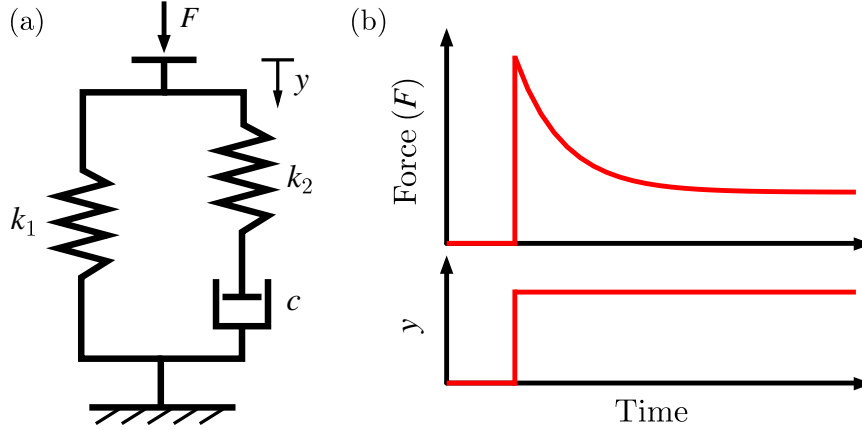


Figure 1.8: (a) Schematic diagram of the standard linear solid model, where the Maxwell model (spring constant  $k_2$  and damping coefficient  $c$ ) is connected in parallel with a second spring (spring constant  $k_1$ ). (b) Force relaxation of a SLS material under constant deformation.

To quantitatively describe the compression of the SLS model, the same assumptions as used to derive Eqs. 1.7 and 1.8 for the Maxwell and Kelvin-Voigt models will be implemented [26]:

1. Components (1 and 2) connected in parallel are compressed equally ( $y_1 = y_2 = y_{\text{tot}}$ ), but share the absorption of the total force ( $F_{\text{tot}} = F_1 + F_2$ ).
2. Components connected in series are opposed by the same total force  $F_1 = F_2 = F_{\text{tot}}$ , but deform differently ( $y_{\text{tot}} = y_1 + y_2$ ).

By implementing these two rules for the SLS connection in Fig. 1.8(a), the following differential equation can be derived

$$\dot{y} = \frac{1}{k_1 + k_2} \left( \dot{F} + \frac{k_2}{c} F - \frac{k_1 k_2}{c} y \right). \quad (1.9)$$

The case-specific solution of Eq. 1.9 describes the time and speed-dependent response of a SLS material to external compressions or forces.

### 1.2.3 Complex fluids

Up until now, the fluid in all theoretical models has been assumed to be purely Newtonian. As introduced in Eq. 1.4, a Newtonian fluid has a constant viscosity, rendering a linear relationship between strain rate and stress. Excluding water, however, many everyday fluids, like ketchup, shampoo, paint, blood, toothpaste, and quicksand, have strong non-Newtonian properties [27]. All of these examples are so called complex fluids, composed of a binary mixture of two different components, typically of different phases (liquid-liquid emulsions, liquid-gas foams, liquid-solid suspensions, or solid-gas granular materials). The geometry of these systems causes restrictions or enhancements of the flow depending on how fast the material is perturbed, resulting in strongly varying viscosities with strain rate.

If a fluid becomes more viscous with increased strain rate, it is defined as shear-thickening. Of the examples above, only quicksand possess this property, whereas the other fluids are shear-thinning, and thereby become less viscous as the strain rate is increased. In addition to these examples, shear-thinning properties have also been observed in various types of biological materials, including heart and brain tissue [35] as well as in vocal cords [36]. Interestingly, although the structure and function of these materials are very different, their gross mechanical properties are mostly governed by the components of the extracellular matrix of the materials [26, 35, 37]. This is exemplified by collagen, which is a prominent structural protein in connective animal tissue [26], including that of the cuticle of *C. elegans*, and which has been shown to be strongly shear-thinning [35, 37–40].

To describe the flow of a complex fluid in a quantitative manner, many different empirical models have been developed [41]. Below, the most well-known and commonly used theoretical approach is introduced.

#### Power-law fluid

It has been empirically verified that the viscosity of several complex fluids decrease as a power law with increased strain rate [41]. Polymer solutions are especially common examples of this, and characterizing their flow properties is of importance for many industrial applications [42]. The Ostwald-de Waele power-law model is the most simple and successful in capturing this non-Newtonian behaviour theoretically by

implementing a non-constant fluid viscosity. The relationship between the effective viscosity and the applied shear rate ( $\dot{\gamma}$ , strain rate caused by shearing, units of  $\text{s}^{-1}$ ) is introduced as

$$\eta_{\text{eff}} = K\dot{\gamma}^{-d}, \quad (1.10)$$

where  $K$  is the consistency index (with units of  $\text{Pa}\cdot\text{s}^{1-d}$ ), corresponding to the viscosity at a strain rate of 1 Hz, and  $d$  is a dimensionless flow behaviour index, which quantifies the deviation from pure Newtonian flow. For a Newtonian fluid, the viscosity is constant and  $d = 0$ . Non-zero values of the flow behaviour index characterize shear-thinning ( $d > 0$ ) or thickening ( $d < 0$ ) properties of the fluid. For polymer solutions,  $d = 0.4 - 0.85$  [41–43], whereas the flow behaviour index for collagen has been determined as  $d = 0.76 \pm 0.01$  [40].

Many real complex fluids, like paint, penicillin broth, and human saliva [44], are Newtonian at very low and high shear strains, but have different viscosities in the two regimes and a shear-thinning transition in between. To capture these kinds of more general flow properties of complex fluids, more extensive, empirical models are necessary [41, 44].

### 1.3 Undulatory microswimming

Up until now, the passive material properties relevant for the modelling of *C. elegans* have been introduced. In this section, the physics needed to understand the active dynamics of the nematode will be discussed.

Undulatory locomotion occurs in a seemingly similar fashion in a wide range of species with different sizes. In this type of motion, wave-like patterns are used in the typically (but not exclusively) limbless body to propel the animal forward. Interestingly, however, the physics behind the motion of a swimming snake and a tiny worm is completely different. For large objects moving through a liquid at high speeds, inertia will dominate the dynamics of the fluid motion, giving rise to turbulence and allowing for long coasting distances [45]. Propulsion in the inertial regime has been studied in, e.g., fish [46–48], snakes [49], and lamprey eels [8]. A very small and slow object, however, will typically move in a purely viscous regime, where inertia can be neglected and laminar fluid flow is characteristic. To understand the

active undulatory motion of the small *C. elegans* nematode, propulsion in the purely viscous environment thereby needs to be approached. In this regime, microorganisms such as spermatozoa, bacteria, and the tiny algae *Chlamydomonas reinhardtii* strive [50]. These are coined as “microswimmers”, and the physical quantity separating them from the swimming in an inertial regime is set by the dimensionless Reynolds number (Re) which will be defined in detail below. In the following section, the hydrodynamics at low Re will first be introduced in general, followed by a detailed description of the physics governing undulatory microswimming.

### 1.3.1 Flow at low Reynolds numbers

To fully describe the fluid flow in any hydrodynamic system, composed of anything from a small sphere falling through honey to a whale swimming in the ocean, the Navier-Stokes equations should be solved. For incompressible fluids (i.e.,  $\nabla \cdot \mathbf{v} = 0$ ) with a viscosity  $\eta$  and density  $\rho$ , these equations can be written in terms of the fluid velocity  $\mathbf{v}$  as<sup>7</sup>

$$\rho \left( \frac{\partial}{\partial t} + \mathbf{v} \cdot \nabla \right) \mathbf{v} = -\nabla p + \eta \nabla^2 \mathbf{v} + \mathbf{f}, \quad (1.11)$$

where  $p$  is the pressure and  $\mathbf{f}$  represents all body forces, such as gravity or centrifugal forces, opposed on the system [12]. For the scope of this thesis, the body forces will from here on be assumed to be zero. The left side of Eq. 1.11 represents the inertial terms of the system, whereas the right side is composed of the stress diverging components, consisting of the pressure and viscous terms. Unfortunately, solving the incompressible Navier-Stokes equations analytically has been proven to be very difficult or even impossible for most systems due to the nonlinear character of the partial differential equations<sup>8</sup>. To describe the flow caused by a microswimmer, simplifications have to be made. Luckily, as will be shown below, the Navier-Stokes equations become linear in the purely viscous regime in which microswimming is relevant.

---

<sup>7</sup> $\nabla = \left( \frac{\partial}{\partial x}, \frac{\partial}{\partial y}, \frac{\partial}{\partial z} \right)$

<sup>8</sup>In fact, as of May 2015, there is no actual proof that solutions to the Navier-Stokes equations exist for all possible situations. Devising such a proof is one of the seven Millennium Prize problems defined by the Clay Mathematics Institute, offering \$1 million to whoever solves it.

## The Reynolds number

To distinguish between the inertial and viscous regimes of fluid flow, the Reynolds number, defined as the ratio between inertial and viscous forces, is introduced [27]. The interpretation of this dimensionless number can be made in many different ways. Here, a scaling law approach will be used [12]. According to Eq. 1.4, the viscous stress on an object with a size of  $L$  scales as  $\sigma_{\text{viscous}} \sim \eta v/L$ , rendering viscous forces of  $f_{\text{viscous}} \sim \eta v L$ , since  $\sigma = f/L^2$ . Furthermore, the inertial stress on the body can be described with a Bernoulli-like dynamic pressure:  $\sigma_{\text{inertial}} \sim \rho v^2$ , making the inertial force scale as  $f_{\text{inertial}} \sim \rho v^2 L^2$ . The ratio between these forces gives us the Reynolds number

$$\text{Re} = \frac{f_{\text{inertial}}}{f_{\text{viscous}}} = \frac{\rho L v}{\eta}. \quad (1.12)$$

For high fluid viscosities ( $\eta$ ), small object sizes ( $L$ ), and low fluid speeds ( $v$ ), Re will be less than unity and viscous forces will govern the flow properties of the system. The Re for bacteria, small fish, and humans in water are on the order of  $10^{-4}$  to  $10^{-5}$ ,  $10^2$ , and  $10^4$ , respectively [51]. As derived in the supplementary information of Paper III (see Appendix A.3), the Reynolds number for *C. elegans* in water lies within the range of  $\text{Re} \sim 0.05 - 0.5$ , and is thus on the border of being considered a microswimmer for which inertia can be ignored.

## Stokes flow

For microswimmers in general, with very small sizes and slow swimming speeds, the Re is typically very close to zero [50]. At the lower limit of  $\text{Re} = 0$ , the inertial terms in the Navier-Stokes Eqs. 1.11 vanish and the nonlinear differential equations simplify to the Stokes equations

$$-\nabla p + \eta \nabla^2 \mathbf{v} = 0. \quad (1.13)$$

In comparison to its predecessor, these equations are linear and independent of time and thereby easier to solve analytically. For the system of a spherical particle moving with a speed  $v$  in a viscous solution, the Stokes equations can be solved to derive Stokes' law, giving the drag force on the bead as [27]

$$F_d = -6\pi\eta Rv, \quad (1.14)$$

where  $R$  is the bead radius. Although the seemingly simple physical system and analytical solution, the mathematical steps connecting Eqs. 1.13 and 1.14 are complex enough to not be included in introductory textbooks. As will be discussed below, solving the Stokes equations for more complicated systems of undulating cylindrical bodies is thereby far from elementary. Furthermore, the time-independence of Eqs. 1.13 governing the motion of microswimmers will turn out to have interesting consequences for the locomotion strategies necessary at low  $Re$ .

### 1.3.2 Propulsion at low Reynolds numbers

The effect the Reynolds number has on swimming is surprising and can best be described by estimating the coasting distance of a fluid-immersed object of size  $L$  decelerating ( $a$ ) with an initial speed of  $v$  [12, 51, 52]. In a high  $Re$  regime, the drag force on the body will be  $f_{\text{drag}} = f_{\text{inertial}} \sim \rho v^2 L^2$ , and the deceleration can, according to Newton's second law, be written as  $a = f_{\text{drag}}/m$ . The actual coasting distance of the object will then scale as  $d \sim v^2/a \sim m/\rho L^2$ . Furthermore, assuming a swimmer density of  $\rho_s = m/L^3$ , the dimensionless coasting distance can be written as the ratio of the densities:  $d/L \sim \rho_s/\rho$ . For a human (with a density very similar to that of water), the coasting distance will thus be on the order of a body length.

In the low  $Re$  regime, however, the situation changes drastically, as can be exemplified by imagining a human trying to swim in a pool of molasses while being restricted to not moving any body parts faster than 1 cm/min [51]. Achieving a net propulsion of a few meters over the time period of a few weeks would qualify this human as a low  $Re$  swimmer. In this regime,  $f_{\text{drag}} = f_{\text{viscous}} \sim \eta v L$ , and with the same reasoning as above,  $d/L \sim \rho_s L v / \eta = Re \cdot \rho_s / \rho$ . For most biological organisms ( $\rho_s \approx \rho$ ) in the purely viscous regime ( $Re \ll 1$ ), the Reynolds number can in other words conveniently be interpreted as a non-dimensional coasting distance. For a bacterium ( $L \approx 1 \mu\text{m}$ ,  $Re \approx 10^{-5}$ ), the physical coasting distance can be estimated as  $d \approx 0.1 \text{ \AA}$ , which is on the order of the radius of a hydrogen atom. All forces produced by a microswimmer are thereby instantaneously absorbed by the viscous medium, and when the force production stops, so does the propulsion. This feature has strong effects on what types of swimming motions produce a net propulsion in the limit of low  $Re$ .

## Time-reversal symmetry breaking

As mentioned in Section 1.3.1, the Stokes Eqs. 1.13 are time-independent. This means that their solutions are independent of whether the motion, like that of a spherical bead falling through a viscous solution, was performed quickly or slowly or was followed forward or backward in time. In terms of locomotion in the low Re regime, this means that any repeated motion that is symmetric with time, i.e., a motion that looks identical when played in reverse, can not produce a net propulsion. This is best exemplified by the opening and closing of the shells of an imaginary low Re scallop, as proposed by the so called Scallop Theorem [51]. When the scallop opens its shells, it will suck in liquid and thereby pull itself forward. When shutting the shells, the squished out liquid will in turn push the scallop backwards. Since all fluid moves according to the Stokes equations, the scallop will be pushed or pulled the same distance during both of the steps, independent of how fast it opened or closed its shells. There can in other words not be any net propulsion of the scallop, since the motion it is producing has a time-reversal symmetry (also called a reciprocal motion) in the low Re regime<sup>9</sup>.

To produce net propulsion at low Re, time-reversal symmetry has to be broken. In real biological systems [50], this is, for example, achieved through the helical beating of bacterial flagella, the intricate motion of cilia covering the surface of many microorganisms, the breast-stroke kind of motion produced by the algae *C. reinhardtii*, as well as through undulatory locomotion, used by spermatozoa and the *C. elegans* nematodes of interest for this thesis. In the following section, one of the most successful theoretical approaches to model the hydrodynamics of a microswimmer will be described.

## Resistive force theory

Taylor approached the question of how undulatory motion produces propulsion in viscous environments by calculating the flow induced around an infinite sheet undulating with small-amplitude, transverse waves [53]. He then continued to study the more realistic geometry of the propagation of transverse waves down an infinitely long,

---

<sup>9</sup>A real scallop of course lives in a high Re regime, and by opening its shells slowly and closing them quickly, the inertial effect will allow it to propel itself backward.

cylindrical body immersed in a viscous fluid [54]. For the case of *C. elegans*, however, the main problem with this approach is the assumption of small swimming amplitudes, which will not accurately describe the physics behind the actual swimming motions used by the nematode. The same holds true for most other real microswimmers, which employ large amplitudes in their propulsion strategies [12]. To capture more realistic, high-amplitude swimming patterns, resistive force theory (RFT, also known as “local drag theory”) was introduced by Gray and Hancock [11, 55] as an alternative theoretical approach, where the slender, i.e., long and thin, shape of typical undulatory microswimmers was taken advantage of. To do so, the flow caused by a deforming slender body, such as a flagellum or nematode, was modelled by replacing the body with a line of singular solutions to the Stokes equations [12, 56]. As introduced in Section 1.3.1, this requires that the hydrodynamic drag forces acting on a small body segment are proportional to the local body velocity of that segment.

The velocity of the local segment of a line, here representing a slender body, can be decomposed into two components, one tangential ( $v_T$ ) and one normal ( $v_N$ ) to the direction of the segment, as illustrated in Fig. 1.9. These two velocity components give rise to their respective drag forces on the segment in question. According to RFT, the constant of proportionality between the drag forces and body velocities is given by the drag coefficients of the body and the viscosity ( $\eta$ ) of the fluid. For a short body segment ( $dl$ ) along the slender body, the drag forces on that segment can

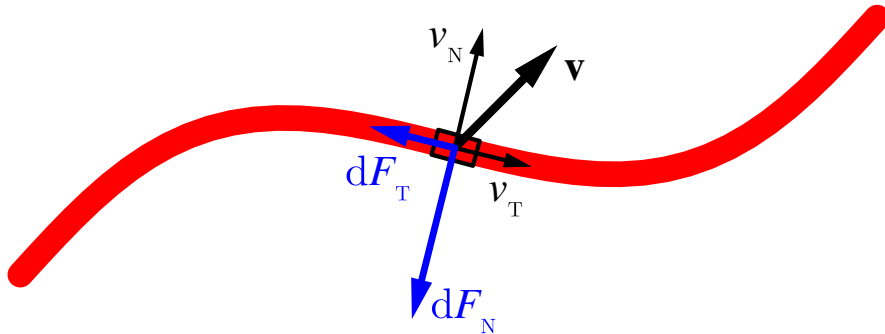


Figure 1.9: The drag forces acting on a short segment of a line moving through a viscous solution with a velocity  $\mathbf{v}$ . The velocity is composed of two perpendicular components, one tangential ( $v_T$ ) and one normal ( $v_N$ ) to the segment.

be written as

$$dF_T = -c_T \eta v_T dl, \quad dF_N = -c_N \eta v_N dl, \quad (1.15)$$

where  $c_i$  denotes the drag coefficient in the normal ( $i = N$ ) and tangential ( $i = T$ ) direction along the body. These drag coefficients are assumed to be constant along the entire cylindrical body. Integrating Eqs. 1.15 along the total body length gives the total drag forces  $F_N$  and  $F_T$  experienced by the swimmer in the normal and tangential directions, respectively. Through this analysis, the propulsive force exerted by the microswimmer can then be calculated.

As presented above, time-reversal symmetry breaking is required for net propulsion to be possible. Another key asymmetry required for an organism to be capable of microswimming lies in the anisotropy of the environmental resistance, which can be quantified by the ratio  $\kappa = c_N/c_T$  between the drag coefficients [52]. For an undulating body, if  $\kappa = 1$ , no net propulsion is possible. If  $\kappa > 1$ , however, net propulsion will occur in the opposite direction to the waves propagated down the slender body, whereas the body waves and net propulsion is in the same direction for  $\kappa < 1$ . Most worm-like shapes have  $\kappa \approx 1.5$ , whereas the limit of an infinite cylinder gives  $\kappa = 2$ . Larger values of the ratio have been shown to be possible in swimming close to solid boundaries [57], as will be presented in Paper IV (Appendix A.4).

The magnitude of the two different drag coefficients of a slender body have been derived theoretically with RFT by many. Gray and Hancock estimated the intrinsic drag coefficients as

$$c_{N,G\&H} = \frac{4\pi}{\ln(2\lambda/R) + 1/2}, \quad c_{T,G\&H} = \frac{2\pi}{\ln(2\lambda/R) - 1/2}, \quad (1.16)$$

where  $R$  is the radius of the cylindrical body and  $\lambda$  is the swimming wavelength [3, 11, 58]. Lighthill later improved on this derivation by taking into account hydrodynamic interactions between different segments along the slender body, giving

$$c_{N,L} = \frac{4\pi}{\ln(2q/R) + 1/2}, \quad c_{T,L} = \frac{2\pi}{\ln(2q/R)}, \quad (1.17)$$

where  $R$  is the radius of the slender body and  $q = 0.09\Lambda$ , where  $\Lambda$  is the swimming wavelength as measured along the body [58]. The coefficients in both of these models

are thus only functions of the geometry of the body and the swimming pattern used.

The limitation of RFT is that it does not include any hydrodynamic long-range interactions between the segments along the body. A more accurate, but also far more complicated theoretical approach is made by using slender body theory [12, 52, 56], which is a more general microswimming model on which RFT is based. Slender body theory has been shown to typically capture swimming dynamics in a wider range of microswimming motions [59], but will not be relevant for the scope of this thesis. Despite the simplicity of RFT, it has for example been shown to successfully capture the locomotion dynamics of sandfish lizards swimming through a low Re environment of granular media [13, 18], and has in addition to that been extensively assumed for the case of *C. elegans*, as will be discussed further in Section 1.5.2.

## 1.4 Interactions in active materials

In very dense solutions of microswimmers, the swimmers will not only be affected by the surrounding, passive fluid as discussed in the section above, but will now also interact with each other. In 1928, Gray reported on observations of interactions between the flagella of individual spermatozoa, which would start swimming perfectly in phase when the sperm cell heads were close enough [53]. Other synchronized swimming patterns and collective behaviour has later been shown to occur in a broad range of biological systems, composed of, for example, different kinds of bacteria [4, 53, 60, 61], cilia [62–65], microtubule filaments [66, 67], sperm cells [68], as well as many other microorganisms, such as *C. reinhardtii* and *Volvox carteri* [69–73].

Materials composed of self-driven, living units, as exemplified above, are defined as “active” [74]. Active matter can also be made up by externally driven passive components, such as self-locomoting slender rods [75] and colloidal particles [76]. The interaction driving the collective behaviour in these low Re systems is rarely controlled by chemical signalling or active communication between the subunits, but is typically of hydrodynamic origin [66, 73]. The key requirement for the collective behaviour is thus a high density of components, rendering small separation distances and strong hydrodynamic interactions. Independent of their origin, the addition of subunit interactions leads to a completely different motion pattern as compared to

what would occur with an individual component in an infinite, passive fluid [77]. The simultaneous change from individual to collective behaviour leads to a complicated temporal or orientational ordering of the fluid, often featured by synchronized waves or other physical patterns on length scales far above those of the subunits themselves [74, 77, 78]. As a consequence, the macroscopic properties of active materials can vastly differ from those of normal soft condensed materials made of passive subcomponents (as discussed in detail in Section 1.2). The activity of a system can, for example, give rise to non-equilibrium phases and phase transitions, as well as different viscoelastic and non-Newtonian properties depending on the character of the local sub-component interactions [79]. A typical trademark of active hydrodynamics is a reduced or enhanced viscosity, which strongly depends on the relaxation time of the collective behaviour. Furthermore, anisotropic viscosities can arise due to the direction of the orientational order and flow.

To model any of the emerging macroscopic material properties, the local interactions between the active subunits need to be understood. The first theoretical description of the collective, phase-locked behaviour of bacterial flagella, as observed by Gray and many others, was developed by Taylor, who modelled the oscillations of two nearby infinite sheets in a purely viscous environment [53]. By including only hydrodynamic interactions between the sheets, the mechanical energy dissipation was found to be minimized during perfect in-phase swimming, and increase monotonically with larger phase-shifts. More advanced, high-amplitude numerical treatments have later shown that also perfect out-of-phase swimming is a stable configuration [12].

In many systems, however, the presence of only hydrodynamic interactions is not sufficient to generate collective motion. Steric interactions have, for example, been shown to be a necessary ingredient for synchronization in some bacterial and colloidal suspensions [76], as well as in densely packed collections of swimming *C. elegans* nematodes [80], as discussed further in Section 1.5.3. In these types of systems, the physical collisions between the actively moving subcomponents give rise to the formation of, e.g., vortices, fluctuating swarms, clustering, and synchronized beating. In some biological systems, also mechanosensory interactions need to be considered [81], as an active touch sensation and response can change the outcome of a collision. The introduction of these, sometimes quite random, additional interactions naturally

makes such a system very complex to model and will for the scope of this thesis not be discussed further. Instead, the curious and much less common example of knotting and tangling of high aspect-ratio components of soft materials will be discussed below, as these can act both to induce or hinder collective behaviour in active materials.

### 1.4.1 Knots and tangles

Biological knots and tangles occur in systems composed of hair [82], the umbilical cord [83], DNA strands [84–86], polymers [87], proteins [83], and flagella in groups of spermatozoa [88, 89] or bacteria [90–94]. Some of these tangles have specific biological purposes, whereas others are undesired consequences of the high aspect-ratio design. In passive systems, the naturally occurring knots in the recombination and replication cycles of DNA are, for example, thought to contribute to gene regulation. In addition to this, from a materials point of view, entanglement of the macromolecules in polymer melts vastly affects the mechanical properties of the bulk material, as exemplified by rubbers and plastics [95]. Tangles also occur in active materials, where they can cause various biological consequences. The so called run-and-tumble motion of bacteria is, for example, enabled by the tangling of several bacterial flagella into a propeller-like bundle, allowing for propulsion in a specific direction. For systems composed of cilia, however, the absence of tangles allows for active fluid pumping as well as transport of many different microorganisms.

To quantify different types of tangles, mathematicians have developed a definition based on the topology of the tangle, as will be described below. Furthermore, the experimental work by others into the knotting and tangling kinetics and probability of various passive strings will be summarized, as these compose the basis of our physical understanding of how and why tangles and knots form and disappear.

#### The Conway notation

In mathematics, a tangle is a region of a knotted string surrounded by a circle, such that the surrounded knot crosses the circle exactly four times [96, 97]<sup>10</sup>. To define

---

<sup>10</sup>*Tangle* theory only deals with the tangles within a knot, whereas *knot* theory is applied to the study of the topology of a knot in a closed loop of a single string. These exact mathematical definitions are, however, not fully relevant for the scope of this thesis, where a more colloquial treatment will be made.

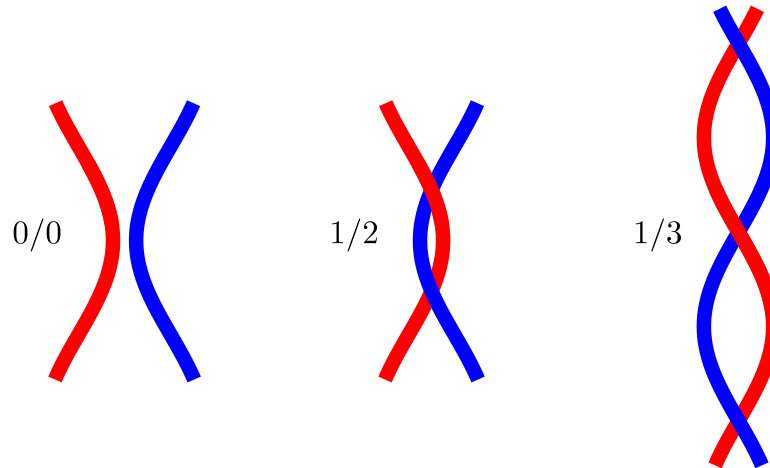


Figure 1.10: Examples of vertical  $0/0$ ,  $1/2$ , and  $1/3$  rational Conway tangles. If rotated by 90 degrees, these would be 0, 2 and 3 horizontal tangles.

different types of tangles (a few of which are shown as examples in Fig. 1.10) between different strings or within a single string, Conway introduced the mathematical concept of rational tangles [96]. These are recognized by the number of overlapping points between the strings, which is equivalent to the number of twists that have been made to form the tangle. A horizontal tangle is defined as a so called integer tangle and denoted by  $n$  ( $n \in \mathbb{Z}$ ), which stands for the number of horizontal twists that were made in the formation of the tangle [97]. Twisting the strings  $n$  times vertically will produce a vertical tangle, which is defined by the notation  $1/n$ . Examples of different types of vertical tangles are shown in Fig. 1.10. If these were rotated by 90 degrees, they would correspond to horizontal tangles. A distinction between vertical and horizontal tangles will not be made in this thesis.

A rational tangle can furthermore be either positive or negative, depending on in which direction the twisting of the strings was made. For the purpose of this thesis, the sign of the tangle is irrelevant and will not be included in the notation, but as an example, the  $1/2$  tangle in Fig. 1.10 is positive since, per definition, the top left incoming string passes above the top right one [97]. If the red string would pass below the blue one in the upper crossing, the tangle would be defined as a  $-1/2$  tangle.

## Physical knotting studies

Macroscopic systems consisting of strings, chains, and ropes have been used to study the formation, topology, lifetime, and untying of knots experimentally. Ben-Naim, *et al.* placed a ball chain with a knot tied in its centre on a vibrating plate and followed the unknotting procedure of the string [98]. A power-law scaling between the unknotting time and chain length was discovered, consistent with a diffusive behaviour. By implementing a random walk based theoretical model, the authors were able to achieve quantitative agreement with the experimental results. With an identical setup, Hickford, *et al.* investigated the probability of the knotting of ball chains with different lengths when these were vigorously shaken [99]. The knotting probability was found to be invariant of chain length above a certain critical length, whereas the unknotting probability increased strongly with length. A rate based theoretical model was furthermore derived to describe the knotting probability qualitatively.

Raymer, *et al.* placed ropes with different lengths and stiffnesses in a rotating box [100]. This study reported on a qualitatively very similar knotting probability as was observed by Hickford, but much more complex knots were formed due to the longer ropes used in this study. A sigmoidal function was shown to qualitatively fit their knotting probability data as a function of rope length. Lastly, Belmonte, *et al.* studied the self-knotting of a vertically shaken, hanging ball chain, and reported on the formation likelihood of different knots of varying complexity [101].

## 1.5 Physical studies on *C. elegans*

As a conclusion to this chapter, a brief overview of previous work performed on the physical properties of *C. elegans* will be given.

### 1.5.1 Passive material properties

#### Transverse stiffness

Park, *et al.* were the first to measure the stiffness of *C. elegans* by using a piezoresistive displacement clamp technique to locally push a small bead, attached to a force-sensing cantilever, into the worm body, and thereby probe its elasticity [102, 103]. By doing

so, they found a linear force-deformation relation and derived a Young's modulus ( $E = 10$  MPa) for the outer body shell (see Fig. 1.2), consisting of the cuticle, hypodermis, and muscles [103, 104]. The stiffness was, furthermore, found to be constant along the worm body. The elasticity probed in these studies corresponds to the transverse stiffness of the nematode body, and is a measure of the local radial resistance to compression of the cylindrical shell, as discussed in Section 1.2.1. To perform their experiments, worms were glued onto an underlying agar plate, causing both the worm and agar to be compressed by the bead in their measurements. The decoupling of the agar stiffness from the total measured stiffness was thereby required to quantify the stiffness of only the worm.

As discussed in Section 1.1.1, the stiffness of *C. elegans* has been thought to be caused mainly by the internal hydrostatic pressure, or “skeleton”, of the nematode body [6, 21, 23]. In Park, *et al.* [103], the authors performed experiments with the same technique as described above to probe this suggested pressure effect on the body stiffness of *C. elegans*. The dissipation of the internal pressure was performed either by puncturing the cuticle with a sharp object, or by causing hyperosmotic shock. Interestingly, both of these approaches decreased the measured transverse stiffness by only around 20%, and the internal hydrostatic pressure was, in other words, found to not be a dominant factor contributing to the total body stiffness of *C. elegans*. The authors also experimented on a mutant with altered cuticle proteins (*lon-2*), and measured a 50% increase in the transverse body stiffness as compared to wild type (N2) worms, indicating a strong effect of the outer body shell on the total elasticity of the worm. By using the same technique, the effect of the body-wall muscles on body stiffness was studied by Petzold, *et al.* [104], where it was found that muscle contraction caused worm body shortening and stiffening, whereas muscle relaxation gave rise to the opposite effect. The same group also studied the effect of increased body stiffness on the ability of force sensing, and found a negative correlation between the two [105].

In addition to the above described technique, developed in the groups of Goodman and Pruitt at Stanford University, a similar technique was developed by Nakajima, *et al.* [106], where the buckling of a nanoprobe, used to push into the worm body, was suggested as a stiffness probe.

## Longitudinal stiffness

As introduced in Section 1.2.1, the longitudinal stiffness of a cylindrical body is the more relevant elastic property to consider when studying undulatory propulsion of slender bodies. This stiffness is a measure of the resistance to bending of the cylindrical body as a whole, and thus acts against any active undulatory swimming or crawling motions.

Before the research performed for this thesis, the longitudinal stiffness of *C. elegans* had been measured by two different groups with very different approaches. In Sznitman, *et al.* [107], the authors predict the viscoelastic material properties of the nematode by quantifying its swimming patterns in a low Re regime. The experimental kinematic swimming data was coupled with a linearized model implementing the total internal moment of the worm, composed of the active moment of the contracting muscles and the passive moment of the elastic worm material. This indirect but non-invasive approach was conveniently used to study the material properties of *C. elegans* in a natural environment. In the paper, the Young's modulus and viscosity of the model organism was determined as  $E = 3.77 \pm 0.62$  kPa and  $\eta = -860.2 \pm 99.4$  Pa·s. The achieved negative viscosity was explained by the tissue generating rather than dissipating energy. The longitudinal stiffness was that of the outer body shell, and is three orders of magnitude smaller than the directly measured transverse stiffness of Park, *et al.* [103]. This large difference is in excellent agreement with the anisotropy of the worm material and the functional design of the worm body in general [23]. As discussed in Papers I and II, we have furthered the investigation of the viscoelasticity of *C. elegans*.

In another study by Sznitman, *et al.* [108], the passive material properties were predicted in fluids with different viscosities, affecting the swimming gait and kinematics of the worms. Both the stiffness and absolute viscosity of the worm material were found to strongly increase with fluid viscosity, and it was hypothesized that the stiffening of the worm body was caused by the shortening of sarcomeres and a higher muscle cell density in environments with higher resistance, where the worm is forced to produce more mechanical work. The observation of an increase in the absolute apparent internal viscosity in environments with higher fluid viscosities is very interesting. In the work presented in this thesis (Papers I and II in Appendices

A.1 and A.2), we have found the viscous component of *C. elegans* to behave as a shear-thinning fluid. The slower beating of the worm body in the higher viscosity fluids, as observed by Sznitman, would give rise to a different apparent viscosity of a non-Newtonian internal worm fluid, as discussed in Section 1.2.3. Implementing this kind of interpretation would have rendered the worm material shear-thinning, as was discovered with a more direct approach in our work.

The second quantification of the longitudinal stiffness of *C. elegans* was performed by Fang-Yen, *et al.* [10]. In their work, a worm was held by its tail by a micropipette and its head was pulled down to bend the body to the dorsal or ventral side and then let to quickly relax up to its original position. The relaxation was monitored with a high-speed camera and the experimentally determined relaxation time was used to derive values for the worm body stiffness and viscosity. Through this approach, the Young's modulus of the cuticle was estimated as  $E \sim 13$  MPa, which is significantly higher than the shell stiffness predicted by Sznitman. This difference could be due to the assumption of no muscle activity in the work by Fang-Yen, rendering a higher apparent stiffness as it likely also includes the active response of the bent, unanesthetized worm.

## 1.5.2 Active undulatory locomotion

### Kinematics and gait modulation

The kinematics of *C. elegans* moving in liquids and on a gel surface has been studied extensively. Karbowski, *et al.*, investigated the conservation of various kinematic variables of the nematode, including both wild type and mutant worms, as well as other *Caenorhabditis* species crawling on different agar substrates [109]. They found that the normalized crawling wavelength is a conserved quantity for all of the nematodes studied. The velocity of forward propulsion was furthermore found to scale linearly with the velocity of the muscular wave. Some exceptions from the otherwise conserved quantities were found in mutants with different cuticle structures, which was suggested to be partly due to a change in the stiffness of these mutants, indicating the significance of the biomechanical body properties on the resulting undulatory locomotion.

A few theoretical attempts have been made to model the intricate elasto-capillary-hydrodynamical interplay present in the crawling locomotion on soft and wet viscoelastic gel substrates. In a model by Sauvage, *et al.* [110], the authors included the pinning down of the worm due to the thin liquid layer capillarity, the hydrodynamics of the lubrication film between the worm and the substrate, as well as the substrate and worm body elasticity, to determine the ratio between the transverse and longitudinal friction coefficients of the worm body on the gel. The maximum drag coefficient ratio achieved was derived to be 2, and is lower than what has been predicted experimentally. Implementing the plasticity of the gel substrate into the model was suggested to potentially improve this discrepancy.

In the group of Arratia at the University of Pennsylvania, the swimming kinematics of *C. elegans* in normal buffer solutions [107, 108, 111], in viscoelastic fluids [112], in wet granular media [113], in fluids with polymer networks [114], and in shear-thinning fluids [115], has been examined. By investigating the decay of the fluid velocity away from a swimming nematode in different viscosities, the worm, with a questionably large size, was shown to behave like a low Re swimmer [111]. In addition to this, the locomotion in saturated particulate system [116], structured microfluidic environments [117, 118], and in fluid flow [119] have been studied.

Significant attempts have been made to study the gait modulation of *C. elegans* in different viscosities [108, 120–123]. Fang-Yeng, *et al.*, showed that the worm slows down and decreases its swimming wavelength with increased fluid viscosity, and that the motion in fluids with extremely high viscosities (28 000-fold increase with respect to that of water) is identical to that used in crawling on agar [10]. In the same study, it was determined that the muscle power exerted by the nematode during the swimming gait is primarily devoted to the bending of the elastic body. During the crawling gait, however, comparable muscle power was found to be used to drive the external load and the elastic body.

## Dynamics

Several different attempts have been made to estimate the forces used by *C. elegans* during swimming. Sznitman, *et al.*, performed indirect force measurements on swimming worms by using RFT in combination with particle tracking and velocimetry

methods applied on kinematic data [111]. The propulsive thrust was thereby predicted to be within the order of a few nanonewtons, and the drag coefficient ratio was estimated as  $\kappa \approx 1.4$ . Also Fang-Yen, *et al.* used RFT to estimate the propulsive thrust and thereby calculate the produced swimming power of *C. elegans* [10]. The total power output was shown to remain constant over a broad range of fluid viscosities, indicating the necessity of gait modulation of the swimmer as it enters regions of higher external resistance.

Before the work for this thesis, the only direct approach to measure locomotion forces was performed by Ghanbari, *et al.* [124], where the authors used the deflections of gel micropillars as force probes arranged in a periodic matrix. The observed maximum force level was  $61.94 \mu\text{N}$ . A similar experimental micropillar approach was performed by Doll, *et al.* [125], where an average peak force of  $2.5 \pm 2.5 \mu\text{N}$  was measured. These forces are three to four orders of magnitude higher than the swimming forces estimated by Sznitman, and it is unlikely that the worms, although certainly capable of producing forces this high, would exert such forces in its swimming gait. In the work for this thesis (see Paper III in Appendix A.3), we have performed the first direct and time-resolved measurements on the forces experienced by *C. elegans* when swimming in a buffer solution. With this direct approach, we proved the previously assumed suitability of RFT to model the swimming dynamics of *C. elegans*, and were also able to determine the drag coefficients of the worm. We have also studied the swimming dynamics and change in the drag coefficients of *C. elegans* in two-dimensional confinement (Paper IV in Appendix A.4) and in fluids with increased viscosities (Paper V in Appendix A.5).

The crawling dynamics of *C. elegans* has also been studied experimentally. In Shen, *et al.* [126], the authors predicted the drag coefficient ratio as 10 for *C. elegans* nematodes crawling on agar surfaces using experimentally achieved kinematic data and a hydrodynamic model based on lubrication theory. In our work on crawling dynamics [127], as briefly summarized in Appendix B.1, the drag forces were directly measured with micropipette deflection and the ratio between the drag coefficients were determined as 2-10, depending on the speed of the worm (increasing ratio with decreasing speed).

### 1.5.3 Collective swimming and crawling

As discussed in Section 1.4, collective behaviour can arise between actively moving microswimmers in dense systems. Not many studies have to this date been performed to probe the collective interactions between *C. elegans* nematodes. Yuan, *et al.* recently investigated the interactions between highly packed *C. elegans* nematodes swimming confined between two planes [80]. By analyzing a large number of nematode pairs, the authors found that the worms indeed swim collectively when close enough, but explained this with purely steric interactions. Interestingly, no signs of hydrodynamic interactions were in other words discovered, which could be due to the  $Re$  being closer to unity than zero for the model organism.

In the work by Gart, *et al.* [128], the collective motion of worms crawling on an agar plate was investigated. The initial aggregation of two or more worms was reported to be driven by random collisions, whereas the continued collective crawling motion was explained with the attractive force caused by the surface tension of the liquid layer on top of the gel substrate.

Neither of these two studies reported on any signs of mecahnosensation between the interacting worms, indicating that the steric forces were too low to trigger these types of neurological responses.



# Chapter 2

## Experimental details

This chapter is designed to cover all experimental procedures used in the research performed for this thesis. In the first section, the micropipette deflection technique is introduced and a detailed description of its application to *C. elegans* is given. In the second section, maintenance and handling guidelines for working with *C. elegans* are provided.

### 2.1 Micropipette deflection

The focus of my doctoral studies has been to apply the technique of micropipette deflection (MD) to probe the passive and active properties of *C. elegans*. In this technique, the spring-like deflection of a long (1-3 cm) and thin (10-20  $\mu\text{m}$ ) glass capillary is calibrated and used to measure forces as low as tens of piconewtons. In comparison to other, standardized mechanical probes, MD fills an interesting mesoscopic gap in its force-displacement (F-d) range, as illustrated in Fig. 2.1. Microscopic probes such as atomic force microscopy (AFM) as well as optical and magnetic tweezers (OT and MT, respectively) are typically used to characterize the biodynamic properties in a range spanned from single biomolecules, such as DNA, up to entire cells [129]. All of these microscopic probes are, however, restricted in the upper bounds of their F-d range. On the other hand, macroscopic probes such as dynamometers, force gauges, and load cells are only capable of working in much larger F-d regimes, well above those of the microscopic probes.

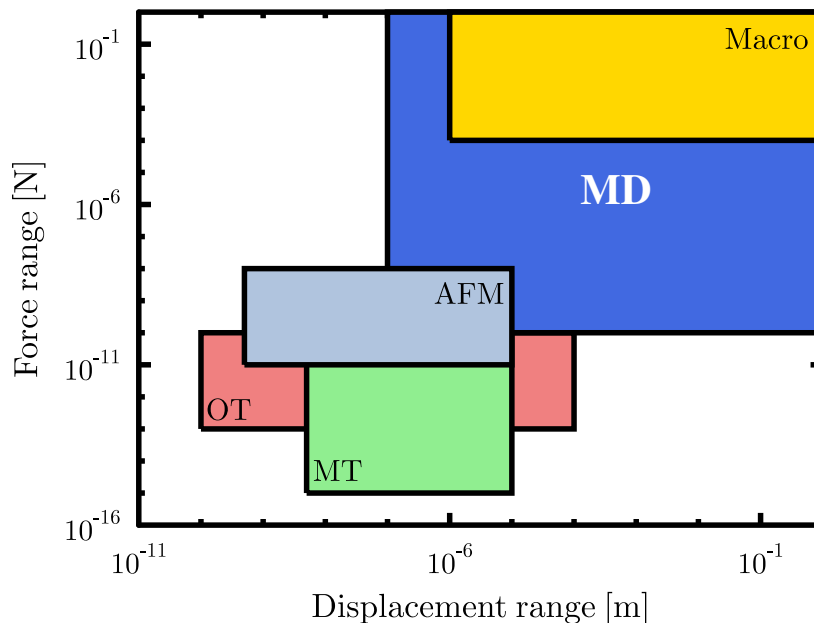


Figure 2.1: The force-displacement range of standard force probes, including atomic force microscopy (AFM), optical tweezers (OT), magnetic tweezers (MT) [129], and macroscopic (macro) probes like dynamometers, force gauges, and load cells. Micropipette deflection (MD) fills the gap between these micro and macro regimes.

The accessible F-d range of MD falls right between the microscopic and macroscopic probe regimes, and has deemed the micropipette technique highly suitable for biomechanical studies of, e.g., vesicles and cells [130–135] as well as cellular aggregates [136]. MD thereby adds to the more standardized micropipette aspiration technique [137–140], applicable to a much smaller regime within the F-d range set by MD. The limiting features of MD is the thermal vibrations ( $< 0.1 \mu\text{m}$ ) of the micropipette when immersed in liquid, rendering a force resolution of around 0.1 nN. By making shorter, stiffer pipettes, there is no limit (within reasonable bounds) in the other extreme.

The original MD setup in our lab was designed and built by Dr. M.-J. Colbert and is described in detail in her M.Sc. and Ph.D. theses [141, 142]. In the sections below, the manufacturing and calibration of the pipettes as performed for this thesis will be described. Furthermore, the specifics of all experimental setups will be discussed. In all experiments, pipettes were filled with deionized water by attaching a rubber tube at the end of the capillary and pushing in water with a syringe attached to the other end



Figure 2.2: Inverted optical microscopy image of a young adult *C. elegans* worm caught by its head by a force-calibrated micropipette.

of the tube. The same syringe was then used to either push out more water, as in the case of a calibration experiment (see Section 2.1.2), or to apply suction to grab hold of a worm before a measurement (see Sections 2.1.3-2.1.5). All experiments were imaged with an inverted optical microscope with magnifications in the range of 5X-20X, as exemplified in Fig. 2.2, where a young adult worm has been caught by its head with a micropipette. The deflection of the pipette has been analyzed with an in-house cross-correlation image analysis Matlab script (Adam4MJCorrelationLotsGray.m) written by Drs. A. Raegan and M.-J. Colbert. The temporal resolution of all of our experiments was thereby set (limited) by the speed of the camera. The actual force is obtained by multiplying the deflection with the spring constant ( $k_p$ ) of the pipette.

### 2.1.1 Pipette manufacturing

Micropipettes were stretched from glass capillaries (152 mm long, 1/0.58 OD/ID (mm), World Precision Instruments) with a pipette puller (Narishige Group PN-30), resulting in hollow cylinders with a length of 1-4 cm and an outer diameter within the range of 10-50  $\mu\text{m}$ . The end of the pipettes were cut by looping the capillary around a hot wire (0.5 mm in diameter, 90% Ir-10% Pt, Alfa Aesar), heated by connecting a voltage across the wire with a DC power supply (Xantrex HPD 30-10). When the voltage was turned off, the soft glass solidified and contracted, resulting in a sharp

cut of the pipette and an open pipette end. To bend these pipettes into the desired shape, a thinner (0.2 mm) Ir-Pt wire was used in the same way as described above, but with lower wire temperatures to avoid sticking of the glass to the wire. With the help of an optical microscope (Meiji techno, Model SKT 28209, 2X), bends as short as  $\sim 200 \mu\text{m}$  were possible.

To perform experiments on very small worms, the end of the pipette had to be made thinner than the typical 10-15  $\mu\text{m}$  achievable with the pipette puller. To do this, the pipette was pulled away from the hot wire during the cutting stage, causing a slight stretching of the part of the glass touching the wire. When the voltage was turned off, the pipette was, with some luck, cut at the thinnest part. With this additional step, pipettes with openings as thin as 5  $\mu\text{m}$  could be produced.

### 2.1.2 Pipette calibration

To calibrate the micropipettes, two different approaches were used as described below.

#### Straight pipettes

In the calibration of a completely straight pipette, a small water droplet was hung as a weight at the end of the pipette, causing a certain, measurable pipette deflection. Knowing the drop volume and pipette deflection, the spring constant of the pipette could be calculated. To perform the calibration, the pipette was mounted horizontally above the inverted microscope and filled with ultra pure water. A small water drop was then pushed out from the pipette and left to cover the outside of the glass capillary, as shown in Fig. 2.3(a). Here, the pipette was viewed from the side by placing a mirror (piece of a silicon wafer) at a 45 degree angle very close to the pipette and focusing on the mirror image instead of the real image of the pipette. As more water (with a mass  $m$ ) was pushed into the drop, its weight ( $\mathbf{F} = m\mathbf{g}$ ) increased, leading to a change in the deflection ( $\Delta x$ ) of the pipette, as shown in Fig. 2.3(b). The water in the drop could also be let to evaporate to achieve a more continuous and slow change in its mass.

To quantify the weight of the droplet, its volume was first calculated by assuming an ellipsoidal shape with the volume of  $V = 4\pi d_{\min}^2 d_{\max}/3$ , where  $d_{\min}$  and  $d_{\max}$  are the minimum and maximum diameters of the drop, respectively. Here we assume radial

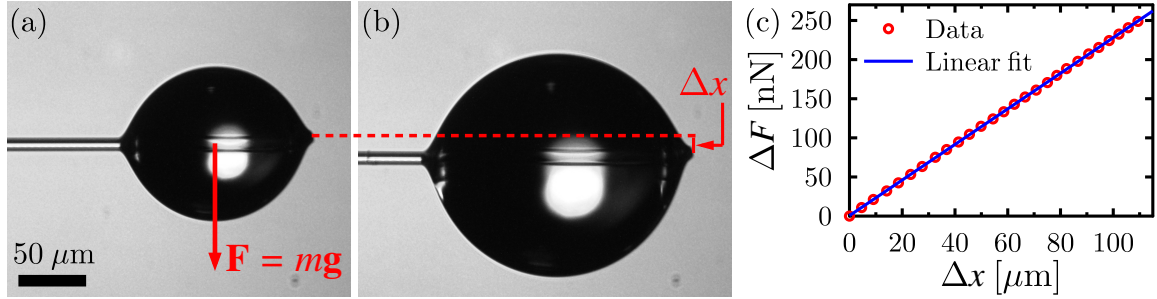


Figure 2.3: (a) In the calibration of a straight pipette, a small water droplet with a known mass ( $m$ ) was used as a weight ( $F$ ). (b) By increasing the size of the drop, a larger pipette deflection ( $\Delta x$ ) was detected. (c) The change of droplet weight plotted as a function of change in pipette deflection. The slope of the linear data corresponds to the spring constant of the pipette.

symmetry with respect to the axis of the pipette, i.e., that the minimum diameter is invariant with viewing angle. This is a refinement of the previously developed image analysis procedure, where a spherical droplet shape was assumed [142]. As the glass capillary clearly deforms especially smaller drops, as shown in Fig. 2.3(a), the assumption of an ellipsoidal three-dimensional shape is more correct. The weight of the drop can then easily be calculated as  $F = V\rho_{\text{H}_2\text{O}}g$ , where the density  $\rho_{\text{H}_2\text{O}}$  of pure water is assumed. In Fig. 2.3(c), the change in droplet weight is plotted as a function of change in pipette deflection. The slope of the clearly linear data corresponds to the spring constant of the pipette in units of  $\text{nN}/\mu\text{m}$ .

### Bent pipettes

To calibrate a pipette with a bent end, the water droplet technique was not ideal as the bent pipette corner typically deformed the surrounding drop, making any assumptions of its three-dimensional shape difficult to make. Instead, a previously calibrated straight pipette (spring constant  $k_s$ ) was used as a force sensor to calibrate any bent pipettes. To do so, the calibrated straight pipette was mounted on a stepping motor and placed parallel to the pipette that was to be calibrated, as shown in Fig. 2.4(a).

By moving the straight pipette ( $x_s$ ) with a constant speed into the bent pipette ( $x_b$ ), the relative deflection of the former before and after contact could be used to calculate the force applied to the bent pipette. In Fig. 2.4(b), the deflection of the

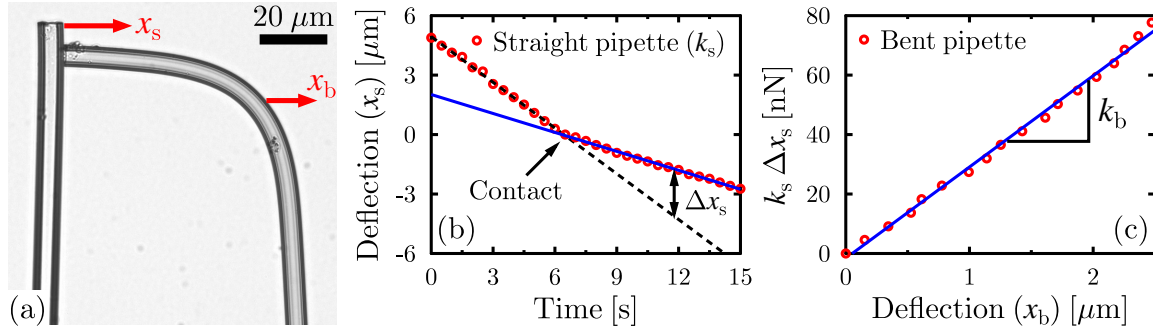


Figure 2.4: (a) The experimental setup for the calibration of a bent pipette (right) with a previously calibrated straight pipette (left). By moving the straight pipette ( $x_s$ ) into the bent pipette ( $x_b$ ), the spring constant of the latter can be quantified. (b) The deflection of the straight pipette, moved at a constant speed by a stepping motor. After contact between the two pipettes, the deflection speed of the straight pipette is decreased as it now also acts to deflect the bent pipette. The change in deflection caused by the bent pipette on the straight one is defined as  $\Delta x_s$ . (c) The force applied by the straight pipette as a function of the bent pipette deflection. The slope corresponds to the spring constant of the bent pipette.

straight pipette is plotted as a function of time. Before contact with the bent pipette, the straight pipette moves with a constant speed. After contact, the deflection speed is decreased due to the deflection of the bent pipette. The force applied to the bent pipette corresponds to  $k_s \Delta x_s$ , where  $\Delta x_s$  is the relative deflection of the straight pipette before and after contact [see Fig. 2.4(b)]. The force applied by the straight pipette is plotted as a function of the bent pipette deflection in Fig. 2.4(c), and the slope of the linear data corresponds to the spring constant ( $k_b$ ) of the bent pipette.

### Spring constants

The typical spring constants of the pipettes used in the work for this thesis were in the range of  $k_p \sim 1 - 20 \text{ nN}/\mu\text{m}$ . By varying the length and thickness of the cantilever, pipettes with different stiffnesses could easily be manufactured. The relative error associated with the spring constant was less than 10%, where the uncertainty stems from determining the volume of the elliptical drop through the image analysis described above, performing the linear fits to the force-deflection data, as well as from variations between several calibration experiments performed on the same pipette.

### 2.1.3 Bending experiment

The first goal of my doctoral research was to measure the longitudinal bending stiffness of *C. elegans*. To do so, a three-point bending measurement (see Section 1.2.1) of the worm was performed. To set up the bending experiment, a few drops of M9 containing  $\text{NaN}_3$  (see Section 2.2.1) were placed on a thin glass cover slip (22x40 mm<sup>2</sup>, VWR micro cover glass) and worms were picked into the liquid and paralyzed within a few minutes. A chamber was then built around the drop with two (2 mm tall) rubber spacers and a second glass cover slip on the top, as illustrated by a top view in Fig. 2.5(a), and was finally secured by two metal clamps, placed over the spacers. The chamber was then filled up with more of the M9- $\text{NaN}_3$  buffer, resulting in a capillary bridge between the two glass slides, which, for this reason, had to be spaced at a distance close to the capillary length of water ( $\sim 2$  mm for clean water).

The finalized chamber was placed on top of an inverted microscope and two different pipettes were then mounted into the chamber from the opposite sides. First, a force-calibrated pipette bent into a Z-shape [see Fig. 2.5(a)] was mounted on the right side onto a  $xyz$ -translational stage. The second pipette was the so called support pipette, which was a thicker ( $\sim 50 \mu\text{m}$ ) straight glass capillary with its end shaped as a U. This pipette was attached to a stage connected to two stepping motors in the

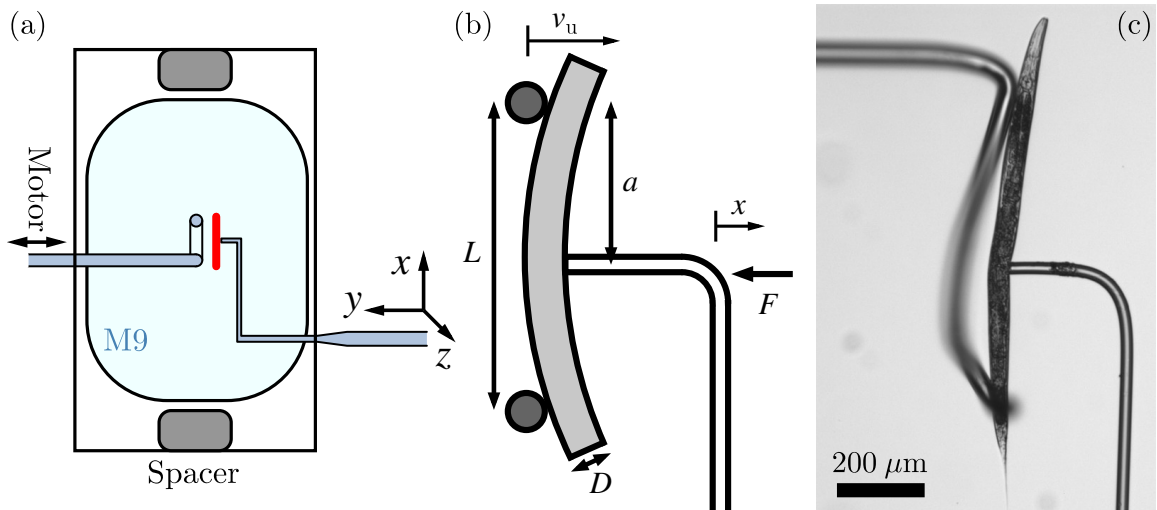


Figure 2.5: (a-b) Schematic diagram (top view, not to scale) of the experimental bending setup. (c) Optical microscopy image of the bending of a young adult worm.

$xy$ -directions and with manual  $z$ -translation, and placed facing the first pipette. To start an experiment, a worm was grabbed by the vulva (for consistency) and placed between the two vertical parts of the U-shaped pipette, as shown in the schematic illustration of Fig. 2.5(b) and in the optical microscopy image of Fig. 2.5(c). The bending was then performed by moving the support with a constant speed in the  $x$ -direction, causing a deflection ( $x$ ) of the pipette to the right and a spring-like force ( $F = k_p x$ , where  $k_p$  is the spring constant of the pipette) applied to the worm to the left. Various experiments were performed by bending the worm with different speeds and using a smaller support to bend different body parts locally. To perform relaxation measurements, the support was moved a certain, controlled distance (typically 30-50  $\mu\text{m}$ ) with a high speed onto the worm, after which the motor was stopped and the worm was left to relax under the force applied by the deflected pipette. Independent of experiment, they were all set up on an Olympus IX71 inverted optical microscope standing on an anti-vibration table (Halcyonics MOD-1). The CCD camera (QImaging, Retiga 2000R) and stepping motor (Newport LTA-HS, controlled by ESP3000) were controlled by an in-house LabView script (MJ\_summer07\_matilda.vi). Images were captured at a rate of 2 Hz, setting the time resolution of these experiments. For faster (10 Hz) capturing, the QCapture Pro software is recommended.

## Analysis

To calculate the bending stiffness  $EI$  (see Section 1.2.1), the worm diameter ( $D$ ), the distance between the supports ( $L$ ), and the distance between the upper support and the position of the applied force ( $a$ ) [all shown in the schematic of Fig. 2.5(b)] were measured on an optical microscopy image from the experiment in question with a simple Matlab script. Three length measurements were performed for each quantity to obtain an average and standard deviation, used for any subsequent error analysis. The cross-correlation code (Adam4MJCorrelationLotsGray.m) was used to analyze the deflection of the pipette as well as obtain the exact speed ( $v_u = x_u t$ ) of the supporting, U-shaped pipette. No values were taken directly from the motor, since acceleration and backlash (0.00786 mm for our stepping motor) issues made these unreliable. The force ( $F = k_p x$ ) was then plotted as a function of the bending of the worm, which was defined as  $y = x_u - x$ , i.e., the difference between the motion

of the support and deflection of the pipette. The slope of the initially linear data corresponds to the Hookean stiffness of the worm

$$k_w = \frac{3LEI}{a^2(L-a)^2}, \quad (2.1)$$

as introduced in Eq. 1.3 of Section 1.2.1, where  $EI$  is the bending stiffness of the nematode.

In the Supplementary Information of Paper I in Appendix A.1, a detailed derivation of the viscoelastic Maxwell model (Eq. 1.7) applied to this system is given. The key point in this derivation, as well as all other similar derivations in this work, was to realize that the MD experiments can not be performed or represented as pure creep or stress relaxation systems (see Section 1.2.2). The pipette is responsible both for the force sensing and material deformation, and these can, therefore, not be decoupled to, for instance, keep the force constant and let the deformation relax<sup>1</sup>. A simple stress or strain relaxation equation can therefore not be applied. This issue was taken into account in the derivation of the viscoelastic models, all based on Eqs. 1.7, 1.8, and 1.9, rendering analytically solvable differential equations. All viscoelastic fits to force-bending-time data in Papers I and II were performed either with Matlab or with the open source software GLE (Graphics Layout Engine).

### 2.1.4 Swimming experiment

A new micropipette deflection setup was built to perform high-speed measurements on actively swimming *C. elegans* nematodes. An inverted microscope (Olympus IX71) was placed on an anti-vibration table (Halcyonics) and  $xyz$ -translational stages were mounted with optical posts (all from Thorlabs) onto the table. A 56 Hz CCD camera (Allied Vision Technologies, GT1660) was finally attached to the microscope and connected to the computer with an ethernet cable.

In swimming experiments with a single worm, the nematodes were picked into a cylindrical container (diameter = 1.2 cm, height = 4 cm) made from a rubber tube

---

<sup>1</sup>In theory, this could be done by implementing a feedback loop connected to the motor, which would adjust its position to keep, e.g., the pipette deflection constant. This would, however, require real-time acquiring of the pipette position, which is not possible with the current image analysis approach. Reflecting a laser beam off the pipette and onto a photo diode could, for instance, be used for this purpose.

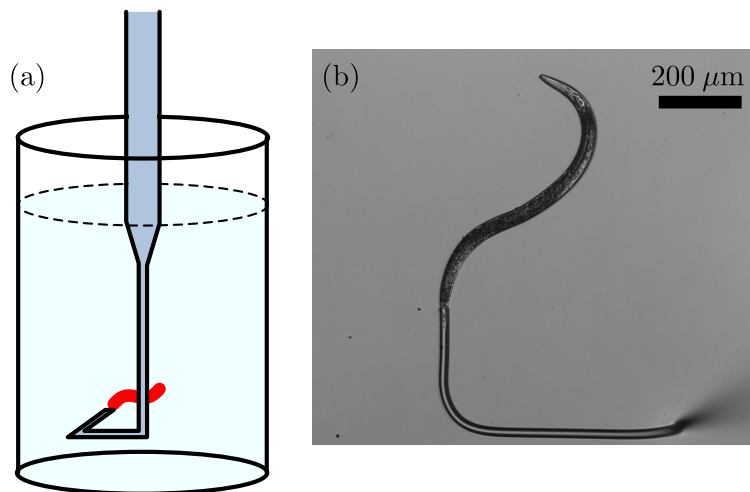


Figure 2.6: (a) Schematic diagram (not to scale) of the experimental swimming setup. (b) Optical microscopy image of a young adult worm swimming.

and filled with M9, as illustrated in Fig. 2.6(a). The pipettes for these experiments were of a “three-dimensional” design to measure forces in both the propulsive and lateral swimming directions of the worm. A worm was caught with this pipette by following it as it swam along the bottom of the chamber and applying suction close to its tail, resulting in the final configuration shown in the optical microscopy image of Fig. 2.6(b). Since the worms typically swim in the same plane as the bottom of the chamber, they kept on swimming in the imaging plane when captured by the pipette and brought away from the surface. All measurements were performed in an “infinite” fluid, far from any boundaries, and the thin part of the pipette was always completely immersed in the liquid, as asymmetric meniscus deformation effects were found to give rise to drift in the pipette position.

All analysis for this work is described in detail in Papers III-V (Appendix A.3-A.5) and in the M.Sc. thesis of R. Schulman [143].

### 2.1.5 Tangling experiment

The chamber setup for the tangling experiment was the same as that developed for the bending experiments (Section 2.1.3). The chamber was filled with M9 and placed on the high-speed inverted microscope setup developed for the swimming experiments

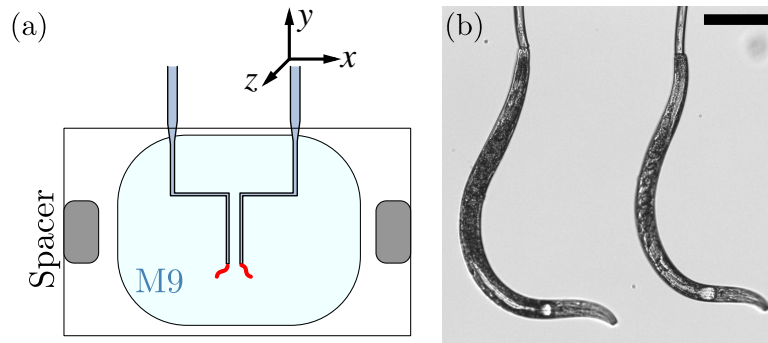


Figure 2.7: (a) Schematic diagram (not to scale) of the experimental tangling setup. (b) Optical microscopy image of two young adult worms. The scale bar represents  $200 \mu\text{m}$ .

(Section 2.1.4). Two pipettes were then mounted on separate  $xyz$ -translational stages from the same side, as shown in the schematic illustration in Fig. 2.7(a). To get the pipette ends very close to each other, the pipettes were bent as shown in the diagram, where each straight part was approximately 1 cm long. Two similarly sized worms were finally grabbed by their tails and left to swim very close to each other, as shown in the optical image of Fig. 2.7(b).

The tangling analysis relied on the deflection of both of the flexible pipettes and is described in detail in the Supplementary Information of Paper VI in Appendix A.6. The rational 3 tangles were identified and counted by looking through the entire image series of each experiment performed at reasonably close distances. To track the sinusoidal lateral motion of the worm heads, sequential images were opened with Matlab and the head positions were located by manual clicking. This manual approach was deemed necessary due to the frequent overlapping between the worm bodies, making any automatized image analysis approach similar to that applied to a single worm highly non-trivial.

## 2.2 *C. elegans* maintenance

The *C. elegans* nematodes (from the Caenorhabditis Genetics Center) and all worm related materials were acquired, starting in November of 2011, from the lab of Dr. Ryu at the University of Toronto. The worms were kept on bacteria-covered gel surfaces

held in petri dishes (9 cm in diameter) and maintained in an incubator (Thermo Scientific Heratherm) at a constant temperature of 20°C. The incubator was cleaned several times a year with a 70% ethanol in water mixture to prevent mould growth and to clean out any other contamination. The worm materials used in this work were prepared by technicians in Dr. Ryu's lab and all chemicals were sourced from Sigma-Aldrich. The maintenance procedures are described in detail below.

## 2.2.1 Materials

### Agar plates

The worm gel plates were prepared from nematode growth media (NGM) according to standard procedures [144]. The agar plates were then covered by a "lawn" of *Escherichia coli* (OP50) bacteria, acting as a food source for the worms. The growth of this bacterium is limited on NGM plates, resulting in a thin layer of bacteria which allows for easier observation of the worms as well as better worm mating [19]. All bacteria covered NGM plates were brought from Toronto a few times a year, stacked in clean plastic bags and kept in a refrigerator at 4°C in Dr. Fradin's lab at McMaster. Any plates containing worms were sealed with Parafilm to avoid water evaporation from the gel and potential worm death.

### M9 buffer

To perform experiments in a fluid environment, a so called M9 buffer containing various salts is typically used with *C. elegans* (placing worms in deionized water is to be avoided due to the risk of osmotic shock). The M9 buffer used in all of our micropipette deflection experiments was mixed according to the following, standard recipe [19]:

3 g  $\text{KH}_2\text{PO}_4$   
6 g  $\text{Na}_2\text{HPO}_4$   
5 g  $\text{NaCl}$   
1 ml 1 M  $\text{MgSO}_4$   
 $\text{H}_2\text{O}$  to 1 L

The buffer was finally sterilized by autoclaving. Three large (1 L) bottles of M9 were brought from Toronto during 2011-2014. A large consumption, occasional salt aggregation (causing clogging of our pipettes or dirt in the field of view during the experiments), as well as contamination were the main reasons to acquiring new buffer solutions.

## Drugs

To anesthetize *C. elegans*, various chemicals were used. The most common approach was to use the muscle relaxant  $\text{NaN}_3$  dissolved in water (1 M solution acquired from Toronto). To achieve the appropriate concentration (8-15 mM) for the bending experiments, the drug was further diluted with M9 in our lab. Care was to be taken when handling high concentrations of  $\text{NaN}_3$ , as the chemical is both explosive and lethally poisonous to humans. The usage of this drug gave rise to paralyzed, straight, rod-shaped worms as shown in Fig. 2.5(c). No differences were noted in the material properties of the worms with increased  $\text{NaN}_3$  concentration, but care had to be taken not to perform experiments on dead nematodes. To ensure live worms, the lowest drug concentration resulting in paralysis was used and all experiments were performed within 2 hours from placing the worms in the media.

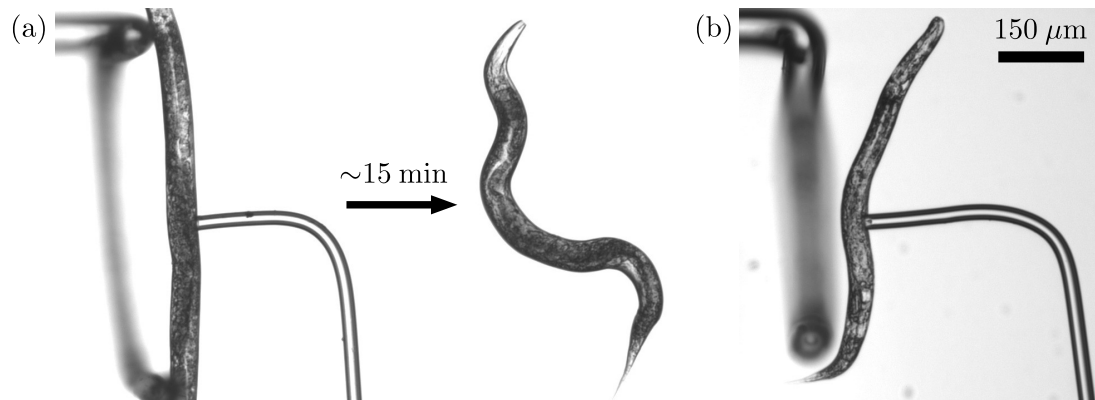


Figure 2.8: (a) Bending measurements on *C. elegans* in a M9 buffer with 0.3 M BDM had to be performed within 15 minutes. After this, the worm went from a rod to a zig zag shape due to muscle contraction. (b) The immediate effect of muscimol on *C. elegans*, making any bending measurements impossible with this muscle contracting drug. The scale bar applies to all images.

In addition to this, 0.3 M 2,3-Butanedione monoxime (BDM) in M9 and various concentrations of muscimol and levamisole dissolved in M9 were tried. All of these drugs, however, caused paralysis of the worms, featured by random and intense muscle contractions, resulting in undesired zig zag shapes of the worm bodies, as shown in Fig. 2.8. BDM could be used as long as the bending experiments were set up and finished within 15 minutes from placing the worms in the media. After this time, the muscle contraction started deforming the previously straight worm body [Fig. 2.8(a)]. This time window allowed for the bending of 1-2 worms per experiment (3 trials per worm), requiring the entire experiment to be set up in less than a couple of minutes.

In Fig. 2.8(b), the immediate result of muscimol on the worm body is shown. No bending experiments were possible with either muscimol or levamisole due to the zig zag worm shapes caused by the drug induced muscle contractions.

## 2.2.2 Chunking

To keep the worms viable, they had to be transferred to new bacteria covered agar plates with an interval of 2-3 days, corresponding to the time for the lack of food and plate overcrowding to become apparent. Using worms from too old plates showed differences in both the passive material properties, caused mostly by the intestine being completely empty, as well as in the active swimming behaviour of the worms. In the latter case, worms were more sensitive to being placed in the buffer and caught by pipettes, resulting in frequent halts in their movements and unusual swimming motions, as well as a faster apparent death.

To transfer (or “chunk”) worms to a new plate, a spatula was first sterilized by dipping it in ethanol and burning off the alcohol using an alcohol burner. After this, a  $\sim 1 \text{ cm}^2$  piece of the old, worm-covered agar was cut out and placed upside-down on the fresh, bacteria-covered plate. This new plate could then be used for experiments in 1-4 days after chunking, depending on the size of the chunked piece (the higher the number of worms transferred, the faster they would reproduce and manage to cover the new plate) and the temperature of the incubator (the worms develop faster at higher temperatures). The actual transfer was to be performed as fast as possible to avoid contamination of the fresh agar plate. In the case of apparent mould on any of the old plates, these were quickly discarded and another, clean plate was used for the

chunking. Plates as old as 2-3 months could be used for chunking since all of these contained Dauer state worms (see Section 1.1.2), which would develop into normal worms when placed in a food rich environment. For this reason, several plates from various dates were stored in the incubator to always have usable worms and avoid acquiring new ones from Toronto. All unwanted plates were finally discarded in the biowaste bin in Dr. Fradin's lab.

### 2.2.3 Picking

Before an experiment, worms were picked from the surface of an appropriate agar plate, as discussed above, into a drop of buffer. The picker was made by carefully melting the tip of a glass pasteur pipette in the flame of an alcohol burner and placing a platinum wire ( $\sim 2$  mm thick,  $\sim 2$ -3 cm long) into the soft glass. The pipette was then moved out of the flame, causing the wire to firmly freeze into the now solid glass. The picking was done under a dissecting stereomicroscope (Leica StereoZoom SZ4, 0.7-3X), where the end of the sharp picker was carefully placed under the worm of interest and then used to scoop up the worm and finally place it in the drop of buffer. As the worms were easily injured and/or killed by careless picking techniques, caution was necessary to gently lift the worms off the agar and then place them into the drop without squishing them into the supporting glass slide. The transfer between the agar and the buffer was to be done quickly, as the worms die within tens of seconds after being placed on a dry surface.

Between each pick, the picker was sterilized by dipping it in ethanol and burning off the alcohol using the alcohol burner. As ethanol works as an anesthetic to *C. elegans*, it was important to burn off all alcohol before picking the next worm. Furthermore, care had to be taken not to pick worms with a burning hot picking wire, which naturally would kill or seriously injure the small crawlers. To avoid this, the picker was cooled down by sticking it into the agar along the edge of the petri dish before a worm was approached. This also made the platinum wire more sticky, simplifying the scooping up of the worms.



# Chapter 3

## Summary of papers

In this chapter, the published work of my *C. elegans* research is summarized. For all of these publications (appended in Appendix A), I contributed significantly to the design, research, and final outcome of the project. All of my additional PhD publications, either related to *C. elegans* or fields not relevant for the focus of this thesis, are listed and briefly described in Appendix B.

The focus of my *C. elegans* research performed by micropipette deflection can be divided into three parts: probing the passive material properties of *C. elegans*, understanding the active swimming dynamics of the microswimmer, and investigating the active interactions between two swimming worms. In Papers I and II, the passive material properties of *C. elegans* are discussed. In Paper I, the viscoelastic properties of the model organism were studied by performing three-point bending measurements on the worms at all life stages and with a focus on different anatomical parts. It was shown that a widely used and accepted viscoelastic model failed to describe the material properties of the nematode, and that the worm is shear-thinning. These findings shed new light onto the already studied mechanical features of the model organism. In Paper II, the complex internal flow of the worm was further quantified by force relaxation measurements and described with an extended viscoelastic model, incorporating the non-Newtonian aspects of the biological tissue.

In Papers III-V, the active swimming dynamics of single worms was probed (see Appendix B.1 for a brief description of our work on the crawling dynamics of *C. elegans* nematodes). The drag forces experienced by the swimmer were directly mea-

sured in a time-resolved manner and successfully modelled with resistive force theory. In Paper III, we investigated the dynamics of *C. elegans* in a water-like buffer and quantified the drag coefficients of the slender body. To investigate the gait modulation and drag coefficients in environments with increased resistance, the worms were confined to swim close to one or two boundaries (Paper IV), or in fluids with increased viscosities (Paper V). The gait modulation was found to only depend on the external resistance of the fluid, and not on the means of how the resistance was increased.

In Paper VI, the interactions between two microswimming nematodes in an infinite fluid are finally investigated. The two “active string”-like worms were found to tangle in a reproducible and predictable manner, and a simple geometric model was introduced to describe the seemingly complicated system. This work introduces an interesting avenue to study complex interactions in active materials, and can be linked to highly packed systems of cilia and flagella.

### 3.1 Paper I: Viscoelasticity

*Viscoelastic properties of the nematode *Caenorhabditis elegans*, a self-similar, shear-thinning worm*

M. Backholm, W. S. Ryu, and K. Dalnoki-Veress, Proceedings of the National Academy of Sciences of the United States of America **110**, 4528-4533 (2013).

This paper represents our first attempt on understanding the viscoelastic properties of *C. elegans* by using a direct biomechanical approach, and is the first within our collaboration with Dr. William Ryu at the University of Toronto. In this work, we implemented the technique of micropipette deflection to measure the longitudinal bending stiffness of the model organism on a biologically and structurally relevant length scale. Three-point bending measurements were performed by holding on to the side of anaesthetized worms with a force-calibrated micropipette and by moving a simple support onto the worm, causing it to bend under the applied force of the deflected pipette. The worm material was initially modelled as purely Hookean, and the bending stiffness was achieved from the slope of the linear regime of the force-deformation data. Nematodes in all life stages were probed, and the scaling of the bending stiffness with worm diameter was shown to be in agreement with the assumption of a cylindrical distribution of stiff material. Interestingly, Dauer state nematodes were shown to have a higher stiffness as compared to similarly sized, normal life stage worms, indicating the strong contribution of the cuticle to the total body stiffness. By performing local bending measurements along the body of young adult worms, the contribution of the relaxed body muscles to the total stiffness was furthermore verified.

The most significant finding in this work was made when investigating the viscoelastic properties of the worm. Kelvin-Voigt and Maxwell models were applied to our system and the theoretical solutions were fit to the experimental force-deformation data. It was shown that the previously assumed Kelvin-Voigt model failed to capture the data, whereas the Maxwell model successfully described the bending dynamics of the worm. By applying the Maxwell model to our data, the damping coefficient of young adult worms were probed in experiments performed with different bending speeds. The viscous component of *C. elegans* was in this way shown to be shear-

thinning, and the implications of this non-Newtonian internal property was related to the gait modulation of the worm in different environments.

In this work, I designed the experimental setup, made and calibrated all pipettes, collected and analyzed all experimental data, derived the theoretical models, and wrote the first draft of the manuscript.

## 3.2 Paper II: Complex relaxation

*The nematode *C. elegans* as a complex viscoelastic fluid*

M. Backholm, W. S. Ryu, and K. Dalnoki-Veress, European Physical Journal E **38**, 36 (2015).

Here, the non-Newtonian (complex) flow of *C. elegans* was investigated in detail. Dynamic relaxation measurements were performed with micropipette deflection to closely probe the internal viscosity of the model organism and further explore the shear-thinning properties discovered in Paper I. To successfully capture the viscoelastic response of the soft tissue, the standard linear solid model was applied to the experimental data. First, a simplistic model assuming a purely Newtonian internal fluid was used. The failure of the initial approach was then corrected by implementing a power-law fluid into the viscoelastic model. Our extended SLS model was shown to successfully capture the dynamics in the relaxation regime, and the non-Newtonian properties of *C. elegans* could thereby be probed in a more general way. The flow consistency and power-law indices were quantified for young adult and adult nematodes, and the worm material was once again proven to be strongly shear-thinning. The effective damping coefficient of the worm was calculated for the biologically relevant cases of typical swimming and crawling motions, and were shown to differ by a factor of three. These results emphasize the importance of achieving a detailed knowledge of the internal material properties of a natural swimmer or crawler, as its active locomotion strategy can not be assumed to be affected only by the external environment.

In this project, I initiated, designed, and performed all experiments and data analysis. I also derived all theoretical models applied to our system and wrote the first draft of the manuscript. Early discussions with Drs. Alexander Morozov, Elie Raphaël, and Olivier Dauchot, as well as ongoing conversations with Rafael Schulman are gratefully acknowledged.

### 3.3 Paper III: Swimming dynamics

*Dynamic force patterns of an undulatory microswimmer*

R. D. Schulman, M. Backholm, W. S. Ryu, and K. Dalnoki-Veress, Physical Review E: Rapid Communications **89**, 050701 (2014).

In this paper, we laid the groundwork for our new focus to probe the active swimming dynamics of *C. elegans* by using micropipette deflection. Actively swimming nematodes were caught by their tails with calibrated micropipettes designed to measure the drag forces experienced by the microswimmer in both the lateral and propulsive directions. These experiments represent the first direct and time-resolved force measurements of an undulatory microswimmer. The net propulsive force was determined for nematodes in different life stages and found to be in agreement with previously predicted drag forces. By combining the acquired force data with resistive force theory, this simple and well used model could be verified for the case of *C. elegans*. Furthermore, the analytical approach could successfully provide the first measured values of the drag coefficients of the model organism, and the results were shown to agree well with the theoretical predictions made by Lighthill. Finally, a simple scaling argument of the drag forces as a function of body length was made and verified experimentally in both the propulsive and lateral directions.

For this project, I designed and performed the initial experiments demonstrating how the drag forces experienced by a swimming *C. elegans* nematode could be probed with micropipette deflection. Furthermore, I was highly involved in the design and building of the new, “high-speed” micropipette deflection setup purposed for these time-resolved, dynamic measurements. I then trained M.Sc. student Rafael Schulman in all components related to the micropipette deflection experiments on *C. elegans*, and he then collected all final data under my co-supervision for his M.Sc. thesis. We developed the theory as well as the data analysis scripts and procedures in close collaboration. Finally, I was strongly involved with the preparation of the first draft of the manuscript as well as its continuous editing. Interesting discussions with Konstantine Palanski and Yegor Rabets at the University of Toronto are gratefully acknowledged.

### 3.4 Paper IV: Swimming near boundaries

*Undulatory microswimming near solid boundaries*

R. D. Schulman, M. Backholm, W. S. Ryu, and K. Dalnoki-Veress, *Physics of Fluids* **26**, 101902 (2014).

In this project, we used micropipette deflection to investigate how the swimming dynamics of *C. elegans* was affected as nematodes were confined by solid boundaries. The drag forces were seen to increase significantly as a function of decreasing distance to a single boundary, whereas the ratio between the drag coefficients remained constant. We also confined worms between two plates and detected a vast increase in the drag forces experienced by the nematode as compared to the case of a single boundary. By decreasing the separation between the two walls in the channel experiments, the drag coefficient ratio was seen to increase by more than two folds. The drag coefficients derived in these experiments were compared to the theories of Lighthill for swimming far away from the surfaces, and Katz, *et al.*, for swimming close to the solid walls. Our data was shown to be in excellent agreement with the two theoretical models. In both of the experiments, the swimming amplitude of the nematode was shown to decrease with confinement. This change corresponds to a gait modulation of the worm, as caused by the increase in the drag forces experienced by the worm in environments with higher confinements.

For this paper, R. Schulman was the the leading author. During the project, I contributed with continuous assistance to design the experimental setup, and solve experimental and analysis issues. I was strongly involved with the continuous interpretation of the results, and edited several early drafts of the manuscript.

### 3.5 Paper V: High-viscosity swimming

*The effects of viscosity on the undulatory swimming dynamics of *C. elegans**

M. Backholm, A. K. S. Kasper, R. D. Schulman, W. S. Ryu, and K. Dalnoki-Veress, submitted to *Physics of Fluids* (2015).

Here, we investigated the swimming dynamics of *C. elegans* in fluids with different viscosities. The gait modulation of the tail-tethered nematodes was quantified by increasing the fluid viscosity, and the swimming frequency, wavelength, and amplitude were shown to decrease in environments with higher resistance. By using micropipette deflection, we measured the drag forces experienced by the worms, and modelled the data with resistive force theory. The resulting drag coefficients were compared to the classical theoretical models of Lighthill as well as Gray and Hancock, and an interesting transition was observed between the theory of Lighthill at low viscosities, and that of Gray and Hancock at high viscosities. This could be partly explained by the gait modulation of the worm, transitioning from a high-amplitude swimming motion to a more conventional undulatory motion with a low amplitude. The gait modulation was shown to occur to maintain a constant power output of the swimming worm as the external viscous resistance was increased. The ability of varying its gait ensures the survival of the nematode in continuously changing environments of, e.g., water, mud, and soil. We also compared the swimming amplitude of the worms with the findings of Paper IV, where the drag forces were increased by bringing the swimmers close to one or two solid boundaries. We found no difference between the kinematics of the two systems, and thus show that the only relevant force affecting the gait modulation of the nematodes is of a hydrodynamic origin.

In this work, I designed the experimental setup and carried out the first experiments. I then trained B.Sc. thesis student Alexandra Kasper in micropipette deflection, worm maintenance, and solution preparation. She finally carried out the experimental work under mine and R. Schulman's continuous co-supervision. All co-authors contributed to the interpretation of the results, I then analyzed the final data and wrote the first draft of the manuscript.

## 3.6 Paper VI: Tangling

*Tangling of tethered swimmers: Interactions between two nematodes*

M. Backholm, R. D. Schulman, W. S. Ryu, and K. Dalnoki-Veress, Physical Review Letters **113**, 138101 (2014).

In this paper, we investigated the interactions between two swimming *C. elegans* nematodes, held close together with two micropipettes. When brought to short enough separations, the worms were found to twist into rational tangles of two different orders. The critical ratio between body length and pipette separation was derived with a simple geometrical model, implementing the helical structure of the three-dimensional tangles. These ratios, predicting the onset of 2 and 3 rational tangles, were shown to be in excellent agreement with our experimental observations. The lifetime of the tangling events was furthermore investigated at short and long separations. Finally, the tangling probability was derived analytically by considering the sinusoidal motion of the worm heads and the likelihood of these overlapping enough to form a tangle. The resulting probability was successfully fit to the experimental data, showcasing how a seemingly complicated process can be analytically investigated and quantitatively understood. In addition, this work increased our understanding of the everyday problem of tangling strings, as well as the intricate interactions present in active materials composed of, for example, closely packed arrays of cilia or actively beating and interacting bacterial flagella.

In this project, I initiated and designed the experiment, and collected and analyzed all experimental data. The theory was developed in close collaboration with R. Schulman. I wrote the first draft of the manuscript. Early discussions with Solomon Barkley and Dr. Christian Wagner are gratefully acknowledged.



# Chapter 4

## Conclusions and outlook

In this PhD thesis, the biomechanical properties of the nematode and model organism *C. elegans* have been investigated to understand the contributions of passive body properties, active swimming dynamics, and inter-worm interactions on undulatory microswimming in general. Micropipette deflection has served as a novel experimental technique, implementing a force-calibrated micropipette to, for the first time, directly probe these dynamic quantities in a time-resolved and biologically relevant manner. Our work has focused on investigating the validity of previously assumed physical models. In addition to this, our findings have provided new insight into the complex material properties of the model organism as well as the forces involved in its undulatory motion.

The first goal of this PhD work was to measure the stiffness of *C. elegans*. Our results in Paper I on the scaling of the bending stiffness with worm body size, as well as the contribution of different anatomical parts to the total stiffness of the nematode, resolve several open questions in the biomechanical field. In the process of determining the worm elasticity, new viscoelastic and non-Newtonian properties were furthermore found. The bending of the worm body was determined to be best described by the viscoelastic Maxwell model, although our work in Paper II furthermore showed that the standard linear solid model successfully captures also the relaxation aspect of the soft material. Applying these models to the data from two different experiments, the worm material was decisively found to be shear-thinning. This result represents an advancement in our knowledge of the material properties of *C. elegans*, and should

be part of any future attempts to model and understand the motion of the nematode in different environments. The gait-modulation between swimming and crawling can no longer be assumed to be driven solely by a change in the resistance of the external medium, but will clearly also be affected by the variables determining the internal resistance to bending. As a shear-thinning property makes it easier for the nematode to bend its own body at higher rather than lower speeds, it might transition into swimming earlier than previously assumed when only taking a decrease of the external fluid viscosity into account.

The second goal of this thesis, as described in Papers III–V, was to use micropipette deflection to investigate new physics in the active swimming dynamics of *C. elegans*. By holding on to a worm by its tail, the drag forces experienced by the swimmer could be probed in a direct and time-resolved manner. The drag forces were successfully modelled using resistive force theory, and the drag coefficients of the undulatory microswimmer were determined. Experiments were performed close to one and two boundaries, as well as in fluids with different viscosities, and the results were compared to the classical theoretical models of Lighthill, Katz, and Gray and Hancock. In order to maintain a constant power output in the systems of increased resistance, the nematodes actively modulated their swimming gaits by decreasing their swimming frequency, wavelength, and amplitude. The gait modulation was finally shown to be caused only by hydrodynamic forces.

The development of micropipette deflection into a high-speed technique during this PhD project also enabled further investigations of *C. elegans* in the field of collective behaviour and interactions. In the experiments of Paper VI, we forced two nematodes to swim at different separations. This experimental setup allowed us to probe different inter-worm interactions in a controlled manner. The most dominant interaction was found to be the frequent twisting of the worms into tangles of different orders. The achieved understanding of the system could be linked to other active materials as well as the everyday snarling of strings and ropes. Most importantly, the final part of my PhD work also created several new and interesting questions within the field of collective swimming. As discussed in this thesis and also investigated in initial work by B.Sc. thesis student Alexandra Kasper in our group, no hydrodynamic interactions have been found between nematodes swimming at close distances in a

normal buffer solution. To enhance the drag forces between the worms, their rather high Reynolds number would need to be decreased. This could be achieved by, for example, introducing confinement or by increasing the fluid viscosity. As was shown in Paper V, the  $Re$  for young adult worms can be decreased with an order of magnitude by increasing the viscosity of the surrounding fluid by a factor of 4. Probing the binary hydrodynamic interactions between two microswimmers in a high viscosity fluid would be the natural next step to take.

To conclude, the overall strategy of the work behind this thesis has been to combine direct high-quality micromechanical experiments with simple theoretical models to shed new light on a seemingly complicated biological system. In doing so, we have spanned the breadth of an interdisciplinary field focused on understanding the slithering motion of a slender body from the perspectives of physics, engineering, biology, and mathematics. The work presented in this PhD thesis has also provided new avenues into future research in active materials.



# Bibliography

- [1] A. T. Jones, *The gliding of a snake*, Physics **4**, 164–165 (1933).
- [2] J. Gray, *The mechanism of locomotion in snakes*, J. Exp. Biol. **23**, 101–120 (1946).
- [3] J. Gray, *Undulatory propulsion*, Q. J. Microsc. Sci. **94**, 551–578 (1953).
- [4] J. Gray and H. W. Lissmann, *The locomotion of nematodes*, J. Exp. Biol. **41**, 135–154 (1964).
- [5] R. G. Cox, *The motion of long slender bodies in a viscous fluid. Part 1. General theory*, J. Fluid Mech **44**, 791–810 (1970).
- [6] E. Niebur and P. Erdus, *Theory of the locomotion of nematodes: Dynamics of undulatory progression on a surface*, Biophys. J. **60**, 1132–1146 (1991).
- [7] Z. V. Guo and L. Mahadevan, *Limbless undulatory propulsion on land*, Proc. Natl. Acad. Sci. USA **105**, 3179–3184 (2008).
- [8] E. D. Tytell, C.-Y. Hsu, T. L. Williams, A. H. Cohen, and L. J. Fauci, *Interactions between internal forces, body stiffness, and fluid environment in a neuromechanical model of lamprey swimming*, Proc. Natl. Acad. Sci. USA **107**, 19832–19837 (2010).
- [9] D. L. Hu, J. Nirody, T. Scott, and M. J. Shelley, *The mechanics of slithering locomotion*, Proc. Natl. Acad. Sci. USA **106**, 10081–10085 (2009).

- 
- [10] C. Fang-Yen, M. Wyart, J. Xie, R. Kawai, T. Kodger, S. Chen, Q. Wen, and A. D. T. Samuel, *Biomechanical analysis of gait adaptation in the nematode *Caenorhabditis elegans**, Proc. Natl. Acad. Sci. USA **107**, 20323–20328 (2010).
- [11] J. Gray and G. Hancock, *The propulsion of sea-urchin spermatozoa*, J. Exp. Biol. **32**, 802–814 (1955).
- [12] E. Lauga and T. R. Powers, *The hydrodynamics of swimming microorganisms*, Rep. Prog. Phys. **72**, 096601 (2009).
- [13] R. D. Maladen, Y. Ding, C. Li, and D. I. Goldman, *Undulatory swimming in sand: Subsurface locomotion of the sandfish lizard*, Science **325**, 314–317 (2009).
- [14] Y. Ding, S. S. Sharpe, A. Masse, and D. I. Goldman, *Mechanics of undulatory swimming in a frictional fluid*, PLoS Comput. Biol. **8**, e1002810 (2012).
- [15] G. Tokic and D. K. P. Yue, *Optimal shape and motion of undulatory swimming organisms*, Proc. R. Soc. B **279**, 3065–3074 (2012).
- [16] M. S. Triantafyllou, G. S. Triantafyllou, and D. K. P. Yue, *Hydrodynamics of fishlike swimming*, Annu. Rev. Fluid Mech. **32**, 33–53 (2000).
- [17] J. H. Long and K. S. Nipper, *The importance of body stiffness in undulatory propulsion*, Amer. Zool. **36**, 678–694 (1996).
- [18] D. I. Goldman, *Colloquium: Biophysical principles of undulatory self-propulsion in granular media*, Rev. Mod. Phys. **86**, 943–958 (2014).
- [19] B. Wood, *The nematode *Caenorhabditis elegans** (Cold Spring Harbor Laboratory Press, New York, 1988).
- [20] A. Brown, *In the beginning was the worm: Finding the secrets of life in a tiny hermaphrodite* (Columbia University Press, New York, 2003).
- [21] J. E. Harris and H. D. Crofton, *Structure and function in the nematodes: internal pressure and cuticular structure in *Ascaris**, J. Exp. Biol. **34**, 116–130 (1957).

- [22] L. Byerly, R. Cassada, and R. Russell, *The life cycle of the nematode *Caenorhabditis elegans*: I. Wild-type growth and reproduction*, Dev. Biol. **51**, 23–33 (1976).
- [23] G. N. Cox, S. Staprans, and R. S. Edgar, *The cuticle of *Caenorhabditis elegans*: II. Stage-specific changes in ultrastructure and protein composition during postembryonic development*, Dev. Biol. **86**, 456–470 (1981).
- [24] N. A. Croll, J. M. Smith, and B. M. Zuckerman, *The aging process of the nematode *Caenorhabditis elegans* in bacterial and axenic culture*, Exp. Aging Res. **3**, 175–189 (1977).
- [25] C. G. Knight, M. N. Patel, R. B. R. Azevedo, and A. M. Leroi, *A novel mode of ecdysozoan growth in *Caenorhabditis elegans**, Evol. Dev. **4**, 16–27 (2002).
- [26] Y. C. Fung, *Biomechanics: Mechanical properties of living tissue* (Springer-Verlag, New York, 1993), 2nd edition.
- [27] R. A. L. Jones, *Soft Condensed Matter* (Oxford University Press, Oxford, 2002).
- [28] E. Kreyszig, *Advanced Engineering Mathematics* (John Wiley & Sons, Singapore, 2006), 9th edition.
- [29] R. Cross, *Elastic and viscous properties of Silly Putty*, Am. J. Phys. **80**, 870–875 (2012).
- [30] S. Leeman and A. Peyman, *The Maxwell model as a soft tissue descriptor*, Acoust. Imag. **25**, 357–361 (2002).
- [31] G. Constantinides, Z. I. Kalcioğlu, M. McFarland, J. F. Smith, and K. J. V. Vliet, *Probing mechanical properties of fully hydrated gels and biological tissues*, J. Biomech. **41**, 3285 – 3289 (2008).
- [32] G. Schmid-Schönbein, K. Sung, H. Tözeren, R. Skalak, and S. Chien, *Passive mechanical properties of human leukocytes*, Biophys. J. **36**, 243–256 (1981).
- [33] K. Guevorkian, M.-J. Colbert, M. Durth, S. Dufour, and F. Brochard-Wyart, *Aspiration of biological viscoelastic drops*, Phys. Rev. Lett. **104**, 218101 (2010).

- [34] K. Guevorikan, D. Gonzalez-Rodriguez, C. Carlier, S. Dufour, and F. Brochard-Wyart, *Mechanosensitive shivering of model tissues under controlled aspiration*, Proc. Natl. Acad. Sci. USA **108**, 13387–13392 (2011).
- [35] N. Phan-Thien, S. Nasserri, and L. E. Bilston, *Oscillatory squeezing flow of a biological material*, Rheol. Acta. **39**, 409–417 (2000).
- [36] R. W. Chan and I. R. Titze, *Viscoelastic shear properties of human vocal fold mucosa: Measurement methodology and empirical results*, J. Acoust. Soc. Am. **106**, 2008–2021 (1999).
- [37] H. Oxlund and T. T. Andreassen, *The roles of hyaluronic acid, collagen and elastin in the mechanical properties of connective tissues*, J. Anat. **131**, 611–620 (1980).
- [38] J. M. McPherson, P. W. Ledger, S. Sawamura, A. Conti, S. Wade, H. Reihanian, and D. G. Wallace, *The preparation and physicochemical characterization of an injectable form of reconstituted, glutaraldehyde cross-linked, bovine corium collagen*, J. Biomed. Mater. Res. **20**, 79–92 (1986).
- [39] F. H. Silver, A. Ebrahimi, and P. B. Snowhill, *Viscoelastic properties of self-assembled type I collagen fibers: Molecular basis of elastic and viscous behaviors*, Connect. Tissue Res. **43**, 569–580 (2002).
- [40] L. Duan, J. Li, C. Li, and G. Li, *Effects of NaCl on the rheological behavior of collagen solution*, Korea-Aust. Rheol. J. **25**, 137–144 (2013).
- [41] B. B. Bird, R. C. Armstrong, and O. Hassager, *Dynamics of polymeric liquids* (John Wiley & Sons, New York, 1977).
- [42] W. W. Graessley, *The entanglement concept in polymer rheology*, Adv. Polym. Sci. **16**, 1–179 (1974).
- [43] K. Dalnoki-Veress, B. G. Nickel, C. Roth, and J. R. Dutcher, *Hole formation and growth in freely standing polystyrene films*, Phys. Rev. E **59**, 2153–2156 (1999).

- [44] G. P. Roberts, H. A. Barnes, and P. Carew, *Modelling the flow behaviour of very shear-thinning liquids*, Chem. Eng. Sci. **56**, 5617–5623 (2001).
- [45] M. Gazzola, M. Argentina, and L. Mahadevan, *Scaling macroscopic aquatic locomotion*, Nature Phys. **10**, 758–761 (2014).
- [46] J. Gray, *Studies in animal locomotion: I. The movement of fish with special reference to the eel*, J. Exp. Biol. **19**, 88–104 (1933).
- [47] M. J. Lighthill, *Large-amplitude elongated-body theory of fish locomotion*, Proc. R. Soc. Lond. B **179**, 125–138 (1971).
- [48] T. J. Pedley and S. J. Hill, *Large-amplitude undulatory fish swimming: Fluid mechanics coupled to internal mechanics*, J. Exp. Biol. **202**, 3431–3438 (1999).
- [49] G. Taylor, *Analysis of the swimming of long and narrow animals*, Proc. R. Soc. A **214**, 158–183 (1952).
- [50] E. Lauga and R. E. Goldstein, *Dance of the microswimmers*, Physics Today **65**, 30–35 (2012).
- [51] E. M. Purcell, *Life at low Reynolds-number*, Am. J. Phys. **45**, 3–11 (1977).
- [52] N. Cohen and J. H. Boyle, *Swimming at low Reynolds number: A beginners guide to undulatory locomotion*, Contemp. Phys. **51**, 103–123 (2010).
- [53] G. Taylor, *Analysis of the swimming of microscopic organisms*, Proc. R. Soc. Lond. A **209**, 447–461 (1951).
- [54] G. Taylor, *The action of waving cylindrical tails in propelling microscopic organisms*, Proc. R. Soc. A **211**, 225–239 (1952).
- [55] G. Hancock, *The self-propulsion of microscopic organisms through liquids*, Proc. R. Soc. Lond. A **217** (1128), 96–121 (1953).
- [56] R. E. Johnson and C. J. Brokaw, *Flagellar hydrodynamics: A comparison between resistive-force theory and slender-body theory*, Biophys. J. **25**, 113–127 (1979).

- [57] D. Katz, J. Blake, and S. Paveri-Fontana, *On the movement of slender bodies near plane boundaries at low reynolds number*, J. Fluid Mech. **72**, 529–540 (1975).
- [58] J. Lighthill, *Flagellar hydrodynamics - The John von Neumann Lecture, 1975*, SIAM Review **18**, 161–230 (1976).
- [59] B. Rodenborn, C.-H. Chen, H. L. Swinney, B. Liu, and H. P. Zhang, *Propulsion of microorganisms by a helical flagellum*, Proc. Natl. Acad. Sci. USA **110**, E338–E347 (2013).
- [60] M. F. Copeland and D. B. Weibel, *Bacterial swarming: a model system for studying dynamic self-assembly*, Soft Matter **5**, 1174–1187 (2009).
- [61] J. Dunkel, S. Heidenreich, K. Drescher, H. H. Wensink, M. Bär, and R. E. Goldstein, *Fluid dynamics of bacterial turbulence*, Phys. Rev. Lett. **110**, 228102 (2013).
- [62] L. Gheber and Z. Priel, *Synchronization between beating cilia*, Biophys. J. **55**, 183–191 (1989).
- [63] S. Gueron, K. Levit-Gurevich, N. Liron, and J. J. Blum, *Cilia internal mechanism and metachronal coordination as the result of hydrodynamical coupling*, Proc. Natl. Acad. Sci. USA **94**, 6001–6006 (1997).
- [64] P. Lenz and A. Ryskin, *Collective effects in ciliar arrays*, Phys. Biol. **3**, 285–294 (2006).
- [65] S. Michelin and E. Lauga, *Efficiency optimization and symmetry-breaking in a model of ciliary locomotion*, Phys. Fluids **22**, 111901 (2010).
- [66] T. Sanchez, D. Welch, D. Nicastro, and Z. Dogic, *Cilia-like beating of active microtubule bundles*, Science **333**, 456–459 (2011).
- [67] T. Sanchez, D. T. N. Chen, S. J. DeCamp, M. Heymann, and Z. Dogic, *Spontaneous motion in hierarchically assembled active matter*, Nature **491**, 431–435 (2012).

- [68] Y. Yang, J. Elgeti, and G. Gompper, *Cooperation of sperm in two dimensions: Synchronization, attraction, and aggregation through hydrodynamic interactions*, Phys. Rev. E **78**, 061903 (2008).
- [69] R. E. Goldstein, M. Polin, and I. Tuval, *Noise and synchronization in pairs of beating eukaryotic flagella*, Phys. Rev. Lett. **103**, 168103 (2009).
- [70] D. R. Brumley, M. Polin, T. J. Pedley, and R. E. Goldstein, *Hydrodynamic synchronization and metachronal waves on the surface of the colonial alga *Volvox carteri**, Phys. Rev. Lett. **109**, 268102 (2012).
- [71] K. C. Leptos, K. Y. Wan, M. Polin, I. Tuval, A. I. Pesci, and R. E. Goldstein, *Antiphase synchronization in a flagellar-dominance mutant of *Chlamydomonas**, Phys. Rev. Lett. **111**, 158101 (2013).
- [72] K. Y. Wan, K. C. Leptos, and R. E. Goldstein, *Lag, lock, sync, slip: the many 'phases' of coupled flagella*, J. R. Soc. Interface **11**, 20131160 (2014).
- [73] D. R. Brumley, K. Y. Wan, M. Polin, and R. E. Goldstein, *Flagellar synchronization through direct hydrodynamic interactions*, eLife **3**, e02750 (2014).
- [74] M. C. Marchetti, J. F. Joanny, S. Ramaswamy, T. B. Liverpool, J. Prost, M. Rao, and R. A. Simha, *Hydrodynamics of soft active matter*, Rev. Mod. Phys. **85** (3), 1143–1189 (2013).
- [75] D. Saintillan and M. J. Shelley, *Orientational order and instabilities in suspensions of self-locomoting rods*, Phys. Rev. Lett. **99**, 058102 (2007).
- [76] A. Bricard, J.-B. Caussin, N. Desreumaux, O. Dauchot, and D. Bartolo, *Emergence of macroscopic directed motion in populations of motile colloids*, Nature **503**, 95–98 (2013).
- [77] T. Vicsek and A. Zafeiris, *Collective motion*, Phys. Rep. **517**, 71–140 (2012).
- [78] D. L. Koch and G. Subramanian, *Collective hydrodynamics of swimming microorganisms: Living fluids*, Annu. Rev. Fluid Mech. **43**, 637–659 (2011).

- [79] S. Ramaswamy, *The mechanics and statistics of active matter*, Annu. Rev. Condens. Matter Phys. **1**, 323–345 (2010).
- [80] J. Yuan, D. M. Raizen, and H. H. Bau, *Gait synchronization in *Caenorhabditis elegans**, Proc. Natl. Acad. Sci. USA **111**, 6865–6870 (2014).
- [81] R. O’Hagan and M. Chalfie, *Mechanosensation in *Caenorhabditis elegans**, Int. Rev. Neurobiol. **69**, 169–203 (2005).
- [82] D. T. English and H. E. Jones, *Trichonodosis*, Arch. Dermatol. **107**, 77–79 (1973).
- [83] J. A. Calvo, K. C. Millett, E. J. Rawdon, and A. Stasiak (Eds.), *Physical and Numerical Models in Knot Theory* (World Scientific, Singapore, 2005).
- [84] S. A. Wasserman and N. R. Cozzarelli, *Biochemical topology: Applications to DNA recombination and replication*, Science **232**, 951–960 (1986).
- [85] E. Ercolini, F. Valle, J. Adamcik, G. Witz, R. Metzler, P. De Los Rios, J. Roca, and G. Dietler, *Fractal dimension and localization of DNA knots*, Phys. Rev. Lett. **98**, 058102 (2007).
- [86] J. Tang, N. Du, and P. S. Doyle, *Compression and self-entanglement of single DNA molecules under uniform electric field*, Proc. Natl. Acad. Sci. USA **108** (39), 16153–16158 (2011).
- [87] P.-G. de Gennes, *Tight knots*, Macromolecules **17**, 703–704 (1984).
- [88] K. J. Eckelbarger, C. M. Young, and J. L. Cameron, *Ultrastructure and development of dimorphic sperm in the abyssal echinoid *Phrissocystis multispina* (echinodermata: Echinoidea): Implications for deep sea reproductive biology*, Biol. Bull. **176**, 257–271 (1989).
- [89] D. M. Woolley and G. G. Vernon, *A study of helical and planar waves on sea urchin sperm flagella, with a theory of how they are generated*, J. Exp. Biol. **204**, 1333–1345 (2001).

- [90] C. J. Ingham and E. Ben-Jacob, *Swarming and complex pattern formation in paenibacillus vortex studied by imaging and tracking cells*, BMC Microbiology **8**, 36 (2008).
- [91] D. O. Serra, A. M. Richter, G. Klauck, F. Mika, and R. Hengge, *Microanatomy at cellular resolution and spatial order of physiological differentiation in a bacterial biofilm*, mBio **4** (2), e00103–13 (2013).
- [92] L. Turner, W. S. Ryu, and H. C. Berg, *Real-time imaging of fluorescent flagellar filaments*, J. Bacteriol. **182** (10), 2793–2801 (2000).
- [93] R. M. Macnab, *Bacterial flagella rotating in bundles: A study in helical geometry*, Proc. Natl. Acad. Sci. USA **74** (1), 221–225 (1977).
- [94] M. Kim, J. C. Bird, A. J. Van Parys, K. S. Breuer, and T. R. Powers, *A macroscopic scale model of bacterial flagellar bundling*, Proc. Natl. Acad. Sci. USA **100** (126), 15481–15485 (2003).
- [95] P.-G. de Gennes, *Scaling concepts in polymer physics* (Cornell University Press, Ithaca, 1979).
- [96] J. H. Conway, “*An enumeration of knots and links, and some of their algebraic properties*” in *Computational Problems in Abstract Algebra* (Pergamon Press, Oxford and New York, 1969).
- [97] L. H. Kauffman and S. Lambropoulou, *On the classification of rational tangles*, Adv. Appl. Math. **33**, 199–237 (2004).
- [98] E. Ben-Naim, Z. A. Daya, P. Vorobieff, and R. E. Ecke, *Knots and random walks in vibrated granular chains*, Phys. Rev. Lett. **86** (8), 1414–1417 (2001).
- [99] J. Hickford, R. Jones, S. Courrech du Pont, and J. Eggers, *Knotting probability of a shaken ball-chain*, Phys. Rev. E **74**, 052101 (2006).
- [100] D. M. Raymer and D. E. Smith, *Spontaneous knotting of an agitated string*, Proc. Natl. Acad. Sci. USA **104** (42), 16432–16437 (2007).

- [101] A. Belmonte, M. J. Shelley, S. T. Eldakar, and C. H. Wiggins, *Dynamic patterns and self-knotting of a driven hanging chain*, Phys. Rev. Lett. **87** (11), 114301 (2001).
- [102] S.-J. Park, M. B. Goodman, and B. L. Pruitt, *Measurement of mechanical properties of Caenorhabditis elegans with a piezoresistive microcantilever system*, Proceedings of the 3rd Annual International IEEE EMBS Special Topic Conference on Microtechnologies in Medicine and Biology, pp. 400–403 (2005).
- [103] S.-J. Park, M. B. Goodman, and B. L. Pruitt, *Analysis of nematode mechanics by piezoresistive displacement clamp*, Proc. Natl. Acad. Sci. USA **104**, 17376–17381 (2007).
- [104] B. C. Petzold, S.-J. Park, P. Ponce, C. Roozeboom, C. Powell, M. B. Goodman, and B. L. Pruitt, *Caenorhabditis elegans body mechanics are regulated by body wall muscle tone*, Biophys. J. **100**, 1977–1985 (2011).
- [105] B. C. Petzold, S.-J. Park, E. A. Mazzochette, M. B. Goodman, and B. L. Pruitt, *MEMS-based force-clamp analysis of the role of body stiffness in C. elegans touch sensation*, Integr. Biol. **5**, 853–864 (2013).
- [106] M. Nakajima, M. R. Ahmad, S. Kojima, M. Homma, and T. Fukuda, *Local stiffness measurements of C. elegans by buckling nanoprobe inside an environmental SEM*, The 2009 IEEE/RSJ International Conference on Intelligent Robots and Systems pp. 4695–4700 (2009).
- [107] J. Sznitman, P. K. Purohit, P. Krajacic, T. Lamitina, and P. E. Arratia, *Material properties of Caenorhabditis elegans swimming at low Reynolds number*, Biophys. J. **98**, 617–626 (2010).
- [108] J. Sznitman, X. Shen, P. K. Purohit, and P. E. Arratia, *The effects of fluid viscosity on the kinematics and material properties of C. elegans swimming at low Reynolds number*, Exp. Mech. **50**, 1303–1311 (2010).
- [109] J. Karbowski, C. J. Cronin, A. Seah, J. E. Mendel, D. Cleary, and P. W. Sternberg, *Conservation rules, their breakdown, and optimality in Caenorhabditis sinusoidal locomotion*, J. Theor. Biol. **242**, 652–669 (2006).

- [110] P. Sauvage, M. Argentina, J. Drappier, T. Senden, J. Siméon, and J.-M. Di Meglio, *An elasto-hydrodynamical model of friction for the locomotion of *Caenorhabditis elegans**, J. Biomech. **44**, 1117–1122 (2011).
- [111] J. Sznitman, X. Shen, R. Sznitman, and P. E. Arratia, *Propulsive force measurements and flow behavior of undulatory swimmers at low Reynolds number*, Phys. Fluids **22**, 121901 (2010).
- [112] X. N. Shen and P. E. Arratia, *Undulatory swimming in viscoelastic fluids*, Phys. Rev. Lett. **106**, 208101 (2011).
- [113] G. Juarez, K. Lu, J. Sznitman, and P. E. Arratia, *Motility of small nematodes in wet granular media*, Eur. Phys. Lett. **92**, 44002 (2010).
- [114] D. A. Gagnon, X. N. Shen, and P. E. Arratia, *Undulatory swimming in fluids with polymer networks*, Eur. Phys. Lett. **104**, 14004 (2013).
- [115] D. A. Gagnon, N. C. Keim, and P. E. Arratia, *Undulatory swimming in shear-thinning fluids: experiments with *Caenorhabditis elegans**, J. Fluid Mech. **758**, R3 (2014).
- [116] S. Jung, **Caenorhabditis elegans* swimming in a saturated particulate system*, Phys. Fluids **22**, 031903 (2010).
- [117] S. Park, H. Hwang, S.-W. Nam, F. Martinez, R. H. Austin, and W. S. Ryu, *Enhanced *Caenorhabditis elegans* locomotion in a structured microfluidic environment*, PLoS One **3**, e2550 (2008).
- [118] T. Majmuddar, E. E. Keaveny, J. Zhang, and M. J. Shelley, *Experiments and theory of undulatory locomotion in a simple structured medium*, J. R. Soc. Interface **9**, 1809–1823 (2012).
- [119] J. Yuan, D. M. Raizen, and H. H. Bau, *Propensity of undulatory swimmers, such as worms, to go against the flow*, Proc. Natl. Acad. Sci. USA **112**, 3606–3611 (2015).

- [120] S. Berri, J. H. Boyle, M. Tassieri, I. A. Hope, and N. Cohen, *Forward locomotion of the nematode *C. elegans* is achieved through modulation of a single gait*, HFSP J. **3**, 186–193 (2009).
- [121] J. T. Pierce-Shimomura, B. L. Chen, J. J. Mun, R. Ho, R. Sarkis, and S. L. McIntire, *Genetic analysis of crawling and swimming locomotory patterns in *C. elegans**, Proc. Natl. Acad. Sci. USA **105**, 20982–20987 (2008).
- [122] J. H. Boyle, S. Berri, and N. Cohen, *Gait modulation in *C. elegans*: an integrated neuromechanical model*, Front. Comput. Neurosci. **6**, 10 (2012).
- [123] J. Korta, D. A. Clark, C. V. Gabel, L. Mahadevan, and A. D. T. Samuel, *Mechanosensation and mechanical load modulate the locomotory gait of swimming *C. elegans**, J. Exp. Biol. **210**, 2383–2389 (2007).
- [124] A. Ghanbari, V. Nock, S. Johari, R. Blaikie, X. Chen, and W. Wang, *A micropillar-based on-chip system for continuous force measurement of *C. elegans**, J. Micromech. Microeng. **22**, 095009 (2012).
- [125] J. C. Doll, N. Harjee, N. Klejwa, R. Kwon, S. M. Coulthard, B. Petzold, M. B. Goodman, and B. L. Pruitt, *SU-8 force sensing pillar arrays for biological measurements*, Lab Chip **9**, 1449–1454 (2009).
- [126] X. N. Shen, J. Sznitman, P. Krajacic, T. Lamitina, and P. E. Arratia, *Undulatory locomotion of *Caenorhabditis elegans* on wet surfaces*, Biophys. J. **102**, 2772–2781 (2012).
- [127] Y. Rabets, M. Backholm, K. Dalnoki-Veress, and W. S. Ryu, *Direct measurements of drag forces in *C. elegans* crawling locomotion*, Biophys. J. **107**, 1980–1987 (2014).
- [128] S. Gart, D. Vella, and S. Jung, *The collective motion of nematodes in a thin liquid layer*, Soft Matter **7**, 2444–2448 (2011).
- [129] K. C. Neuman and A. Nagy, *Single-molecule force spectroscopy: optical tweezers, magnetic tweezers and atomic force microscopy*, Nat. Methods **5**, 491–505 (2008).

- [130] M.-J. Colbert, A. N. Raegen, C. Fradin, and K. Dalnoki-Veress, *Adhesion and membrane tension of single vesicles and living cells using a micropipette-based technique*, Eur. Phys. J. E **30**, 117–121 (2009).
- [131] M.-J. Colbert, F. Brochard-Wyart, C. Fradin, and K. Dalnoki-Veress, *Squeezing and detachment of living cells*, Biophys. J. **99**, 3555–3562 (2010).
- [132] D. Mitrossilis, J. Fouchard, A. GUIROY, N. Desprat, N. Rodriguez, B. Fabry, and A. Asnacios, *Single-cell response to stiffness exhibits muscle-like behavior*, Proc. Natl. Acad. Sci. USA **106**, 18243–18248 (2009).
- [133] D. Mitrossilis, J. Fouchard, D. Pereira, F. Postic, A. Richert, S.-J. Michel, and A. Asnacios, *Real-time single-cell response to stiffness*, Proc. Natl. Acad. Sci. USA **107**, 16518–16523 (2010).
- [134] J. M. Frostad, M. C. Collins, and G. L. Leal, *Cantilevered-capillary force apparatus for measuring multiphase fluid interactions*, Langmuir **29**, 4715–4725 (2013).
- [135] J. M. Frostad, M. Seth, S. M. Bernasek, and G. L. Leal, *Direct measurement of interaction forces between charged multilamellar vesicles*, Soft Matter **10**, 7769–7780 (2014).
- [136] D. Gonzalez-Rodriguez, L. Bonnemay, J. Elgeti, S. Dufour, D. Cuvelier, and F. Brochard-Wyart, *Detachment and fracture of cellular aggregates*, Soft Matter **9**, 2282 (2013).
- [137] J. M. Mitchison and M. M. Swann, *The mechanical properties of the cell surface: I. The cell elastimeter*, J. Exp. Biol. **31**, 443–460 (1954).
- [138] E. A. Evans, *New membrane concept applied to the analysis of fluid shear- and micropipette-deformed red blood cells*, Biophys. J. **13**, 941–954 (1973).
- [139] E. Evans, K. Ritchie, and R. Merkel, *Sensitive force technique to probe molecular adhesion and structural linkages at biological interfaces*, Biophys. J. **68**, 2580–2587 (1995).

- 
- [140] R. M. Hockmuth, *Micropipette aspiration of living cells*, J. Biomech. **33**, 15–22 (2000).
- [141] M.-J. Colbert, *A novel approach to measurement of the adhesion strength of a single cell on a substrate*, Master's thesis, McMaster University (2005).
- [142] M.-J. Colbert, *Mechanics of lipid vesicles and living cells*, Ph.D. thesis, McMaster University (2010).
- [143] R. D. Schulman, *Micropipette deflection experiments on the nematode C. elegans*, Master's thesis, McMaster University (2014).
- [144] S. Brenner, *The genetics of Caenorhabditis elegans*, Genetics **77**, 71–94 (1974).
- [145] W. C. Young and R. G. Budynas, *Roark's Formulas for Stress and Strain* (McGraw-Hill, New York, 2002).
- [146] C. M. Wang, J. N. Reddy, and K. H. Lee, *Shear deformable beams and plates: relationship with classical solutions* (Elsevier, Oxford, 2000).

# Appendix A

## Appended papers

### A.1 Paper I

*Viscoelastic properties of the nematode *Caenorhabditis elegans*, a self-similar, shear-thinning worm*

M. Backholm, W. S. Ryu, and K. Dalnoki-Veress, Proc. Natl. Acad. Sci. USA **110**, 4528-4533 (2013).

# Viscoelastic properties of the nematode *Caenorhabditis elegans*, a self-similar, shear-thinning worm

Matilda Backholm<sup>a</sup>, William S. Ryu<sup>b</sup>, and Kari Dalnoki-Veress<sup>a,c,1</sup>

<sup>a</sup>Department of Physics and Astronomy and the Brockhouse Institute for Materials Research, McMaster University, Hamilton, ON, Canada L8S 4M1;

<sup>b</sup>Department of Physics and the Donnelly Centre, University of Toronto, Toronto, ON, Canada M5S 1A7; and <sup>c</sup>Laboratoire de Physico-Chimie Théorique, Gulliver, Unité Mixte de Recherche 7083, Centre National de la Recherche Scientifique-École Supérieure de Physique et de Chimie Industrielles, 75005 Paris, France

Edited by David A. Weitz, Harvard University, Cambridge, MA, and approved February 11, 2013 (received for review November 16, 2012)

Undulatory motion is common to many creatures across many scales, from sperm to snakes. These organisms must push off against their external environment, such as a viscous medium, grains of sand, or a high-friction surface; additionally they must work to bend their own body. A full understanding of undulatory motion, and locomotion in general, requires the characterization of the material properties of the animal itself. The material properties of the model organism *Caenorhabditis elegans* were studied with a micromechanical experiment used to carry out a three-point bending measurement of the worm. Worms at various developmental stages (including dauer) were measured and different positions along the worm were probed. From these experiments we calculated the viscoelastic properties of the worm, including the effective spring constant and damping coefficient of bending. *C. elegans* moves by propagating sinusoidal waves along its body. Whereas previous viscoelastic approaches to describe the undulatory motion have used a Kelvin–Voigt model, where the elastic and viscous components are connected in parallel, our measurements show that the Maxwell model, where the elastic and viscous components are in series, is more appropriate. The viscous component of the worm was shown to be consistent with a non-Newtonian, shear-thinning fluid. We find that as the worm matures it is well described as a self-similar elastic object with a shear-thinning damping term and a stiffness that becomes smaller as one approaches the tail.

biomechanics | viscoelasticity

The undulatory motion of snakes and fish as they crawl or swim through a medium is considered a superior form of locomotion in terms of its adoption across a broad range of length scales and efficiency (1). Several attempts have been made to achieve the same level of performance artificially (2), but the agility seen in nature is far from being reproduced in manmade systems. A number of experimental model systems have been used to study undulatory motion (3–7). To achieve a deeper understanding of this form of motility, the biomechanics has been studied theoretically for snake-like systems (8, 9). Recently, computational fluid dynamic models of organismal swimming have been developed to simulate fluid–body interactions, including internal forces and body stiffness (10, 11). However, a requirement for a successful, systems-level model is a detailed knowledge of the material properties of the crawler—insight that can only be achieved experimentally.

*Caenorhabditis elegans*, a millimeter-sized nematode, has been used as a model organism to study undulatory motion experimentally (12–15). One fundamental, unresolved question is how difficult is it for the worm to bend its own body as it moves (16). In other words, what is the bending stiffness of the model organism? Efforts have been made to measure the stiffness of *C. elegans* (17–20), but a conclusive result is yet to be reached for several reasons.

Direct comparisons between transverse and longitudinal stiffness values have caused confusion. Here, the former quantity is the elasticity probed by a local compression of the worm, whereas the latter corresponds to the stiffness related to a nonlocal

bending of the entire worm. As the nematode is known to consist of anisotropic materials (21), the two stiffnesses should not be considered the same. Additionally, the elasticity related to undulatory motion is the longitudinal stiffness, as the worm needs to bend its entire body to swim or crawl. There exist experimental limitations in directly measuring the longitudinal stiffness, and many measurements have been made indirectly through modeling assumptions (18, 19). Models used to elucidate the mechanics of undulatory motion typically involve assumptions of the material properties of *C. elegans* that are yet to be proven experimentally (22, 23).

Here, we present a method used to probe the dynamic viscoelastic properties of *C. elegans* at a biologically, physically, and structurally relevant length scale. Direct micromechanical measurements were performed, and a simple elastic model was used to gather results for the bending stiffness of *C. elegans* at all of its life stages. Furthermore, we have measured the viscoelastic response to bending, and show that commonly used models do not adequately describe the measured material properties of *C. elegans*. By modeling the viscoelasticity of the worm, our dynamic experiments reveal unexpected viscous properties. The Young's modulus of the worm as a whole is reported, and an attempt to decouple the contributions from cuticle and muscles to the total stiffness is made.

## Results and Discussion

Micropipette deflection (MD) (24) was used to perform three-point bending measurements on anesthetized *C. elegans* nematodes to probe their force–deflection response. The experiment is illustrated in Fig. 1A, and described in more detail at the end of this paper. In short, the worm was held with a flexible force-calibrated pipette through suction, and bent by moving a simple support toward the “holding” pipette (from left to right in the figure) with a constant speed  $v_u$ . The deflection  $x$  of the holding pipette produces a certain force  $F = k_p x$ , where  $k_p$  is the spring constant of the pipette. The bending  $y = x_u - x$  of the worm is defined as the difference between the motion of the support ( $x_u$ ) and the deflection of the pipette. Optical microscopy images from the beginning (*Upper*) and end (*Lower*) of a bending experiment performed on an adult worm are shown in Fig. 1B. The total deflection of the pipette is indicated by the dashed line.

**Elastic and Viscoelastic Theoretical Models.** Two different theoretical models were used to achieve an understanding of the worm material. A simple linearized Hookean model was applied to describe the purely elastic properties of *C. elegans*. To gain deeper insight,

Author contributions: M.B., W.S.R., and K.D.-V. designed research; M.B. performed research; M.B., W.S.R., and K.D.-V. contributed new reagents/analytic tools; M.B. analyzed data; and M.B., W.S.R., and K.D.-V. wrote the paper.

The authors declare no conflict of interest.

This article is a PNAS Direct Submission.

<sup>1</sup>To whom correspondence should be addressed. E-mail: dalnoki@mcmaster.ca.

This article contains supporting information online at [www.pnas.org/lookup/suppl/doi:10.1073/pnas.1219965110/-DCSupplemental](http://www.pnas.org/lookup/suppl/doi:10.1073/pnas.1219965110/-DCSupplemental).

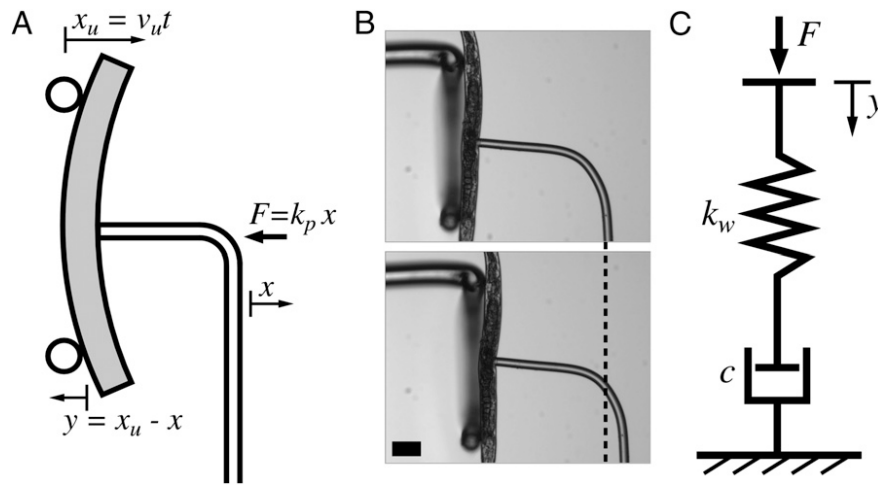


**Fig. 1.** (A) Schematic diagram of the experimental micropipette deflection setup used to study the bending stiffness of *C. elegans*. A support (two circles) is moved from left to right with a constant speed,  $v_u$ . This induces a bending  $y$  of the worm due to the force  $F = k_p x$  applied by the pipette, where  $k_p$  is the spring constant of the pipette. The deflection of the pipette and motion of the support are defined as  $x$  and  $x_u$ , respectively, and the bending  $y$  of the worm is defined as the difference between these. (B) Optical microscopy images of an adult worm in the beginning (Upper) and end (Lower) of a bending experiment, with the total pipette deflection indicated by the dashed line. The supporting structure is a thicker, U-shaped glass pipette, into which the worm can be bent as it would be simply supported. Scale bar, 100  $\mu\text{m}$ . (C) Diagram of the worm modeled as a viscoelastic Maxwell material, consisting of a spring (spring constant  $k_w$ ) and dashpot (damping coefficient  $c$ ) connected in series. The bending  $y$  of the worm corresponds to the compression of the system due to the force  $F$  applied by the pipette.

a non-Hookean viscoelastic Maxwell model was introduced. In the limit of small deformations and short times these two models are equivalent.

Euler–Bernoulli elastic beam theory (EBT) (25) was used to analyze the elasticity of the worm by approximating it as a spring-like beam. The bending  $y$  at the position of the applied force  $F$  is given as

$$y = \frac{a^2(L-a)^2}{3LEI} F = \frac{1}{k_w} F, \quad [1]$$

where  $L$  is the distance between the supports and  $a$  is the distance between the upper support and the position of the applied force (pipette). The spring constant  $k_w$  of the worm is a function of both the geometry of the experiment, as well as the bending stiffness  $EI$  of the worm. The bending stiffness is equivalent to the product of the Young's modulus  $E$  of the material, and the area moment of inertia  $I$  of the beam. For simplicity we assume that the cross-sectional distribution of stiff material in *C. elegans* is cylindrical (17), giving  $I = (D^4 - d^4)\pi/64$  (26), where  $D$  and  $d$  are the outer and inner diameters of the cylindrical shell, respectively (Supporting Information, Area Moment of Inertia for a Cylinder). We note that much of our data will be reported as  $EI$ , because this product is independent of any assumptions in  $I$ .

To model the worm as a non-Hookean material, a viscous component was introduced to the system as shown in Fig. 1C. The compression  $y$  of the spring and dashpot connected in series corresponds to the bending of our worm. This viscoelastic model is known as the Maxwell model (27), and describes the relationship between force and compression as

$$\dot{y} = \frac{F}{c} + \frac{\dot{F}}{k_w}, \quad [2]$$

where  $c$  and  $k_w$  are the damping coefficient and spring constant of the material, respectively. By applying the Maxwell model to the geometry of our specific system, the exact solution to Eq. 2 can be solved as (see Supporting Information for a detailed derivation)

$$y(t) = v_u \left( t - \frac{c}{k_p} \left[ 1 - e^{-k_p k_w / [c(k_p + k_w)] t} \right] \right), \quad [3]$$

where  $v_u$  is the speed of the support and  $k_p$  is the spring constant of the holding pipette. Furthermore, the force–deformation relationship can be written as

$$F(y) = \frac{k_p v_u c}{k_p + k_w} \left( -1 + \sqrt{1 + \frac{2k_w(k_p + k_w)}{k_p v_u c} y} \right). \quad [4]$$

The Kelvin–Voigt viscoelastic model, where a spring and a dashpot are connected in parallel (27), has been used by others to describe the material properties of *C. elegans* (18, 19), based on the theory of snake-like creatures in general (9). The analytical solution of the Kelvin–Voigt model applied to our system is shown in Supporting Information (the derivation is analogous to that sketched above).

The results from an MD experiment on a young adult worm is shown in the main graph of Fig. 2, where the bending of the worm is plotted as a function of time. The analytical solutions to the theoretical models (EBT, Maxwell, and Kelvin–Voigt) have been fit to the data. The residuals of the fits are shown in the bottom graph, where  $\Delta$  is the difference between the best-fit line and the data for each case.

As expected, the linearized EBT is valid only within the initial time regime, after which it is inadequate as a model due to the apparent viscosity of the material as well as nonlinear bending contributions. The Kelvin–Voigt model shows systematic deviations from the data, whereas the Maxwell model captures the data within the uncertainty of the measurement. Thus, the Maxwell model is a more appropriate method to characterize the viscoelasticity present in the bending of *C. elegans*. We note that the Maxwell model provided a consistently superior description of the data for all worms studied.

Fig. 2 (Inset) shows the force–deformation data from the same experiment as illustrated in the main graph. The solid line is the best fit of Eq. 4 to the experimental data. The fits used in Fig. 2 only require two fitting parameters  $c$  and  $k_w$ , because the rest of

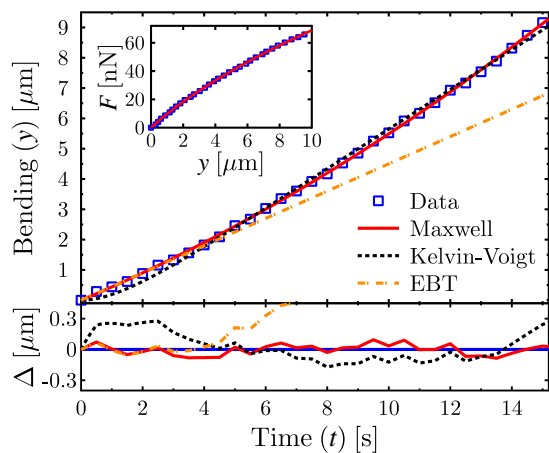


**Fig. 2.** Comparison between experimental bending results and viscoelastic theories. (Upper) Main graph shows the bending of a young adult worm as a function of time ( $\square$ ). The data have been fitted by the exact solutions from the Maxwell (Eq. 3, solid line) and Kelvin-Voigt (dashed line) models, as well as the EBT (dashed-dotted line). (Lower) Graph shows the difference  $\Delta$  between theory and experiment (same legend as for Upper), and thus illustrates the quality of the different theoretical models. (Inset) Force is plotted as a function of bending, with the Maxwell force-deformation prediction (Eq. 4) drawn as a solid line.

the constants in Eqs. 3 and 4, such as the speed of the support  $v_u$  and spring constant of the pipette  $k_p$  are known experimental parameters. By applying the Maxwell model to our data, we therefore obtain values for not only the stiffness, but also for the damping coefficient of *C. elegans*. The spring constant obtained from the EBT and Maxwell model is the same.

**Viscoelastic Properties of *C. elegans*.** To investigate the viscoelastic properties of *C. elegans*, bending experiments were performed at different bending speeds  $v_u$ . The Maxwell model was used to analyze the data; the resulting speed dependence of the spring constant and damping coefficient of the worm is shown in Fig. 3. The spring constant is independent of speed, which is an expected feature of the elasticity of a material. The viscous component, however, is inversely proportional to the bending speed. This strong decrease of the damping coefficient is a characteristic of a shear-thinning, complex fluid (28). Specifically, the damping coefficient shows a clear power-law dependence over two decades in bending speed:  $c \propto v_u^{-1.0 \pm 0.1}$ . The viscous component of *C. elegans*

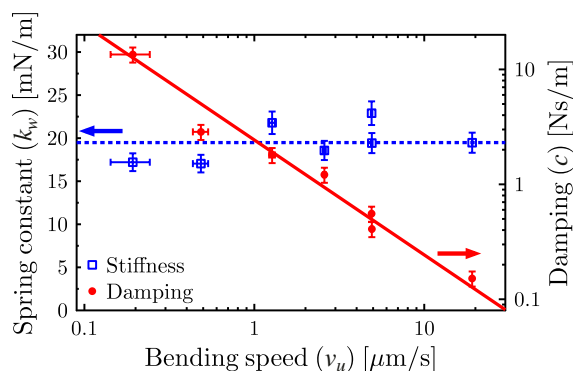


**Fig. 3.** Speed dependence of the spring constant  $k_w$  (left y axis), and the damping coefficient  $c$  (right y axis), of the worm as a function of bending speed  $v_u$ . The damping coefficient is an inversely proportional function of the bending speed.

should thus be modeled as a power-law fluid, as described by the Ostwald-de Waele model (29).

Shear thinning has been observed in several biological tissue types, such as heart and brain tissue (30) as well as in vocal cords (31). Although the structure and function of these tissue types are vastly different, the gross mechanical behavior is commonly governed by components in the extracellular matrix (ECM) (30, 32). Shear-thinning properties have been measured in the ECM component collagen (33, 34), and, as the cuticle of *C. elegans* is predominantly composed of cross-linked collagen (35), the non-Newtonian results reported here might be explained by the properties of the cuticle.

Shear-thinning properties have also been noticed in the legs of insects (36). To describe this, a friction-based structural damping model (37) was introduced instead of the more commonly used viscous damping approach. Structural damping cannot, however, describe the relaxation of a stressed material; as we have observed the worm material relax under static conditions (data shown in Supporting Information), the viscoelastic Maxwell model is better suited to describe the inelastic properties of *C. elegans*.

The implication of the shear-thinning property of *C. elegans* is that it is easier for the worm to bend its own body quickly rather than slowly. This is because the internal viscous resistance is lower at higher deformation speeds. The shape of an undulating crawler is due to the dynamic balance between elastic, hydrodynamic, and muscular forces. As a result, the shear-thinning property of the worm may influence the dynamics of motility, and shear thinning should be integrated into a full locomotory model. The actual bending speed of an adult *C. elegans* crawling on an agar surface can be calculated as  $v_{\text{crawl}} = 104 \mu\text{m/s}$ , based on the frequency and amplitude of its motion (22). This choice of bending speed is much higher than what was probed in the MD experiment, and corresponds to a speed regime with negligible internal viscous resistance. The gait transition between crawling and swimming can be noted by, among other things, an increase in bending speed (18), which is thought to be made possible by the lower external resistance from a fluid than from a gel substrate. This gait adaptation of *C. elegans* may, however, be driven to minimize not only external losses, but also internal viscous dissipation.

The bending stiffness of *C. elegans* was measured at all of its life stages, and is shown as a function of worm diameter in Fig. 4. As can be seen in the graph, the bending stiffness of *C. elegans* increases by almost 4 orders of magnitude as the worm grows from the L1 to the adult stage. The actual values correspond to the spring constant of the worm normalized by the geometry of the system according to Eq. 1,  $EI = a^2(L - a)^2k_w/3L$ . The errors in Fig. 4, as well as in all of the following graphs, are the SDs from several measurements performed on the same worm.

The images at the top of Fig. 4 show snapshots from the MD experiments performed with worms at the L1, L2, L3, and L4 life stages, and the colors and markers correspond to the respective data set plotted in the main graph. The power-law line  $EI \propto D^4$  shown in the graph corresponds to the best-fitting function to the data (the exact value of the best-fit exponent is 4.02). As discussed above, if the worm is modeled as a cylindrical tube with an outer and inner diameter of  $D$  and  $d \propto D$ , respectively, the bending stiffness will scale as  $EI \propto ED^4$ , consistent with experimental observations. We conclude that treating the worm as a cylindrical structure, with a stiffness that is self-similar, is a valid approximation—that is, the distribution and amount of stiff material scales with the size of the worm, and can be nondimensionalized by  $D$ . Thus, one need not treat the young and adult worms as mechanically different when properly nondimensionalized.

The slope of the power-law line in Fig. 4 can be used to calculate the Young's modulus  $E$  of the nematode. If *C. elegans* is thought of as a rod-shaped worm consisting of a uniform distribution of "worm material," the Young's modulus of this material would be  $E_{\text{rod}} = 110 \pm 30 \text{ kPa}$ . When modeling the bending

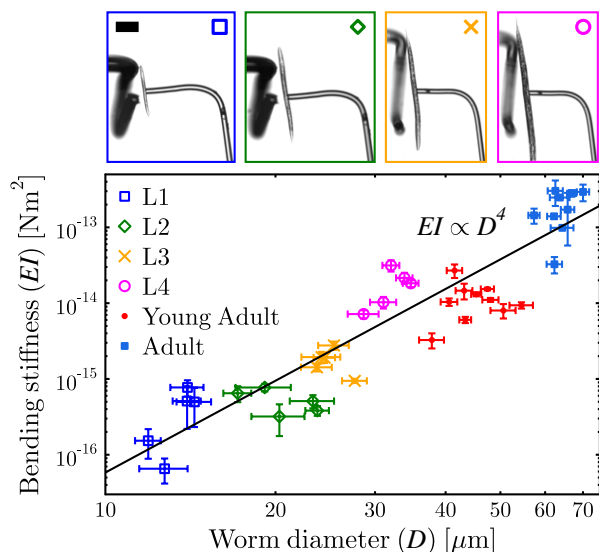


**Fig. 4.** Bending stiffness at all life stages of *C. elegans* as a function of worm diameter. The power-law fit shows a  $D^4$  dependence, consistent with modeling the stiffness of the worm as a self-similar cylinder. Images on the top show snapshots from the experiments, with an L1, L2, L3, and L4 worm from left to right. Images of experiments done on a young adult and adult worm can be found in Figs. 5A and 1B, respectively. Colors and markers correspond to the respective data sets. Scale bar, 100  $\mu\text{m}$ .

of *C. elegans* in theory and simulations, this value is what should be used in combination with an area moment of inertia of  $I = \pi D^4/64$ , where  $D$  is the diameter of the worm. In reality, it is well known that the worm does not consist of a uniform distribution of the same material. On the contrary, *C. elegans* is a complex biological system made up of multiple tissue types, which are organized at different scales (cuticle, muscle, organs). The concept of bending stiffness is robust and independent of these complexities, and is therefore unambiguous when used to describe the complex mechanical structure. The Young's modulus reported here is only to be used when considering the worm as a whole, without taking substructural components into account. Furthermore, the stiffness measured in this work is the longitudinal stiffness, which is the relevant geometry to consider when studying the bending of *C. elegans*.

**Contributions from the Muscles and Cuticle.** To probe the local stiffness along the body of a young adult worm, a smaller spacing  $L$  between the supports was used. The vulva was considered a reference point for the coordinate system due to its visibility in all of the experiments. The distance from the position of the pipette (i.e., the applied force) to the vulva was defined as  $l$ , with the head oriented in the positive direction. At the top of Fig. 5A, snapshots from measurements performed at different body positions are shown. The arrows indicate the position of the vulva. To factor out effects from changes in the diameter along the body of the worm, the local bending stiffness was divided by  $D_{\text{local}}^4$  for each experiment, where  $D_{\text{local}}$  is the local diameter of the worm at the position of the pipette. The resulting "effective" Young's modulus is shown in the main graph of Fig. 5A, whereas the local bending stiffness is shown in the inset.

From these measurements, it is clear that the tail is significantly (up to 50%) less stiff than the rest of the body. From the vulva to the head, the stiffness was, within error, the same. The strong decrease in relative stiffness of the tail compared with the rest of the body can be explained by the smaller amount of muscles in the tail (21).

The anesthetic sodium azide ( $\text{NaN}_3$ ) used throughout this work acted as a muscle relaxant, resulting in worms that were still and straight. Different concentrations of this drug did not affect the measured bending stiffness of the nematode. To further confirm that the  $\text{NaN}_3$  did not affect the material properties of *C. elegans*, another muscle relaxing drug (2,3 Butanedione monoxime, BDM) was tried. As shown by the triangle in Fig. 5B, the average bending stiffness of adult worms anesthetized with BDM is the same, i.e., independent of choice of drug.

In this work we have probed the passive material properties of a relaxed worm. Having tried two different drugs ( $\text{NaN}_3$  and BDM) and studied worms exposed to different concentrations of the anesthetics for different times, we get consistent and reproducible results. Thus, the drug did not affect the probed passive material properties of the nematode. As an active worm

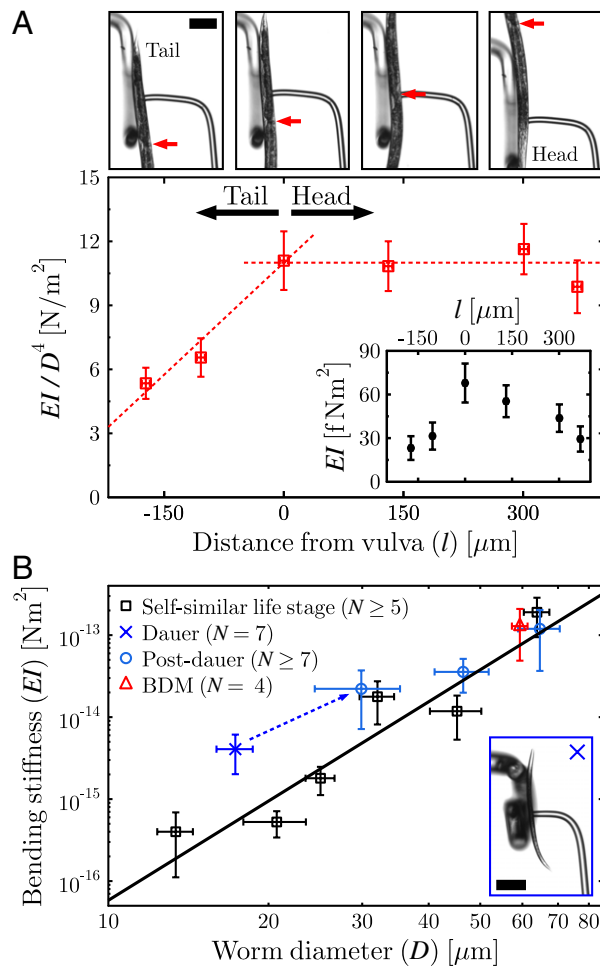


**Fig. 5.** (A) Bending stiffness along the body of a young adult worm. (Upper) Images show snapshots from experiments performed at different positions (tail on the left, head on the right) of the worm. Arrows indicate the position of the vulva, and  $l$  is the distance from this to the middle of the pipette. (Lower) In the main graph, the local  $D^4$  dependence has been factored out from the bending stiffness, and a local "effective" Young's modulus is thus plotted. The dashed lines are meant to guide the eye. (Inset) Local bending stiffness as a function of distance from the vulva. (B) Bending stiffness as a function of worm diameter of the self-similar worms ( $\square$ ) averaged over each life stage.  $N$  indicates the number of worms per data point, and the line is the same power-law function as used in Fig. 4. Bending stiffness of the dauer ( $\times$ ) and post-dauer ( $\circ$ ) state worms are shown, and illustrate the deviation from self-similarity of the former. The use of another muscle relaxant (BDM) did not affect the measured bending stiffness of adult worms ( $\triangle$ ). (Inset) A dauer worm. Scale bar, 100  $\mu\text{m}$ .

moves, the contraction of its muscles could be thought to modify the total bending stiffness of the worm. It is the dynamic modulation of the passive bending stiffness which enables undulatory locomotion.

Under stress, such as lack of food or in environments of high temperatures, the young L1 worms turn into the so-called dauer state, in which they can survive for months (21). It has been shown that dauer-state worms have a thicker cuticle with respect to total body thickness compared with nematodes at normal life stages. Specifically, the fraction between the thickness of the cuticle and the diameter of the worm is 1/36th for a dauer worm, whereas this fraction is 1/88th for all other life stages (35). By measuring the bending stiffness of dauer-state worms, the cuticle contribution to the total stiffness could therefore be studied, as this worm potentially has more stiff material than an equally sized, self-similar worm. The results from MD measurements performed on dauer-state worms (×) are shown in Fig. 5B. The dauer worm is significantly stiffer than what would be the case for a self-similar worm. Thus, the stiffness of *C. elegans* is highly dependent on the cuticle thickness.

If the cuticle were the only component contributing to the total stiffness of the worm, then the worm's body could be modeled as a cylindrical shell. The Young's modulus of this shell would be  $E_{\text{cuticle}} = 1.3 \pm 0.3$  MPa, which corresponds to the upper extreme value of this material-specific property of *C. elegans*. In contrast, the lower limit, obtained above as  $E_{\text{rod}} = 110 \pm 30$  kPa, resulted from modeling the worm as a uniform rod. If one were to assign a Young's modulus to the worm, detailed knowledge of the distribution of the elastic material within the worm would be required. However, the modulus must be bound by these two limiting assumptions.

Measurements were also performed on post-dauer-state worms, as shown by circles in Fig. 5B. The results illustrate how the material properties of *C. elegans* return back to normal as the nematode exits the dauer state.

## Conclusions

Here we have presented the use of a micromechanical technique to probe the viscoelastic material properties of *C. elegans*. The bending stiffness was measured at all life stages of the worm, and was shown to scale in a self-similar cylindrical way with the diameter of the worm. If assuming a uniform distribution of stiff worm material within the rod-shaped worm, the Young's modulus of this material was determined to be  $E_{\text{rod}} = 110 \pm 30$  kPa. The different stiff body parts contributing to the total stiffness of the worm were investigated, and the cuticle was found to be responsible for a large fraction of the bending stiffness of *C. elegans*.

Furthermore, measurements along the body of the worm showed a higher stiffness of the head than the tail, indicating a strong contribution from the muscles as well.

The viscoelasticity of *C. elegans* was shown to be best modeled as a Maxwell material. By using this theoretical model, the nematode was found to be shear thinning—a complex fluid property that can be expected to influence the dynamics of motility of the worm. We conclude that the *Caenorhabditis elegans* nematode can be modeled as a self-similar, shear-thinning object.

## Materials and Methods

**Bending Measurements.** The micropipette deflection technique was used as described in ref. 24. A flexible micropipette with the length of ~1 cm and diameter of ~20  $\mu\text{m}$  was bent into an L shape and used as a spring-like cantilever. The manufacturing and calibration of this force-sensing pipette was performed as in ref. 38. The support used in the bending experiments was a 50- $\mu\text{m}$ -thick micropipette bent into the shape of a U, with which the worm could be supported. The optical microscopy images were analyzed with MATLAB (MathWorks) by performing cross-correlation image analysis on pictures taken at 2 Hz.

Unless mentioned otherwise, all bending experiments were performed in an M9 buffer with a 10-mM concentration of the anesthetic  $\text{NaN}_3$ . The measurements were performed within 2 h of drugging the worms. Different concentrations of the  $\text{NaN}_3$  did not give rise to changes in the measured bending stiffness. To further verify that the drug did not change the bending stiffness of the worm, a buffer of 0.3 M BDM in M9 was used. In this experiment, the worms were studied within 15 min after being put into the buffer, as they lost their rod-like shape after this time.

The results shown from measurements performed on only one worm were all reproduced with several other worms (*Supporting Information*). All of the worms were bent in the dorsal-ventral plane. Repeated experiments performed on the same worm with different bending speeds were done with enough waiting time (around 3 min) in between measurements to give the worm time to relax. The results from these measurements were independent of changing the speed in an increasing or decreasing fashion. For the results in Fig. 4, at least three measurements were performed per worm.

**Worm Strains, Cultivation, and Preparation.** Wild-type worms (N2) were acquired from the *Caenorhabditis* Genetics Center and were cultivated according to standard methods (39) on *Escherichia coli* (OP50) nematode growth media (NGM) plates at 20 °C. Dauer-state worms were produced by moving L1 worms to an NGM plate without bacteria, and letting them develop for several weeks. The post-dauer states (first generation) were studied as the dauer worms exited the rest state after they had been moved back to a bacteria-covered NGM plate. All chemicals were sourced from Sigma-Aldrich.

**ACKNOWLEDGMENTS.** The financial support by Natural Sciences and Engineering Research Council of Canada is gratefully acknowledged.

1. Tokić G, Yue DKP (2012) Optimal shape and motion of undulatory swimming organisms. *Proc Biol Sci* 279(1740):3065–3074.
2. Triantafyllou MS, Triantafyllou GS, Yue DKP (2000) Hydrodynamics of fishlike swimming. *Annu Rev Fluid Mech* 32:33–53.
3. Gray J (1946) The mechanism of locomotion in snakes. *J Exp Biol* 23(2):101–120.
4. Gray J (1953) Undulatory propulsion. *Q J Microsc Sci* 94(4):551–578.
5. Gray J, Lissmann HW (1964) The locomotion of nematodes. *J Exp Biol* 41(1):135–154.
6. Gillis GB (1998) Neuromuscular control of anguilliform locomotion: Patterns of red and white muscle activity during swimming in the american eel *anguilla rostrata*. *J Exp Biol* 201(Pt 23):3245–3256.
7. Maladen RD, Ding Y, Li C, Goldman DI (2009) Undulatory swimming in sand: Sub-surface locomotion of the sandfish lizard. *Science* 325(5938):314–318.
8. Niebur E, Erdős P (1991) Theory of the locomotion of nematodes: Dynamics of undulatory progression on a surface. *Biophys J* 60(5):1132–1146.
9. Guo ZV, Mahadevan L (2008) Limbless undulatory propulsion on land. *Proc Natl Acad Sci USA* 105(9):3179–3184.
10. Tytell ED, Hsu C-Y, Williams TL, Cohen AH, Fauci LJ (2010) Interactions between internal forces, body stiffness, and fluid environment in a neuromechanical model of lamprey swimming. *Proc Natl Acad Sci USA* 107(46):19832–19837.
11. Majmudar T, Keaveny EE, Zhang J, Shelley MJ (2012) Experiments and theory of undulatory locomotion in a simple structured medium. *J R Soc Interface* 9(73):1809–1823.
12. Pierce-Shimomura JT, et al. (2008) Genetic analysis of crawling and swimming locomotory patterns in *C. elegans*. *Proc Natl Acad Sci USA* 105(52):20982–20987.
13. Stephens GJ, Johnson-Kerner B, Bialek W, Ryu WS (2008) Dimensionality and dynamics in the behavior of *C. elegans*. *PLoS Comput Biol* 4(4):e1000028.
14. Sauvage P, et al. (2011) An elasto-hydrodynamical model of friction for the locomotion of *Caenorhabditis elegans*. *J Biomech* 44(6):1117–1122.
15. Shen XN, Arratia PE (2011) Undulatory swimming in viscoelastic fluids. *Phys Rev Lett* 106(20):208101.
16. Long JH, Nipper KS (1996) The importance of body stiffness in undulatory propulsion. *Am Zool* 36(6):678–694.
17. Park S-J, Goodman MB, Pruitt BL (2007) Analysis of nematode mechanics by piezoresistive displacement clamp. *Proc Natl Acad Sci USA* 104(44):17376–17381.
18. Fang-Yen C, et al. (2010) Biomechanical analysis of gait adaptation in the nematode *Caenorhabditis elegans*. *Proc Natl Acad Sci USA* 107(47):20323–20328.
19. Sznitman J, Purohit PK, Krajacic P, Lamitina T, Arratia PE (2010) Material properties of *Caenorhabditis elegans* swimming at low Reynolds number. *Biophys J* 98(4):617–626.
20. Petzold BC, et al. (2011) *Caenorhabditis elegans* body mechanics are regulated by body wall muscle tone. *Biophys J* 100(8):1977–1985.
21. Wood B (1988) *The Nematode Caenorhabditis elegans* (Cold Spring Harbor Lab Press, New York).
22. Karbowski J, et al. (2006) Conservation rules, their breakdown, and optimality in *Caenorhabditis* sinusoidal locomotion. *J Theor Biol* 242(3):652–669.
23. Karbowski J, Schindelman G, Cronin CJ, Seah A, Sternberg PW (2008) Systems level circuit model of *C. elegans* undulatory locomotion: Mathematical modeling and molecular genetics. *J Comput Neurosci* 24(3):253–276.

24. Colbert M-J, Raegen AN, Fradin C, Dalnoki-Veress K (2009) Adhesion and membrane tension of single vesicles and living cells using a micropipette-based technique. *Eur Phys J E Soft Matter* 30(2):117–121.
25. Wang CM, Reddy JN, Lee KH (2000) *Shear Deformable Beams and Plates: Relationship with Classical Solutions* (Elsevier, Oxford).
26. Young WC, Budynas RG (2002) *Roark's Formulas for Stress and Strain* (McGraw-Hill, New York).
27. Fung YC (1993) *Biomechanics: Mechanical Properties of Living Tissue* (Springer, New York).
28. Barnes HA (1997) Thixotropy - A review. *J Non-Newton Fluid Mech* 70:1–33.
29. Bird RB, Stewart WE, Lightfoot EN (1960) *Transport Phenomena* (Wiley, New York).
30. Phan-Thien N, Nasser S, Bilston LE (2000) Oscillatory squeezing flow of a biological material. *Rheol Acta* 39:409–417.
31. Chan RW, Titze IR (1999) Viscoelastic shear properties of human vocal fold mucosa: Measurement methodology and empirical results. *J Acoust Soc Am* 106(4 Pt 1): 2008–2021.
32. Oxlund H, Andreassen TT (1980) The roles of hyaluronic acid, collagen and elastin in the mechanical properties of connective tissues. *J Anat* 131(Pt 4):611–620.
33. McPherson JM, et al. (1986) The preparation and physicochemical characterization of an injectable form of reconstituted, glutaraldehyde cross-linked, bovine corium collagen. *J Biomed Mater Res* 20(1):79–92.
34. Silver FH, Ebrahimi A, Snowhill PB (2002) Viscoelastic properties of self-assembled type I collagen fibers: Molecular basis of elastic and viscous behaviors. *Connect Tissue Res* 43(4):569–580.
35. Cox GN, Staprans S, Edgar RS (1981) The cuticle of *Caenorhabditis elegans*. II. Stage-specific changes in ultrastructure and protein composition during postembryonic development. *Dev Biol* 86(2):456–470.
36. Dudek DM, Full RJ (2006) Passive mechanical properties of legs from running insects. *J Exp Biol* 209(Pt 8):1502–1515.
37. Nashif A, Jones D, Henderson J (1985) *Vibration Damping* (Wiley, New York).
38. Colbert M-J, Brochard-Wyart F, Fradin C, Dalnoki-Veress K (2010) Squeezing and detachment of living cells. *Biophys J* 99(11):3555–3562.
39. Brenner S (1974) The genetics of *Caenorhabditis elegans*. *Genetics* 77(1):71–94.

# Supporting Information

Backholm et al. 10.1073/pnas.1219965110

## Area Moment of Inertia for a Cylinder

The definition of the area moment of inertia for a symmetrical cross-section is (1)

$$I = I_x = I_y = \int_A y^2 dA. \quad [S1]$$

This can be rewritten in polar coordinates ( $dA = r dr d\theta$ ,  $y = r \sin \theta$ ) and solved for the case of a cylindrical shell as

$$I = \int_0^{2\pi} \sin^2 \theta d\theta \int_{d/2}^{D/2} r^3 dr = \frac{\pi}{64} [D^4 - d^4], \quad [S2]$$

where  $D$  and  $d$  are the outer and inner diameters of the cylinder, respectively.

## Maxwell Model

We model the worm as a system with a purely viscous damper (damping coefficient  $c$ ) connected in series with a purely elastic spring (spring constant  $k_w$ ), as shown in Fig. 2C in the main text. In this system, both of the components will be affected by the same force, but will deflect in different ways. According to theory, one then gets the differential equation (Eq. 2 in the main text)

$$\dot{y} = \frac{F}{c} + \frac{\dot{F}}{k_w}, \quad [S3]$$

where  $y$  is the bending of the worm, and the dot indicates a time derivative. The force applied to the system can, in our case, be written as  $F = k_p x$ , where  $k_p$  and  $x$  are the stiffness and the deflection of the pipette, respectively. Furthermore, the pipette deflection can be written as  $x = x_u - y$ , where  $x_u = v_u t$  is the motion of the U-shaped pipette, moving at a constant speed  $v_u$ . This gives us  $F = k_p(v_u t - y)$  and

$$y = v_u t - \frac{F}{k_p} \quad [S4]$$

as well as

$$\dot{y} = v_u - \frac{\dot{F}}{k_p}. \quad [S5]$$

By plugging Eq. S5 into S3, we get

$$v_u - \frac{\dot{F}}{k_p} = \frac{F}{c} + \frac{\dot{F}}{k_w},$$

and after reordering

$$\dot{F} \left[ \frac{1}{k_p} + \frac{1}{k_w} \right] + \frac{F}{c} = v_u$$

$$\dot{F} + \frac{k_p k_w}{c(k_p + k_w)} F = \frac{v_u k_p k_w}{k_p + k_w}$$

$$\dot{F} + AF = B,$$

where  $A$  and  $B$  are constants ( $B = A c v_u$ ). This linear nonhomogeneous ordinary differential equation can be analytically solved (2) as

$$F(t) = \frac{B}{A} [1 + C_1 e^{-At}],$$

where  $C_1$  is a constant of integration. With the initial condition  $F(t=0) = 0$ , we get  $C_1 = -1$  and

$$F(t) = v_u c \left[ 1 - e^{-k_p k_w / (c(k_p + k_w)) t} \right]. \quad [S6]$$

A combination of Eqs. S4 and S6 results in

$$y(t) = v_u \left( t - \frac{c}{k_p} \left[ 1 - e^{-k_p k_w / (c(k_p + k_w)) t} \right] \right), \quad [S7]$$

giving us an expression for how the bending of the worm varies as a function of time (this is the same as Eq. 3 in the main text).

To get an expression for the bending as a function of the force, Eq. S6 is solved for  $t$ , giving

$$t(F) = -\frac{c(k_p + k_w)}{k_p k_w} \ln \left( 1 - \frac{F}{c v_u} \right), \quad [S8]$$

resulting in

$$y(F) = -\frac{v_u c}{k_p} \left[ \frac{k_w + k_p}{k_w} \ln \left( 1 - \frac{F}{v_u c} \right) + \frac{F}{v_u c} \right], \quad [S9]$$

when plugging Eq. S8 into Eq. S7. This is the exact deformation-force solution for the Maxwell model. The initial slope of Eq. S9 can be calculated as

$$\lim_{F \rightarrow 0} \frac{dy}{dF} = \frac{1}{k_w},$$

and corresponds to that expected in the EBT.

To get the force-deformation expression, we need to rewrite Eq. S9 as  $F(y)$ . This equation is not, however, analytically solvable for  $F$ , and the natural logarithm in Eq. S9 thus needs to be Taylor expanded (to the second order), giving

$$y(F) = -\frac{v_u c}{k_p} \left[ \frac{k_w + k_p}{k_w} \left( -\frac{F}{v_u c} \left[ 1 + \frac{F}{2 v_u c} \right] \right) + \frac{F}{v_u c} \right].$$

Reordering and solving the quadratic equation of  $F$  as a function of  $y$  finally gives (Eq. 4 in the main text)

$$F(y) = \frac{k_p v_u c}{k_p + k_w} \left( -1 + \sqrt{1 + \frac{2 k_w (k_p + k_w)}{k_p v_u c} y} \right). \quad [S10]$$

This approximate force-deformation solution was shown to give very similar values for  $k_w$  and  $c$  as the exact deformation-force solution in Eq. S9, and is thus valid to use when describing the data.

## Kelvin-Voigt Model

The differential equation characterizing a spring and a dashpot connected in parallel can be written as

$$F = k_w y + c \dot{y}. \quad [S11]$$

This equation is solved in the same way as described above, resulting in an expression for the bending as a function of time

$$y(t) = \frac{k_p v_u c}{(k_p + k_w)^2} \left[ \frac{k_p + k_w}{c} t - 1 + e^{-\frac{k_p + k_w}{c} t} \right]. \quad [\text{S12}]$$

This is the functional form used for the Kelvin–Voigt fit in Fig. 2 in the main text.

### Reproducibility of Experimental Results

**Varying Bending Speeds.** Results from bending measurements performed with different speeds on different worms are shown in Fig. S1.

The difference in the constant stiffness values is due to different diameters of the studied worms. The damping coefficient is inversely proportional to bending speed.

**Along the Body Measurements.** Results from micropipette deflection experiments performed along the body of three different young adults are shown in Fig. S2. The stiffness has been normalized by the stiffness at the vulva to make it easier to compare results between different worms. The head is stiffer than the tail in all cases, and the dashed lines act to guide the eye.

### Viscous Relaxation of the Worm

In Fig. S3 all the force–deformation data from a bending experiment on a young adult worm are shown.

Before contact between the support and the worm, there is no deflection of the pipette and the negative bending values are thus an artifact from the definition of  $y = x_u - x$  (defined as 0 at the contact point). After the bending was performed, the support was stopped and the worm was left to relax. The force decreased as a function of time (0.5 s between each data point), which is a strong implication of a viscous relaxation.

1. Young WC, Budynas RG (2002) *Roark's Formulas for Stress and Strain* (McGraw-Hill, New York).

2. Kreyszig E (2006) *Advanced Engineering Mathematics* (Wiley, New York), p 27.

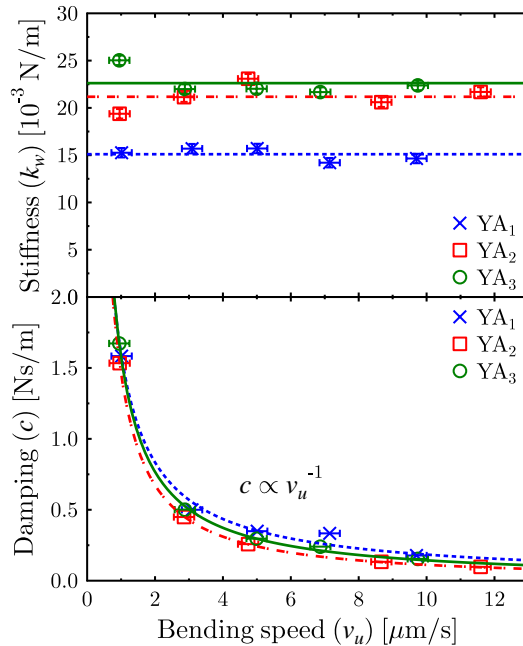


Fig. S1. (Upper) Stiffness and (Lower) damping coefficient as function of bending speed for three different young adult worms.

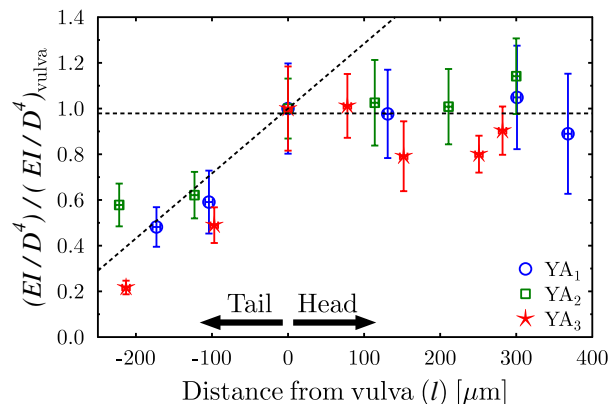
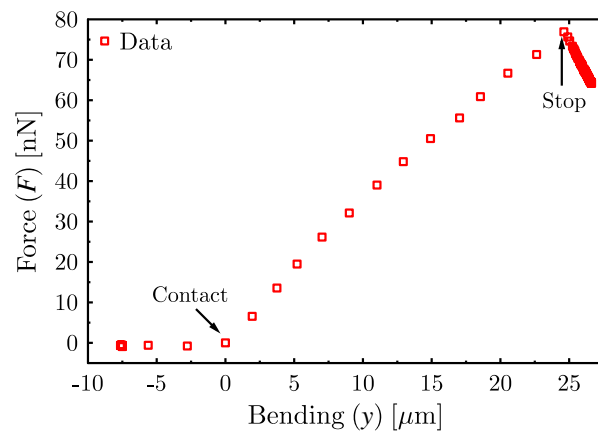


Fig. S2. The effective Young's modulus as a function of position along the body of three different young adult worms. The modulus has been normalized by the value measured at the vulva for each worm.



**Fig. S3.** Entire force–deformation from a bending experiment of a young adult worm. Bending starts at the contact point between the worm and the support and the material clearly relaxes after the motion of the support has been seized (after “stop”).

## **A.2 Paper II**

*The nematode *C. elegans* as a complex viscoelastic fluid*

M. Backholm, W. S. Ryu, and K. Dalnoki-Veress, *Eur. Phys. J. E* **38**, 36 (2015).

# The nematode *C. elegans* as a complex viscoelastic fluid

Matilda Backholm<sup>1</sup>, William S. Ryu<sup>2</sup>, and Kari Dalnoki-Veress<sup>1,3,a</sup>

<sup>1</sup> Department of Physics & Astronomy and the Brockhouse Institute for Materials Research, McMaster University, Hamilton, ON, Canada

<sup>2</sup> Department of Physics and the Donnelly Centre, University of Toronto, Toronto, ON, Canada

<sup>3</sup> PCT Lab, UMR CNRS 7083 Gulliver, ESPCI ParisTech, PSL Research University, Paris, France

Received 1 December 2014 and Received in final form 13 March 2015

Published online: 13 May 2015 – © EDP Sciences / Società Italiana di Fisica / Springer-Verlag 2015

**Abstract.** The viscoelastic material properties of the model organism *C. elegans* were probed with a micropipette deflection technique and modelled with the standard linear solid model. Dynamic relaxation measurements were performed on the millimetric nematode to investigate its viscous characteristics in detail. We show that the internal properties of *C. elegans* can not be fully described by a simple Newtonian fluid. Instead, a power-law fluid model was implemented and shown to be in excellent agreement with experimental results. The nematode exhibits shear thinning properties and its complex fluid characteristics were quantified. The bending-rate dependence of the internal damping coefficient of *C. elegans* could affect its gait modulation in different external environments.

## 1 Introduction

*Caenorhabditis elegans* is a millimeter-long, transparent nematode used as a model organism in biology to study, *e.g.*, genetics, cancer, and aging [1]. The small worm has recently gained popularity as an ideal model for studies of motility due to its elegant undulatory locomotion: an efficient form of motion shared with sperm cells, worms, and snakes ranging several orders of magnitude in size. The motion of *C. elegans* has been extensively studied in liquids to probe the active micro-swimming kinematics and dynamics of the worm in a purely viscous environment [2–7]. The crawling motion of the nematode on a gel substrate has also been investigated [8–10], as well as the interactions between worms, both in fluid and on agar [11–13]. The smooth modulation between the gaits of swimming and crawling has furthermore been the focus of many studies [3, 7, 14–16].

To form a complete understanding of the undulatory locomotion of *C. elegans*, a knowledge of the passive material properties of the nematode is required. The material properties affect how much energy the worm has to spend on bending its own body as it performs its undulating motion and simultaneously pushes off against the surrounding medium. Extensive work has been performed to study the elasticity of the model organism, either through direct measurements or by utilizing the swimming kinematics of the worm [3, 17–20]. In many of these studies, however, the results rely heavily on theoretical assumptions of the viscoelasticity of the soft biological tissue. In previous work,

we probed the material properties of *C. elegans* directly and implemented the Maxwell model, a well-known model for viscoelasticity, to capture the bending dynamics of the worm [20]. We showed that the viscous component of this model, responsible for relaxation, responds as a shear thinning fluid when the nematode is bent at different bending speeds. This shear thinning property of *C. elegans* suggests that it is easier for the worm to bend its own body quickly, than to produce the same motion slowly. Such an internal body property could strongly affect the gait modulation of the nematode in different environments.

Here we present a detailed experimental study of the viscous relaxation of the nematode and apply a well-known viscoelastic model to describe the worm material. We will show that a pure Newtonian fluid can not correctly capture the viscous component responsible for relaxation, but that the implementation of a complex, power-law fluid is necessary to understand its relaxation. We find that the worm is strongly shear thinning and quantify the viscoelastic properties of young adult and adult *C. elegans* nematodes.

## 2 Experiment

Micropipette deflection was used to measure the material properties of *C. elegans* as shown in the schematic illustration of fig. 1(a) and in the optical microscopy image of fig. 1(b). In this technique, the deflection of a long (1–2 cm) and thin ( $\sim 20 \mu\text{m}$ ) glass micropipette, which acts as force measuring spring, is force-calibrated and used as a sensor capable of measuring forces down to the nN

<sup>a</sup> e-mail: dalnoki@mcmaster.ca

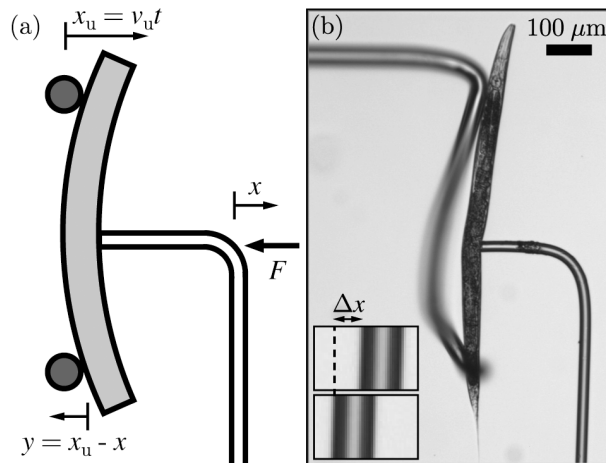


**Fig. 1.** a) Schematic diagram of the experimental micropipette deflection setup. b) Optical microscopy image of the bending of a young adult worm. The insets show a zoom in of the pipette deflection ( $\Delta x = 11.4 \pm 0.1 \mu\text{m}$ ) between the points of worm-support contact (bottom) and the end of the bending part of the experiment (top).

range. This technique was previously introduced to probe the elastic properties of *C. elegans* by simply bending the worm [20], and has since then been used to study the active dynamics of the nematode crawling on a gel surface [10] as well as swimming in an infinite fluid [6] and close to solid boundaries [7]. Micropipette deflection has furthermore been applied to, *e.g.*, probe the adhesion dynamics of vesicles, cells, and cellular aggregates [21–25], as well as the cellular response to stiffness [26, 27].

In our experiments, the micropipettes were manufactured and calibrated (spring constant  $k_p$ ) as described in [20–22]. Before an experiment, worms were picked from agar plates into a drop of M9 buffer containing 10 mM of  $\text{NaN}_3$  that acted as an anesthetic. This drug has been shown to not affect the material properties of the nematode [20]. A chamber consisting of two thin glass cover slips was then built around the drop with two 2 mm tall spacers on both sides and filled up with more M9- $\text{NaN}_3$  solution. The worm-containing chamber was then carefully moved onto an inverted microscope where the force-sensing pipette was mounted onto an  $xyz$ -translational stage and moved into the chamber. To directly probe the viscoelastic material properties, three-point bending measurements were performed on the worm bodies. An anesthetized worm was held by the pipette at the point of the vulva by applying suction, and centered between two simple supports. As in our previous experiments [20], the support was made of a thicker ( $\sim 50 \mu\text{m}$ ) micropipette curved into the shape of a U and mounted on the opposite side of the chamber to a motorized translation stage. The worm could then be bent by pushing it into the gap between the two sides of the U-shaped support, which was done by moving the support ( $x_u$ , from left to right in fig. 1) with a constant speed ( $v_u$ ) towards the worm. This causes a deflection ( $x$ ) of the pipette to the right, a spring-like force ( $F = k_p x$ ) to the left and the worm to bend

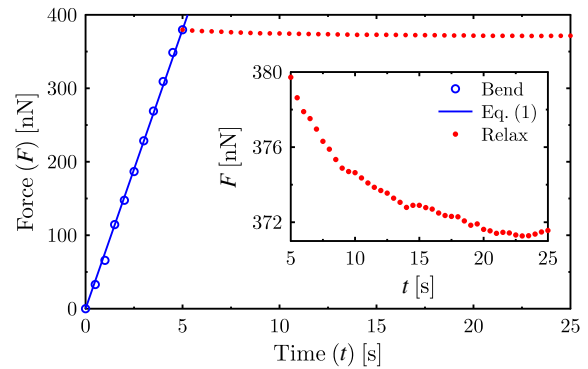


**Fig. 2.** Force as a function of time for the bending (blue circles) and relaxation (red dots) parts of the experiment. The Hookean model of eq. (1) has been fit to the bending data, as shown by the blue line. The inset shows a zoom in on the relaxation data.

( $y = x_u - x = v_u t - x$ ). The experiments were run using an in-house LabView code controlling the motor and camera. All wild type (N2) *C. elegans* nematodes used in this work were young adults or adults. The worms were acquired from the Caenorhabditis Genetics Center and were cultivated according to standard methods [28] on *Escherichia coli* (OP50) nematode growth media (NGM) plates at  $20^\circ\text{C}$ . All chemicals were sourced from Sigma-Aldrich.

The experiments in this work consisted of two parts. First the worm was quickly bent by moving the support as described above. In the second and main part of the experiment, the motion of the support was stopped and the worm was left to relax under the applied force. To measure actual forces, images of the experiments were captured with a camera at a rate of 2 fps and the pipette deflection was extracted with cross-correlation image analysis performed with an in-house Matlab script. The deflection was then multiplied by the spring constant of the pipette ( $k_p \sim 2\text{--}6 \text{ nN}/\mu\text{m}$ ), giving the force with an uncertainty of less than 10%. In fig. 2, the force from such an experiment is plotted as a function of time, and the two different regimes are denoted by different markers. The change in the force due to relaxation of the worm is always significantly smaller than due to the initial bending, as highlighted in the inset of fig. 2. As the focus of this work was to probe the viscoelastic relaxation of the worm material, the initial bending experiment was performed with a high speed of the supports ( $30\text{--}50 \mu\text{m}/\text{s}$ ) during just a few seconds to minimise any viscous dissipation to occur before the start of the pure relaxation part of the experiment. Here it is important to notice that both the force and worm deformation vary as a function of time since the force-sensing pipette causes the worm to bend as the force relaxes. This is taken into account in the models, as described below.

### 3 Model

The initial bending part of our experiment was performed with high speeds to exclude any viscous dissipation, and the material is thereby assumed to behave in a purely

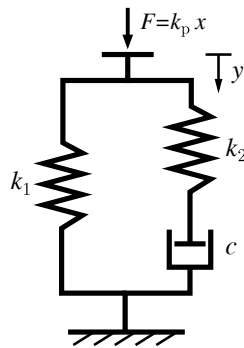


**Fig. 3.** The standard linear solid (SLS) model, with two elastic springs (spring constants  $k_1$  and  $k_2$ ) and a viscous dashpot (damping coefficient  $c$ ). The compression ( $y$ ) of this connection corresponds to the bending of the worm and the force ( $F$ ) is that applied by the deflected pipette.

Hookean manner. The worm bending can thus be written as  $y_b = F_b/k$ , where  $k$  is the total spring constant of the worm and the subscript b denotes the bending regime. For our experiment, the force can also be written as  $F_b(t) = k_p x_b(t) = k_p (v_u t - y_b)$ . Combining these two expressions gives

$$F_b(t) = \frac{k_p v_u k}{k + k_p} t. \quad (1)$$

For the relaxation part of the experiment, we model the worm material with the standard linear solid (SLS) model [29], where a purely viscous dashpot (damping coefficient  $c$ ) is connected with two purely elastic springs (spring constants  $k_1$  and  $k_2$ ) as shown in fig. 3. The series connection of  $c$  and  $k_2$  is known as the Maxwell model and has been shown to successfully describe the viscoelastic properties of *C. elegans* in dynamic bending experiments [20]. In order to study material relaxation, the parallel connection of a second spring is necessary to prevent continuous viscous flow at long times, which would not be representative of a soft biological tissue.

The SLS model relates the applied force  $F$  with the material deformation  $y$  as [29]

$$\dot{y} = \frac{1}{k_1 + k_2} \left( \dot{F} + \frac{k_2}{c} F - \frac{k_1 k_2}{c} y \right). \quad (2)$$

Comparing the SLS and Hookean models,  $k = k_1 + k_2$  and corresponds to the initial elastic response of the viscoelastic material.

### 3.1 Newtonian fluid

First, we assume a theoretical dashpot containing a purely Newtonian fluid. During the relaxation part of the experiment,  $F_r(t) = k_p x_r(t) = k_p (s_0 - y_r(t))$  and  $\dot{F}_r = -k_p \dot{y}_r$ , where  $s_0$  is the distance the support was moved during the initial bending, and time has been restarted so that  $t = 0$  when the relaxation starts. Solving eq. (2) with these substitutions and the boundary condition  $F_r(0) = k_p (s_0 - y_0)$ ,

where  $y_0$  is the initial worm bending, gives

$$F_r = \frac{k_1 k_p s_0}{k_1 + k_p} - k_p \left( y_0 - \frac{k_p s_0}{k_1 + k_p} \right) e^{-\kappa t}, \quad (3)$$

where

$$\kappa = \frac{k_2 (k_1 + k_p)}{c (k_1 + k_2 + k_p)}.$$

We want to stress that the SLS model is necessary to describe the worm material as a whole, *i.e.*, both in the bending and relaxation regimes. The Maxwell model itself can only describe the active bending of the nematode [20], whereas the Kelvin-Voigt model, where a spring is connected in parallel with a dashpot [29], has the same functional solution as the SLS model in the relaxation regime. The SLS model thus captures the physics of both regimes and should be used when investigating the pure material properties of the worm, as is done here. In the case of a living, actively moving worm, however, solving the Maxwell model in the bending regime is sufficient to properly describe the viscoelastic properties of the nematode.

### 3.2 Power-law fluid

To take any non-Newtonian (complex) viscous properties of the worm into account, the Ostwald-de Waele power-law fluid model [30] was implemented. This model has been widely used to describe the flow of many different complex fluids and was, furthermore, shown to describe the viscous component of *C. elegans* in our previous work [20]. As we will show below, the power-law fluid is necessary due to the failure of the purely Newtonian model to describe the observed relaxation. In the Ostwald-de Waele model, an effective damping coefficient is used to account for the change of flow as a function of bending rate:

$$c_{\text{eff}} = a \dot{\gamma}^{-d}. \quad (4)$$

Here  $a$  is the *flow consistency index* (damping coefficient at bending rate  $1 \text{ s}^{-1}$ ) and  $d$  the *power-law index* (a measure of the deviation from pure Newtonian flow). For a Newtonian fluid,  $d = 0$  and the damping coefficient would be constant as in sect. 3.1. When  $d > 0$ , however, the fluid is shear thinning. The bending rate in our system has been defined as  $\dot{\gamma} = \dot{y}/L$ , where  $L$  is the distance between the two simple supports. Substituting eq. (4) into eq. (2) and solving for the relaxation case gives

$$F_r^* = C + \frac{k_p}{A} \left[ (B - A y_0)^{\frac{d}{d-1}} + \frac{A d}{a^{\frac{1}{1-d}} (1-d)} t \right]^{\frac{d-1}{d}}, \quad (5)$$

where  $A$ ,  $B$ , and  $C$  are the following constants:

$$A = \frac{k_2 (k_1 + k_p)}{k_1 + k_2 + k_p}, \quad B = \frac{k_2 k_p s_0}{k_1 + k_2 + k_p}, \quad C = \frac{k_1 k_p s_0}{k_1 + k_p}.$$

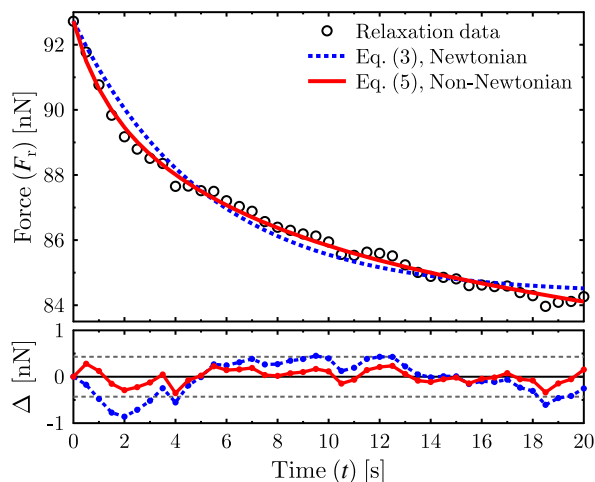


**Fig. 4.** Relaxation force as a function of time. The dashed blue line is the fit from the Newtonian SLS model of eq. (3) and the solid red line shows the fit from the power-law fluid model of eq. (5). The fit residuals ( $\Delta$ ) are shown in the bottom graph, where the dashed grey lines denote the experimental uncertainty.

## 4 Results and discussion

### 4.1 Newtonian relaxation

Since the first part of the experiment was performed with high bending speeds to minimise any viscous dissipation, the force was purely linear as a function of time during the initial worm bending. As shown by the best fit line in fig. 2, eq. (1) was successfully fit to the force data in this regime and  $k$  could thereby be determined, reducing the number of fitting parameters necessary for the relaxation part of the experiment. The total spring constant was in other words used when fitting the Newtonian model of eq. (3) to the relaxation data, so that only two fitting parameters were necessary:  $k_1$  and  $c$ , while  $k_2$  is fixed by  $k - k_1$ . The result is shown in fig. 4, where the relaxation force is plotted as a function of time. The SLS model is fit (dashed blue line) to the data and the residual between theory and experiment is shown in the bottom graph of fig. 4, where the expected experimental uncertainty (forces corresponding to pipette deflections of less than  $0.1 \mu\text{m}$ ) is drawn with dashed lines. It is clear that this viscoelastic model does not capture the data within the uncertainty of the measurements. The failure of the model is especially clear in the beginning of the relaxation, where the force and worm deformation change rapidly.

### 4.2 Non-Newtonian relaxation

In previous work, we showed that the worm possesses shear thinning properties when bent with different bending speeds [20]. The worm bending rate  $\dot{\gamma}$  remains constant throughout such an experiment, and the assumption

of a constant damping coefficient (for that specific experiment) is therefore valid. However, during the relaxation stage of our current experiments,  $\dot{\gamma}$  changes rapidly and fitting for a constant damping coefficient for the relaxation of this complex viscoelastic material is thus not correct. We therefore implemented the power-law fluid model as described in sect. 3.2 to model the mechanical relaxation of the nematode. As shown by the solid red line of fig. 4, the non-Newtonian fluid model of eq. (5) is successfully fit to the relaxation data. Again,  $k$  has been fixed by the initial bending portion of the experiment, and the data is fit with three fitting parameters:  $k_1$ ,  $a$ , and  $d$ . There is a significant improvement of the fit when implementing the non-Newtonian damping coefficient as compared to the Newtonian case, and the non-Newtonian model clearly captures the data within the experimental uncertainty, as highlighted by the residuals.

Tens of relaxation experiments were performed with different nematodes (of similar size) and eq. (5) was successfully fit to all data sets. The flow consistency and power-law indices could thereby be determined as  $a = 0.10 \pm 0.03 \text{ mNs}^{1-d}/\text{m}$  and  $d = 0.9 \pm 0.1$ . Since  $d > 0$ , the nematode is shown to consist of a shear thinning viscous component. Furthermore, the power-law scaling  $c \propto \dot{\gamma}^{-0.9 \pm 0.1}$  is in excellent agreement with that found previously by bending the worm with different bending speeds, where  $c \propto \dot{\gamma}^{-1 \pm 0.1}$  [20]. *C. elegans* thus shows stronger shear-thinning properties than typical complex fluids made of macromolecules like polymers, for which the power-law indices are in the range of  $d_{\text{polymers}} = 0.4\text{--}0.85$  [30–32]. The complex fluid property of *C. elegans* could be due to its collagen-rich cuticle [33], since this extracellular matrix component has been shown to be strongly shear thinning [34–36], with a power-law index of  $d_{\text{collagen}} = 0.76 \pm 0.01$  [37].

Other factors or complexities that could render shear thinning properties of *C. elegans* include the different cross-sectional structure of the worm along its body, where various tissues will be deformed differently during bending. In this work, we consider the viscous flow component of the worm as a composite parameter in a viscoelastic model, and not necessarily as actual flow of internal body fluids. For the case of a nematode, however, there is in fact some internal motion of the heterogenous tissues and fluids as the body is deformed. This flow could contribute to the shear thinning properties of the worm. Finally, the high hydrostatic pressure of the nematode body cavity could affect the viscous characteristics of the worm. However, as our experiments were performed with low amplitude bends, changes in the internal pressure due to bending would not be significant. These avenues could be further investigated by performing relaxation experiments on mutants with different developmental defects or with cuticle or muscle variations.

Knowing the quantitative power-law fluid properties of *C. elegans*, it is now also possible to calculate the effective damping coefficient experienced by the nematode during its active undulatory locomotion. When crawling on agar, the adult *C. elegans* worm bends its body at a speed of  $\dot{\gamma}_{\text{crawl}} \approx 104 \mu\text{m/s}$  [38] and with a wavelength

of  $\lambda_{\text{crawl}} = 650 \pm 30 \mu\text{m}$  [3], corresponding to an effective damping coefficient of  $c_{\text{eff,crawl}} = a(\dot{y}_{\text{crawl}}/0.5\lambda_{\text{crawl}})^{-d} = 0.29 \pm 0.07 \text{ mNs/m}$ . The effective internal damping coefficient of the worm swimming in a fluid with a water-like viscosity ( $\dot{y}_{\text{swim}} \approx 970 \mu\text{m/s}$ ,  $\lambda_{\text{swim}} = 1540 \pm 40 \mu\text{m}$  [3,4]) can in the same way be calculated as  $c_{\text{eff,swim}} = 0.08 \pm 0.03 \text{ mNs/m}$ , and is significantly lower than that used in higher viscosity environments. The internal properties of the worms can thereby not be considered invariant, but depend strongly on the type of motion performed by the nematode. The change in the internal viscous properties of *C. elegans* should thus be accounted for when studying its gait modulation in response to varying environmental factors, such as an increased viscosity or confinement.

## 5 Conclusions

In this work, the viscoelastic material properties of the model organism *C. elegans* were probed experimentally with a dynamic and time-resolved micropipette deflection technique. Direct relaxation experiments were performed, and the nematode deformation was described with the viscoelastic standard linear solid model. It was shown that the viscous component of the worm material could not be described as a Newtonian fluid. Instead the Ostwald-de Waele power-law fluid model was implemented and shown to be in excellent agreement with our experimental observations. The viscous relaxation of *C. elegans* is characterized by a shear thinning power-law fluid with a flow consistency and power-law index of  $a = 0.10 \pm 0.03 \text{ mNs}^{1-d}/\text{m}$  and  $d = 0.9 \pm 0.1$ , respectively. The strong bending-rate dependence of the internal properties of the worm, showing a lower effective viscosity at higher bending speeds, could affect the gait modulation of the undulating motion in various environments.

The financial support by NSERC of Canada is gratefully acknowledged. The authors also thank Rafael Schulman for interesting discussions.

## References

1. B. Wood, *The Nematode Caenorhabditis Elegans* (Cold Spring Harbor Laboratory Press, New York, 1988).
2. S. Park, H. Hwang, S.W. Nam, F. Martinez, R.H. Austin, W.S. Ryu, *PLoS One* **3**, e2550 (2008).
3. C. Fang-Yen, M. Wyart, J. Xie, R. Kawai, T. Kodger, S. Chen, Q. Wen, A.D.T. Samuel, *Proc. Natl. Acad. Sci. U.S.A.* **107**, 20323 (2010).
4. J. Sznitman, X. Shen, R. Sznitman, P.E. Arratia, *Phys. Fluids* **22**, 121901 (2010).
5. X.N. Shen, P.E. Arratia, *Phys. Rev. Lett.* **106**, 208101 (2011).
6. R.D. Schulman, M. Backholm, W.S. Ryu, K. Dalnoki-Veress, *Phys. Rev. E* **89**, 050701 (2014).
7. R.D. Schulman, M. Backholm, W.S. Ryu, K. Dalnoki-Veress, *Phys. Fluids* **26**, 101902 (2014).
8. P. Sauvage, M. Argentina, J. Drappier, T. Senden, J. Siméon, J.M. Di Meglio, J. Biomech. **44**, 1117 (2011).
9. A. Ghanbari, V. Nock, S. Johari, R. Blaikie, X. Chen, W. Wang, J. Micromech. Microeng. **22**, 095009 (2012).
10. Y. Rabets, M. Backholm, K. Dalnoki-Veress, W.S. Ryu, *Biophys. J.* **107**, 1980 (2014).
11. S. Gart, D. Vella, S. Jung, *Soft Matter* **7**, 2444 (2011).
12. J. Yuan, D.M. Raizen, H.H. Bau, *Proc. Natl. Acad. Sci. U.S.A.* **111**, 6865 (2014).
13. M. Backholm, R.D. Schulman, W.S. Ryu, K. Dalnoki-Veress, *Phys. Rev. Lett.* **113**, 138101 (2014).
14. J.T. Pierce-Shimomura, B.L. Chen, J.J. Mun, R. Ho, R. Sarkis, S.L. McIntire, *Proc. Natl. Acad. Sci. U.S.A.* **105**, 20982 (2008).
15. S. Berri, J.H. Boyle, M. Tassieri, I.A. Hope, N. Cohen, *HFSP J.* **3**, 186 (2009).
16. J.H. Boyle, S. Berri, N. Cohen, *Front. Comput. Neurosci.* **6**, 10 (2012).
17. S.J. Park, M.B. Goodman, B.L. Pruitt, *Proc. Natl. Acad. Sci. U.S.A.* **104**, 17376 (2007).
18. J. Sznitman, P.K. Purohit, P. Krajacic, T. Lamitina, P.E. Arratia, *Biophys. J.* **98**, 617 (2010).
19. B.C. Petzold, S.J. Park, P. Ponce, C. Roozeboom, C. Powell, M.B. Goodman, B.L. Pruitt, *Biophys. J.* **100**, 1977 (2011).
20. M. Backholm, W.S. Ryu, K. Dalnoki-Veress, *Proc. Natl. Acad. Sci. U.S.A.* **110**, 4528 (2013).
21. M.J. Colbert, A.N. Raegen, C. Fradin, K. Dalnoki-Veress, *Eur. Phys. J. E* **30**, 117 (2009).
22. M.J. Colbert, F. Brochard-Wyart, C. Fradin, K. Dalnoki-Veress, *Biophys. J.* **99**, 3555 (2010).
23. D. Gonzalez-Rodriguez, L. Bonnemay, J. Elgeti, S. Dufour, D. Cuvelier, F. Brochard-Wyart, *Soft Matter* **9**, 2282 (2013).
24. J.M. Frostad, M.C. Collins, G.L. Leal, *Langmuir* **29**, 4715 (2013).
25. J.M. Frostad, M. Seth, S.M. Bernasek, G.L. Leal, *Soft Matter* **10**, 7769 (2014).
26. D. Mitrossilis, J. Fouchard, A. Guioy, N. Desprat, N. Rodriguez, B. Fabry, A. Asnacios, *Proc. Natl. Acad. Sci. U.S.A.* **106**, 18243 (2009).
27. D. Mitrossilis, J. Fouchard, D. Pereira, F. Postic, A. Richert, S.J. Michel, A. Asnacios, *Proc. Natl. Acad. Sci. U.S.A.* **107**, 16518 (2010).
28. S. Brenner, *Genetics* **77**, 71 (1974).
29. Y.C. Fung, *Biomechanics: Mechanical Properties of Living Tissue* (Springer-Verlag, New York, 1993).
30. B.B. Bird, R.C. Armstrong, O. Hassager, *Dynamics of Polymeric Liquids* (John Wiley & Sons, New York, 1977).
31. W.W. Graessley, *Adv. Polym. Sci.* **16**, 1 (1974).
32. K. Dalnoki-Veress, B.G. Nickel, C. Roth, J.R. Dutcher, *Phys. Rev. E* **59**, 2153 (1999).
33. G.N. Cox, S. Staprans, R.S. Edgar, *Dev. Biol.* **86**, 456 (1981).
34. H. Oxlund, T.T. Andreassen, *J. Anat.* **131**, 611 (1980).
35. N. Phan-Thien, S. Nasserri, L.E. Bilston, *Rheol. Acta.* **39**, 409 (2000).
36. F.H. Silver, A. Ebrahimi, P.B. Snowhill, *Connect. Tissue Res.* **43**, 569 (2002).
37. L. Duan, J. Li, C. Li, G. Li, *Korea-Aust. Rheol. J.* **25**, 137 (2013).
38. J. Karbowski, C.J. Cronin, A. Seah, J.E. Mendel, D. Cleary, P.W. Sternberg, *J. Theor. Biol.* **242**, 652 (2006).

## A.3 Paper III

*Dynamic force patterns of an undulatory microswimmer*

R. D. Schulman, M. Backholm, W. S. Ryu, and K. Dalnoki-Veress, Phys. Rev. E: Rapid Communications **89**, 050701 (2014).



## Dynamic force patterns of an undulatory microswimmer

Rafael D. Schulman,<sup>1</sup> Matilda Backholm,<sup>1</sup> William S. Ryu,<sup>2</sup> and Kari Dalnoki-Veress<sup>1,3,\*</sup>

<sup>1</sup>*Department of Physics and Astronomy and The Brockhouse Institute for Materials Research, McMaster University, 1280 Main Street West, Hamilton, Ontario, Canada L8S 4M1*

<sup>2</sup>*Department of Physics, University of Toronto, 60 St. George Street, Toronto, Ontario, Canada M5S 1A7*

<sup>3</sup>*Laboratoire de Physico-Chimie Théorique, UMR CNRS Gulliver 7083, ESPCI, Paris, France*

(Received 23 January 2014; published 30 May 2014)

We probe the viscous forces involved in the undulatory swimming of the model organism *C. elegans*. Using micropipette deflection, we attain direct measurements of lateral and propulsive forces produced in response to the motion of the worm. We observe excellent agreement of the results with resistive force theory, through which we determine the drag coefficients of this organism. The drag coefficients are in accordance with theoretical predictions. Using a simple scaling argument, we obtain a relationship between the size of the worm and the forces that we measure, which well describes our data.

DOI: 10.1103/PhysRevE.89.050701

PACS number(s): 87.19.ru, 47.63.Gd, 47.15.G–

Locomotion through a fluid environment is common to organisms over a wide range of length scales, from whales and humans to primitive algae and bacteria. However, the physics of “microswimming,” which is the propulsion at very small length scales, differs vastly from that applicable to macroscopic swimmers. Studying the principles of locomotion in this regime is crucial for our fundamental understanding of a diverse collection of organisms, including bacteria, sperm, and a variety of other microorganisms. Furthermore, microswimmers offer a wide variety of applications including robotic microswimmers capable of cargo towing for biomedical purposes, such as advanced drug targeting [1,2], collective swimming of bacteria to induce mixing in microfluidic devices [3,4], and fluid pumping [5–7].

The Reynolds number is a quantity that measures the relative magnitude of viscous and inertial forces in a fluid. At small length scales, the Reynolds number is typically less than unity, which implies that viscous forces are dominant and inertia can be neglected. In addition, to achieve propulsion in this regime, it is obligatory to perform a motion that is not time reversible, according to the scallop theorem [8]. This theorem asserts that if a swimmer performs a sequence of motions that is unchanged when played in reverse, such as a scallop, which simply opens and closes, it will not acquire any net displacement. There are numerous ways of breaking this symmetry, such as the helical beating of a flagellum [8–10], and motions similar to a human breast stroke, as is performed by the simple alga cell *Chlamydomonas reinhardtii* [11,12]. Another common way to break this symmetry is to propagate traveling waves down a body, which is successfully achieved by undulatory swimmers [13–16].

Undulatory locomotion is known to be a very efficient mechanism of propulsion and is effective over a large range of length scales [17]. Extensive theoretical efforts have been put forth in understanding the locomotion of a slender undulator, in which the length of the swimmer is much larger than its width [10,15,16,18,19]. Among these, resistive force theory (RFT) is a simple model in which the viscous force on a body segment moving through a low Reynolds number fluid

can be decomposed into a component tangential and normal to that segment [10,15,16,18,20]. Each of these components is linearly proportional to the speed of the segment in that direction and related through the normal and tangential drag coefficients,  $c_N$  and  $c_T$ . The ratio  $c_N/c_T$  has important implications in the propulsion of the swimmer. Namely, if  $c_N/c_T > 1$ , propulsion is directed contrary to the direction of the traveling wave. If  $c_N/c_T < 1$ , we are faced with the curious case of the undulator moving in the same direction as its traveling wave, while the swimmer can attain no net propulsion if  $c_N/c_T = 1$ . In RFT, the difficulty lies in determining the drag coefficients. Several theoretical studies have derived

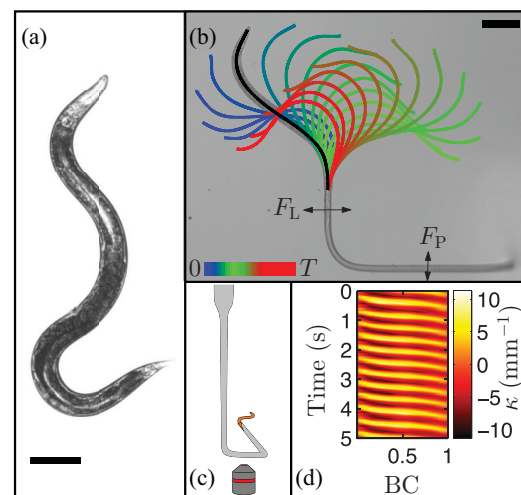


FIG. 1. (Color online) (a) *C. elegans*. The scale bar represents 100  $\mu\text{m}$ . (b) Time lapse of the worm’s centerline over one period ( $T$ ), with colors representing time. A sample centerline is overlaid on the worm in black. Arrows indicate motion of the end of the pipette as a result of the two orthogonal forces. The scale bar represents 150  $\mu\text{m}$ . (c) Schematic of the micropipette used in our experiments with a worm held at the end (not to scale). (d) Curvature color plot for the swimming. BC (body coordinate) denotes the distance along the worm, where 0 represents the head and 1 represents the portion of the worm nearest the pipette. Positive curvatures are indicated by lighter color and denote the convex side to the left.

\*dalnoki@mcmaster.ca

values for the coefficients; however, assumptions regarding the swimming and approximations must be made [10,15,18,20]. Indeed, experimental measurements are crucial in order to evaluate the validity of RFT and to determine the magnitude of the drag coefficients. There have been experiments which have evaluated RFT for a variety of single-celled organisms using kinematic data from high-speed imaging [21–23]. Other experiments have performed average force measurements of nonundulatory microorganisms in optical traps [24,25]. However, to date, direct and time-resolved measurements of drag forces on an undulating microswimmer are still lacking. Furthermore, direct verification of the applicability of RFT for swimmers at length scales where the Reynolds number may not be much less than unity is still needed.

Many experiments on undulatory microswimmers have focused on the model organism *Caenorhabditis elegans* [Fig. 1(a)], a millimeter sized hermaphroditic nematode [26]. These studies have characterized the kinematics of *C. elegans* in various environments, including swimming in a buffer of various viscosities [27,28], viscoelastic media [29], crawling on agar [30], structured environments [31,32], and through complex environments such as granular materials [33,34]. Attempts have been made to measure crawling forces using pillars as force transducers for *C. elegans* crawling on agar [35,36]. In another work, the viscous forces of swimming *C. elegans* were inferred from particle tracking and particle image velocimetry [28]. However, these studies, though insightful, have not succeeded in performing direct measurements of forces and drag coefficients in fluid.

Here we present a method to directly measure the time-varying propulsive and lateral forces of *C. elegans*. A comparison between our experimentally determined forces and the calculated forces from RFT demonstrates an excellent agreement. The experimental and theoretical force curves are used to deduce values for the drag coefficients of *C. elegans* swimming. Finally, a simple scaling argument is presented which postulates a relationship between the size of the worm and the mean propulsive and rms lateral force. We find our experimental data to be well described by the scaling argument.

We use a micropipette deflection technique to measure the forces generated by the undulatory microswimmer [37–39]. In this technique, a flexible glass micropipette that is more than three orders of magnitude thinner than its length deflects when subjected to an external force. Since the bending stiffness of the pipette has been determined through calibration, forces can be computed from deflections of the pipette. We catch worms by their tail end by applying suction, and hold them with the end of our pipettes. The micropipettes are capable of deflecting along the worm's swimming axis, as well as along the corresponding in-plane perpendicular direction. Thus, we can measure forces in two orthogonal directions [Figs. 1(b) and 1(c)] [39]. As the nematodes move, they generate forces in their propulsive and lateral directions, which we independently measure using the micropipette as a force transducer [Fig. 1(c)]. The deflections of the pipette are much smaller than length scales associated with the motion of the worms [39].

Upon capture, the worms perform a highly reproducible and periodic sequence of body movements, in which traveling waves are propagated down the body, which is akin to free

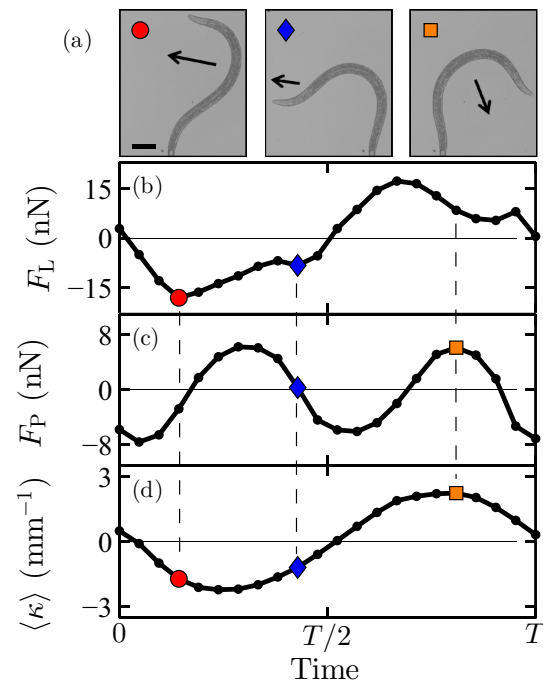


FIG. 2. (Color online) (a) Snapshots of a young adult worm at different stages of one swimming cycle. The labels refer to the markers in the graphs below and the arrows indicate the main velocity of the body. The scale bar represents  $100 \mu\text{m}$ . (b) The lateral force experienced by the worm over one period, where a positive force denotes a force directed to the left. The peak negative force (red circle) corresponds to the worm moving directly left, generating a drag force to the right (negative direction). Secondary peaks (blue diamond) correspond to turning points in the swimming cycle, when an extra push in the lateral direction is instigated. This point roughly coincides with a zero in the propulsive force. (c) The propulsive force on the worm over one period, where a positive force denotes a force directed up (in the swimming direction). The maximum propulsive force (orange square) corresponds to the worm pushing fluid behind itself, generating a drag force forward. This point roughly coincides with a maximum in the curvature. (d) The mean curvature of the worm over one period.

swimming of *C. elegans* [Fig. 1(b)] [27,28]. However, when held fixed at one end, the traveling waves are of larger amplitude than in free swimming and have a node at the fixed end. The temporal oscillations of the curvature of the worm exhibit a well defined frequency, which remains constant at  $2.4 \pm 0.2$  Hz for worms of various lengths [Fig. 1(d)]. The spatial and temporal oscillations in the curvature compare well with what has been measured for free swimming [27,28,31].

Figure 2 shows direct *simultaneous measurements* of the force generated in the lateral and propulsive directions as well as images of the motion that caused specific forces [39]. Microswimmers inhabit a low Reynolds number environment, and as such, the net forces involved in swimming are dominated by viscous drag forces. The estimated Reynolds numbers for the worms in these experiment lie within the range 0.05–0.5 [39]. Thus, we are in a regime where inertial effects may not be negligible. However, it is known from previous work that *C. elegans* swimming in a buffer can indeed be treated as a

low Reynolds number swimmer, which suggests that viscous effects may dominate in our system [28]. Using this reasoning, the peak lateral forces ( $F_L$ ) occur when the worm is moving with the greatest speed in the lateral direction [Fig. 2(b)]. Conversely, the largest propulsive forces ( $F_P$ ) are generated when the worms push the greatest amount of fluid behind themselves [Fig. 2(c)]. Small secondary peaks can be found in the lateral force curve corresponding to turning points in the worm's cycle, in which the lateral motion experiences a small spike, and there is minimal motion in the propulsive direction. The maximum propulsive forces approximately coincide with the points of highest mean worm curvature  $\langle \kappa \rangle$  [Fig. 2(d)].

In the low Reynolds number regime, drag forces are simply linearly proportional to velocities. According to RFT, one can deconstruct the drag force ( $dF$ ) acting on each length segment ( $dl$ ) of a slender body into forces in two orthogonal directions,

$$dF_T = -c_T v_T \mu dl, \quad dF_N = -c_N v_N \mu dl, \quad (1)$$

where  $\mu$  and  $v$  denote the dynamic viscosity and speed respectively,  $c$  is the drag coefficient per unit length, and T and N denote directions tangential and normal to the length segment [15]. Since a slender body has little variation in thickness,  $c_N$  and  $c_T$  can be approximated as constants over the entire length of the swimmer. Although an experimental measurement of these two drag coefficients individually for this microscopic undulator is still needed, the ratio  $c_N/c_T$  has been determined through theory and experiment to be approximately 1.5 for body and swimming parameters characteristic of *C. elegans* [10,16,28]. If  $c_N$  and  $c_T$  are known, using this prescription, and given the speed of each segment of the undulator's body, it is possible to calculate the total drag force the swimmer experiences. Since our experiment is performed in conjunction with high-speed imaging, we can extract the velocities of the worm body. Using numerical integration, we generate the RFT prediction for the lateral and propulsive force curves. Subsequently, using two free parameters, we fit the RFT prediction of the two force curves to our lateral and propulsive data (Fig. 3). In our analysis, we fix  $c_N/c_T$  at 1.5 because our fits are not sensitive enough given the experimental error in the data to accurately determine this ratio. Thus, the first free parameter in our fitting controls the magnitude of the two drag coefficients, and functions as a vertical stretch on the curves. We find these drag coefficients to vary little for worms of all sizes ranging from  $\sim 400$  to  $\sim 1200 \mu\text{m}$  (this agrees with the theoretical prediction of a weak logarithmic dependence on geometry, in which there is no dependence if the swimmer is self-similar for all sizes [10,15,18]), and measure  $c_N = 5.1 \pm 0.3$ , and  $c_T = 3.4 \pm 0.2$ . We have thus made an experimental quantification of the magnitude of the drag coefficients for *C. elegans* swimming in a fluid.

The second fitting parameter allows for a small horizontal time shift in the data. A phase shift is to be expected for several reasons, including damping of the force transducer, inertial effects of the worm, and imaging artifacts such as overexposure in the body's direction of travel. The observed phase shifts were always smaller than  $T/20$ , with  $T$  the period of the motion. Deviations between data and theory may be attributed to various sources of error [39].

Although other studies have generated predictions of the forces and powers involved in undulatory microswimming at

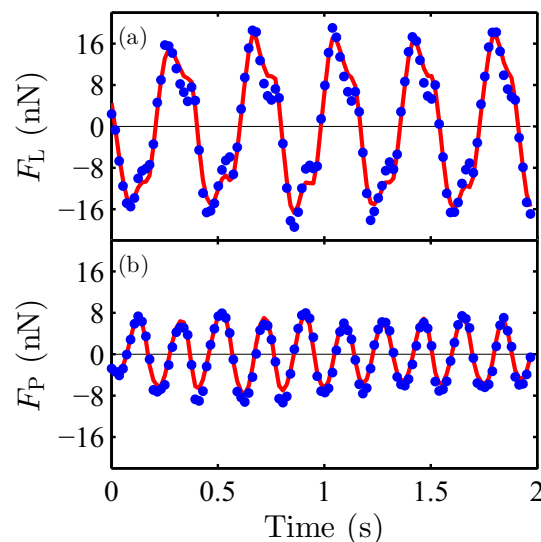


FIG. 3. (Color online) (a) The lateral and (b) propulsive force plotted as a function of time over several periods. The blue circular markers denote the experimental data which contain a systematic error of roughly 10% from uncertainty in the spring constant of the micropipette. The red solid curve represents the prediction from RFT which has been fit to the data. The error in the RFT curve is estimated to be 5%.

larger length scales, they are reliant on theoretical models, including RFT [27,28]. The close agreement between the predictions of RFT and our experimental data demonstrates the applicability of this model in generating quantitative predictions in undulatory systems (Fig. 3). For the purposes of comparing our measured drag coefficients with theoretical predictions by Lighthill [10], we can use  $1.0 \pm 0.2 \text{ mm}$  as an estimated wavelength, and  $45 \pm 5 \mu\text{m}$  as the typical thickness of a young adult. Substituting these parameters into Lighthill's expressions, we get  $c_N = 4.9 \pm 0.4$ , and  $c_T = 3.0 \pm 0.3$ , which fall within the error of our experimental values.

Slender body theory (SBT) is a more general model of microswimming, on which the simpler RFT is based [40]. SBT is expected to generate accurate predictions over a wider range of swimming parameters than RFT. However, since RFT captures our data within experimental error, it follows that it is in also in agreement with SBT [39].

Using simple scaling arguments, one can determine the dependence of the magnitudes of typical propulsive and lateral forces upon the worm size. In our experiments, we find that the drag coefficients are largely independent of the size of the worm. Thus, once the forces in Eq. (1) have been integrated over the worm's body, the forces will scale as  $F \propto v L_{\text{out}}$ , where  $v$  is a typical speed and  $L_{\text{out}}$  is the length of the worm outside of the pipette. The typical speed depends on the product of the amplitude ( $A$ ) of the oscillations and the frequency ( $f$ ) of the swimming. Therefore, the forces will scale as  $F \propto A f L_{\text{out}}$ . We make the approximation that the swimming of the worm is self-similar for all life stages, which implies that  $A$  will scale linearly with  $L_{\text{out}}$ . This assumption is influenced by previous measurements which showed that mechanical properties of the

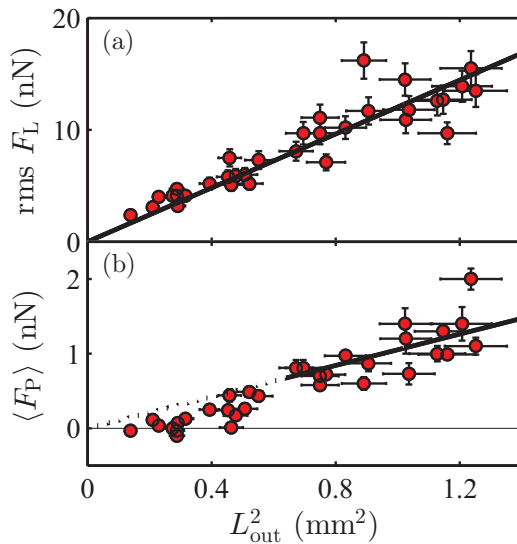


FIG. 4. (Color online) (a) The root-mean-squared lateral force and (b) the mean propulsive force as a function of the square worm length outside of the pipette. The mean and rms are taken over many cycles.

worms can be treated as self-similar [38]. In our experiments, we find that  $f$  does not depend on the worm size. Thus, we see that the typical viscous forces generated should scale as  $F \propto L_{\text{out}}^2$ . A plot of the root-mean-squared (rms) lateral force as a function of  $L_{\text{out}}^2$  yields approximately a straight line passing through the origin, in accordance with the scaling argument [Fig. 4(a)]. Since the worms are attempting to swim forward, one would expect there to be no net force in the lateral

direction over one period. Indeed, for the worms, we measure a mean lateral force of  $0.1 \pm 0.7$  nN. Consistent with the scaling argument we find that the mean propulsive force  $\langle F_P \rangle$  also scales with  $L_{\text{out}}^2$  at large worm lengths [Fig. 4(b)]. However, at small worm lengths ( $\lesssim 800$   $\mu\text{m}$ ), the mean force drops. We attribute this to the fact that small worms undergo motions that are quite different from traveling waves and more “hooklike.” This type of motion does not yield appreciable propulsion. The mean propulsive forces of larger worms we measure here are comparable to other estimates for *C. elegans* [28].

Here we report a direct measurement of the forces experienced by an undulatory microswimmer. Using micropipette deflection, we attain a high-resolution time sequence of drag forces felt by *C. elegans* while swimming in a buffer. By using these force measurements in conjunction with the low Reynolds number model resistive force theory, we demonstrate the success of this simple model in describing the locomotion of slender microswimmers. This direct verification of the theory, which has previously been assumed to apply at this Reynolds number, provides a better understanding of undulatory microswimming at length scales larger than of unicellular organisms. Furthermore, using RFT to describe our data, we extract measured values of drag coefficients for *C. elegans*, a highly studied model organism and microswimmer. These coefficients are in congruence with theoretical values, and will allow future studies to perform direct calculations of the forces generated by free swimmers simply by using high-speed imaging. Finally, simple scaling arguments successfully explain how the magnitude of lateral and propulsive forces scale with the size of the swimmer.

The financial support by Natural Science and Engineering Research Council of Canada is gratefully acknowledged.

- [1] N. Darnton, L. Turner, K. Breuer, and H. Berg, *Biophys. J.* **86**, 1863 (2004).
- [2] D. Weibel, P. Garstecki, D. Ryan, W. Diluzio, M. Mayer, J. Seto, and G. Whitesides, *Proc. Natl. Acad. Sci. USA* **102**, 11963 (2005).
- [3] M. Kim and K. Breuer, *Phys. Fluids* **16**, L78 (2004).
- [4] M. J. Kim and K. S. Breuer, *Anal. Chem.* **79**, 955 (2007).
- [5] Y. W. Kim and R. R. Netz, *Phys. Rev. Lett.* **96**, 158101 (2006).
- [6] M. J. Kim and K. S. Breuer, *Small* **4**, 111 (2008).
- [7] E. Lauga and T. R. Powers, *Rep. Prog. Phys.* **72**, 096601 (2009).
- [8] E. Purcell, *Am. J. Phys.* **45**, 3 (1977).
- [9] M. Silverman and M. Simon, *Nature (London)* **249**, 73 (1974).
- [10] J. Lighthill, *SIAM Rev.* **18**, 161 (1976).
- [11] U. Ruffer and W. Nultsch, *Cell Motil.* **5**, 251 (1985).
- [12] M. Polin, I. Tuval, K. Drescher, J. P. Gollub, and R. E. Goldstein, *Science* **325**, 487 (2009).
- [13] G. Taylor, *Proc. R. Soc. London, Ser. A* **209**, 447 (1951).
- [14] J. Gray, *Q. J. Microsc. Sci.* **94**, 551 (1953).
- [15] J. Gray and G. Hancock, *J. Exp. Biol.* **32**, 802 (1955).
- [16] J. Gray and H. W. Lissmann, *J. Exp. Biol.* **41**, 135 (1964).
- [17] G. Tokic and D. K. P. Yue, *Proc. R. Soc. B* **279**, 3065 (2012).
- [18] R. Cox, *J. Fluid Mech.* **44**, 791 (1970).
- [19] R. S. Berman, O. Kenneth, J. Sznitman, and A. M. Leshansky, *New J. Phys.* **15**, 075022 (2013).
- [20] G. Hancock, *Proc. R. Soc. London, Ser. A* **217**, 96 (1953).
- [21] B. Friedrich, I. Riedel-Kruse, J. Howard, and F. Jülicher, *J. Exp. Biol.* **213**, 1226 (2010).
- [22] K. Drescher, J. Dunkel, L. H. Cisneros, S. Ganguly, and R. E. Goldstein, *Proc. Natl. Acad. Sci. USA* **108**, 10940 (2011).
- [23] N. C. Darnton, L. Turner, S. Rojevsky, and H. C. Berg, *J. Bacteriol.* **189**, 1756 (2007).
- [24] R. P. McCord, J. N. Yukich, and K. K. Bernd, *Cell Motil. Cytoskel.* **61**, 137 (2005).
- [25] S. Chattopadhyay, R. Moldovan, C. Yeung, and X. Wu, *Proc. Natl. Acad. Sci. USA* **103**, 13712 (2006).
- [26] S. Brenner, *Genetics* **77**, 71 (1974).
- [27] C. Fang-Yen, M. Wyart, J. Xie, R. Kawai, T. Kodger, S. Chen, Q. Wen, and A. D. Samuel, *Proc. Natl. Acad. Sci. USA* **107**, 20323 (2010).
- [28] J. Sznitman, X. Shen, R. Sznitman, and P. E. Arratia, *Phys. Fluids* **22**, 121901 (2010).
- [29] X. N. Shen and P. E. Arratia, *Phys. Rev. Lett.* **106**, 208101 (2011).
- [30] X. N. Shen, J. Sznitman, P. Krajačić, T. Lamitina, and P. E. Arratia, *Biophys. J.* **102**, 2772 (2012).

- [31] S. Park, H. Hwang, S.-W. Nam, F. Martinez, R. H. Austin, and W. S. Ryu, *PLoS One* **3**, e2550 (2008).
- [32] T. Majmudar, E. E. Keaveny, J. Zhang, and M. J. Shelley, *J. R. Soc. Interface* **9**, 1809 (2012).
- [33] G. Juarez, K. Lu, J. Sznitman, and P. Arratia, *Europhys. Lett.* **92**, 44002 (2010).
- [34] S. Jung, *Phys. Fluids* **22**, 031903 (2010).
- [35] A. Ghanbari, V. Nock, S. Johari, R. Blaikie, X. Chen, and W. Wang, *J. Micromech. Microeng.* **22**, 095009 (2012).
- [36] J. C. Doll, N. Harjee, N. Klejwa, R. Kwon, S. M. Coulthard, B. Petzold, M. B. Goodman, and B. L. Pruitt, *Lab Chip* **9**, 1449 (2009).
- [37] M.-J. Colbert, A. N. Ragen, C. Fradin, and K. Dalnoki-Veress, *Eur. Phys. J. E* **30**, 117 (2009).
- [38] M. Backholm, W. S. Ryu, and K. Dalnoki-Veress, *Proc. Natl. Acad. Sci. USA* **110**, 4528 (2013).
- [39] See Supplemental Material at <http://link.aps.org/supplemental/10.1103/PhysRevE.89.050701> for experimental details, movies of the worm swimming and the forces produced, a calculation of the Reynolds number, and discussion of sources of error and slender body theory.
- [40] B. Rodenborn, C.-H. Chen, H. L. Swinney, B. Liu, and H. Zhang, *Proc. Natl. Acad. Sci. USA* **110**, E338 (2013).

# Supplemental Information for “Dynamic Force Patterns of an Undulatory Microswimmer”

Rafael D. Schulman,<sup>1</sup> Matilda Backholm,<sup>1</sup> William S. Ryu,<sup>2</sup> and Kari Dalnoki-Veress<sup>1,3,\*</sup>

<sup>1</sup>*Department of Physics and Astronomy and the Brockhouse Institute for Materials Research, McMaster University, 1280 Main St. W, Hamilton, ON, L8S 4M1, Canada*

<sup>2</sup>*Department of Physics, University of Toronto, 60 St. George St., Toronto, ON, M5S 1A7, Canada*

<sup>3</sup>*Laboratoire de Physico-Chimie Théorique, UMR CNRS Gulliver 7083, ESPCI, Paris, France*

## Force measurements and Analysis

The micropipette deflection technique was employed in the same manner as outlined in Refs. [1, 2]. The micropipette has a straight portion which is roughly 3 cm long, and terminates in an L-shaped bend, in which each length is about 300-600  $\mu\text{m}$  (Fig. 1). The pipette has an outer diameter of  $\sim 20 \mu\text{m}$  and inner diameter of  $\sim 10 \mu\text{m}$ . The fabrication and subsequent calibration procedure is described in Ref. [3]. Since the long, straight part is very flexible (compared to the L-shaped bend), it is the only portion that deflects significantly. By observing this L-shape from below, we can measure its displacements in two orthogonal directions.

In this study, we measure forces generated by L3, L4, young adult, and adult worms. In our experiments, worms were picked off the NGM plates and placed inside a transparent cylindrical container containing M9 buffer, which was placed atop an inverted optical microscope. The micropipette would subsequently be inserted into the cylinder from above, with the L-shaped bend being in a horizontal plane close to the bottom boundary where the worms are found. The cylindrical container was deep enough to immerse the entire flexible portion of the micropipette within fluid - this is important because if the fluid interface were in contact with the flexible part of the pipette, then the surface tension could cause deflections that interfere with the desired measurement. Worms were captured by positioning the end of the micropipette near the tail of a worm and subsequently applying suction through a syringe connected to the micropipette. Experiments where the worms were sucked in more than 15% of their length were not used. Worms swim in the same plane as the L-shape before being captured, and thus, remain in this plane after capture. Upon capturing a worm, the pipette was raised several millimeters away from the bottom boundary, such that the worm could be treated as swimming in an infinite fluid medium. We only collected data when the worm was seen to be swimming symmetrically about the propulsive direction. Images were taken with a high-speed camera (Allied Vision Technologies, Model: GT1660) at 56 fps.

The images from our experiments were analyzed in MATLAB. We used a cross correlation image analysis technique to precisely measure displacements of the L-shape of the micropipette in lateral and propulsive direc-

tions. To determine the pipette position corresponding to zero force, we waited for a worm to perform an  $\Omega$ -turn, during which it curls up into a spiral shape. When it is in this configuration, it moves very little, and thus, does not generate appreciable viscous forces. Therefore, this allows us to determine the zero point for our force curves. We also employ image analysis techniques to determine the centerline of the worm’s body, and subsequently, calculate the body curvature, and find the body velocities used to compute the RFT force prediction. The RFT curve (e.g. Fig. 3) is only evaluated at the same points in time as the data. This image analysis script was also used to determine the arclength of the worms.

While the agreement between RFT and the direct force measurements is excellent, small deviations between data and theory may be attributed to several factors. The body velocities are attained from an average of differences in body position over time. Although employing a high frame rate in our experiment provides us with good estimates of the body’s velocities, they are not exact. Furthermore, during swimming, the worm generates a flow around itself. This flow will in turn generate a drag force on the pipette, which contributes to the deviations we see. Note that since the swimmer tries to swim forward, it generates a net flow directed behind itself, and as such, will cause the measured force to be smaller on average. Furthermore, the value  $c_N/c_T=1.5$  has been derived for sinusoidal undulations, and may be subject to minor corrections for the swimming observed.

The mean propulsive force is calculated over many cycles of the RFT curve. The horizontal error bars in Fig. 4 stem from uncertainties in determining the worm’s arclength using an image analysis script. The vertical error bars have contributions from uncertainties in the micropipette spring constant, uncertainties in the calculated RFT curves, and temporal variations of the worms’ mean propulsive force and rms lateral force.

## Worm strains and cultivation

We attained Wild-type worms (N2) from the Caenorhabditis Genetics Center and cultivated these worms according to standard procedures described in Ref. [4] on Escherichia coli OP50 NGM plates at 20 °C.

### Reynolds Number Calculation

We can estimate the Reynolds number (Re) for this system by likening the worm to a rod with the same radius, moving side to side at the typical oscillation speed of the worm. The average oscillation speed is  $4A/T$ , where  $A$  is the typical swimming amplitude (roughly 0.65 mm for a young adult) and  $T$  is the period ( $\sim 0.4$  s for all worms). The relevant length scale is the radius of the rod ( $\sim 20\text{-}25\ \mu\text{m}$  for a young adult). Substituting these values, along with the density and viscosity of water (assumed to be roughly equal to that of the buffer), into the expression for the Reynolds number yields a value of approximately 0.15. One may also choose the diameter of the worm as the relevant length scale, which would imply  $\text{Re} = 0.3$ . In addition, repeating the calculation for all size worms in our study, and using either the radius or diameter of the worm as the length scale, yields a range of Reynolds numbers of  $\text{Re} \sim 0.05\text{-}0.5$ . Therefore, the relevant Reynolds numbers for the worms in our experiment lie in the range 0.05-0.5.

### RFT vs. SBT

For helical swimming, there is experimental evidence for full quantitative agreement between SBT and mea-

sured data for a broad range of swimming parameters [5]. For the study of the helical swimmer, RFT fails in the regime  $L > 3\lambda$ , where  $L$  and  $\lambda$  are the length and wavelength of the helix as measured along its axis, due to hydrodynamic interactions between body segments becoming important. Although undulatory swimming is qualitatively different, in our system, we have  $L \sim \lambda$ , which yields small enough hydrodynamic interactions for RFT to be successful in predicting the viscous forces, as it is in our study.

---

\* dalnoki@mcmaster.ca

- [1] M.-J. Colbert, A. N. Ragen, C. Fradin, and K. Dalnoki-Veress, *Eur. Phys. J.* **30**, 117 (2009).
- [2] M. Backholm, W. S. Ryu, and K. Dalnoki-Veress, *Proc. Natl. Acad. Sci. USA.* **110**, 4528 (2013).
- [3] M.-J. Colbert, F. Brochard-Wyart, C. Fradin, and K. Dalnoki-Veress, *Biophys. J.* **99**, 3555 (2010).
- [4] S. Brenner, *Genetics* **77**, 71 (1974).
- [5] B. Rodenborn, C.-H. Chen, H. L. Swinney, B. Liu, and H. Zhang, *Proc. Natl. Acad. Sci. USA.* **110**, E338 (2013).

## A.4 Paper IV

*Undulatory microswimming near solid boundaries*

R. D. Schulman, M. Backholm, W. S. Ryu, and K. Dalnoki-Veress, *Physics of Fluids* **26**, 101902 (2014).

## Undulatory microswimming near solid boundaries

R. D. Schulman,<sup>1</sup> M. Backholm,<sup>1</sup> W. S. Ryu,<sup>2</sup> and K. Dalnoki-Veress<sup>1,3,a)</sup>

<sup>1</sup>*Department of Physics and Astronomy and the Brockhouse Institute for Materials Research, McMaster University, Hamilton, Ontario L8S 4M1, Canada*

<sup>2</sup>*Department of Physics and the Donnelly Centre, University of Toronto, Toronto, Ontario M5S 1A7, Canada*

<sup>3</sup>*Laboratoire de Physico-Chimie Théorique, UMR CNRS Gulliver 7083, ESPCI, Paris, France*

(Received 23 June 2014; accepted 26 September 2014; published online 16 October 2014)

The hydrodynamic forces involved in the undulatory microswimming of the model organism *C. elegans* are studied in proximity to solid boundaries. Using a micropipette deflection technique, we attain direct and time-resolved force measurements of the viscous forces acting on the worm near a single planar boundary as well as confined between two planar boundaries. We observe a monotonic increase in the lateral and propulsive forces with increasing proximity to the solid interface. We determine normal and tangential drag coefficients for the worm, and find these to increase with confinement. The measured drag coefficients are compared to existing theoretical models. The ratio of normal to tangential drag coefficients is found to assume a constant value of  $1.5 \pm 0.1(5)$  at all distances from a single boundary, but increases significantly as the worm is confined between two boundaries. In response to the increased drag due to confinement, we observe a gait modulation of the nematode, which is primarily characterized by a decrease in the swimming amplitude.

© 2014 AIP Publishing LLC. [<http://dx.doi.org/10.1063/1.4897651>]

### I. INTRODUCTION

Locomotion through a fluid environment at small length scales, or “microswimming,” is interesting because the relevant physics differs considerably from that applicable to macroscopic swimmers. Microorganisms dwell in a regime where viscous forces dominate and swimmers have negligible inertia.<sup>1</sup> That is, the Reynolds number (Re), which is a measure quantifying the ratio of inertial to viscous forces in a fluid, is typically much smaller than unity for microscopic swimmers. The activity within this field has increased substantially in recent years. This growth is, in part, due to rapidly improving experimental techniques capable of performing measurements of motile microorganisms, as well as more developed analytical and computational treatments of these systems. Beyond studies which have succeeded in providing precise kinematic observations of small swimmers, in the last decade, there have been direct force measurements of unicellular organisms using optical traps.<sup>2,3</sup> This large drive towards developing a better understanding of low Re locomotion is warranted, as it offers exciting application and research avenues, such as fluid pumping,<sup>4–6</sup> collective motion of bacteria to generate mixing in microfluidic devices,<sup>7,8</sup> and microscopic artificial swimmers capable of transporting loads for biomedical purposes such as advanced drug targeting and robotic surgery.<sup>9,10</sup> Furthermore, enhancing our ability to describe the relevant physics is a crucial step towards developing a more complete picture of the behaviours, capabilities, and interactions of bacteria, sperm, and other microorganisms.

There are numerous biologically relevant systems in which microorganisms move near a boundary, such as in surface-associated bacterial infections,<sup>11,12</sup> sperm locomotion in the female reproductive tract,<sup>13</sup> and biofilm formation.<sup>14,15</sup> To attain a complete picture of these systems, it is imperative to understand how the physics of a microswimmer differs upon proximity to an interface. However,

<sup>a)</sup>Electronic mail: [dalnoki@mcmaster.ca](mailto:dalnoki@mcmaster.ca)

microswimmers are typically studied while swimming in an effectively infinite fluid and few studies have investigated the effects of a nearby interface. In particular, due to the nearby no-slip boundary condition at a fluid-solid interface, there will be an increase in the shear of the velocity field near such a boundary. This increase in shear will cause an increase in viscous forces, which will influence the motility of organisms. Experiments have verified changes in both propulsion and trajectories of swimmers near solid boundaries at low  $Re$ .<sup>6,16–18</sup>

A unique aspect of low  $Re$  locomotion is that, according to the Scallop Theorem, to achieve propulsion it is necessary to undergo a sequence of motions that is not time-reversible.<sup>1</sup> Microorganisms have developed various swimming mechanisms that satisfy this constraint, such as motions akin to a human breast stroke, as characterized by the alga cell *Chlamydomonas reinhardtii*,<sup>19,20</sup> or the helical rotation of a bacterium's flagellum.<sup>1,21,22</sup> Undulatory locomotion, in which a swimmer propagates travelling waves down the length of its body, is another non-time-reversible mechanism, and is often employed by nematodes and sperm.<sup>23–26</sup>

Undulatory locomotion has proved to be a highly efficient means of propulsion which is present over length scales ranging from micrometers to tens of meters.<sup>27</sup> The locomotion of slender undulatory swimmers has been investigated by a multitude of theoretical studies.<sup>22,25,26,28,29</sup> A common approach is to derive resistance coefficients for the swimmer, such that given the velocity of the segments of the swimmer's body, it is possible to compute the force. Such a framework is called resistive force theory (RFT). In this model, one can decompose the force acting on each body segment into a component tangential and normal to the body, each of which is proportional to the speed of the segment along the corresponding direction, and related by the normal and tangential drag coefficients,  $c_N$  and  $c_T$ . In particular, the ratio  $K = c_N/c_T$  is a quantity of interest, as it determines the magnitude and direction of propulsion of the swimmer. These drag coefficients have been derived for a slender undulator in an unbounded fluid<sup>22,25</sup> and for slender cylinders near boundaries.<sup>30,31</sup> In particular, the results of Katz *et al.* predict  $K = 2$  for a cylinder moving parallel to a nearby fluid-solid interface, and also predict  $K$  to increase past a value of 2 when the cylinder is confined between parallel solid plates.<sup>30</sup> Recently, the drag coefficients of an undulatory microswimmer in an infinite fluid were found using direct force measurements, and compared well with the theoretical result.<sup>32</sup> However, there have been no direct force or drag coefficient measurements for undulatory swimmers in proximity to a solid boundary, which is the focus of this study.

Experiments focusing on undulatory locomotion often employ the model organism *Caenorhabditis elegans*,<sup>33</sup> a millimeter sized nematode, as its subject. The viscoelastic material properties of this worm have been determined,<sup>34</sup> as well as its kinematic properties in a wide variety of media.<sup>35–43</sup> In addition, there has been much interest in the gait modulation of *C. elegans* from swimming to crawling, which involves a decrease in frequency and wavelength of undulatory motion.<sup>35–37</sup> The gait modulation is known to occur in response to changing environmental resistance, which has been realized in experiments by changing viscosity,<sup>35,36</sup> and by pressing the worm down onto an agar surface with a glass plate.<sup>44</sup> Direct force measurements have been attained for *C. elegans* crawling on agar<sup>45,46</sup> and recently for *C. elegans* swimming in a buffer.<sup>32</sup> Although there have been some studies which have involved confining the worm,<sup>44,47</sup> no experiments have measured swimming forces in proximity to an interface, nor have the kinematics been studied for confinement of the worm near solid boundaries. Despite this, many studies of free swimming *C. elegans* employ experimental designs in which the worm swims near a solid boundary, even though the effects of the boundary, in terms of changing drag coefficients and modulations in kinematics of the worm, are not properly understood. Studying the behaviour and forces experienced by *C. elegans* in confinement provides insight into the impact of the physical constraints that nematodes face in their true habitats (e.g., soils and other materials with small interstitial spaces).

In this paper, we perform direct force measurements using micropipette deflection<sup>32,34,48,49</sup> on the undulatory microswimmer and model organism *C. elegans* at controlled distances from a single solid boundary and between two solid boundaries. The structure of the paper is as follows. In Sec. II, we describe the experimental methods, including details of micropipette deflection and image analysis. In Sec. III A, we present measurements of forces and drag coefficients of the worm at varying distances from a single planar solid boundary, and compare these to existing theoretical models. In Sec. III B, we determine drag coefficients for the worm swimming midway between two

planar solid boundaries with different spacings, and compare the measurements to theory. We discuss and present evidence of a gait modulation of the worm in response to increasing drag coefficients in confinement in Sec. III C. Finally, we provide a summary and conclusions in Sec. IV. We find that for increasing confinement, the drag coefficients and viscous forces generated by *C. elegans* increase monotonically. The drag coefficients are compared to theoretical models and exhibit partial agreement. We determine the drag coefficient ratio  $K$ , and find that it is constant at all distances from the single boundary, but find it to increase as the worm is confined between two boundaries. In addition, as the drag coefficients increase, the worm is seen to exhibit a gait modulation.

## II. EXPERIMENTAL METHODS

### A. Micropipette deflection

As in previous work, we employ a micropipette deflection technique to measure time-resolved forces in dynamic, microscale systems.<sup>32,34,48,49</sup> In this experimental technique, a flexible glass micropipette that is more than three orders of magnitude thinner than it is long, deflects when subjected to an external force. The pipette can be calibrated by ejecting a small droplet through the pipette which then hangs off the pipette tip. By imaging the droplet, and calculating its volume, the mass of the droplet can be found. Observing the deflection of the pipette in response to the droplet's weight allows the spring constant to be determined. Once the spring constant is known, a pipette can be used as a force transducer, for which the deflections away from the equilibrium position indicate the applied force. For instance, the pipette can be pushed against a soft material to measure its properties.<sup>34,49</sup> Since the pipette is hollow, suction can be applied to catch objects at the end of the pipette. Using this set up, one can perform friction and adhesion measurements,<sup>48</sup> or measure the forces generated by an active object.<sup>32</sup>

In this study, two types of pipettes are employed. In the first part of the study, a straight pipette with an L-shaped bend at its end is used (Fig. 1(a)). The L-shaped bend, in which each length is about 300–600  $\mu\text{m}$ , is highly rigid compared to the long straight portion of the pipette, which is roughly 3 cm long. For this reason, only the long straight portion exhibits appreciable deflection. Therefore, this micropipette is capable of deflecting in two perpendicular directions: along the worm's swimming axis, as well as along the corresponding in-plane perpendicular direction (Fig. 1(b)). Thus, using this pipette, we can measure both the propulsive and lateral hydrodynamic forces generated by the worm, by simply observing the L-shaped bend from below (the same approach has previously been employed<sup>32</sup>). In the second part of the study, a completely straight pipette which is roughly 3 cm long is used (Fig. 1(c)). Such a pipette can only deflect side-to-side, and can thus only measure

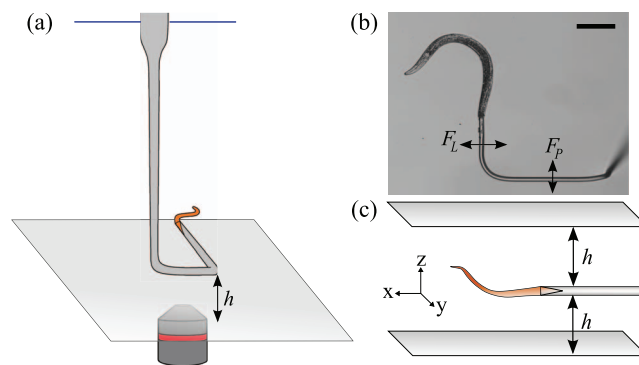


FIG. 1. (a) Experimental set up for the single boundary experiments. A straight pipette with an L-shaped bend at its end is used to measure forces of the worm swimming at a distance  $h$  from the boundary. The blue horizontal line represents the location of the buffer meniscus. (b) An image taken of a young adult worm swimming as it is being held with the L-shaped bend of a pipette. By observing the L-shaped bend move, we can measure both lateral ( $F_L$ ) and propulsive ( $F_P$ ) forces. The scalebar represents 200  $\mu\text{m}$ . (c) Experimental set up for the channel confinement experiments. A straight pipette is used to measure lateral forces of the worm swimming in the  $x$ - $y$  plane at a distance  $h$  from each boundary.

the lateral forces generated by the worm. All pipettes in this study have an outer diameter of  $\sim 20 \mu\text{m}$  and an inner diameter of  $\sim 10 \mu\text{m}$ . The spring constants of all pipettes are within the range of 2.7–8.9 nN/ $\mu\text{m}$ , with no more than 10% uncertainty in each spring constant. The deflections of the pipettes in these experiments are much smaller than length scales associated with swimming of the worms. Thus, pipettes can be treated as linear springs, and drag forces acting on the pipette are small compared to the forces driving it.

## B. Experimental design

In this study, force measurements are performed on worms in the so called L4, young adult, and adult life stages. For the purpose of our study, these are different sized worms that behave in the same way when captured. Wild-type worms (N2) were obtained from the Caenorhabditis Genetics Center and cultivated according to standard procedures.<sup>33</sup> The worms are picked off NGM plates and placed inside a chamber filled with M9 for the force measurements (see Fig. 1). Worms are captured by positioning the end of the micropipette in proximity to the worm's tail and applying suction through a syringe connected to the micropipette. Worms are never sucked in by more than 15% of their total length. Upon capture, the  $z$ -position of the pipette is adjusted and monitored using a digital actuator. The nematodes perform a highly reproducible undulatory motion when being held by the micropipettes. Since the worm is being constrained in its motions, we expect the propulsive forces generated by a tethered worm to be smaller than a freely swimming worm. Worms are seen to swim in the plane of focus (parallel to the plane of the boundaries) during the majority of the experiments, as they are captured while swimming parallel to this plane. In each type of experiment, the system is observed from below with a microscope. Images of the swimming are taken with a high-speed camera (Allied Vision Technologies, Model: GT1660) at 56 fps. Data in which there are out of plane swimming results in the worm's body being out of focus during a portion of the swimming cycle – such data are discarded.

Worms are studied in two types of confinement: near a single planar boundary and inside a channel. For the single planar boundary experiment, a transparent cylindrical container is used.<sup>32</sup> In this case, the micropipette with the L-shaped bend is inserted into the chamber from above such that the thin flexible portion is fully immersed in the fluid, as seen in Fig. 1(a), where the horizontal line indicates the location of the buffer meniscus. By letting the thick stiff portion of the pipette pass through the meniscus, we prevent capillary forces at the contact line from disturbing the force measurements. The L-shaped bend is in a plane parallel to the bottom boundary. For the measurements, the worm is positioned to be at a desirable  $h$  away from the bottom boundary. The distance  $h$  is measured by moving the pipette until it is in contact with the bottom surface, and subsequently raising the pipette while keeping track of the relative change in height using the digital actuator.

For the channel confinement experiment, the channel is composed of two parallel glass slides spaced and held together by a chosen number of layers of melted Parafilm to achieve a desired channel height,  $2h$  (Fig. 1(c)). The channel heights range from 58  $\mu\text{m}$  to 1700  $\mu\text{m}$ . This channel is mounted within a larger chamber filled with buffer in which the worms are placed, composed of two horizontal glass slides separated by rubber spacers. The buffer remains in the chamber due to surface tension. In these experiments, the straight pipette is inserted into the larger chamber from the side. For the measurements, the worm is captured from the larger chamber and positioned such that it is equidistant from the top and bottom plates of the internal channel, at a distance  $h$  from either plate. The flexible portion of the pipette is mainly in the larger chamber, and only a small portion at the end (containing the worm) is placed within the channel in order to reduce the drag force on the pipette. Again, we ensure that the meniscus of the buffer is only in contact with the thicker portion of the pipette. The height of the channel  $2h$  and the corresponding midpoint position are determined using the same technique as for the single boundary.

## C. Image analysis

The deflections of the micropipettes are analyzed using a cross-correlation technique, which, given the magnification of the microscope used in the experiment, is able to resolve deflections to

a precision of  $\sim 0.1 \mu\text{m}$ . This translates into a sub nN precision in our force measurements for the range of pipette spring constants used.

The nematode's motion during swimming is analyzed as follows. First, each snapshot of the swimming is thresholded into a binary image. Subsequently, each binary image is processed to attain a centerline of the worm's body. The raw data of each centerline are smoothed using a spline curve. From the resultant smoothed centerline, which is composed of 1000 equally spaced points, it is possible to compute quantities such as body curvatures and the amplitude of the swimming. The velocity of a body point in a given frame (used for the RFT computations) is calculated by measuring the difference in position of the point in the previous frame to that in the next frame. This procedure leads to a  $\sim 5\%$  error in computing the velocities. All above analysis was done using inhouse code written in MATLAB. The worm's radius is measured near its vulva using ImageJ.

### III. RESULTS AND DISCUSSION

#### A. Single planar boundary

##### 1. Force measurements

At any distance from the boundary, lateral and propulsive force curves over a swimming cycle of the worm were obtained. The force curves were reproducible over time as well as from worm to worm. Examples of force curves for a single period of swimming at a distance close and far from the boundary are shown in Figs. 2(a) and 2(b). The Reynold's number of this system is in the range

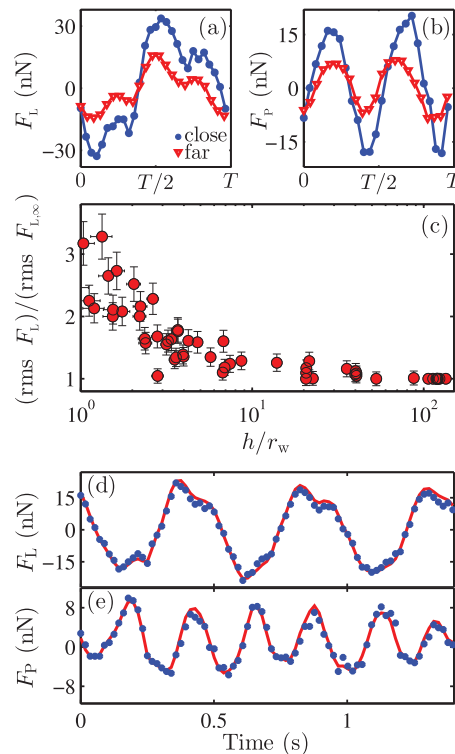


FIG. 2. The (a) lateral ( $F_L$ ) and (b) propulsive ( $F_P$ ) forces over one period of a young adult worm's swimming, close ( $h = 35 \pm 4 \mu\text{m}$ ) and far ( $h = 2524 \pm 4 \mu\text{m}$ ) from a single boundary. (c) The rms lateral force normalized to its value at infinity ( $h/r_w > 100$ ) as a function of the distance to the boundary ( $h$ ) normalized by the worm radius ( $r_w$ ), for young adult worms. The vertical error bars come from uncertainties in the spring constant of the pipette and temporal variations of the forces. The horizontal error bars stem from uncertainties in determining the distance from the boundary and measuring the worm's radius. The vertical error bars increase for larger forces, since the percentage error for all data points is similar. (d) Lateral and (e) propulsive forces (blue circle markers) for a young adult worm swimming near a single boundary ( $h/r_w \sim 2.8$ ) plotted as a function of time over several periods. The solid red curves correspond to simultaneous RFT fits to the lateral and propulsive force data. In this case,  $c_N = 7.8 \pm 1.2$  and  $c_T = 5.1 \pm 0.8$ .

of 0.05–0.5,<sup>32</sup> and previous studies have demonstrated that the physics describing the locomotion of *C. elegans* is compatible with that of a low Re swimmer.<sup>32,36</sup> For such low Re swimmers, the forces we measure are dominated by viscous forces.<sup>32</sup> As such, a maximum in the lateral force, for instance, roughly corresponds to the point in the worm's swimming cycle in which it moves with maximal velocity in the negative lateral direction (defined to be right in our experiments). Using the same logic, when the worm has a maximal velocity component in the negative propulsive direction, we measure a maximum force in the forwards swimming direction.

At close distances to the planar boundary, we observe significant increases in the forces generated by the worms. As seen in Figs. 2(a) and 2(b), the lateral and propulsive force curves are plotted as a function of time over one swimming period. Near the boundary, the force curves appear vertically stretched in comparison to the corresponding force curves of the same worm far from the boundary. At large distances from the planar boundary (roughly  $h \sim 3000 \mu\text{m}$ , or  $h/r_w > 100$ , where  $r_w$  is the radius of the worm), we observe the swimming of the worms to be similar in form and frequency as in previous work in an unbounded fluid.<sup>32</sup> Furthermore, at large distances, the magnitudes of the forces we measure compare well with past work. In Fig. 2(c), the normalized root-mean-square (rms) lateral force is plotted as a function of  $h/r_w$ . The rms lateral force increases continuously as the worms are brought closer to the boundary. The rms lateral force increases most significantly below  $h/r_w \sim 10$ , and at very close approaches to the boundary it can be more than 3 times larger than in an unbounded fluid. For the mean propulsive force, we measure  $\langle F_P \rangle = 3 \pm 1 \text{ nN}$  at  $h/r_w = 1.8 \pm 0.3$  for worms with  $L_{\text{out}} = 880 \pm 60 \mu\text{m}$ , where  $L_{\text{out}}$  is the length of the worm found outside of the pipette. In comparison, for worms of similar size in an unbounded fluid,  $\langle F_P \rangle = 0.8 \pm 0.2 \text{ nN}$ .<sup>32</sup> Thus, in our experiments, the worms attain significantly larger mean propulsive forces when they swim near the boundary. Near the boundary, viscous drag forces are larger due to the nearby no-slip interface. Since the propulsion of microswimmers is derived from viscous forces, the propulsive forces are expected to increase near the solid boundary because of the increasing velocity gradient.

## 2. Drag coefficients

For a swimmer moving through a fluid, the velocity of each infinitesimal segment of the swimmer's body can be decomposed into two perpendicular directions, a component tangential ( $v_T$ ) and normal ( $v_N$ ) to the body. In RFT, these velocities generate infinitesimal drag forces ( $dF$ ) on the corresponding body segment ( $dl$ ), which are given by

$$dF_T = -c_T v_T \mu dl \quad \text{and} \quad dF_N = -c_N v_N \mu dl, \quad (1)$$

where  $\mu$  is the dynamic viscosity,  $c$  represents the drag coefficient per unit length, and T and N denote directions tangential and normal to the body segment.<sup>25</sup> The ratio  $c_N/c_T$  has been estimated through theoretical as well as experimental studies to be approximately 1.5 for *C. elegans* in an infinite fluid medium.<sup>22,26,36</sup> We previously measured these drag coefficients for *C. elegans* in an unbounded fluid to be  $c_N = 5.1 \pm 0.3$  and  $c_T = 3.4 \pm 0.2$ , where the ratio of the drag coefficients,  $K$ , was fixed to be 1.5.<sup>32</sup> However, these coefficients have not been experimentally determined in the proximity to a boundary.

If  $c_N$  and  $c_T$  as well as the speed of each segment of the worm's body are known, one may integrate Eq. (1) to find the total viscous force acting on the undulator. From image analysis of our high speed image sequences attained during experiments, we can extract kinematic data, including body segment speeds, for the worm's swimming. Since  $c_N$  and  $c_T$  are not known in the presence of a solid boundary, we can treat these as free parameters in calculating RFT's prediction of the lateral and propulsive forces, as each of these forces has contributions from both tangential and normal forces acting on the worm. Using this procedure, we can fit the RFT force curves to the experimental force curves, and as such, extract best fit values for  $c_N$  and  $c_T$ . A third free parameter is employed in our fits which allows for a relative phase shift between the theoretical and experimental force curves. This horizontal time shift may be present for several reasons, including viscous damping of the micropipette, inertial effects of the worm, and various imaging artifacts. These phase shifts are always smaller than  $T/20$ , where  $T$  is the period of the worm's motion. Examples of RFT fits to

lateral and propulsive force data for a young adult worm swimming near a boundary are shown in Figs. 2(d) and 2(e), where the data are plotted alongside the RFT prediction. As seen in these figures, the RFT fit describes the data within experimental error. In addition, as seen in Figs. 2(d) and 2(e), the experimental force curves are reproducible over time.

The fits are performed at several values of  $h/r_w$  for L4, young adult, and adult worms. The swimming of these worms is observed to be approximately self-similar, meaning that the swimming motions and waveforms all scale with the size of the worm. The self-similarity allows these different sized worms to be compared. The resultant values of  $c_N$  and  $c_T$  are plotted as a function of  $h/r_w$  in Figs. 3(a) and 3(b). As demonstrated in these plots, the data collapse for a large range of values of  $h/r_w$ , since both  $h$  and  $r_w$  ( $\sim 14 \mu\text{m}$  to  $\sim 35 \mu\text{m}$ ) are varied, this suggests that this ratio is an important controlling parameter.

Katz *et al.* incorporated the effects of a nearby solid planar boundary into the calculation of the drag coefficients for a straight cylinder.<sup>30</sup> Their values of  $c_N$  and  $c_T$ , which contain no free parameters, are plotted along with the data in Figs. 3(a) and 3(b), represented by the solid curves. In their analysis, the resultant resistance coefficients are derived in the regime  $r_0 \ll h \ll l/2$ , where  $r_0$  and  $l$  are the radius and length of the cylinder, respectively. For a young adult worm in our experiments,  $r_w \sim 24 \mu\text{m}$  and  $L_{\text{out}}/2 \sim 450 \mu\text{m}$ . The point at which  $h/r_w \sim (L_{\text{out}}/2)/r_w$  (i.e.,  $h \sim L_{\text{out}}/2$ ) is indicated by a vertical arrow on the  $x$ -axis of Fig. 3(b). Evidently, there is no value of  $h$  which is much larger than the worm radius, and simultaneously much smaller than half the worm length. Thus, *C. elegans* falls outside of the ideal regime for which the derivation by Katz *et al.* is applicable.

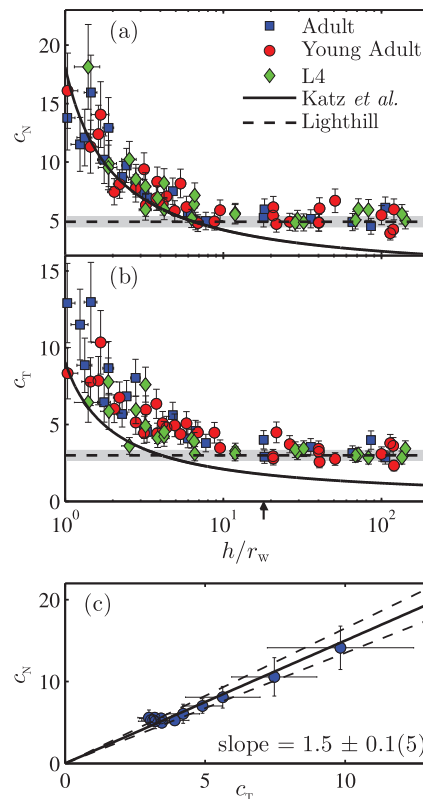


FIG. 3. (a)  $c_N$  and (b)  $c_T$  plotted against the normalized distance from the boundary for adult, young adult, and L4 worms. The vertical error bars come from uncertainty in the spring constant of the pipette and the fitting procedure. The solid and dashed curves correspond to the predictions of Katz *et al.* and Lighthill.<sup>22,30</sup> The grey area denotes the uncertainty range in evaluating Lighthill's drag coefficients. The vertical arrow on the  $x$ -axis of (b) represents the point at which  $h \sim L_{\text{out}}/2$ . (c) Binned values of  $c_N$  and  $c_T$  from (a) and (b), respectively, demonstrating that a linear fit (solid line) with a slope of  $1.5 \pm 0.1(5)$  describes the data within error. The dashed lines correspond to lines given by the upper and lower bounds of the slope. The error bars of the data points come from the scatter in the binning of (a) and (b).

However, there are no studies which incorporate boundary effects into a calculation for the drag coefficients of an undulating cylinder. Thus, although limited in its applicability to our system, the study of Katz *et al.* provides the most relevant comparison near a boundary. Despite this, as seen in Fig. 3(a), their predictions describe the  $c_N$  data well for  $h/r_w \lesssim 4$ . On the other hand, one can see in Fig. 3(b) that there is a consistent underestimate of  $c_T$  compared to our measurements for all  $h/r_w$ . In the limit  $h \gg r_w$ , the worm can be well approximated as swimming in an unbounded fluid, where the theoretical predictions of drag coefficients for an undulatory swimmer become applicable.<sup>22,25</sup> In this regime, the wavelength of the swimming is a more relevant length scale than the distance from the boundary, and the prediction of Katz *et al.*, which does not take into account the effects of undulations, is expected to fail. Since Lighthill's resistance coefficients have been shown to exhibit excellent agreement with experimental values in an unbounded fluid,<sup>22,32</sup> we expect the data for  $c_N$  and  $c_T$  to match this theoretical prediction in the  $h \gg r_w$  regime. Indeed, as seen in Figs. 3(a) and 3(b), Lighthill's resistance coefficients, given by  $c_N = 4.9 \pm 0.4$ , and  $c_T = 3.0 \pm 0.3$ ,<sup>22</sup> represented by dashed lines, agree with the data for  $h/r_w \gtrsim 10$ . In generating this prediction, we have used parameters characteristic of young adult worms:  $1.0 \pm 0.2$  mm as an estimated wavelength, and  $r_w = 45 \pm 5$   $\mu$ m, but since the swimming can be approximated as self-similar,<sup>32</sup> the theoretical drag coefficients for adults and L4's are within error of the values above.

In Fig. 3(c), binned averaged values of  $c_N$  are plotted as a function of binned averaged values of  $c_T$ . The binning is performed evenly as a function of  $\log_{10}(h/r_w)$  with bin sizes of 0.15, large enough to have sufficient data in each bin. An average value within each bin is subsequently computed. We fit these data to a line constrained to pass through the origin, and obtain a slope of  $K = 1.5 \pm 0.1(5)$ . Thus, the ratio  $K = c_N/c_T$  assumes a constant, distance-independent value of  $1.5 \pm 0.1(5)$  for undulatory swimming in a plane parallel to a solid planar boundary. In the straight cylinder calculation of Katz *et al.*, a constant value of  $K = 2$  is derived. Lighthill's calculation yields  $K = 1.6 \pm 0.2$ , which is in agreement with our experimental value for all  $h/r_w$ . Interestingly, theoretical and experimental estimates which have suggested that  $K \sim 1.5$  have been carried out for an infinite fluid medium,<sup>22,26,36</sup> yet our results imply that this ratio remains valid in the proximity of a solid planar boundary.

As a consistency check, it is worthwhile comparing to see that the increase in the magnitude of the forces we measure close to a boundary, scale with the increase in drag coefficients. Nearby the boundary ( $h/r_w = 1.8 \pm 0.3$ ), where we found  $\langle F_p \rangle = 3 \pm 1$  nN,  $c_N$  and  $c_T$  are both roughly 2.5 times larger than in an unbounded fluid, where  $\langle F_p \rangle = 0.8 \pm 0.2$  nN.<sup>32</sup> The mean propulsive force and rms lateral forces should scale linearly with the magnitude of the drag coefficients. Thus, we would expect  $\langle F_p \rangle$  near the boundary to be roughly 2.5 times larger than in an unbounded fluid, or  $\langle F_p \rangle \sim 2$  nN, which agrees with the measured value within experimental error. Furthermore, the rms lateral force near the boundary is found to be  $2.3 \pm 0.2$  times larger than in an unbounded fluid. This increase is roughly consistent with the 2.5 times increase in the drag coefficients.

## B. Channel confinement

For the studies of a worm confined between two solid boundaries (Fig. 1(c)), the confining geometry restricted us to a straight pipette and only lateral forces could be measured. Thus, our resistive force theory curves are, in this case, only fit to lateral force data.<sup>50</sup> In the same way as before, we can extract the values of  $c_N$  and  $c_T$  from our free fits. The results are shown as a function of  $h/r_w$  in Figs. 4(a) and 4(b) for adult, young adult, and L4 worms. For the smallest channel, the drag coefficients are more than an order of magnitude larger compared to in an unbounded fluid. Thus, we see that the effect of a second solid boundary is not simply additive in terms of the increase in the drag coefficients experienced by the worm. Instead, the second boundary imposes a significant restriction on the fluid flow surrounding the worm's body compared to in the single boundary case, causing this large increase in viscous drag.

In their study, Katz *et al.* also investigate the case of parallel plate confinement of a straight cylinder moving in the central plane of the channel.<sup>30</sup> Once again, the derivation is carried out for a straight cylinder in the  $r_0 \ll h \ll l/2$  limit, and is thus limited in its applicability to our

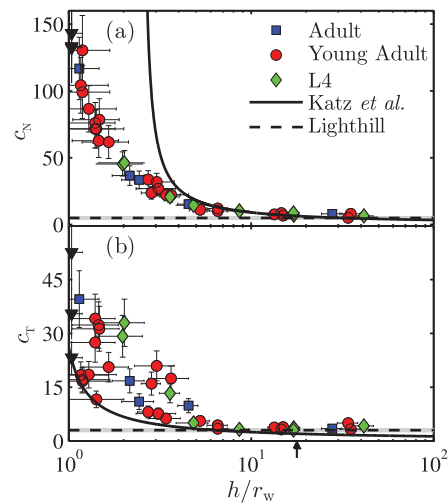


FIG. 4. (a)  $c_N$  and (b)  $c_T$  as a function of the normalized distance to each boundary in channel confinement for adult, young adult, and L4 worms. The predictions of Katz *et al.* and Lighthill are plotted as solid and dashed curves. The vertical arrow on the x-axis of (b) represents the point at which  $h \sim L_{\text{out}}/2$ . The black triangle markers correspond to three measurements on the same worm at three separate  $y$ -positions (Fig. 1(c)). This translation affects  $c_T$  more significantly than  $c_N$ .

system. Nevertheless, for comparison, this theoretical prediction for the drag coefficients, as well as Lighthill's results, are plotted alongside the data in Figs. 4(a) and 4(b). Here we see that the predictions of Katz *et al.* are in agreement with data near the intersection with Lighthill's drag coefficients. For larger  $h/r_w$ , Lighthill's results capture our data within error. For smaller  $h/r_w$ , the results of Katz *et al.* overestimate  $c_N$  and underestimate  $c_T$ . The failure is not a failure of the theory, rather it is to be expected since *C. elegans* falls outside of the regime in which the derivation of Katz *et al.* is carried out. Despite this, as mentioned previously, the study of Katz *et al.* provides the most relevant theoretical comparison of drag coefficients near a boundary.

The data of  $c_T$  contain more scatter than the data for  $c_N$ . We believe that this can in part be attributed to  $c_T$  being more influenced by changes in geometry of the experiment. The thin chambers that we use may not be perfectly parallel ( $\pm 0.5^\circ$ ) and the swimming plane of the worm may also be subject to a tilt ( $\pm 2^\circ$ ), such that the swimming of the worm is not exactly in plane with the chamber walls. Furthermore, there is an inherent error in determining the midpoint of the chamber ( $\pm 2 \mu\text{m}$ ). These sources of scatter would be more significant for experiments with higher confinement. To demonstrate the possibility of scatter due to uncertainties in geometry, we performed an experiment in which we placed the worm at the center of a very thin chamber, and measured the drag coefficients at three separate  $y$ -positions (Fig. 1(c)), each a few hundred micrometers apart. These three measurements are represented by the black triangle markers in Fig. 4. As seen in the figure, this procedure resulted in significant scatter in the value of  $c_T$ , yet relatively little scatter in the value of  $c_N$ , where two of the data points are so close that they are indistinguishable in the plot. Another source of scatter may stem from the RFT fitting. Since the final contribution of tangential body motion to the lateral force is smaller than the contribution from normal body motion, our fits will be more sensitive to determining  $c_N$  precisely.

Interestingly, the predictions of Katz *et al.* involve a monotonically increasing value of  $K$  upon increasing the confinement within the channel, in contrast with the case of the single boundary. In our experiments, we find that for very large channels (at  $h/r_w = 35 \pm 6$ ),  $K = 1.8 \pm 0.7$ , which is in agreement with the results for an essentially unbounded fluid (i.e., far from the single plane boundary). On the other hand, for very narrow channels (at  $h/r_w = 1.3 \pm 0.1$ ), we find  $K = 5 \pm 2$ . Thus, when confined between two plates there is an increase in  $K$  for highly confined worms, whereas we obtain a constant value of  $K$  for an undulatory swimmer near a single plane boundary.

### C. Gait modulation

For very wide channels, or at large distances from a single boundary, the same swimming is seen as for an unbounded fluid.<sup>32</sup> However, as the worm is placed into channels of high confinement, there is a significant difference in the swimming of the worm (see movies in the supplementary material (Multimedia view)<sup>50</sup>). Most noticeably, the amplitude of the motion is greatly reduced compared to that seen in an unbounded fluid. Time-lapses of the nematode's centerline over one period of motion are shown in Figs. 5(a) and 5(b), for  $h/r_w = 28 \pm 4$  and  $h/r_w = 1.1 \pm 0.3$ . For the highly confined worm, the shape of the worm's body is more akin to a sinusoid about the swimming axis, and more similar to the free swimming waveform of *C. elegans*.<sup>35,36</sup> In Fig. 5(c), the lateral position of the head of the worm ( $x_{\text{head}}$ ) is plotted as a function of time for the worm in low and high channel confinements, corresponding to Figs. 5(a) and 5(b). As seen, the amplitude of the worm's head motion is much larger when it is not confined (red open circle markers) compared to under high confinement (blue filled circle markers). In addition, the confined worm is seen to swim with a reduced frequency.

To quantify the change of amplitude discussed above, experienced by the worm as it modulates its gait, we measure the mean angular amplitude,  $A_\theta$ , which is defined as half the angle swept out by the worm's head during swimming. As seen in Figs. 5(a) and 5(b), the angular amplitude is significantly smaller for the confined worm. Since it is known that *C. elegans* experiences a gait modulation in response to increasing environmental resistance (such as increasing viscosity), it is not surprising that the swimming form will change with increasing values of  $c_N$  and  $c_T$ . In our system, we quantify the amount of environmental resistance by the sum  $c_N + c_T$ , which increases by a factor of 20 from an unbounded fluid to the most confined worms studied (analogous to a 20-fold increase in viscosity from that of a buffer, as seen in Eq. (1)). The angular amplitude is plotted as a function of  $c_N + c_T$  in Fig. 5(d) for worms swimming in channel confinement as well as in the presence

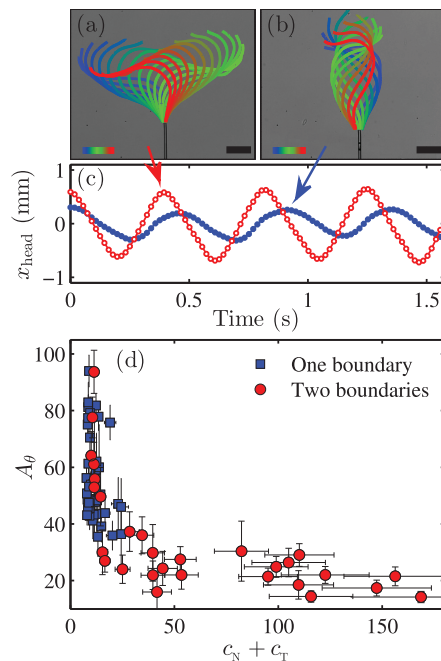


FIG. 5. Time-lapses of the worm's centerline over one swimming period for (a) very low ( $h/r_w = 28 \pm 4$ ) and (b) very high ( $h/r_w = 1.1 \pm 0.3$ ) confinement, in which only every other centerline in the image sequence is plotted. The colourbar indicates the temporal progression along the single period (from  $t = 0$  to  $t = T$ ) and the scalebar represents  $200 \mu\text{m}$ . (c) The lateral position of the head ( $x_{\text{head}}$ ) of the worm in high and low channel confinement as a function of time for several swimming periods. The red open circles and the blue filled circles correspond to the worms in (a) and (b). (d) The angular amplitude as a function of  $c_N + c_T$  for young adult and adult worms swimming near a single boundary (blue squares) and in channel confinement (red circles).

of a single boundary. The angular amplitude decreases as a function of  $c_N + c_T$ . This decrease is most rapid for  $c_N + c_T \lesssim 30$ . In addition, since the worm simply modulates its gait in response to changing resistance, the results for the single boundary and for the channel confinement fall on the same curve. Included in this gait modulation is a slight decrease in the swimming frequency from  $2.4 \pm 0.2$  Hz for an unbounded fluid,<sup>32</sup> to  $2.07 \pm 0.13$  Hz for  $c_N + c_T = 108 \pm 9$ .

The significant difference in swimming amplitude that we measure by confining the worm has not been seen over the same range of increasing environmental resistance in studies of gait modulation in which the fluid viscosity has been changed.<sup>35,36</sup> In these studies, the amplitude of free swimming worms was found to remain relatively constant over a 20-fold increase in the viscosity from that of a buffer. However, the fact that our worm is tethered at the tail is a crucial difference, and the swimming amplitude we measure in the unbounded buffer differs from that of a free swimming worm. Therefore, it is not surprising that some kinematic parameters, such as the amplitude, may exhibit different behaviours in the gait modulation of our system. Studies on gait modulation in *C. elegans* measure a decrease in the swimming frequency of roughly 10%–20% from that in a buffer,<sup>35,36</sup> which is consistent with our findings. In studying gait modulation by changing the viscosity, the chemical composition of the fluid is altered, which may have implications on the behaviour of the worm. In addition, the osmotic pressure of the solution is changed, which may upset the ionic balance of the nematode. Therefore, our results indicate that confinement near solid boundaries is another complimentary way in which gait modulation can be investigated without changing composition of the fluid.

#### IV. SUMMARY AND CONCLUSIONS

In this study, we present an experimental investigation into drag forces acting on an undulatory microswimmer in proximity to solid boundaries. We employ micropipette deflection to directly measure the viscous forces during the swimming of the model organism *C. elegans* in a plane parallel to nearby boundaries. This represents the first direct force measurement of a microswimmer in which boundary effects have been investigated. We witness large increases in the lateral and propulsive forces of the worm as it approaches a single boundary. Using kinematic data from the high speed image sequences of the swimming in conjunction with our force measurements, we are able to extract the normal and tangential drag coefficients for the worm. The drag coefficients decrease as a function of the distance away from the solid boundary. Despite the study being limited in its applicability to our experimental system, the predictions of Katz *et al.* capture the general trends of  $c_N$  and  $c_T$  near the boundary, but with some deviations. Lighthill's results for  $c_N$  and  $c_T$  are successful at large separations from the boundary. We find  $K = c_N/c_T = 1.5 \pm 0.1(5)$  at *all* distances from the boundary. This is an interesting result, as it suggests that a propulsive force increase of an undulator swimming in plane with a nearby boundary cannot be attributed to a changing ratio of the drag coefficients.

For confinement between two planar boundaries, the drag coefficients increase by a factor of 20 for the highest confinements compared to in an unbounded fluid, and we observe an increase in  $K$  for high confinements. In this geometry, Lighthill's results are still in agreement with our data for very large channels. Our results suggest that the analytical results for the drag coefficients in proximity to a boundary are not entirely suitable for this system, and require reconsideration by further theoretical studies. For both channel and single boundary geometries, as the drag coefficients increase, the nematode is seen to undergo a gait modulation characterized by a large decrease in the amplitude of its swimming. This gait modulation is independent of whether the worm is swimming near one or two boundaries, and is only a function of the drag coefficients it is experiencing. These results offer a promising new means of investigating the gait modulation of *C. elegans* by confining the worm, rather than changing the viscosity and hence altering the chemical composition of the fluid.

#### ACKNOWLEDGMENTS

The financial support by Natural Science and Engineering Research Council of Canada is gratefully acknowledged. The authors also thank Alexandra Kasper for useful comments.

- <sup>1</sup>E. M. Purcell, "Life at low Reynolds-number," *Am. J. Phys.* **45**, 3–11 (1977).
- <sup>2</sup>R. P. McCord, J. N. Yukich, and K. K. Bernd, "Analysis of force generation during flagellar assembly through optical trapping of free-swimming *Chlamydomonas reinhardtii*," *Cell Motil. Cytoskel.* **61**, 137–144 (2005).
- <sup>3</sup>S. Chattopadhyay, R. Moldovan, C. Yeung, and X. L. Wu, "Swimming efficiency of bacterium *Escherichia coli*," *Proc. Natl. Acad. Sci. U.S.A.* **103**, 13712–13717 (2006).
- <sup>4</sup>Y. W. Kim and R. R. Netz, "Pumping fluids with periodically beating grafted elastic filaments," *Phys. Rev. Lett.* **96**, 158101 (2006).
- <sup>5</sup>M. J. Kim and K. S. Breuer, "Microfluidic pump powered by self-organizing bacteria," *Small* **4**, 111–118 (2008).
- <sup>6</sup>E. Lauga and T. R. Powers, "The hydrodynamics of swimming microorganisms," *Rep. Prog. Phys.* **72**, 096601 (2009).
- <sup>7</sup>M. J. Kim and K. S. Breuer, "Enhanced diffusion due to motile bacteria," *Phys. Fluids* **16**, L78–L81 (2004).
- <sup>8</sup>M. J. Kim and K. S. Breuer, "Controlled mixing in microfluidic systems using bacterial chemotaxis," *Anal. Chem.* **79**, 955–959 (2007).
- <sup>9</sup>N. Darnton, L. Turner, K. Breuer, and H. C. Berg, "Moving fluid with bacterial carpets," *Biophys. J.* **86**, 1863–1870 (2004).
- <sup>10</sup>D. B. Weibel, P. Garstecki, D. Ryan, W. R. DiLuzio, M. Mayer, J. E. Seto, and G. M. Whitesides, "Microoxen: Microorganisms to move microscale loads," *Proc. Natl. Acad. Sci. U.S.A.* **102**, 11963–11967 (2005).
- <sup>11</sup>G. L. Cooper, A. L. Schiller, and C. C. Hopkins, "Possible role of capillary action in pathogenesis of experimental catheter-associated dermal tunnel infections," *J. Clin. Microbiol.* **26**, 8–12 (1988).
- <sup>12</sup>G. Harkes, J. Dankert, and J. Feijen, "Bacterial migration along solid surfaces," *Appl. Environ. Microbiol.* **58**, 1500–1505 (1992).
- <sup>13</sup>S. S. Suarez and A. A. Pacey, "Sperm transport in the female reproductive tract," *Hum. Reprod. Update* **12**, 23–37 (2006).
- <sup>14</sup>J. W. Costerton, Z. Lewandowski, D. E. Caldwell, D. R. Korber, and H. M. Lappin-Scott, "Microbial biofilms," *Annu. Rev. Microbiol.* **49**, 711–745 (1995).
- <sup>15</sup>M. C. Van Loosdrecht, J. Lyklema, W. Norde, and A. J. Zehnder, "Influence of interfaces on microbial activity," *Microbiol. Rev.* **54**, 75–87 (1990).
- <sup>16</sup>D. F. Katz, T. D. Bloom, and R. H. Bondurant, "Movement of bull spermatozoa in cervical mucus," *Biol. Reprod.* **25**, 931–937 (1981).
- <sup>17</sup>E. Lauga, W. R. DiLuzio, G. M. Whitesides, and H. A. Stone, "Swimming in circles: Motion of bacteria near solid boundaries," *Biophys. J.* **90**, 400–412 (2006).
- <sup>18</sup>W. R. DiLuzio, L. Turner, M. Mayer, P. Garstecki, D. B. Weibel, H. C. Berg, and G. M. Whitesides, "*Escherichia coli* swim on the right-hand side," *Nature (London)* **435**, 1271–1274 (2005).
- <sup>19</sup>U. Ruffer and W. Nultsch, "High-speed cinematographic analysis of the movement of *Chlamydomonas*," *Cell Motil.* **5**, 251–263 (1985).
- <sup>20</sup>M. Polin, I. Tuval, K. Drescher, J. P. Gollub, and R. E. Goldstein, "*Chlamydomonas* swims with two "gears" in a eukaryotic version of run-and-tumble locomotion," *Science* **325**, 487–490 (2009).
- <sup>21</sup>M. Silverman and M. Simon, "Flagellar rotation and the mechanism of bacterial motility," *Nature (London)* **249**, 73–74 (1974).
- <sup>22</sup>J. Lighthill, "Flagellar hydrodynamics – The John von Neumann Lecture, 1975," *SIAM Rev.* **18**, 161–230 (1976).
- <sup>23</sup>G. Taylor, "Analysis of the swimming of microscopic organisms," *Proc. R. Soc. London A* **209**, 447–461 (1951).
- <sup>24</sup>J. Gray, "Undulatory propulsion," *Q. J. Microsc. Sci.* **94**, 551–578 (1953).
- <sup>25</sup>J. Gray and G. J. Hancock, "The propulsion of sea-urchin spermatozoa," *J. Exp. Biol.* **32**, 802–814 (1955).
- <sup>26</sup>J. Gray and H. W. Lissmann, "The locomotion of nematodes," *J. Exp. Biol.* **41**, 135–154 (1964).
- <sup>27</sup>G. Tokic and D. K. P. Yue, "Optimal shape and motion of undulatory swimming organisms," *Proc. R. Soc. B* **279**, 3065–3074 (2012).
- <sup>28</sup>R. G. Cox, "The motion of long slender bodies in a viscous fluid. Part 1. General theory," *J. Fluid Mech.* **44**, 791–810 (1970).
- <sup>29</sup>R. S. Berman, O. Kenneth, J. Sznitman, and A. M. Leshansky, "Undulatory locomotion of finite filaments: Lessons from *Caenorhabditis elegans*," *New J. Phys.* **15**, 075022 (2013).
- <sup>30</sup>D. F. Katz, J. R. Blake, and S. L. Paveri-Fontana, "On the movement of slender bodies near plane boundaries at low Reynolds number," *J. Fluid Mech.* **72**, 529–540 (1975).
- <sup>31</sup>N. J. De Mestre, "Low-Reynolds-number fall of slender cylinders near boundaries," *J. Fluid Mech.* **58**, 641–656 (1973).
- <sup>32</sup>R. D. Schulman, M. Backholm, W. S. Ryu, and K. Dalnoki-Veress, "Dynamic force patterns of an undulatory microswimmer," *Phys. Rev. E* **89**, 050701 (2014).
- <sup>33</sup>S. Brenner, "The genetics of *Caenorhabditis elegans*," *Genetics* **77**, 71–94 (1974).
- <sup>34</sup>M. Backholm, W. S. Ryu, and K. Dalnoki-Veress, "Viscoelastic properties of the nematode *Caenorhabditis elegans*, a self-similar, shear-thinning worm," *Proc. Natl. Acad. Sci. U.S.A.* **110**, 4528–4533 (2013).
- <sup>35</sup>C. Fang-Yen, M. Wyart, J. Xie, R. Kawai, T. Kodger, S. Chen, Q. Wen, and A. D. T. Samuel, "Biomechanical analysis of gait adaptation in the nematode *Caenorhabditis elegans*," *Proc. Natl. Acad. Sci. U.S.A.* **107**, 20323–20328 (2010).
- <sup>36</sup>J. Sznitman, X. Shen, R. Sznitman, and P. E. Arratia, "Propulsive force measurements and flow behavior of undulatory swimmers at low Reynolds number," *Phys. Fluids* **22**, 121901 (2010).
- <sup>37</sup>X. N. Shen, J. Sznitman, P. Krajacic, T. Lamitina, and P. E. Arratia, "Undulatory locomotion of *Caenorhabditis elegans* on wet surfaces," *Biophys. J.* **102**, 2772–2781 (2012).
- <sup>38</sup>X. N. Shen and P. E. Arratia, "Undulatory swimming in viscoelastic fluids," *Phys. Rev. Lett.* **106**, 208101 (2011).
- <sup>39</sup>P. Sauvage, M. Argentina, J. Drappier, T. Senden, J. Siméon, and J.-M. Di Meglio, "An elasto-hydrodynamical model of friction for the locomotion of *Caenorhabditis elegans*," *J. Biomech.* **44**, 1117–1122 (2011).
- <sup>40</sup>S. Park, H. Hwang, S.-W. Nam, F. Martinez, R. H. Austin, and W. S. Ryu, "Enhanced *Caenorhabditis elegans* locomotion in a structured microfluidic environment," *PLoS One* **3**, e2550 (2008).
- <sup>41</sup>T. Majmudar, E. E. Keaveny, J. Zhang, and M. J. Shelley, "Experiments and theory of undulatory locomotion in a simple structured medium," *J. R. Soc. Interface* **9**, 1809–1823 (2012).

- <sup>42</sup>G. Juarez, K. Lu, J. Sznitman, and P. E. Arratia, "Motility of small nematodes in wet granular media," *Europhys. Lett.* **92**, 44002 (2010).
- <sup>43</sup>S. Jung, "Caenorhabditis elegans swimming in a saturated particulate system," *Phys. Fluids* **22**, 031903 (2010).
- <sup>44</sup>F. Lebois, P. Sauvage, C. Py, O. Cardoso, B. Ladoux, P. Hersen, and J.-M. Di Meglio, "Locomotion control of *Caenorhabditis elegans* through confinement," *Biophys. J.* **102**, 2791–2798 (2012).
- <sup>45</sup>A. Ghanbari, V. Nock, S. Johari, R. Blaikie, X. Chen, and W. Wang, "A micropillar-based on-chip system for continuous force measurement of *C. elegans*," *J. Micromech. Microeng.* **22**, 095009 (2012).
- <sup>46</sup>J. C. Doll, N. Harjee, N. Klejwa, R. Kwon, S. M. Coulthard, B. Petzold, M. B. Goodman, and B. L. Pruitt, "SU-8 force sensing pillar arrays for biological measurements," *Lab Chip* **9**, 1449–1454 (2009).
- <sup>47</sup>R. Ghosh and J. Sznitman, "Visualization of nematode *Caenorhabditis elegans* swimming in a liquid drop," *J. Vis.* **15**, 277–279 (2012).
- <sup>48</sup>M.-J. Colbert, A. N. Ragen, C. Fradin, and K. Dalnoki-Veress, "Adhesion and membrane tension of single vesicles and living cells using a micropipette-based technique," *Eur. Phys. J. E* **30**, 117–121 (2009).
- <sup>49</sup>M.-J. Colbert, F. Brochard-Wyart, C. Fradin, and K. Dalnoki-Veress, "Squeezing and detachment of living cells," *Biophys. J.* **99**, 3555–3562 (2010).
- <sup>50</sup>See supplementary material at <http://dx.doi.org/10.1063/1.4897651> for examples of RFT fits for swimming near one and two boundaries, and for movies of the worm swimming before and after confinement.

# Supplemental information for “Undulatory microswimming near solid boundaries”

R. D. Schulman,<sup>1</sup> M. Backholm,<sup>1</sup> W. S. Ryu,<sup>2</sup> and K. Dalnoki-Veress<sup>1,3, a)</sup>

<sup>1)</sup>Department of Physics & Astronomy and the Brockhouse Institute for Materials Research, McMaster University, Hamilton, ON, L8S 4M1, Canada

<sup>2)</sup>Department of Physics and the Donnelly Centre, University of Toronto, Toronto, ON, M5S 1A7, Canada

<sup>3)</sup>Laboratoire de Physico-Chimie Théorique, UMR CNRS Gulliver 7083, ESPCI, Paris, France

## S1. RFT FITS

From the high-speed image sequence of the swimming worms, we can compute body velocities over time. From these velocities, along with the equations of RFT (Eq. 1 in the main text), we can generate theoretical predictions of the viscous forces that can be fit to the experimental data with three parameters. The first two free parameters are the drag coefficients  $c_N$  and  $c_T$ . The third free parameter is a horizontal phase shift between the experimental and theoretical curves, which we find is always smaller than  $T/20$ . In the case of the worm swimming near a single boundary, a pipette with an L-shaped bend is used, which implies that we can measure both lateral and propulsive forces. As such, the RFT fits can be performed simultaneously on the worm’s lateral and propulsive force curves, as exemplified in Fig. S1. In the figure, the experimental lateral and propulsive forces are plotted

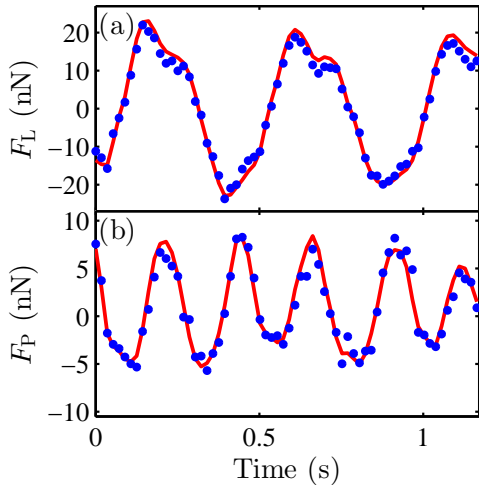


FIG. S1. (a) Lateral ( $F_L$ ) and (b) propulsive ( $F_P$ ) force curves (blue circle markers) for a young adult worm swimming near a single boundary ( $h/r_w \sim 2.8$ ) plotted as a function of time. The red curves correspond to simultaneous RFT fits to the lateral and propulsive force data. In this case,  $c_N = 7.8 \pm 1.2$  and  $c_T = 5.1 \pm 0.8$ .

as a function of time. The fitted RFT prediction is plot-

ted in Fig. S1 as well, and as seen, captures the data very well. In the case of the worm in channel confinement, a completely straight pipette is used which can only measure lateral forces. For this reason, the RFT fit is only performed on the lateral force curve, as seen in Fig. S2. In the figure, the experimental lateral force is plotted as a function of time along with the RFT prediction. The RFT fit successfully captures the data.

The RFT curves are only evaluated at the same points in time as the data is acquired. The error in the RFT curves is estimated to be roughly 5%.

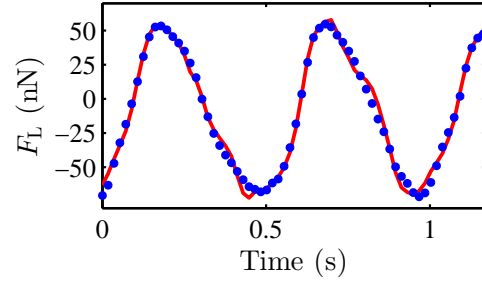


FIG. S2. (a) Lateral force curve (blue circle markers) for a young adult worm confined between two planar boundaries ( $h/r_w \sim 1.2$ ) plotted as a function of time. The red curve corresponds to an RFT fit to the data. In this case,  $c_N = 99 \pm 20$  and  $c_T = 17 \pm 3$ .

## S2. VIDEOS

In this section, we include videos of the typical swimming of a young adult with low and high confinement. In Fig. S3, we show a still image from the video “Fig\_S3.mpg”, in which the worm is swimming in a channel with low confinement ( $h/r_w \sim 35$ ). In Fig. S4, we show a still image from the video “Fig\_S4.mpg”, in which the worm is swimming in a channel in which it is very confined ( $h/r_w \sim 1.5$ ). The angular amplitude of the highly confined worm is significantly smaller. Furthermore, due to the increase in drag coefficients, the pipette deflections (and, hence, lateral forces) of the highly confined worm are much larger.

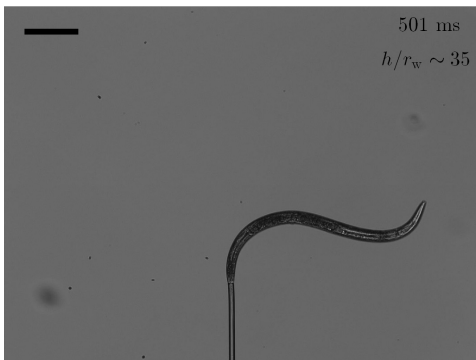


FIG. S3. Still image from the video “Fig\_S3.mpg” of a swimming worm in a channel with very low confinement. The swimming is akin to that in an unbounded fluid. The scale bar represents  $200 \mu\text{m}$ .

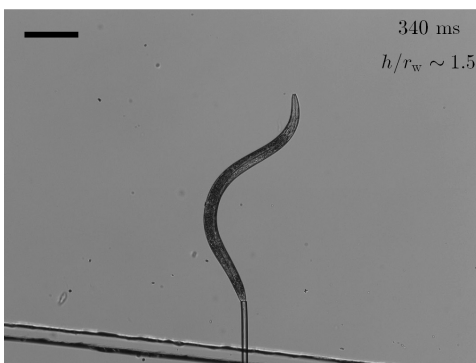


FIG. S4. Still image from the video “Fig\_S4.mpg” of a swimming worm in a channel with very high confinement. The swimming is characterized by a much smaller angular amplitude than seen in Fig. S3. The diagonal lines near the bottom are the edges of the internal channel as described in Sec. II B. The majority of the pipette is located in the larger chamber. Since the drag coefficients are increased compared to at low confinement, the pipette deflections (and, hence, lateral forces) are much larger than in Fig. S3. The scale bar represents  $200 \mu\text{m}$ .

---

<sup>a)</sup>Electronic mail: dalnoki@mcmaster.ca

## A.5 Paper V

*The effects of viscosity on the undulatory swimming dynamics of C. elegans*

M. Backholm, A. K. S. Kasper, R. D. Schulman, W. S. Ryu, and K. Dalnoki-Veress,  
submitted to Phys. Fluids (2015).

# The effects of viscosity on the undulatory swimming dynamics of *C. elegans*

M. Backholm,<sup>1</sup> A. K. S. Kasper,<sup>1</sup> R. D. Schulman,<sup>1</sup> W. S. Ryu,<sup>2</sup> and K. Dalnoki-Veress<sup>1,3, a)</sup>

<sup>1)</sup>*Department of Physics & Astronomy and the Brockhouse Institute for Materials Research, McMaster University, Hamilton, ON, L8S 4M1, Canada*

<sup>2)</sup>*Department of Physics and the Donnelly Centre, University of Toronto, Toronto, ON, M5S 1A7, Canada*

<sup>3)</sup>*PCT Lab, UMR CNRS 7083 Gulliver, ESPCI ParisTech, PSL Research University, Paris, France*

(Dated: 6 August 2015)

The undulatory swimming dynamics of the millimetric nematode *Caenorhabditis elegans* was investigated in fluids with different viscosities. The technique of micropipette deflection was used to directly measure the drag forces experienced by the swimming worm in both the lateral and propulsive direction. Gait modulation due to increasing viscosity in our tethered system was found to be qualitatively similar to that of freely swimming worms. Resistive force theory was used to determine the drag coefficients of the slender swimmer, and the experimental values were compared to the classical theories of Lighthill as well as Gray and Hancock. The gait modulation was shown to be independent of how the environmental resistance is changed, indicating the relevance of only the fluid resistance on the swimming kinematics and dynamics of the nematode.

PACS numbers: 47.63.Gd, 47.15.G-, 87.19.ru

Keywords: Locomotion, Gait modulation, Microswimming, *C. elegans*

## I. INTRODUCTION

Undulatory locomotion is used by crawlers and swimmers, such as snakes and sperm, at length scales spanning almost seven orders of magnitude. In this form of locomotion, the organism moves by propagating waves down its body in an agile and efficient manner. In nature, these slender creatures are forced to adapt to complex environments, such as liquid, sand, and mud<sup>1</sup>. To accomplish this versatility, the organism has two seemingly distinct gaits: crawling on high-friction surfaces<sup>2-4</sup> or through highly viscous fluids<sup>5</sup>, and swimming when immersed in water<sup>6</sup> or sand<sup>7,8</sup>. Understanding the kinematics and dynamics behind the gait transition is an important challenge, and would contribute towards a more general comprehension of the motion of crawlers and swimmers as seen in nature.

The transition between swimming and crawling has been extensively studied with the model organism *C. elegans*<sup>9-12</sup>: a millimetric nematode known for its elegant slithering motion<sup>13</sup>. Interestingly, it has been shown that, instead of transitioning between two distinct gaits, the small worm modulates one single gait continuously as the external resistance is changed<sup>9,11</sup>. Several experimental studies have probed the swimming kinematics of *C. elegans* in different viscosities, finding a decrease in the swimming speed, frequency, and wavelength with an increased fluid viscosity<sup>5,14,15</sup>. Furthermore, in the experimental approach by Yuan, *et al.*, the gait modulation of several worms trapped in a channel was studied, and steric confinement interactions were shown to induce gait synchronization between the swimmers<sup>16</sup>. In

recent work, the same group studied the kinematics of *C. elegans* nematodes in the presence of fluid flow<sup>17</sup>. By introducing a simple micropipette-based technique, we have recently probed the material properties<sup>18,19</sup>, swimming and crawling dynamics<sup>20,21</sup>, as well as the swimming interactions<sup>22</sup> of *C. elegans*. In addition, we have investigated the swimming dynamics and gait modulation of the nematode close to one and two solid boundaries, where the viscous drag forces were increased by decreasing the distance to the interface<sup>23</sup>. We found the amplitude and frequency of the worm's swimming to decrease in response to proximity to the boundary.

Given its small size, *C. elegans* has a Reynolds number (Re) slightly less than one in water-like liquids<sup>20</sup>. By studying the decay of fluid velocities away from a swimming nematode in different viscosities, the worm has been shown to indeed behave like a low Re swimmer, or "microswimmer"<sup>15</sup>. Microswimmers live in a viscous environment, where inertial effects can be neglected. If, furthermore, assuming no long-ranged hydrodynamic interactions between different body parts of the swimmers, the drag forces they experience as they move can be modelled with resistive force theory (RFT)<sup>24,25</sup>. According to RFT, the drag forces on a short slender body segment,  $dl$ , immersed in a fluid can be related to the segment velocity,  $v_i$ , as

$$dF_T = -C_T v_T dl, \text{ and } dF_N = -C_N v_N dl, \quad (1)$$

where  $C_i$  denotes the extrinsic drag coefficient (in units of Pa·s) in the normal ( $i = N$ ) and tangential ( $i = T$ ) direction along the body. By integrating Eq. (1) along the entire body length, the total drag forces  $F_N$  and  $F_T$  experienced by the swimmer in the normal and tangential directions can be calculated.

We define the *extrinsic* drag coefficients as  $C_i = c_i \eta$ , where  $c_i$  are the *intrinsic* drag coefficients of the body

---

<sup>a)</sup>Electronic mail: dalnoki@mcmaster.ca

and  $\eta$  is the fluid viscosity. In order to attain net propulsion, an anisotropy in the environmental resistance is required<sup>24</sup>. This asymmetry is quantified by the ratio of the drag coefficients  $K = c_N/c_T$ . If  $K = 1$ , no net propulsion is possible for an undulating body in the low Re regime. If  $K > 1$ , net propulsion will occur in the opposite direction to the waves propagated down the slender body, whereas the converse is true for  $K < 1$ . Both experiments and theory have determined  $K \approx 1.5$  for *C. elegans*<sup>15,26,27</sup>, but only recently have the two intrinsic drag coefficients been directly measured as  $c_N = 5.1 \pm 0.3$  and  $c_T = 3.4 \pm 0.2$  in a water-like buffer<sup>20</sup>.

The magnitude of the two different intrinsic drag coefficients of an undulating body have been theoretically estimated by Gray and Hancock as

$$c_{N,G\&H} = \frac{4\pi}{\ln\left(\frac{2\lambda}{R}\right) + \frac{1}{2}}, \text{ and } c_{T,G\&H} = \frac{2\pi}{\ln\left(\frac{2\lambda}{R}\right) - \frac{1}{2}}, \quad (2)$$

where  $R$  is the radius of the cylindrical body and  $\lambda$  is the swimming wavelength<sup>6,26,28</sup>. Lighthill later improved on this derivation by taking into account hydrodynamic interactions between different segments along the slender body, giving

$$c_{N,L} = \frac{4\pi}{\ln\left(\frac{0.18\Lambda}{R}\right) + \frac{1}{2}}, \text{ and } c_{T,L} = \frac{2\pi}{\ln\left(\frac{0.18\Lambda}{R}\right)}, \quad (3)$$

where  $\Lambda$  is the swimming wavelength as measured along the body<sup>26</sup>. This refined model of Lighthill has been shown to be in excellent agreement with experiments in a buffer with the same viscosity as water<sup>20</sup>. In both of the above described models, a change in the swimming wavelength will result in a small change in the drag coefficients.

The drag coefficients of Eqs. (2) and (3) are derived in the context of an infinite swimmer propagating a sinusoidal wave without a small amplitude restriction. However, the crucial difference arises from the way in which the body is divided into segments of uniform force per unit length. Gray and Hancock equate one wavelength to a segment, which implies that the entire wavelength experiences a constant force. Although this violates an important assumption that this constant force region should be small in comparison to  $\lambda$ , it produced better agreement between experiment and theory. Lighthill refined the expressions of Gray and Hancock by choosing a smaller size for the region of uniform force, and in doing so, produced the resistance coefficients given by Eq. (3). To date, experimental results have been compared to the predictions of both of these models with varying success<sup>20,23,29–32</sup>. Therefore, it is important to continuously test both of these theories to better understand within which circumstance each prediction is more successful and applicable.

In this work, we have investigated the swimming dynamics of *C. elegans* in fluids of different viscosity. By holding the worm by its tail with a force-calibrated micropipette, the drag forces experienced by the worm in the lateral (side to side) and propulsive (forward and

backwards) direction were directly measured. Both the kinematics and dynamics of the tail-tethered microswimmer were analyzed. Using resistive force theory, the drag coefficients were measured and compared to the theoretical models of Lighthill as well as Gray and Hancock. To the best of our knowledge, no previous experimental work has investigated how the intrinsic drag coefficients of *C. elegans* change as the viscosity of the fluid is increased and the swimmer is forced to modulate its gait. We observe a gait modulation induced transition from one model to the other as the viscosity is increased. Furthermore, we show that the gait modulation is independent of the means by which the drag of the system is increased.

## II. EXPERIMENTAL METHODS

### A. Micropipette deflection

Micropipette deflection was used to investigate the swimming dynamics of single *C. elegans* nematodes in fluids with increasing viscosities. In this technique, the deflection of a long (1 – 3 cm) and thin ( $\sim 20 \mu\text{m}$ ) microcapillary is calibrated and used to measure forces with sub-nanonewton resolution. To manufacture the force probes, micropipettes were stretched from glass capillaries with outer and inner diameters of 1 and 0.58 mm (World Precision Instruments) with a pipette puller (Narishige Group PN-30). The end of the pipettes were cut open by looping the capillaries around a hot wire and then quickly quenching the system by turning off the voltage applied across the wire. This rapid cooling causes the glass to solidify and contract, resulting in a sharp cut of the pipette end. The shaping of the pipettes was performed by bending the capillaries over a similar hot wire. The pipettes were calibrated by pushing out a small droplet of water to hang on the outside of the capillary. The pipette and droplet could be imaged with optical microscopy. From the images, the droplet volume, and hence the mass, could be obtained as a function of the pipette deflection, yielding the spring constant. The spring constants of the pipettes used in this work were in the range of 4.6 – 8.9 nN/ $\mu\text{m}$  and the force–deflection was entirely linear in the range used.

To study the swimming dynamics of the worms in both the lateral and propulsive directions, the pipettes were shaped as shown in the schematic illustration of Fig. 1(a). Two short ( $\sim 200 \mu\text{m}$ ), orthogonal segments of the pipette end were bent in the plane of the swimming motion of the worm. The rest of the pipette was angled at 90 degrees out of the swimming plane to act as a force-sensing cantilever. Here it is important to note that the deflection of the two shorter segments is negligible in comparison to the long cantilever-part of the pipette. In our swimming experiments, the micropipette was mounted on an *xyz*-translational stage from above, and placed within a cylindrical chamber, which was filled

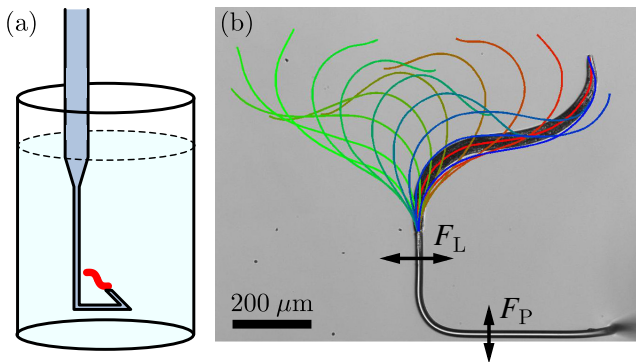


FIG. 1. (a) Schematic diagram (not to scale) of the experimental setup with the force-calibrated micropipette mounted in a cylindrical container. (b) Optical microscopy image of a *C. elegans* nematode caught by its tail. The different lines show a time-lapse of the centreline over one swimming cycle. As the pipette deflects in the two orthogonal directions, the lateral ( $F_L$ ) and propulsive ( $F_P$ ) drag forces experienced by the nematode can be directly measured.

with the fluid in which the worms swim. The fluid filled chamber was placed upon the  $xy$  translation stage of the inverted microscope so that the region of interest within the chamber as well as the micropipette could always be brought into the field of view.

Before an experiment, tens of worms were picked into a chamber filled with M9 buffer. A nematode was then caught by its tail by applying suction, and left to swim as shown by the optical microscopy image in Figure 1(b). After the measurement in the regular buffer, the same worm, still held by the pipette, was carefully transferred to a new chamber containing a fluid with a different viscosity. The transfer to new chambers was continued until all desired viscosities had been probed. After this, the worm was let go and the same procedure was then repeated by catching a new nematode in the initial chamber. In this way, all higher-viscosity experiments could be compared to the reference swimming behaviour of the same worm in the water-like buffer. We note that in sampling different viscosity environments, care was taken so as to change the order in which the worms were exposed to the different chambers (not simply from lowest to highest) in order to avoid biases.

## B. Image analysis

During the experiment, the swimming motion of the worm was followed at 56 fps with a CCD camera (Allied Vision Technologies, GT1660). MATLAB was then used as described in Refs.<sup>20,23</sup> to track the motion of the entire nematode body and derive swimming kinematics quantities such as frequency, amplitude, and wavelength. By monitoring the motion of the two orthogonal pipette segments, the lateral ( $F_L$ ) and propulsive ( $F_P$ ) drag forces experienced by the nematode were directly measured.

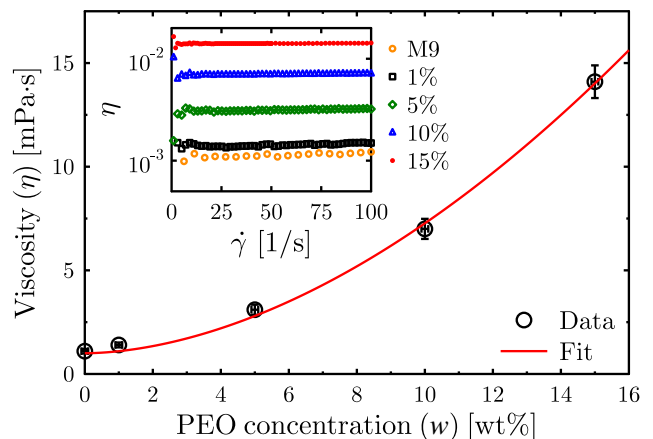


FIG. 2. Viscosity of PEO dissolved in M9 as a function of polymer mass concentration. The line shows the best fit to the data. The error bars correspond to the standard deviation. In the inset, the viscosity is plotted as a function of shear rate ( $\dot{\gamma}$ ) for the five different concentrations.

Using the image analysis data, the instantaneous velocity of each segment of the worm's body was calculated. From Eq. (1), we compute the forces acting normal and tangential to this individual body segment, which is then further deconstructed into a lateral and propulsive component. Finally, we numerically integrate each body segment's contribution to find the total lateral and propulsive forces acting on the worm.

## C. Viscous solutions

Swimming experiments were performed in M9 solutions with different viscosities. M9 is the standard buffer used for *C. elegans* and consists of various dilute salts required to maintain a suitable osmotic pressure to sustain life<sup>13</sup>. Higher viscosity solutions were achieved by mixing polyethylene oxide (PEO, 10 kg/mol, Sigma-Aldrich) with M9. The molecular weight and polymer combination was selected to ensure a Newtonian fluid behaviour over the range of shear rates relevant to the swimming of the worms as will be shown below. Nematodes were not negatively affected below a PEO mass concentration of 17%. At higher concentrations, worms were seen to either die or stop moving. All experiments in this work were therefore performed at concentrations below 15%.

To obtain fluid viscosities, rheology measurements (MCR301, Anton Paar USA Inc, USA) were performed on five different solutions (mass concentrations of 0%, 1%, 5%, 10%, and 15% PEO in M9). The result is shown in Fig. 2, where the viscosity is plotted as a function of PEO mass concentration ( $w$ ). The best fit to the data is  $\eta(w) = \eta_{\text{H}_2\text{O}} + 0.099w^{1.8}$  mPa·s, where  $\eta_{\text{H}_2\text{O}} = 1$  mPa·s is the viscosity of water at 20°C. This equation was used to calculate all viscosities in this work.

As shown in the inset of Fig. 2, the rheology experi-

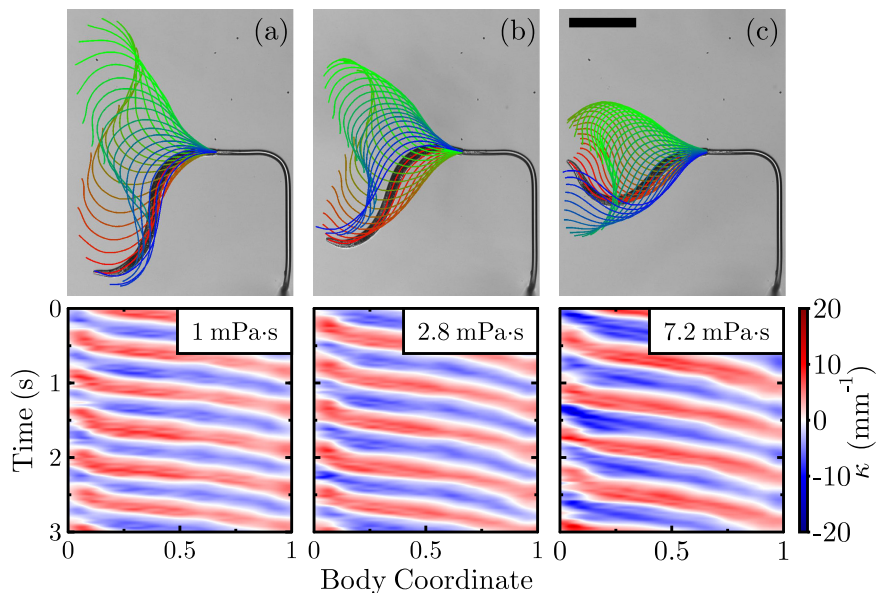


FIG. 3. Time-lapse images (top) of a young adult worm swimming in fluid with viscosities of (a) 1, (b) 2.8, and (c) 7.2 mPa·s. The scale bar represents 200  $\mu\text{m}$ . The bottom graphs show the curvature plots for the worms in the top images over several swimming cycles. The body coordinate is defined as the distance along the worm body, where the head is represented by 0 and the tail (portion closest to the pipette) by 1.

ments were performed at shear rates ( $\dot{\gamma}$ ) between 0 and 100  $\text{s}^{-1}$  to rule out any shear-thinning flow caused by the dissolved polymers. Since *C. elegans* has been shown<sup>14,33</sup> to use a shear rate within the range of 10 – 20  $\text{s}^{-1}$ , our polymer solutions can safely be assumed to be Newtonian.

#### D. *C. elegans* maintenance

Wild-type nematodes (N2) were acquired from the Caenorhabditis Genetics Center and were cultivated on *Escherichia coli* (OP50) nematode growth media (NGM) plates at 20°C according to standard methods<sup>34</sup>. Only young adult worms were used in the experiments. All chemicals were sourced from Sigma-Aldrich.

### III. RESULTS AND DISCUSSION

In this section, the kinematics of the tail-tethered worms will first be quantified as the viscosity of the surrounding fluid is increased. Then, the swimming dynamics of the nematodes will be investigated, and the resulting drag coefficients will be compared to the theoretical estimates of Lighthill as well as Gray and Hancock. Finally, the power output will be calculated and the gait modulation will be compared to a previously investigated system wherein the drag forces were increased by introducing nearby solid boundaries<sup>23</sup>.

#### A. Swimming kinematics

The change in the swimming kinematics of *C. elegans* in increased viscosities is visualized in Fig. 3, where a time-lapse of optical microscopy images of a worm is shown over one swimming cycle (see the Supplementary Information for movies from the same experiments). A clear decrease in the swimming amplitude (or beating amplitude) is seen. Along the bottom panel of the same figure, the curvature plots from the same experiments as the time-lapse images are shown. In these plots, the swimming curvature is illustrated as a function of time and body coordinate, which defines the position of each segment of the worm's body (head = 0, portion nearest to pipette = 1). To best understand these plots, one should first consider a horizontal line through the graph: the variation of the curvature along this line describes the shape of the worm at that specific point in time. On the other hand, the curvature changes along a vertical line describe the motion of a specific body segment as a function of time. From the curvature plots in Fig. 3, the swimming frequency can be seen to decrease slightly with viscosity (greater temporal spacing between lines of equal curvature), whereas the curvature itself increases (greater range in the intensity associated with the curvature). In Fig. 4(a), the change in swimming frequency compared to that of the M9 buffer ( $\Delta f = f_{\text{M9}} - f_{\eta}$ , where  $f_{\text{M9}}$  is the swimming frequency of the same worm in M9) is plotted as a function of viscosity. The average swimming frequency in M9 was measured as  $f_{\text{M9,ave}} = 2.0 \pm 0.2$ . The frequency then decreased by around 0.2 Hz between 1 and 4 mPa·s, to finally remain stable as the viscosity

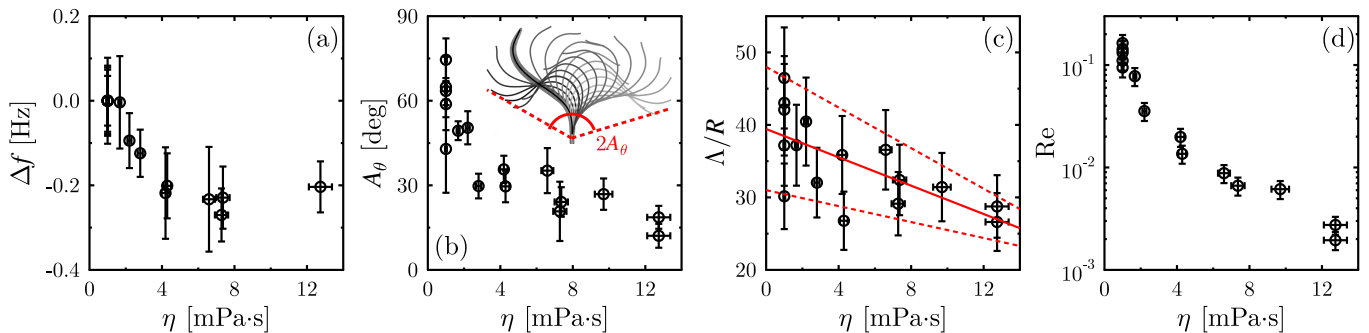


FIG. 4. (a) Change in frequency ( $\Delta f = f_{M9} - f_{\eta}$ ), (b) angular amplitude (defined as half the average swimming angle,  $2A_{\theta}$ , shown in the inset), (c) length-normalized wavelength as measured along the worm body, and (d) the Reynolds number for young adult *C. elegans* nematodes as a function of viscosity. The error bars correspond to the standard deviations from measurements on several swimming cycles of the same worm. The solid line in (c) is the best linear fit to the data:  $\Lambda/R = -(1 \pm 0.4)\eta + (39 \pm 8)$ , and the dashed lines show the error envelope.

is further increased. The same change in swimming frequency has been observed for free-swimming worms over the same viscosity range<sup>14</sup>.

As is clear from the time-lapse images in Fig. 3, the swimming amplitude decreases significantly as the viscosity is increased. In Fig. 4(b), the angular amplitude ( $A_{\theta}$ ) is plotted as a function of viscosity, where the amplitude is defined as half the average total angle swept out by the worm's head in one complete cycle, as shown in the inset. The angular amplitude decreases from around  $60^{\circ}$  to  $15^{\circ}$  as the worms modulate their gaits in the different viscosities. The angular amplitude is a convenient metric for the change in the gait of the worm. As will be seen in Section III C, this gait modulation is crucial for the swimmer to maintain its power output at a reasonable level.

To calculate the swimming wavelength of the worm, the curvature plots (exemplified in Fig. 3) were used. By fitting lines to the diagonal high and low curvature regions (i.e., the solid bands) in the graphs, the inverse of the wave speed,  $v$ , of the undulatory swimmer can be obtained from the slope<sup>33</sup>. The wavelength along the worm body (i.e., the arc length) can then be calculated as  $\Lambda = v/f$ , where  $f$  is the swimming frequency. In Fig. 4(c), this wavelength has been normalized by the radius ( $R$ ) of the worm, and is plotted as a function of viscosity. The solid line in the graph shows the best linear fit to the data, which will be used in theoretical calculations in Section III B. If we normalize the wavelength by the length of the worm body outside the pipette ( $L$ ), we find that it decreases from around  $\Lambda/L = 1.2$  to  $0.9$  in our viscosity range. Due to the tethering of the worms, the swimming wavelength is around 20 % lower than for free-swimming worms, but decreases similarly with viscosity<sup>5</sup>. To measure the actual swimming wavelength,  $\lambda$  (as normally defined for a sinusoidal function, rather than the arc-length  $\Lambda$ ), the worm body was modelled as a sine wave at several different points in time. The typical sine wave amplitudes were then approximated and used together with the wavelength measured along the

worm body ( $\Lambda$ ) to estimate the ordinary wavelength as  $\lambda = (0.80 \pm 0.07)\Lambda$ . The uncertainty stems from the temporal variations in the shape of the same worm, variations between different worms, as well as as the precision of the sine wave fit to the worm centreline.

To classify as a microswimmer, the Reynolds number of the organism needs to be less than unity. The Reynolds number is given by  $Re = \rho l U / \eta$ , where  $\rho$  and  $\eta$  are the density and dynamic viscosity of the fluid,  $l$  is the characteristic length scale, and  $U$  is the typical speed. For the case of *C. elegans* in our tethered system,  $U \sim 4fL \sin A_{\theta}$ , where  $f$  is the swimming frequency,  $L$  is the worm length outside the pipette, and  $A_{\theta}$  is the angular amplitude, as defined in the inset of Fig. 4(b). The typical length scale in our system can be taken to be the worm radius  $R$ . The density (in units of  $\text{kg}/\text{m}^3$ ) of the PEO solutions can be calculated using the empirical formula  $\rho = 997.07 + 174.41w/100$  (at  $T = 298$  K), where  $w$  is the percent mass concentration of the polymer and the solvent M9 is approximated as water<sup>35</sup>. The resulting  $Re$  is plotted as a function of viscosity in Fig. 4(d) and is shown to decrease by about two orders of magnitude from around  $0.15$  in M9 to  $0.002$  in the highest viscosity fluid ( $\sim 13$  mPa·s). The low Reynolds number at high viscosities suggests that we can safely describe the swimming of *C. elegans* in these media with low Reynolds number physics. In addition, previous experiments have demonstrated the success of the low Reynolds number model RFT even in M9, where the Reynolds number is large enough that one could worry about the presence of inertial effects<sup>20,23</sup>.

All data points in Fig. 4 are an average over several swimming cycles that are representative of the worm's swimming in general, as observed for several minutes. Each data point corresponds to a single worm.

## B. Swimming dynamics

By following the deflection of the micropipette in both orthogonal directions as illustrated in Fig. 1(b), the lateral and propulsive drag forces experienced by the swimming worm were directly measured. In Fig. 5, examples of force versus time data for both the lateral (a–b) and propulsive (c–d) directions are shown in a low (left panels) and high (right panels) viscosity fluid. As has been noted in previous work on the swimming dynamics of *C. elegans* in M9<sup>20</sup>, the lateral force is typically twice as large as the propulsive. We see here that this trend persists for the range of viscosities studied. The maximum and minimum force peaks of the lateral force data in Fig. 5(a) and (b) occur when the worm’s body is moving with the highest speed to the right (max) or left (min), whereas the small shoulders on the peaks of the lateral force data in M9 (Fig. 5(a)) arise when the worm’s head turns around and starts moving in the opposite direction. As expected, the drag forces increase when the worm is moved to a higher viscosity fluid (Fig. 5(b) and (d)). In M9, we measure a mean propulsive force of  $\langle F_P \rangle = 0.3 \pm 0.1$  nN<sup>20</sup>, whereas this quantity increases to  $\langle F_P \rangle = 3 \pm 2$  nN in fluids with the highest viscosities  $\eta = 10 \pm 3$  mPa·s. Furthermore, the shoulders in the lateral data disappear as the swimming amplitude decreases and the swimming motion becomes more sinusoidal, as shown in the time-lapse images of Fig. 3. The worm transitions from a high-amplitude swimming in the low viscosity M9 buffer, to a more crawling-like wave form in a high viscosity fluid.

As is shown by the solid lines in the graphs of Fig. 5, resistive force theory is successfully fit to the experimental data in both orthogonal directions. As was discussed in our previous work in M9<sup>20</sup>, the success of RFT in capturing the drag force data of *C. elegans* in a water-like buffer is not to be taken for granted, as the young adult nematode has a  $Re = 0.15$ , i.e., not very much lower than unity. Therefore, the excellent agreement between RFT and our data indicates that inertial effects can be neglected even for the lowest viscosity studied here. As the  $Re$  decreases in higher viscosity fluids, as was shown in Fig. 4(d), the nematode transitions into a more conventional microswimming regime where only viscous forces are relevant.

The extrinsic drag coefficients are fitting parameters for the RFT fits in Fig. 5. Here we fix the ratio,  $K = C_N/C_T = 1.5$ , to further constrain the fits. (See Fig. S1 in the Supplementary Information for a graph of  $C_N$  vs.  $C_T$  obtained with both drag coefficients as free parameters. The slope in the graph is found to be in good agreement with  $K = 1.5$ .) Furthermore, a horizontal shift was necessary to make up for a small phase shift (less than  $T/20$ , where  $T$  is the swimming period) between the theory and experimental data<sup>20</sup>. The extrinsic drag coefficients were finally divided by the fluid viscosity, and the resulting intrinsic normal drag coefficient is plotted as a function of viscosity in Fig. 6. Since we hold

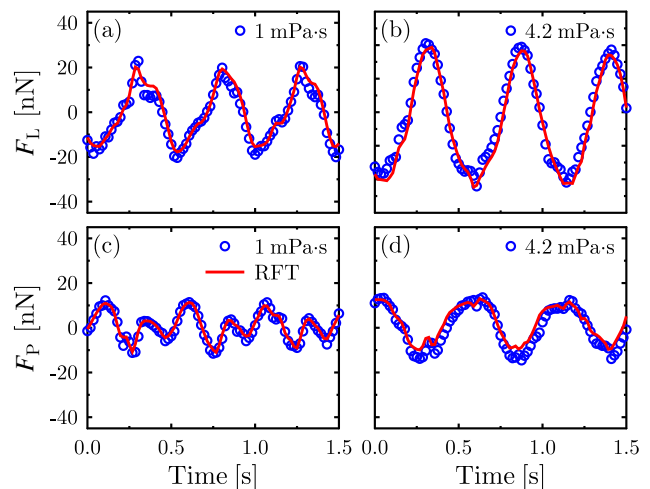


FIG. 5. (a–b) Lateral and (c–d) propulsive force as a function of time in M9 (left) and a high viscosity fluid (right). The resistive force theory fits are shown with a solid line.

$K$  constant, we do not show the graph of  $c_T$  vs.  $\eta$  here, as the same qualitative trends are seen.

To compare our findings to the theoretical models of Lighthill (Eq. (3)) as well as Gray and Hancock (Eq. (2)), the two different swimming wavelengths ( $\lambda$  and  $\Lambda$ ) were first measured as described in Section III A, and normalized with the worm radius ( $R$ ). These values were entered into the equations to calculate the theoretical drag coefficients, and are plotted as crosses (Lighthill) and squares (Gray and Hancock) in Fig. 6. A linear fit was also made to the  $\Lambda/R$  vs.  $\eta$  data (see Fig. 4(c)), and the resulting empirical function ( $\Lambda/R = (-1.0 \mp 0.4)\eta + (39 \pm 8)$ ) was substituted into the drag coefficient equations, producing the solid lines in Fig. 6. The shaded areas in the graph represent the error regions. Both theoretical models predict a slight *increase* in the intrinsic drag coefficients as the fluid viscosity is increased. An interesting feature of the results is that there is an unexpected *decrease* in our experimentally determined intrinsic drag coefficients as the external resistance is increased. Moreover, there appears to be a transition between the excellent agreement with the theoretical results of Lighthill at low viscosities, to full agreement with the theory of Gray and Hancock as the viscosity is increased. This significant transition could act to alter the functional dependence of the drag coefficients on the swimming wavelength. The drag coefficients might start to increase with the prediction of Gray and Hancock as the viscosity is increased beyond what was probed in this work.

The transition between the two models is likely due to the gait modulation of the worm. At viscosities above 6 mPa·s, the experimental data follows the model developed by Gray and Hancock.

In this regime, the worm swimming is more reminiscent of conventional undulatory locomotion of free-swimming worms and the body is less curved onto itself. The pre-

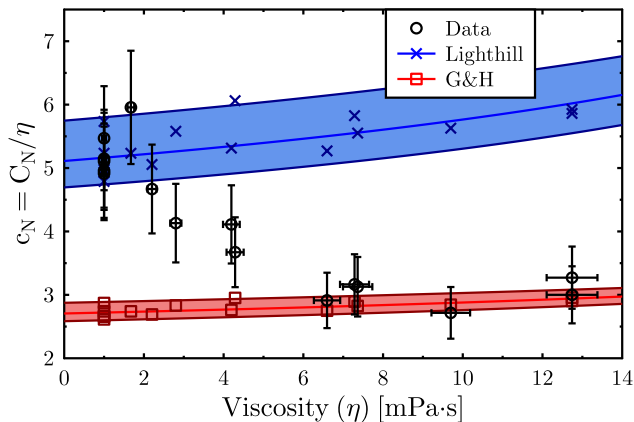


FIG. 6. The intrinsic normal drag coefficient as a function of fluid viscosity. The error bars correspond to the precision of the RFT fits and the error in the spring constant of the pipettes. The cross and square markers represent the theoretical predictions of Lighthill (Eq. (3)) and Gray and Hancock (“G&H”, Eq. (2)) evaluated at the wavelengths and viscosities measured for worms as shown in Fig. 4(c). By substituting the empirical function from the linear fit in Fig. 4(c) into the drag coefficient equations, the solid lines in the graph were obtained. The shaded areas represent the error regions. A transition occurs between the two theories as the viscosity is increased.

dictions of Gray and Hancock (Eq. (2)) are derived in the context of a somewhat coarse grained model. However, their choice of setting the constant force region equal to the wavelength was justified by demonstrating that such a choice produced better agreement with experiments done on freely swimming nematodes. It is, therefore, reasonable that this model succeeds at high viscosities, where the gait-modulating worm has decreased its swimming amplitude significantly, and the worm’s motion is more akin to that of a freely swimming worm. On the contrary, Lighthill’s refined estimate of the drag coefficients is in excellent agreement with our experimental data in the water-like buffer. In these low-viscosity media, the worm’s amplitude is larger and the body is more curved onto itself at times. Therefore, the agreement between Lighthill’s theory and our results in this regime might be linked to the fact that Lighthill’s theory better accounts for hydrodynamic interactions between body segments. To better understand why this transition occurs would require further theoretical or computational studies specifically considering the swimming within our tail-tethered geometry.

### C. Gait modulation

The gait modulation of *C. elegans* occurs to maintain its propulsive thrust whilst sustaining a reasonable power output as the external resistance changes<sup>5</sup>. We have investigated the total power output of the worm, defined

as the sum of the viscous power ( $P_\eta$ ) exerted on the fluid and the elastic power ( $P_e$ ) exerted on the bending of the worm body, giving  $P_{\text{tot}} = P_\eta + P_e$ . To calculate the mean viscous power,  $P_\eta$ , we use a similar procedure as for calculating the RFT curves. First, we compute the infinitesimal power expended in overcoming viscous forces for each body segment  $dF_T v_T + dF_N v_N$ , where  $dF_N$  and  $dF_T$  are given in Eq. (1). Subsequently, this quantity is numerically integrated over the entire body of the worm to find the total power. The mean bending power was calculated as

$$P_e = \frac{EILf\langle\kappa^2\rangle}{2}, \quad (4)$$

where  $L$  is the worm length outside of the pipette,  $\langle\kappa^2\rangle$  is the mean square body curvature,  $f$  is the swimming frequency, and  $EI = (1.2 \pm 0.7) \cdot 10^{-14} \text{ N} \cdot \text{m}^2$  is the bending stiffness for young adult worms obtained from direct bending measurements performed with micropipette deflection<sup>18</sup>.

Calculating the power components as above, we find that both components are constant within experimental error over the viscosity range probed in this work (see Fig. S5 in the Supplementary Information for a graph of the mean viscous and elastic power as a function of viscosity). The average for all young adult worms is  $P_\eta = 0.41 \pm 0.15 \text{ nW}$  and  $P_e = 0.14 \pm 0.03 \text{ nW}$ , which sums up to a total power output of  $P_{\text{tot}} = 0.55 \pm 0.18 \text{ nW}$ . The elastic bending power calculated here deviates from that calculated by Fang-Yen *et al.*<sup>5</sup> ( $P_e \approx 4 \text{ nW}$ ) due to a higher estimation of the bending stiffness in their work ( $EI = (9.5 \pm 1.0) \cdot 10^{-14} \text{ Nm}^2$ ). The constant power output, as has also been reported by Fang-Yen, *et al.*, demonstrates that the worm actively changes its swimming motion to maintain the same level of energy consumption in different environments. This ability is thought to be crucial for the nematode to move through and survive in continuously changing surroundings of, e.g., water, mud, and soil<sup>9</sup>. If not capable of modulating its gait when moving into a region of increased resistance, the nematode would have to increase its power output to maintain the same swimming or crawling waveform, and in that way risk exhaustion and even starvation.

In previous studies, the kinematics of *C. elegans* has been investigated by chemically altering the surrounding fluid, making it more viscous<sup>5,14,15,33</sup>, viscoelastic<sup>36</sup>, or shear-thinning<sup>37</sup>. In our previous work<sup>23</sup>, we enhanced the drag forces experienced by tail-tethered swimming nematodes by holding them close to one solid boundary, or confined between two surfaces. In Fig. 7, the angular amplitude measured in that work (defined in the same way as shown in the inset of Fig. 4(b)) is plotted as a function of the sum of the two extrinsic drag coefficients,  $C_N + C_T = \eta(c_N + c_T)$ . In the same graph, the results of our present study are plotted (circles). Evidently, the gait modulation of the worm is identical within a chemically altered fluid compared with a fluid where the drag forces have been enhanced by changing the physical ge-

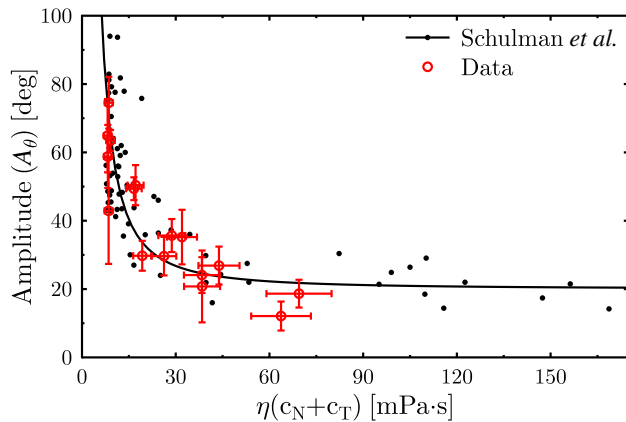


FIG. 7. Angular amplitude (circles) as a function of the sum of the extrinsic drag coefficients. The error bars correspond to the standard deviations from measurements on several swimming cycles of the same worm. The dots are data from Schulman *et al.*<sup>23</sup>, where one and two solid boundaries were brought close to the swimming nematode to enhance the drag experienced by the worm. The solid line is included to guide the eye.

ometry of the system. The kinematics of the nematode is, in other words, affected solely by the change in its extrinsic drag coefficients. By using different mutants, future studies could investigate the effect of, e.g., mechanosensation on the gait modulation of *C. elegans* to probe the biological reasons governing the change in swimming kinematics with increased external resistance.

#### IV. SUMMARY AND CONCLUSIONS

Here we have used the technique of micropipette deflection to probe the undulatory swimming dynamics of the nematode *C. elegans* in fluids with different viscosities. The change in the kinematics of the tail-tethered worm was quantified, and the swimmer was shown to move with a decreased frequency, amplitude, and wavelength as the fluid viscosity was increased. The drag forces experienced by the worm in the lateral and propulsive directions were directly measured over time, and resistive force theory was used to derive the drag coefficients of the microswimmer. The intrinsic drag coefficients were, surprisingly, shown to transition between the classical models of Lighthill at low viscosities, to that of Gray and Hancock at high viscosities. This transition was attributed to the gait modulation of the nematode, adapting from a large-amplitude motion, to a more conventional, small-amplitude undulatory motion. A deeper theoretical treatment of the system would be of future interest to investigate the effects of gait modulation on the intrinsic drag coefficients of an undulatory microswimmer. Furthermore, experimental studies of the swimming dynamics at higher viscosities would shed more light on whether the intrinsic drag coefficients continue to follow

the estimates of Gray and Hancock in the low-amplitude swimming regime.

Finally, the total power output of the nematode was found to remain constant as the environmental resistance changed. That is, the worm modulates its gait to increase propulsion without modifying its power expenditure. The gait modulation was shown to be independent of how the viscous forces of the system are enhanced, indicating that only the hydrodynamic forces of the system influence the undulatory locomotion kinematics and dynamics of the nematode.

#### ACKNOWLEDGMENTS

The authors thank Adam Fortais and Dr. John de Bruyn for assisting with the viscosity measurements. The financial support by Natural Science and Engineering Research Council of Canada is gratefully acknowledged.

- <sup>1</sup>E. Lauga, “The bearable goeyness of swimming,” *J. Fluid Mech.* **762**, 1–4 (2014).
- <sup>2</sup>E. Niebur and P. Erdős, “Theory of the locomotion of nematodes: Dynamics of undulatory progression on a surface,” *Biophys. J.* **60**, 1132–1146 (1991).
- <sup>3</sup>Z. V. Guo and L. Mahadevan, “Limbless undulatory propulsion on land,” *Proc. Natl. Acad. Sci. USA* **105**, 3179–3184 (2008).
- <sup>4</sup>D. L. Hu, J. Nirody, T. Scott, and M. J. Shelley, “The mechanics of slithering locomotion,” *Proc. Natl. Acad. Sci. USA* **106**, 10081–10085 (2009).
- <sup>5</sup>C. Fang-Yen, M. Wyart, J. Xie, R. Kawai, T. Kodger, S. Chen, Q. Wen, and A. D. T. Samuel, “Biomechanical analysis of gait adaptation in the nematode *Caenorhabditis elegans*,” *Proc. Natl. Acad. Sci. USA* **107**, 20323–20328 (2010).
- <sup>6</sup>J. Gray and G. Hancock, “The propulsion of sea-urchin spermatozoa,” *J. Exp. Biol.* **32**, 802–814 (1955).
- <sup>7</sup>R. D. Maladen, Y. Ding, C. Li, and D. I. Goldman, “Undulatory swimming in sand: Subsurface locomotion of the sandfish lizard,” *Science* **325**, 314–317 (2009).
- <sup>8</sup>Y. Ding, S. S. Sharpe, A. Masse, and D. I. Goldman, “Mechanics of undulatory swimming in a frictional fluid,” *PLoS Comput. Biol.* **8**, e1002810 (2012).
- <sup>9</sup>S. Berri, J. H. Boyle, M. Tassieri, I. A. Hope, and N. Cohen, “Forward locomotion of the nematode *C. elegans* is achieved through modulation of a single gait,” *HFSP J.* **3**, 186–193 (2009).
- <sup>10</sup>J. T. Pierce-Shimomura, B. L. Chen, J. J. Mun, R. Ho, R. Sarkis, and S. L. McIntire, “Genetic analysis of crawling and swimming locomotory patterns in *C. elegans*,” *Proc. Natl. Acad. Sci. USA* **105**, 20982–20987 (2008).
- <sup>11</sup>J. H. Boyle, S. Berri, M. Tassieri, I. A. Hope, and N. Cohen, “Gait modulation in *C. elegans*: It’s not a choice, it’s a reflex!” *Front. Behav. Neurosci.* **5**, 10 (2011).
- <sup>12</sup>J. H. Boyle, S. Berri, and N. Cohen, “Gait modulation in *C. elegans*: an integrated neuromechanical model,” *Front. Comput. Neurosci.* **6**, 10 (2012).
- <sup>13</sup>B. Wood, *The nematode Caenorhabditis elegans* (Cold Spring Harbor Laboratory Press, New York, 1988).
- <sup>14</sup>J. Sznitman, X. Shen, P. K. Purohit, and P. E. Arratia, “The effects of fluid viscosity on the kinematics and material properties of *C. elegans* swimming at low Reynolds number,” *Exp. Mech.* **50**, 1303–1311 (2010).
- <sup>15</sup>J. Sznitman, X. Shen, R. Sznitman, and P. E. Arratia, “Propulsive force measurements and flow behavior of undulatory swimmers at low Reynolds number,” *Phys. Fluids* **22**, 121901 (2010).
- <sup>16</sup>J. Yuan, D. M. Raizen, and H. H. Bau, “Gait synchronization in *Caenorhabditis elegans*,” *Proc. Natl. Acad. Sci. USA* **111**, 6865–6870 (2014).

- <sup>17</sup>J. Yuan, D. M. Raizen, and H. H. Bau, “Propensity of undulatory swimmers, such as worms, to go against the flow,” *Proc. Natl. Acad. Sci. USA* **112**, 3606–3611 (2015).
- <sup>18</sup>M. Backholm, W. S. Ryu, and K. Dalnoki-Veress, “Viscoelastic properties of the nematode *Caenorhabditis elegans*, a self-similar, shear-thinning worm,” *Proc. Natl. Acad. Sci. USA* **110**, 4528–4533 (2013).
- <sup>19</sup>M. Backholm, W. S. Ryu, and K. Dalnoki-Veress, “The nematode *C. elegans* as a complex viscoelastic fluid,” *Eur. Phys. J. E* **38**, 36 (2015).
- <sup>20</sup>R. D. Schulman, M. Backholm, W. S. Ryu, and K. Dalnoki-Veress, “Dynamic force patterns of an undulatory microswimmer,” *Phys. Rev. E* **89**, 050701 (2014).
- <sup>21</sup>Y. Rabets, M. Backholm, K. Dalnoki-Veress, and W. S. Ryu, “Direct measurements of drag forces in *C. elegans* crawling locomotion,” *Biophys. J.* **107**, 1980–1987 (2014).
- <sup>22</sup>M. Backholm, R. D. Schulman, W. S. Ryu, and K. Dalnoki-Veress, “Tangling of tethered swimmers: Interactions between two nematodes,” *Phys. Rev. Lett.* **113**, 138101 (2014).
- <sup>23</sup>R. D. Schulman, M. Backholm, W. S. Ryu, and K. Dalnoki-Veress, “Undulatory microswimming near solid boundaries,” *Phys. Fluids* **26**, 101902 (2014).
- <sup>24</sup>N. Cohen and J. H. Boyle, “Swimming at low Reynolds number: A beginners guide to undulatory locomotion,” *Contemp. Phys.* **51**, 103–123 (2010).
- <sup>25</sup>E. Lauga and T. R. Powers, “The hydrodynamics of swimming microorganisms,” *Rep. Prog. Phys.* **72**, 096601 (2009).
- <sup>26</sup>J. Lighthill, “Flagellar hydrodynamics - The John von Neumann Lecture, 1975,” *SIAM Review* **18**, 161–230 (1976).
- <sup>27</sup>J. Gray and H. W. Lissmann, “The locomotion of nematodes,” *J. Exp. Biol.* **41**, 135–154 (1964).
- <sup>28</sup>J. Gray, “Undulatory propulsion,” *Q. J. Microsc. Sci.* **94**, 551–578 (1953).
- <sup>29</sup>J. Sznitman, P. K. Purohit, P. Krajacic, T. Lamitina, and P. E. Arratia, “Material properties of *Caenorhabditis elegans* swimming at low Reynolds number,” *Biophys. J.* **98**, 617–626 (2010).
- <sup>30</sup>B. Friedrich, I. Riedel-Kruse, J. Howard, and F. Jülicher, “High-precision tracking of sperm swimming fine structure provides strong test of resistive force theory,” *J. Exp. Biol.* **213**, 1226–1234 (2010).
- <sup>31</sup>P. Bayly, B. Lewis, E. Ranz, R. Okamoto, R. Pless, and S. Dutcher, “Propulsive forces on the flagellum during locomotion of *Chlamydomonas reinhardtii*,” *Biophys. J.* **100**, 2716–2725 (2011).
- <sup>32</sup>B. Rodenborn, C.-H. Chen, H. L. Swinney, B. Liu, and H. P. Zhang, “Propulsion of microorganisms by a helical flagellum,” *Proc. Natl. Acad. Sci. USA* **110**, E338–E347 (2013).
- <sup>33</sup>J. Korta, D. A. Clark, C. V. Gabel, L. Mahadevan, and A. D. T. Samuel, “Mechanosensation and mechanical load modulate the locomotory gait of swimming *C. elegans*,” *J. Exp. Biol.* **210**, 2383–2389 (2007).
- <sup>34</sup>S. Brenner, “The genetics of *Caenorhabditis elegans*,” *Genetics* **77**, 71–94 (1974).
- <sup>35</sup>P. Gonzalez-Tello, F. Camacho, and G. Blazquez, “Density and viscosity of concentrated aqueous solutions of Polyethylene Glycol,” *J. Chem. Eng. Data* **39**, 611–614 (1994).
- <sup>36</sup>X. N. Shen and P. E. Arratia, “Undulatory swimming in viscoelastic fluids,” *Phys. Rev. Lett.* **106**, 208101 (2011).
- <sup>37</sup>D. A. Gagnon, N. C. Keim, and P. E. Arratia, “Undulatory swimming in shear-thinning fluids: experiments with *Caenorhabditis elegans*,” *J. Fluid Mech.* **758**, R3 (2014).

# Supplementary information for “The effects of viscosity on the undulatory swimming dynamics of *C. elegans*”

M. Backholm,<sup>1</sup> A. K. S. Kasper,<sup>1</sup> R. D. Schulman,<sup>1</sup> W. S. Ryu,<sup>2</sup> and K. Dalnoki-Veress<sup>1,3, a)</sup>

<sup>1)</sup>*Department of Physics & Astronomy and the Brockhouse Institute for Materials Research, McMaster University, Hamilton, ON, L8S 4M1, Canada*

<sup>2)</sup>*Department of Physics and the Donnelly Centre, University of Toronto, Toronto, ON, M5S 1A7, Canada*

<sup>3)</sup>*Laboratoire de Physico-Chimie Théorique, UMR CNRS Gulliver 7083, ESPCI, Paris, France*

(Dated: 6 August 2015)

## S1. RFT FITTING WITH A FREE RATIO $K$

To verify a drag coefficient ratio of  $K = 1.5$ , we also performed the RFT fits with both the drag coefficients as free fitting parameters. In Fig. S1, we plot the normal vs. tangential extrinsic drag coefficients derived from the RFT fits. The solid line in the graph has a slope of  $K = 1.5$ , and the data is in good agreement with this prediction of the ratio. For all results presented in the main paper, we used a fixed  $K$  to decrease the number of free fitting parameters in the RFT analysis.

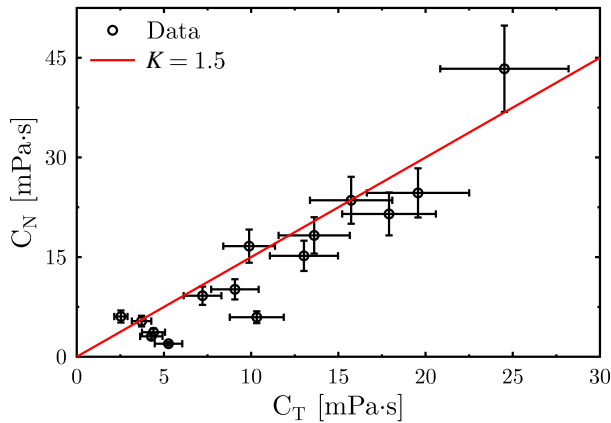


FIG. S1. The normal vs. tangential extrinsic drag coefficients from the RFT analysis performed with the ratio  $K$  as a free fitting parameters. The line has a slope of  $K = 1.5$ , and the data is in good agreement with this ratio.

## S2. VIDEOS

Here, videos of the typical swimming of a young adult worm in M9, an intermediate viscosity, and a high viscosity are included. The time-lapse optical microscopy images of Fig. 3 in the main manuscript correspond to the same experiments.

A still image from the video “Fig.S2.avi” of a worm swimming in the M9 buffer (1 mPa·s) is shown in Fig. S2. In Figs. S3 and S4, still images from movies (“Fig\_S3.avi” and “Fig\_S4.avi”) of the same worm but in higher viscosity fluids (2.8 and 7.2 mPa·s) are shown. The angular amplitude decreases as the fluid viscosity is increased. The pipette deflections in both orthogonal directions can, furthermore, be seen to increase with the fluid viscosity, indicating higher drag forces in the more viscous regimes.

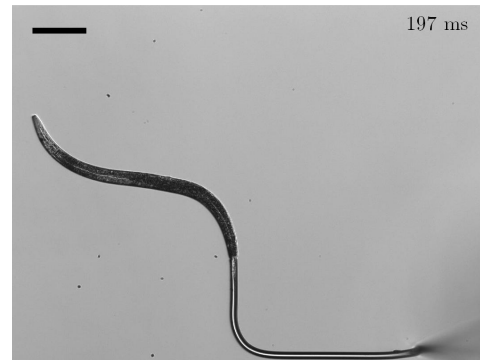


FIG. S2. Still image from the video “Fig.S2.avi” of a swimming worm in the M9 buffer. The scale bar represents 200  $\mu\text{m}$ .

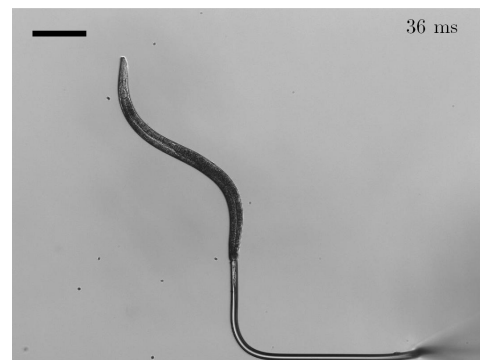


FIG. S3. Still image from the video “Fig.S3.avi” of a worm swimming in an intermediate viscosity fluid (2.8 mPa·s). The angular amplitude is decreased and the drag forces increased with respect to what can be seen in Fig. S2. The scale bar represents 200  $\mu\text{m}$ .

<sup>a)</sup>Electronic mail: dalnoki@mcmaster.ca

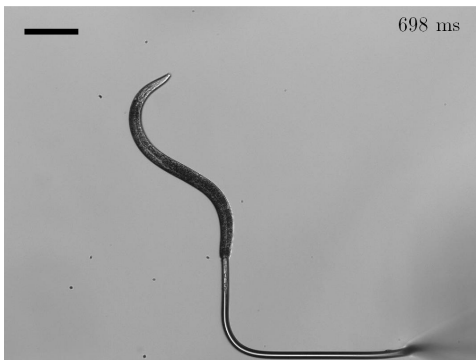


FIG. S4. Still image from the video “Fig\_S4.avi” of a worm swimming in a high viscosity fluid (7.2 mPa.s). An even larger change in the swimming motions is seen as the worm modulates its gait to maintain a constant power output. The scale bar represents 200  $\mu\text{m}$ .

### S3. POWER OUTPUT

In Fig. S5, the mean viscous and elastic power is plotted as a function of viscosity. Within experimental error,

both of these powers remain constant, as shown by the dashed lines in the graph, giving  $P_\eta = 0.41 \pm 0.15$  nW and  $P_e = 0.14 \pm 0.03$  nW. The worm is, in other words, modulating its gait to maintain a constant power output in different environments.

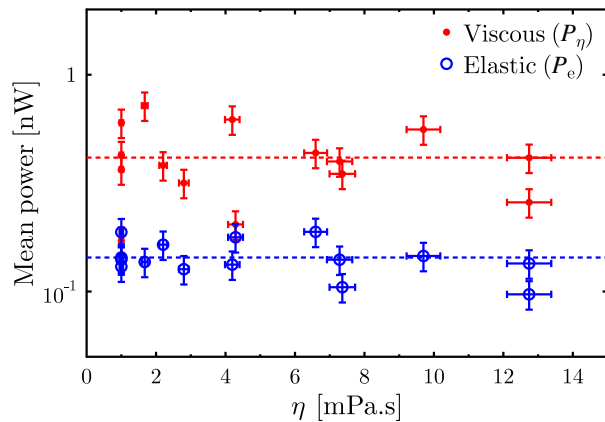


FIG. S5. Mean viscous (filled circles) and elastic (open circles) power as a function of viscosity.

## A.6 Paper VI

*Tangling of tethered swimmers: Interactions between two nematodes*

M. Backholm, R. D. Schulman, W. S. Ryu, and K. Dalnoki-Veress, Phys. Rev. Lett. **113**, 138101 (2014).



## Tangling of Tethered Swimmers: Interactions between Two Nematodes

Matilda Backholm,<sup>1</sup> Rafael D. Schulman,<sup>1</sup> William S. Ryu,<sup>2</sup> and Kari Dalnoki-Veress<sup>1,3,\*</sup>

<sup>1</sup>*Department of Physics & Astronomy and the Brockhouse Institute for Materials Research, McMaster University, Hamilton, Ontario L8S 4M1, Canada*

<sup>2</sup>*Department of Physics and the Donnelly Centre, University of Toronto, Toronto, Ontario M5S 1A7, Canada*

<sup>3</sup>*Laboratoire de Physico-Chimie Théorique, UMR CNRS Gulliver 7083, ESPCI, Paris, France*

(Received 9 June 2014; published 23 September 2014)

The tangling of two tethered microswimming worms serving as the ends of “active strings” is investigated experimentally and modeled analytically. *C. elegans* nematodes of similar size are caught by their tails using micropipettes and left to swim and interact at different separations over long times. The worms are found to tangle in a reproducible and statistically predictable manner, which is modeled based on the relative motion of the worm heads. Our results provide insight into the intricate tangling interactions present in active biological systems.

DOI: 10.1103/PhysRevLett.113.138101

PACS numbers: 87.85.gj, 46.70.Hg, 47.63.Gd

Entanglements are ubiquitous in our everyday lives with headphone cords forming braids and knots in our pockets, collections of small items like staples arranging into large tangled networks [1], and hair strands knotting into disordered snarls [2]. A less common example is the knotting of the umbilical cord which occurs at birth for about 1% of the population [3]. At smaller scales, like in the case of DNA, knots occur naturally in the recombination and replication cycles and are thought to contribute to gene regulation [4–6]. Tangling in polymers [7], proteins [3], and the flagella in groups of spermatozoa [8,9] as well as bacteria are further examples. Flagellar entanglements have been shown to stabilize bacterial networks in biofilms [10,11] and also give rise to the well-studied run-and-tumble motion of bacteria, where several flagella are tangled into a propellerlike bundle, allowing for propulsion in a specific direction [12–14].

Over recent years, active networks of, e.g., highly packed bacteria [15,16], cilia [17–20], nematodes [21,22], sperm cells [23], self-locomoting slender rods [24], microtubule filaments [25,26], and colloidal particles [27] have been studied for the purpose of bioengineering applications [28] and understanding the complex, collective interactions present in these living or active liquids [29,30]. In addition to hydrodynamic coupling and collisions, entanglements play a vital role in determining the final physical properties and biological function of the active material. In the case of cilia, for example, the synchronized beating enables locomotion of a variety of microorganisms as well as the transport of mucus from our lungs. Any tangling of the cilium strands would certainly have severe biological consequences.

Mathematicians and physicists have taken a keen interest in understanding the formation and topology of knots and tangles. To spontaneously form a knot, a long and flexible string with a certain excluded volume and bending stiffness

has to be given enough energy to move around and explore its surroundings [31]. For very small strings, like polymer chains, thermal energy is sufficient to reptate and entangle the molecules [7]. For larger objects, however, extra energy input is needed, as in the case of the driven helical rotation of bacterial flagella [12–14] or for vigorously shaken ball chains and strings [32–35]. Independent of the formation strategy, the tangle topology can be defined by the Conway notation [36–40].

The formation, lifetime, and untying of knots has been investigated experimentally in macroscopic systems consisting of single strings, chains, and ropes of different lengths and stiffnesses [32–35]. Upon shaking these passive strings, self-induced knots of different types were found, and the knotting probability was theoretically modeled. Most knots form and disappear due to the string ends moving in and out of chain loops and around straight segments of the chain. To the best of our knowledge, this intricate chain end motion has not been closely studied, nor has the interaction between two chain ends.

Here we present a time-resolved experimental system illustrated in Fig. 1(a), probing the dynamic tangling of two

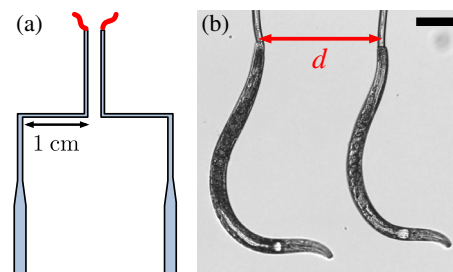


FIG. 1 (color online). (a) Schematic illustration of the experimental setup where two worms were held by Z-shaped micropipettes. (b) Optical microscopy image of two young adult *C. elegans* worms swimming at a separation  $d$ . Scale bar 200  $\mu\text{m}$ .

small worms serving as active, i.e., self-driven, strings on a millimetric scale. The nematode *Caenorhabditis elegans* is a millimeter-sized microswimmer used as a model organism to probe undulatory locomotion experimentally [41–45]. When tail anchored, *C. elegans* has been shown to move in a highly reproducible, undulatory fashion with a well-defined frequency and amplitude [43]. In our experiments, the nematodes were placed in a buffer solution and held by their tails with long ( $\sim 2$  cm) and thin ( $\sim 20$   $\mu\text{m}$ ) micropipettes made as described in Refs. [46,47], and carefully placed side by side at a separation  $d$  as shown in Fig. 1(b) (see the Supplemental Material for more experimental details [48]). The motion of the worms was monitored with a camera (56 fps) as shown in the time-lapse snapshots of Fig. 2(a) (see the Supplemental Material movie SM1.avi [48]). The lateral positions of the worm heads were tracked and are plotted as a function of time in Fig. 2(b), where sinusoidal functions have been fit to the three first noninteracting periods of both worms, showing the smooth, undulatory motion of the swimmers.

At close enough distances, the worms were seen to frequently overlap and form temporary tangles. A typical example of the formation of such a tangle is shown by the head positions in Fig. 2(b). The undulatory motion of the slender bodies remains unchanged throughout a tangle, deeming the attempt frequency to untangle the same as the swimming frequency of the worms, which finally exit the locked configuration by moving their heads apart. The undoing of the tangle is sometimes driven by the motion of only one of the worms.

Here, two different types of tangles shown in Figs. 2(c) and 2(d) were found to occur frequently and in a reproducible manner. These could be recognized by the number of overlapping points and are here defined as a 2- and 3-tangle, respectively (in the Conway notation, these tangles would correspond to vertical rational tangles of type  $1/2$  and  $1/3$  [36]). To understand the formation of these specific tangles, the worms were modeled as strings with an average length  $L \sim L_{\text{left}} \sim L_{\text{right}}$  and radius  $R$ . Consistent with our observations, the lateral position of the string ends (worm heads) were defined as sinusoidal functions with a maximum amplitude of  $A = kL$ , where  $k$  is an experimentally determinable constant. The left and right string end positions could, thus, be written as  $x_L = A \sin(t + \phi)$  and  $x_R = A \sin t + d$ , respectively, where  $\phi \in [0, \pi]$  is the phase shift between the active strings, and  $d > 0$  is the distance between their anchors.

The probability of these strings entangling will vanish at large distances and become increasingly probable as the string ends start to overlap, i.e., at some point in time,  $x_L \geq x_R$ . This results in a critical ratio between the distance and amplitude for any overlap to be possible:  $d/A \leq \sin(t + \phi) - \sin t$ . For an entanglement to be physically possible, it is not sufficient for only the string ends to overlap. Instead, a certain fraction ( $L_c/L$ ) of each string needs to be available to form a full tangle with a minimum length of  $L_c$ . We, therefore, consider that both worms must have a swimming amplitude such that they reach a distance greater than  $L_c$  beyond the symmetry plane [exemplified by the left worm in the second frame of Fig. 2(a)]. Thus, we

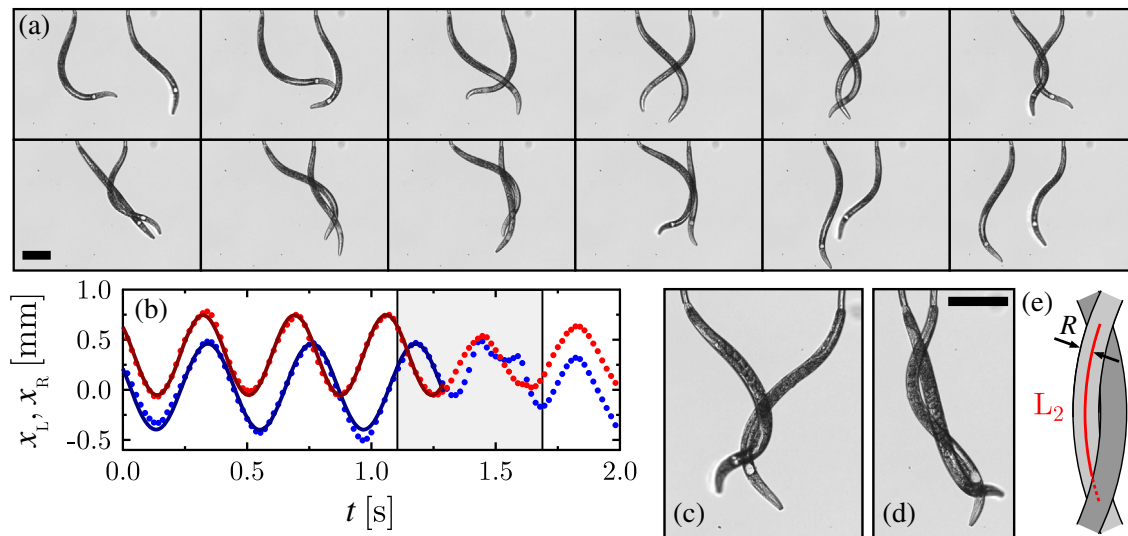


FIG. 2 (color online). (a) Snapshots (0.054 s between each image) showing the tangling of two worms swimming at a distance  $d = 370$   $\mu\text{m}$  apart. (b) The lateral position of the heads of the same worms. The worms slowly shift from in-phase to out-of-phase swimming, allowing the heads to overlap and the worms to wrap around each other's bodies and form a tangle. Subsequently, they exit the tangle in phase with the same sinusoidal motion as prior to the tangling event. The gray zone in the graph denotes the time frame of the snapshots in (a) (image of every third data point shown). The solid lines are sinusoidal fits to the head positions of both of the worms. (c),(d) Two worms at different separations forming a 2- and 3-tangle, respectively. (e) A schematic illustration of a 2 tangle modeled as a helix with radius  $R$ , twist  $\pi$ , and arc length  $L_2$ . All scale bars represent 200  $\mu\text{m}$ .

can state that for a tangle to occur,  $A \geq d/2 + L_c$ , which yields

$$\frac{L}{d} \geq \left[ 2 \left( k - \frac{L_c}{L} \right) \right]^{-1}. \quad (1)$$

This equation corresponds to an upper bound to the critical ratio between the chain length and distance for an entanglement to be theoretically possible.

The lowest-order tangle seen in our system is the 2 rational tangle [Fig. 2(c)] illustrated schematically in Fig. 2(e). This tangle can be described as a helix with a radius  $R$  (the same as the worm radius), curvature  $\kappa$ , and twist  $\pi$ . The arc length (minimum string length required for this tangle) then is  $L_c = L_2 = \pi\sqrt{R/\kappa}$ . The proportionality constant relating the maximum swimming amplitude (see the Supplemental Material [48]) to the worm length has been measured as  $k = 0.8 \pm 0.05$  for single worms. By measuring the mean radius and length of the worms used in this study (young adults and adults,  $R = 29 \pm 2 \mu\text{m}$  and  $L = 1080 \pm 70 \mu\text{m}$ ) and the mean of the absolute curvature of the first (anterior) half of their bodies in a state of normal swimming ( $\kappa = 3.3 \pm 0.2 \text{ mm}^{-1}$ ), an estimate of  $L_2/L = 0.27 \pm 0.02$  could, thus, be made. By applying the helix model to Eq. (1), the predicted critical ratio between the worm length and distance for any entanglement to be possible is  $(L/d)_2 \geq 0.95 \pm 0.10$ . Following the same approach, the critical ratio for a 3 tangle modeled as a helix with a twist of  $2\pi$  is calculated as  $(L/d)_3 = 2.0 \pm 0.3$ .

The experiments were performed at different distances with several pairs of worms of similar size. In a particular experiment, the presence of 2- and 3-tangles were noted. In Fig. 3(a), we plot if a tangle could be observed at a given ratio  $L/d$  and also indicate the type of tangle. The two vertical lines in the graph denote the theoretically predicted critical ratios  $(L/d)_2$  and  $(L/d)_3$ , and the experimental onsets are, within error, in excellent agreement with the model. Note that 2 tangles were always present in experiments in which 3 tangles were observed.

In Figs. 3(b) and 3(c), the distributions of entanglement lifetimes are shown for several experiments performed in the two extreme cases of large ( $L/d = 1.0 \pm 0.2$ ) and small ( $L/d = 5.7 \pm 2.8$ ) separations, respectively (for further details, see the Supplemental Material [48]). At the larger separation, only 2 tangles are possible and have an average lifetime of  $\tau_2 = 0.18 \pm 0.03 \text{ s}$ . However, for the shorter separation, both 2- and 3-tangles were possible, and this is clearly seen in Fig. 3(c) where a shoulder around  $\tau_3 \approx 0.4 \text{ s} \approx 2\tau_2$  has formed due to the occurrence of the more long-lived 3 tangle stabilized by an additional crossing which requires extra time to become undone. Note that, as one might expect, even for short distances, the 3 tangles are much less probable than 2 tangles. A slight shift and widening of the 2 peak at close distances is also apparent

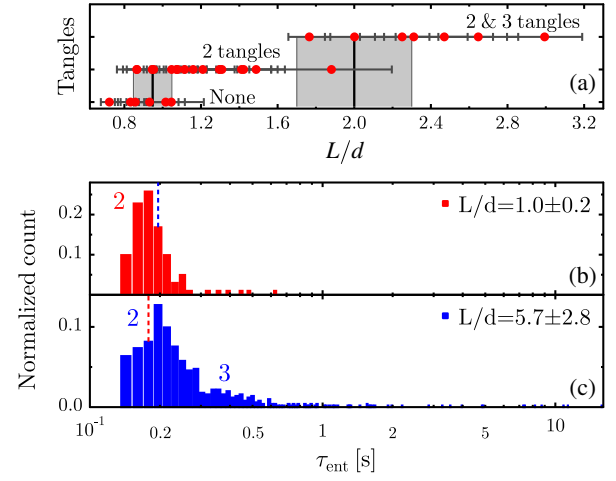


FIG. 3 (color online). (a) The experimental onset of 2- and 3-tangles (filled circles) with horizontal error bars as a function of the worm length-distance ratio. The vertical lines are the theoretical crossover predictions  $(L/d)_2 = 0.95 \pm 0.10$  and  $(L/d)_3 = 2.0 \pm 0.3$ . (b),(c) Histograms of the entanglement lifetimes of several worm pairs far apart [ $L/d = 1.0 \pm 0.2$ , (b)] and close together [ $L/d = 5.7 \pm 2.8$ , (c)]. The count has been normalized with the total number of tangles. The vertical dashed lines indicate the peak position of the other histogram.

when comparing the two distributions [see vertical dashed lines in Figs. 3(b) and 3(c)], indicating more variations in the tangling events as the worms are brought closer together. A few 3 tangles remained stable for around 10 s, which corresponds to over 20 full swimming cycles (untangling attempts). These dynamic tangles were beating and rotating reminiscent of bacterial bundles (see the Supplemental Material movie SM2.avi [48]). Variables that affect the tangle stability are the length, thickness, and bending stiffness of the worms, the attempt frequency to untangle, the friction between the worms [49], as well as contact between the worms eliciting mechanosensory responses [50]. The latter of these has previously been shown not to affect the collective swimming of *C. elegans* [21] and did not seem to strongly affect the tangling dynamics in our experiments either.

To investigate the entanglement probability as  $L/d$  increases above the critical ratios derived above, we now follow the lateral motion of the point ( $x_c$ ) on the worm body located at a distance of  $L_c$  from the head. Since the worm propagates traveling waves down its body,  $x_c(t)$  can also be modeled as a sinusoidal function with an amplitude  $A_c = k_c L$ , where  $k_c$  is an experimentally determinable constant. For the left and right worms, we thereby have  $x_{c,L} = A_c \sin(t + \phi)$  and  $x_{c,R} = A_c \sin t + d$ , respectively. At a given separation distance, these sinusoidal functions intersect at a range of phase shifts above some critical value. For an entanglement to be possible, the maximum value of the difference  $\Delta = x_{c,L} - x_{c,R}$  needs to be greater than zero. Using a trigonometric

identity,  $x_{c,L} - x_{c,R} = 2A_c \cos[(2t + \phi)/2] \sin(\phi/2) - d$ . Maximizing this difference with respect to time yields  $\Delta = 2A_c \sin(\phi/2) - d \geq 0$  and, thus,

$$\phi \geq \phi_c = 2\sin^{-1}\left(\frac{d}{2A_c}\right). \quad (2)$$

This is the critical phase shift needed to form a tangle at a specific  $L/d$  ratio. In other words, the farther apart the worms are, the more out of phase they have to swim in order to intersect and the smaller is the range of phase shifts which yield intersections.

Although the worms have very similar average frequencies ( $f = 2.1 \pm 0.2$  Hz), small temporal variations in this quantity allow the worms to explore all relative phase shifts, as exemplified in Fig. 2(b). Since the worms explore all relative phase shifts over time, and since a certain fraction of intersection events between the worm ends will lead to entanglements, it is reasonable to hypothesize that the entanglement probability will be proportional to the fraction of relative phase shifts which contain an intersection at the separation distance  $d$ . However, we also expect that entanglement events will be more likely to occur if the worm heads have more space (and time) to wrap around each other's bodies. Thus, we make the first-order assumption that the probability of entanglements at a given separation distance is proportional to the fraction of relative phase shifts which contain an intersection but where each phase shift is linearly weighted by the maximum separation between the worm heads, giving

$$p \propto \int_{\phi_c}^{\pi} \frac{\Delta}{L} d\phi, \quad (3)$$

where  $L$  is used to nondimensionalize the weighting. Evaluating this integral and substituting  $A_c = k_c L$  gives

$$p \propto 2k_c \sqrt{4 - \left(\frac{d}{k_c L}\right)^2} - \frac{d}{L} \left[ \pi - 2\sin^{-1}\left(\frac{d}{2k_c L}\right) \right], \quad (4)$$

which shows how the entanglement probability scales with the worm length-distance ratio.

The number of worm entanglements were counted, and the experimental entanglement probability was calculated as the ratio between the number of entanglements and entanglement attempts (the sum of the number of swimming cycles and successful tangling events). The probability is plotted as a function of  $L/d$  in Fig. 4 for all experiments performed with different worm pairs at different distances. The entanglement probability increases sharply at a worm separation close to one worm length. Equation (4) is successfully fit to the data, and the model is clearly in excellent agreement with the experimental observations. Two fitting parameters were used to fit the

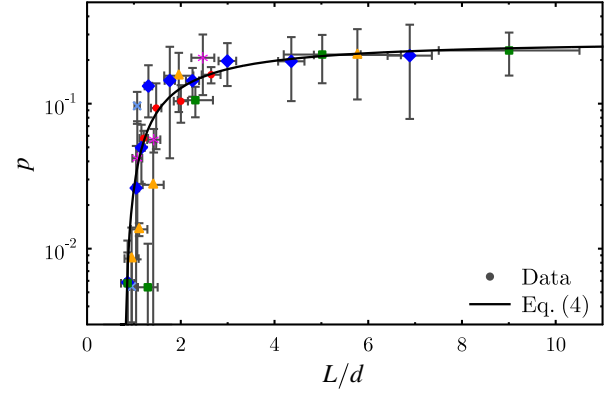


FIG. 4 (color online). The entanglement probability as a function of  $L/d$ . The different markers denote experiments with different worm pairs. The solid line is the analytical fit of Eq. (4) to the data.

data in Fig. 4. The first is a compressing factor ( $0.11 \pm 0.03$ ) in the  $y$  direction, which corresponds to the proportionality prefactor of Eq. (4). Any mechanosensory interactions present between the worms would enter into this factor. The second fitting parameter defines the horizontal shift of the theoretical curve and is given by  $k_c = 0.64 \pm 0.10$ . Comparing this value to that derivable from the helix model giving  $A_{c,\text{helix}}/L = k - L_2/L = 0.53 \pm 0.05$ , we find the two models to be, within error, in excellent agreement.

To form a tangle in our experiments, the worms were forced to deviate from their otherwise planar swimming motion to form a three-dimensional helix. If significant out-of-plane swimming occurred, the entanglement probability was seen to vastly decrease, as easily explained by our geometric model. The clear entanglement difference between the nearly 2D versus a complete 3D motion could, thus, be a significant factor in, e.g., how arrays of cilia avoid tangling due to their sophisticated 3D motion [51]. The aspect ratio of cilia can be as high as  $L/D = 100$  (versus 19 for our worms), where  $D$  is the diameter. Since cilia are typically arranged at distances  $0.27\text{--}0.4 \mu\text{m}$  apart [52],  $(L/d)_{\text{cilia}} = 75$ . The lack of ciliar entanglements is, thus, surprising when compared to our experimental findings in planar swimming and highlights the importance of the specific motion patterns used to avoid or achieve a tangled network. Strong hydrodynamic interactions could also act to modify ciliar entanglements at close distances. Hydrodynamic interactions were not discovered between the worms in our experiments, consistent with the findings of others [21].

Here we have presented a time-resolved, dynamic study of the tangling of active stringlike worms. By describing the system with a simple model based on the overlap probability of the worm heads during their undulatory swimming, the critical ratio between the worm length and distance for any entanglement to be possible was

quantitatively predicted and shown to be in excellent agreement with experimental observations. Furthermore, the entanglement probability was analytically derived and successfully fit to the data. It is clear that the tangling of the active strings is far from random but a statistically predictable process based on the relative motion of their ends. These experiments provide an interesting model system to understand the intricate interactions present in active matter such as cilia and bacterial flagella.

The financial support by NSERC of Canada is gratefully acknowledged. The authors also thank Solomon Barkley for helpful discussions.

---

\*dalnoki@mcmaster.ca

- [1] N. Gravish, S. V. Franklin, D. L. Hu, and D. I. Goldman, *Phys. Rev. Lett.* **108**, 208001 (2012).
- [2] D. T. English and H. E. Jones, *Arch. Dermatol.* **107**, 77 (1973).
- [3] A. Goriely, in *Physical and Numerical Models in Knot Theory*, edited by J. A. Calvo, K. C. Millett, E. J. Rawdon, and A. Stasiak (World Scientific, Singapore, 2005), Chap. 6.
- [4] S. A. Wasserman and N. R. Cozzarelli, *Science* **232**, 951 (1986).
- [5] E. Ercolini, F. Valle, J. Adamcik, G. Witz, R. Metzler, P. De Los Rios, J. Roca, and G. Dietler, *Phys. Rev. Lett.* **98**, 058102 (2007).
- [6] J. Tang, N. Du, and P. S. Doyle, *Proc. Natl. Acad. Sci. U.S.A.* **108**, 16153 (2011).
- [7] P.-G. de Gennes, *Macromolecules* **17**, 703 (1984).
- [8] K. J. Eckelbarger, C. M. Young, and J. L. Cameron, *Biol. Bull.* **176**, 257 (1989).
- [9] D. M. Woolley and G. G. Vernon, *J. Exp. Biol.* **204**, 1333 (2001).
- [10] C. J. Ingham and E. Ben-Jacob, *BMC Microbiol.* **8**, 36 (2008).
- [11] D. O. Serra, A. M. Richter, G. Klauck, F. Mika, and R. Hengge, *mBio* **4**, e00103-13 (2013).
- [12] L. Turner, W. S. Ryu, and H. C. Berg, *J. Bacteriol.* **182**, 2793 (2000).
- [13] R. M. Macnab, *Proc. Natl. Acad. Sci. U.S.A.* **74**, 221 (1977).
- [14] M. Kim, J. C. Bird, A. J. Van Parys, K. S. Breuer, and T. R. Powers, *Proc. Natl. Acad. Sci. U.S.A.* **100**, 15481 (2003).
- [15] M. F. Copeland and D. B. Weibel, *Soft Matter* **5**, 1174 (2009).
- [16] J. Dunkel, S. Heidenreich, K. Drescher, H. H. Wensink, M. Bär, and R. E. Goldstein, *Phys. Rev. Lett.* **110**, 228102 (2013).
- [17] L. Gheber and Z. Priel, *Biophys. J.* **55**, 183 (1989).
- [18] S. Gueron, K. Levit-Gurevich, N. Liron, and J. J. Blum, *Proc. Natl. Acad. Sci. U.S.A.* **94**, 6001 (1997).
- [19] P. Lenz and A. Ryskin, *Phys. Biol.* **3**, 285 (2006).
- [20] S. Michelin and E. Lauga, *Phys. Fluids* **22**, 111901 (2010).
- [21] J. Yuan, D. M. Raizen, and H. H. Bau, *Proc. Natl. Acad. Sci. U.S.A.* **111**, 6865 (2014).
- [22] S. Gart, D. Vella, and S. Jung, *Soft Matter* **7**, 2444 (2011).
- [23] H. S. Fisher, L. Giomi, H. E. Hoekstra, and L. Mahadevan, *Proc. R. Soc. B* **281**, 20140296 (2014).
- [24] D. Saintillan and M. J. Shelley, *Phys. Rev. Lett.* **99**, 058102 (2007).
- [25] T. Sanchez, D. Welch, D. Nicastro, and Z. Dogic, *Science* **333**, 456 (2011).
- [26] T. Sanchez, D. T. N. Chen, S. J. DeCamp, M. Heymann, and Z. Dogic, *Nature (London)* **491**, 431 (2012).
- [27] A. Bricard, J.-B. Caussin, N. Desreumaux, O. Dauchot, and D. Bartolo, *Nature (London)* **503**, 95 (2013).
- [28] N. Darnton, L. Turner, K. Breuer, and H. Berg, *Biophys. J.* **86**, 1863 (2004).
- [29] D. L. Koch and G. Subramanian, *Annu. Rev. Fluid Mech.* **43**, 637 (2011).
- [30] T. Vicsek and A. Zafeiris, *Phys. Rep.* **517**, 71 (2012).
- [31] A. Belmonte, *Proc. Natl. Acad. Sci. U.S.A.* **104**, 17243 (2007).
- [32] A. Belmonte, M. J. Shelley, S. T. Eldakar, and C. H. Wiggins, *Phys. Rev. Lett.* **87**, 114301 (2001).
- [33] E. Ben-Naim, Z. A. Daya, P. Vorobieff, and R. E. Ecke, *Phys. Rev. Lett.* **86**, 1414 (2001).
- [34] J. Hickford, R. Jones, S. Courrech du Pont, and J. Eggers, *Phys. Rev. E* **74**, 052101 (2006).
- [35] D. M. Raymer and D. E. Smith, *Proc. Natl. Acad. Sci. U.S.A.* **104**, 16432 (2007).
- [36] J. H. Conway, in *Computational Problems in Abstract Algebra*, edited by J. Leech (Pergamon Press, New York, 1969), pp. 329–358.
- [37] S. A. Bleiler, *Trans. Am. Math. Soc.* **282**, 385 (1984).
- [38] J. R. Goldman and L. H. Kauffman, *Adv. Appl. Math.* **18**, 300 (1997).
- [39] L. H. Kauffman and S. Lambropoulou, *Adv. Appl. Math.* **33**, 199 (2004).
- [40] D. Meluzzi, D. E. Smith, and G. Arya, *Annu. Rev. Biophys.* **39**, 349 (2010).
- [41] S. Brenner, *Genetics* **77**, 71 (1974).
- [42] M. Backholm, W. S. Ryu, and K. Dalnoki-Veress, *Proc. Natl. Acad. Sci. U.S.A.* **110**, 4528 (2013).
- [43] R. D. Schulman, M. Backholm, W. S. Ryu, and K. Dalnoki-Veress, *Phys. Rev. E* **89**, 050701 (2014).
- [44] P. Sauvage, M. Argentina, J. Drappier, T. Senden, J. Siméon, and J.-M. Di Meglio, *J. Biomech.* **44**, 1117 (2011).
- [45] X. N. Shen and P. E. Arratia, *Phys. Rev. Lett.* **106**, 208101 (2011).
- [46] M.-J. Colbert, A. N. Raegen, C. Fradin, and K. Dalnoki-Veress, *Eur. Phys. J. E* **30**, 117 (2009).
- [47] M.-J. Colbert, F. Brochard-Wyart, C. Fradin, and K. Dalnoki-Veress, *Biophys. J.* **99**, 3555 (2010).
- [48] See Supplemental Material <http://link.aps.org/supplemental/10.1103/PhysRevLett.113.138101> for experimental details and movies of the worms tangling.
- [49] J. H. Maddocks and J. B. Keller, *SIAM J. Appl. Math.* **47**, 1185 (1987).
- [50] R. O'Hagan and M. Chalfie, *International review of neurobiology* **69**, 169 (2005).
- [51] A. Vilfan and F. Jülicher, *Phys. Rev. Lett.* **96**, 058102 (2006).
- [52] Z. Teff, Z. Priel, and L. A. Gheber, *Biophys. J.* **92**, 1813 (2007).

# Supplementary Information for “Tangling of Tethered Swimmers: Interactions between Two Nematodes”

Matilda Backholm,<sup>1</sup> Rafael D. Schulman,<sup>1</sup> William S. Ryu,<sup>2</sup> and Kari Dalnoki-Veress<sup>1,3,\*</sup>

<sup>1</sup>*Department of Physics & Astronomy and the Brockhouse Institute for Materials Research, McMaster University, Hamilton, Ontario L8S 4M1, Canada*

<sup>2</sup>*Department of Physics and the Donnelly Centre, University of Toronto, Toronto, Ontario M5S 1A7, Canada*

<sup>3</sup>*Laboratoire de Physico-Chimie Théorique, UMR CNRS Gulliver 7083, ESPCI, Paris, France*

(Dated: September 9, 2014)

## EXPERIMENTAL DETAILS

Wild-type worms (N2) were acquired from the Caenorhabditis Genetics Center and cultivated in an incubator according to standard methods on *Escherichia coli* (OP50) nematode growth media (NGM) plates at 20°C [1]. Young adult and adult worms were picked from the plates into a droplet of M9 buffer sitting on a thin cover slip. A chamber was then built around the drop with a second cover slip and two (2 mm thick) spacers on both sides. The chamber was filled with more buffer, placed on top of an inverted microscope, and two micropipettes, attached to XYZ translational stages, were finally positioned into the chamber, as shown in Fig. 1. By attaching thin tubes to the back ends of the pipettes and applying suction with syringes, worms were captured by their tails and carefully brought to the middle of the chamber. By capturing the worms as they were swimming at (and in the plane of) the bottom glass slide, both of the worms could be ensured to initially swim in the same plane. Furthermore, by applying a high enough suction to the tails, vast rotation in the pipettes could be avoided.

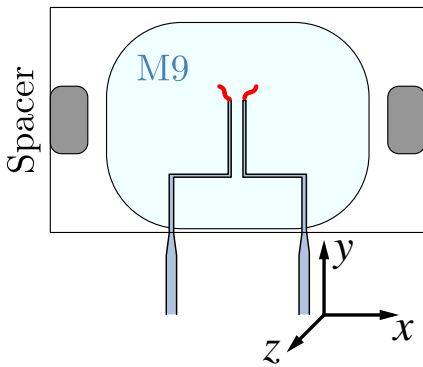


FIG. 1. Schematic diagram of the experimental setup as seen from above.

Optical microscopy images were captured at 56 fps for around 3 minutes per worm distance, corresponding to more than 10 000 images per experiment. With an average worm swimming frequency of  $f = 2.1 \pm 0.2$

Hz, hundreds of swimming cycles were monitored for each separation distance. The pipettes were made to be very flexible, so that the forces produced by the swimming worms would cause the thin glass capillaries to deflect. The deflections of the pipettes were obtained with cross-correlation image analysis using MATLAB (MathWorks). An example data set is shown in Fig. 2, where the pipette deflections are plotted as a function of time. In states of normal swimming, the pipettes can be used as force sensors to probe the viscous forces experienced by the microswimmers (see Ref. [2]). When an entanglement occurs, the pipettes are pulled together and these clear deflections above that of normal swimming (dashed lines) were used to recognize all entanglements in the long experiments.

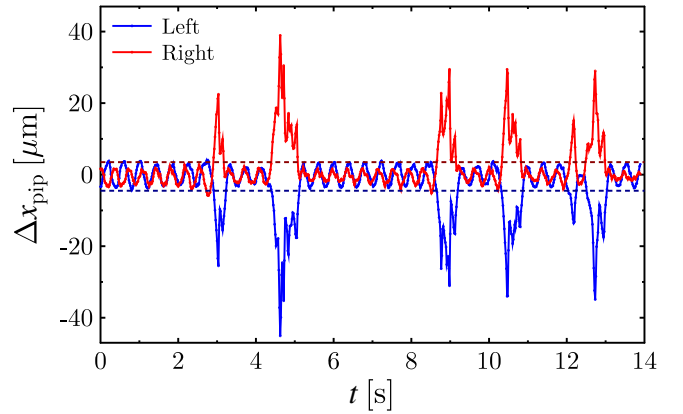


FIG. 2. Pipette deflection as a function of time. During normal swimming, the pipettes follow the undulatory swimming patterns of the worms. The large peaks correspond to entanglements between the worms, pulling the pipettes above the peaks (dashed lines) set by normal swimming.

An entanglement had to, per definition, last longer than at least 8 frames (0.14 s), since tangling events shorter than this did not represent an actual tangle, but occurred when the worms were touching as they swam past each other in slightly different planes. The number and lifetimes of real tangles were then analyzed.

The worms were seen to undergo small changes in their amplitude and/or swimming axis during the experiment. For the analysis, the maximum swimming amplitude was

considered since a critical  $d/A$  ratio was desired.

The vertical error bars in Fig. 4 in the main manuscript represent the standard error of the mean of the entanglement probability at different times of the experiment, propagated together with the standard deviation of the swimming frequencies of both worms and the precision of the analysis. The horizontal error bars were propagated based on the standard deviation of the worm lengths as well as the error in worm separation.

---

\* dalnoki@mcmaster.ca

[1] S. Brenner, *Genetics* **77**, 71 (1974).

[2] R. D. Schulman, M. Backholm, W. S. Ryu, and K. Dalnoki-Veress, *Phys. Rev. E* **89**, 050701 (2014).

# Appendix B

## List of additional papers

The manuscripts listed and briefly summarized below represent other research I have performed during my PhD studies. These papers are not part of the main focus of this thesis.

### B.1 Crawling dynamics

*Direct measurements of drag forces in C. elegans crawling locomotion*, Y. Rabets, M. Backholm, K. Dalnoki-Veress, and W. S. Ryu, *Biophysical Journal* **107**, 1980-1987 (2014).

Here we investigated the drag coefficients and crawling dynamics of *C. elegans* on different types of agar. By using micropipette deflection, the adhesion force and drag coefficients between the worm and the gel surface were directly measured. This was achieved by pulling the worm off, or dragging it over the surface, respectively. Furthermore, the forces involved in the crawling motion of *C. elegans* were investigated and an extension of RFT was applied to reconstruct the measured forces.

I helped Yegor Rabets design a micropipette deflection setup in the lab of W. Ryu at the University of Toronto. I also contributed with continuous input during the project, helped with the interpretation of data, and edited a late version of the manuscript.

## B.2 Hole relaxation in viscous films

*Capillary levelling of a cylindrical hole in a viscous film*, M. Backholm, M. Benzaquen, T. Salez, E. Raphaël, and K. Dalnoki-Veress, *Soft Matter* **10**, 2550-2558 (2014).

During my doctoral studies, I had the opportunity to perform research in the field of polymer physics in close collaboration with Michael Benzaquen, Dr. Thomas Salez, and Dr. Elie Raphaël at the ESPCI in Paris. Our focus has been to continue the work of Dr. Joshua McGraw on the capillary levelling of thin films with initially sharp topographical features, such as steps, trenches, and cylindrical holes. The main goal has been to investigate how such features relax over time as the system is heated above its glass transition temperature.

In this work, we investigated the capillary levelling of cylindrical holes in viscous polystyrene films. I initiated and designed the sample preparation procedure and performed all experiments and data analysis. The theoretical work was led by the team in Paris with my continuous input. I prepared all figures and wrote the first draft of the manuscript, except for the theoretical section which was written by M. Benzaquen and T. Salez.

## B.3 Levelling of trenches in viscous films

*Relaxation and intermediate asymptotics of a rectangular trench in a viscous film*, O. Bäümchen, M. Benzaquen, T. Salez, J. D. McGraw, M. Backholm, P. Fowler, E. Raphaël, and K. Dalnoki-Veress, *Physical Review E* **88**, 035001 (2013).

Here Dr. Oliver Bäümchen led the project on the relaxation of rectangular trenches in viscous polystyrene films. I was brought into the project at its final stage and contributed by performing the experiments on trench levelling in the linear regime, where the depth of the trench was significantly smaller than the thickness of the bottom film. I also edited a late version of the manuscript.

## B.4 Mechanical properties of hydrogels

*Crosslinked bulk hydrogels formed through Diels-Alder coupling of Furan- and Maleimide-modified Poly(methyl vinyl ether-alt-maleic acid)*, S. A. Stewart, M. Backholm, N. A. D. Burke, and H. D. H. Stöver, submitted to Journal of Polymer Science (2015).

During my time at McMaster University, I have been part of the CREATE program for Integrated Development of Extracellular Matrices (IDEM) to contribute with physical modelling and testing of various hydrogels designed for cell encapsulation purposes. Within the framework of this research, I co-supervised Tim Govey, Chris Miranda, and Richard Parg for their undergraduate thesis or summer research projects carried out in our group. We used the in house “bead squisher” to measure the mechanical properties of gels prepared by Rachelle Kleinberger and Alison Stewart under the supervision of Dr. Harald Stöver.

In this project, I trained A. Stewart to use the bead squisher, helped with the data analysis and interpretation of the results and contributed with the theoretical treatment of the elasticity data. Furthermore, I wrote the physical modelling section of the paper.



# Appendix C

## Derivations

### C.1 Area moment of inertia of a hollow cylinder

The area moment of inertia for a symmetrical cross-section, as exemplified by a hollow cylinder in Fig. C.1, is defined as  $I = I_x = I_y = \int y^2 dA$  [145].

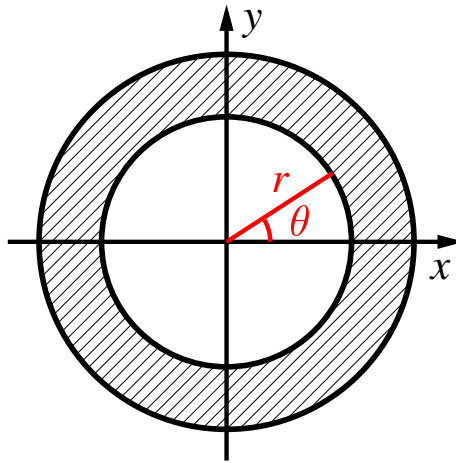


Figure C.1: Cross section of hollow cylinder with inner and outer diameters  $d$  and  $D$ .

Using polar coordinates, i.e.,  $y = r \sin \theta$  and  $dA = r dr d\theta$ , gives

$$I = \int_0^{2\pi} \sin^2 \theta d\theta \int_{d/2}^{D/2} r^3 dr = \frac{\pi}{64} [D^4 - d^4], \quad (\text{C.1})$$

where  $D$  and  $d$  are the outer and inner diameter of the cylinder, respectively.

## C.2 Three-point bending of simply supported beam

In Fig. C.2, a schematic diagram of a three-point bending measurement on a simply supported beam is shown. The distance between the two simple supports is  $L$ , whereas  $a$  corresponds to the distance between the left support and the location of the applied force  $F$ . The origin of the coordinate system as well as the axis of rotation is defined at the left support, as shown in the image.

The assumption of translational and rotational equilibrium gives  $N_1 = F(1 - a/L)$  and  $N_2 = aF/L$ , where  $N_1$  and  $N_2$  are the normal forces from the two simple supports. For the case of  $x \leq a$ , the bending moment can be calculated as  $M(x) = N_1x$  [28]. Assuming that the force is applied right between the supports,  $L = 2a$ , and  $M(x) = Fx/2$ . The Euler-Bernoulli equation, defined for the quasistatic bending of a slender, isotropic beam of a constant cross-section, gives

$$\frac{d^2y(x)}{dx^2} = \frac{M(x)}{EI} = \frac{F}{2EI}x, \quad (\text{C.2})$$

where  $y$  denotes the bending of the beam. Solving this differential equation with the boundary condition for a simply supported beam ( $y(0) = 0$  and  $y'(a) = 0$ ) gives

$$y(x) = \frac{F}{2EI} \left( \frac{1}{6}x^3 - \frac{1}{2}a^2x \right). \quad (\text{C.3})$$

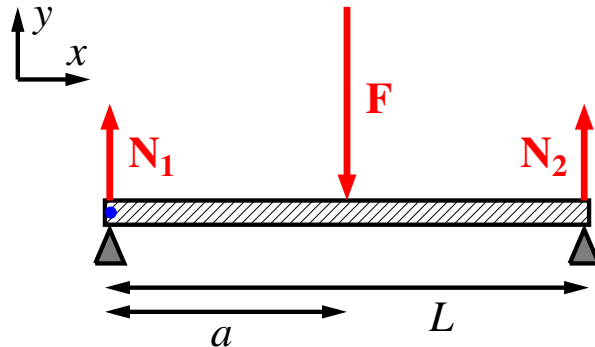


Figure C.2: Schematic diagram of a three-point bending measurement on a simply supported beam. The origin of the coordinate system as well as the axis of rotation is denoted by the blue dot at the left end of the beam.

Evaluating this at  $x = a = L/2$  finally leaves us with the bending of the beam at the position of the applied force

$$y(a) = \frac{L^3}{48EI} F. \quad (\text{C.4})$$

With the same approach, the case of  $L \neq 2a$  (as shown in Fig. 1.5) gives [146]

$$y(a) = \frac{a^2(L-a)^2}{3LEI} F. \quad (\text{C.5})$$